Phase separation and spin domains in quasi-1D spinor condensates

Andrea Invernizzi

THÈSE DE DOCTORAT
de l'Université de recherche
Paris Sciences Lettres – PSL Research University

préparée à l'École normale supérieure

Phase separation and spin domains in quasi-1D spinor condensates

par Andrea Invernizzi

dirigée par Fabrice Gerbier
& Jean Dalibard

École doctorale n°564
Spécialité : Physique
Soutenue le 09.11.2017

Composition du Jury :

Mme. Isabelle Bouchoule
CNRS - Institut d'Optique
Rapporteuse

M. Jan Arlt
Aarhus University
Rapporteur

Mme. Anna Minguzzi
CNRS - LPMMC Grenoble
Examinatrice

M. Fabrice Gerbier
CNRS
Directeur de thèse

M. Jean Dalibard
Collège de France
Co-directeur de thèse

ENS | PSL RESEARCH UNIVERSITY PARIS

Contents

1. Introduction

On June the 5th, 1995, the team led by Eric Cornell and Carl Wieman produced for the first time a Bose-Einstein condensate (BEC). Using the cooling laser techniques developed in the previous years, [27, 29, 143], they cooled down a dilute ensemble of Rb atoms to the quantum degeneracy via evaporative cooling. Slightly later, the team led by Wolfgang Ketterle obtained a condensate of Na atoms. Their discovery, awarded with the Nobel Prize in 2001 [31, 85], gave birth to a new research field, at the crossing point of atomic physics, condensed matter and quantum optics called *Quantum gases*.

The theoretical prediction of BEC condensation dates back to the works [21, 39] by Einstein and Bose. We know from quantum mechanics that the particle-wave duality becomes more and more visible as we lower the temperature. In a system of particles (bosons) at temperature T, we can define for each particle the De Broglie wavelength $\lambda_{\mathrm{dB}} \propto T^{-1/2}$, describing the size of the wave associated to each particle. Lowering the temperature, λ_{dB} increases and will eventually become comparable to the average inter-particle distance $\propto n^{-1/3}$. While fermions tend to avoid each other (Pauli principle), bosons tend to gather into a single state [105]: this phenomenon is BEC.

The Bose-Einstein condensate represents an interesting system by itself. Its phase coherence properties were proofed by making two BEC interfere, [5] and by measuring its long range coherence, [18]. The superfluid nature of the BEC was proofed by the observation of quantised vortices, [110, 108, 1] and of superfluid flow, [150]. An "atom laser" was built from a BEC, exploiting the wave nature of this state of matter, [19, 60]. At the same time, the techniques used for producing BEC were extended to fermions, obtaining the first ultracold degenerate Fermi gas [38].

Dilute systems are characterised by weak interactions, but Feshbach resonances, observed from the early years [72], can be used to change the interaction strength and to switch from repulsive to attractive interactions and vice-versa. Feshbach resonances were also used to produce molecules in Fermi gases to observe the crossover from a BEC of weakly bound molecules to a superfluid composed of Coopers pairs [22, 11].

The first BEC experiments were based on magnetic trapping. A few years later, the development of optical trapping, [170, 57], allowed a great control over the trap geometry. Increasing the confinement along one or two directions permitted the study of systems in lower dimensionality. In 1D traps, the Tonks-Girardeau regime was observed [90, 136] and in 2D traps, the Berezinskii-Kosterlitz-Thouless transition was observed [59]. More recently, a text-book model like the box potential was realised, [49].

In the last years, more complicated trapping potentials have been produced. The light of different laser beams can be made interfere to obtain periodic potentials in 1,2 and 3 dimensions: the optical lattices. Thanks to these potentials different condensed matter models were studied, as the phase transition between superfluid and Mott insulator phase [56, 167, 174, 80] and magnetism on a lattice [177]. Disordered potentials were also produced and quantum localisation phenomena observed [14].

Spinor Bose Gases

Optical trapping provided also a potential independent from the atomic spin. This enabled the study of multicomponent gases. In condensed matter superfluid ^{3}He, [185] and some unconventional superconductors with spin-triplet Cooper pairing [127] are examples of multicomponent quantum fluids. In Bose gases, mixtures composed by different isotopes of the same atom [135] and by different atomic species [114] have been studied, alongside with Fermi gases mixtures, [157], and Bose-Fermi gases mixtures, [46, 155].

Degenerate Bose gases with a spin degree of freedom are called spinor gases and constitute another example of multicomponent quantum fluids. The interplay between external and internal degrees of freedom in these systems gives rise to phenomena unfamiliar from studies of single-component ("scalar") quantum fluids. The macroscopic occupation of the ground state allows to distinguish energy levels whose energy difference ϵ is small compared to the system temperature $\epsilon \ll k_B T$. This quantum-statistical Bose enhancement, [169], allows inter-component interactions, which have typical energies $\sim 1\,\mathrm{nK}$, to order the system just below the Bose-Einstein condensation temperature and makes spinor condensates a good system to study magnetic phases of matter.

Thanks to spin exchange contact interactions between the internal components, spinor condensates present coherent spin oscillations [104, 194, 25] and parametric spin amplification [92]. Moreover, depending on the nature of the spin interaction, ferromagnetic or antiferromagnetic, the magnetic ordering of the BEC results in different possible magnetic phases, [169].
Dipolar interactions, thanks to their long range, give an important contribution to the physics of the system. Dipolar effects are clearly visible in high spin atoms, as chromium, erbium and dysprosium, where density deformations [98] and instability [97] were observed. Dipolar gases present also spin relaxation phenomena [43, 137, 126] and anisotropic exci-

tations [15]. The anisotropy of dipole interactions favours low-energy states characterised by spin textures [190].

Spinor Gases and Stepwise condensation

Part of this thesis is devoted to the study of the thermodynamics of a spin-1 ^{23}Na gas. In particular, we study how the magnetic ordering appear in the system as we lower the temperature and we cross the critical point. Several studies, [188, 79, 40] indicate that without additional constraints, the Bose-Einstein statistics favours ferromagnetism. In our system, however, the longitudinal magnetisation is conserved. This has a deep impact on the thermodynamic phase diagram. From the theoretical point of view the problem has been already studied in a certain number of ways, [73, 192, 82, 100, 182, 145, 83] and the generic solution is that BEC occurs first in one specific component, while magnetic order appears at lower temperatures, when two or more components condense. In the thesis we will present the observation of multi-step condensation in our condensate of sodium atoms.

Spin Domains and Phase transition

In the second part of the thesis we present the study of the spin-1 condensate in an anisotropic trap. In this configuration, the system presents the formation of domains of spins, [173]. This system was already studied in [173, 117, 171], but the ground state configuration of the system in a uniform magnetic field has not yet been studied in detail. The ground state of spin-1 antiferromagnetic Bose gases presents two magnetic phases, [76]: an antiferromagnetic phase and a transverse magnetised phase. For a system with spin domains, the phase transition between these two different phases corresponds also to the transition, respectively, from the miscible to the immiscible regime.
In the thesis we report on the experimental investigation of the ground state of the system in a uniform magnetic field as well as on the observation of the phase transition. The measurement of the response to a magnetic field gradient is also presented.

Thesis Outline

The manuscript is organised as follow:

Chapter 2 is divided in three sections. The first section is a brief introduction to 3D condensates in a harmonic trap. The second section introduces some notions on 1D condensates, we will focus on the phase fluctuations and the concept of quasi-condensate. In the third and final section we introduce the spin-1 ^{23}Na spinor condensate.

Chapter 3 is focused on the experimental techniques used to trap, cool down and image our spinor condensate. After a first part devoted to the experimental sequence to obtain a 3D condensate, we focus on the methods used to manipulate the internal spin degrees of freedom of the atoms. A description of the analysis method used for the images follows. The chapter ends with a description of the transfer of the atoms from the 3D to the 1D trap.

Chapter 4 is devoted to the presentation of the article "Stepwise Bose-Einstein Condensation in a Spinor Gas", [48], a work performed at the beginning of my thesis and already described in [47]. We report the article without modifications.

Chapter 5 is divided into two parts. In the first part we discuss the theory that predicts the ground state of a spin-1 condensate in an anisotropic harmonic trap. In the second part we present the experimental characterisation of the ground state, the measured Equation of State of a polarised cloud (all the atoms in the $m_F = +1$ Zeeman sub-level) and the observed phase transition.

Chapter 6 presents some measurements on the spin-dipole polarisability of the system.

Appendix A contains a theoretical study of the transfer of our condensate from the 3D to the 1D trap.

Appendix B presents the algorithm used to solve the Gross-Pitaevskii equations for a spin-1 Bose gas in a unidimensional system.

2. Elements of Bose-Einstein condensation

Bose-Einstein condensation (BEC) is a second order transition observed in Bose gases defined by the macroscopic occupation of the ground state of the system. The first time Bose-Einstein condensation was observed, [36, 4], the atoms were trapped in a magnetic trap. Nowadays optical dipole traps, produced by focused laser beams, are widely used and enabled the trapping of atoms in different internal states at the same time.
During this thesis work we studied a spin 1 Bose gas of ^{23}Na atoms that we cool down to the quantum degeneracy in optical dipole traps. Optical dipole traps can be approximated, in the neighbourhood of their focus, by a harmonic potential. Hence, we limit our discussion to Bose gases trapped in a potential:

$$V_{\text{ext}}(\mathbf{r}) = \frac{1}{2}m\left(\omega_x x^2 + \omega_y y^2 + \omega_z z^2\right) \tag{2.1}$$

where m is the mass of a single atom and ω_i, with $i \in \{x, y, z\}$, are the harmonic oscillator frequencies along the three coordinates axis. The versatility of these kinds of traps allowed us to study the system in two different geometries: in a 3D configuration, where $\omega_x \sim \omega_y \sim \omega_z$, and in a 1D configuration, where $\omega_x \sim \omega_y \gg \omega_z$.
This chapter presents the basics elements of Bose-Einstein condensation theory in 3D and 1D geometries before focusing on the spin 1 Sodium condensate. The contents introduced here constitute a minimal theory reference necessary to understand the experiments performed on spinor BECs reported in this thesis. We refer the reader to some more general reviews [33, 141, 169].
The content is organised as follow: Section 2.1 and Section 2.2 present the theory of single component scalar BEC in 3D and 1D harmonic traps, respectively. Section 2.3 describes the theory of spin-1 spinor condensates.

2.1. The scalar Bose-Einstein condensate in a 3d harmonic trap

This Section is devoted to a brief presentation of the Bose-Einstein condensation in 3D harmonic trap. We introduce the $T = 0$ theory for an ideal Bose gas, before describing

the effects of interactions and the local density approximation. The $T > 0$ theory, with the Bogoliubov and Hartree-Fock approximations follow.

2.1.1. The ideal Bose gas

The ground state wavefunction of the non interacting Bose gas, trapped of a potential like (2.1), corresponds to the ground state of the 3-dimensional harmonic oscillator:

$$\Psi = \sqrt{N} \prod_{x,y,z} \left(\frac{1}{\pi a_{i,ho}^2} \right)^{\frac{1}{4}} exp\left(- \frac{x_i^2}{a_{i,ho}^2} \right) \tag{2.2}$$

where

$$a_{i,ho} = \sqrt{\frac{\hbar}{m\,\omega_i}} \tag{2.3}$$

is the harmonic oscillator length. We need a description of the atoms in the excited states; we do so by adopting a semi-classical approximation [147]. We obtain an analytical formula for the density of thermal atoms :

$$n_{\rm th} = \frac{1}{\lambda_{\rm th}^3} \mathrm{g}_{3/2}(\mathrm{e}^{\beta(\mu - V_{\rm ext})}) \tag{2.4}$$

where $\lambda_{\rm th} = h/\sqrt{2\pi m k_{\rm B} T}$ is the thermal wavelength and $\mathrm{g}_{3/2}$ is a polylogarithmic function, or Bose function of the general form $\mathrm{g}_\alpha(x) = \sum_{j=1}^{+\infty} \frac{x^j}{j^\alpha}$. If we integrate over the entire system we find that the total number of thermal atoms is

$$N = \left(\frac{k_{\rm B} T}{\hbar \bar{\omega}} \right)^3 \mathrm{g}_3(\mathrm{e}^{\beta\mu}) \tag{2.5}$$

where $\bar{\omega} = (\omega_x\,\omega_y\,\omega_z)^{1/3}$ is a geometrical average of the three harmonic oscillator frequencies. The chemical potential $\mu < 0$ is fixed by the condition $N_{\rm tot} = N + N_0$, where N_0 is the number of atoms in the ground state. At a fixed temperature, if we increase the number of atoms in the system, μ grows until $\mu = 0$ in (2.5). The Bose function $\mathrm{g}_3(x)$ reaches at $x = 1$ its maximum value and this corresponds to a maximum value for the number of atoms in the excited states N. Bose functions are not defined for values $x > 1$, physically this means that if we add more particles to the system, they will not populate the already saturated excited states, but they will start to condense in the ground state $N_0/N_{\rm tot} \neq 0$. This saturation of the excited states marks the onset of Bose-Einstein condensation.

2.1.2. The role of interactions

Even when atomic gases are extremely dilute, they are far from ideal gases. Interactions play very important roles and must be taken into account to predict the experimental observations [33]. As soon as the condensate forms, the density inside the degenerate cloud rises significantly such that the interactions become important to quantitatively

describe the system. We introduce here the nature of interatomic interactions relevant for this work and the formalism to treat them. Furthermore, we discuss the impact of interactions on the shape of the condensate and of the thermal component.

Ultracold collisions

Ultracold atom systems have very low particle densities on the order $10^{13} - 10^{15}\,\mathrm{cm}^{-3}$, so we can describe them as dilute. In this regime, only two-body collisions are important[1]. Collisions between two atoms can be modelled as two colliding plane waves, whose scattering product is expressed as a superposition of partial waves with increasing angular momentum. Due to the low energies involved, scattering events are treated in the low energy limit, for which only the components with low angular momentum can overcome the centrifugal barrier and explore the interaction region. The lowest angular momentum partial wave $l = 0$ (denoted historically by letter s) corresponds to spherically symmetric scattering. s-wave scattering is entirely described by the scattering length a. When a is positive, interactions are repulsive, vice versa, for negative a, interactions are attractive. For sodium atoms, $a = 54.54\,a_B = 2.89\,\mathrm{nm}$, where a_B is the Bohr radius, see [93]. For a complete treatment of elastic collisions in the slow particle limit, we refer the reader to [99].
Instead of using the real interaction potential, to simplify the calculation one usually introduces an effective potential with the same scattering length. A widely used choice is the contact potential introduced by Fermi:

$$\hat{V}(\mathbf{r} - \mathbf{r}') = \frac{4\pi\hbar^2 a}{m}\delta(\mathbf{r} - \mathbf{r}') \tag{2.6}$$

where $\delta(\mathbf{r} - \mathbf{r}')$ is the Dirac delta function and where we define the coupling constant:

$$g = \frac{4\pi\hbar^2 a}{m}. \tag{2.7}$$

2.1.3. The mean-field approximation at $T = 0$

In the following we address the physics of BEC in many-body systems with interactions modeled by the potential given in (2.6). The many-body Hamiltonian for the interacting Bose gas in the second quantisation formalism [147] is:

$$\hat{H} = \int d\mathbf{r}\,\hat{\Psi}^\dagger(\mathbf{r})\left(-\frac{\hbar^2\Delta}{2m} + \hat{V}_{\mathrm{ext}}(\mathbf{r})\right)\hat{\Psi}(\mathbf{r}) + \frac{g}{2}\int d\mathbf{r}\,\hat{\Psi}^\dagger(\mathbf{r})\,\hat{\Psi}^\dagger(\mathbf{r})\,\hat{\Psi}(\mathbf{r})\,\hat{\Psi}(\mathbf{r}), \tag{2.8}$$

where g is the coupling constant defined in (2.7) and $\hat{\Psi}(\mathbf{r})$ is the field annihilation operator which destroys a particle at position $\mathbf{r}$. The ground state of the system, in principle,

[1] Inelastic three-body collisions can be identified in sufficiently dense systems since they are usually associated with atom loss. Given that the densities of our systems are sufficiently low, we neglect elastic N-body collisions with $N > 2$.

has to be computed starting from the Hamiltonian (2.8), but we need to make some approximation to solve the problem. We adopt a mean-field approximation at $T = 0$, for which all the atoms in the ground state share the same single-particle wavefunction. Minimizing the Gibbs free-energy $G = \langle H \rangle - \mu N$, we obtain the Gross-Pitaevskii equation, see [147]:

$$\left(-\frac{\hbar^2 \Delta}{2m} + \hat{V}_{\text{ext}}(\mathbf{r}) + g|\Psi(\mathbf{r})|^2 \right) \Psi(\mathbf{r}) = \mu \Psi(\mathbf{r}), \tag{2.9}$$

from which we can compute this wavefunction for the condensed part. If we set $g = 0$ we recover the harmonic oscillator (2.2).
We now focus our attention to an approximated solution of (2.9), in the limit of strong interactions. The Thomas-Fermi approximation then consists in neglecting the kinetic energy with respect to the interaction energy. The importance of interactions is described by the dimensionless ratio:

$$N \frac{a}{a_{\text{ho}}}, \tag{2.10}$$

that must be much bigger than one for the Thomas-fermi approximation to hold. For $N = 1.6 \cdot 10^4$ and $\omega_z = 2\pi \cdot 4\,\text{Hz}$ the ratio is ~ 52, hence for our 1D geometry, we can use this approximation[2]. In the Thomas-Fermi limit we obtain an analytic solution for the ground state wavefunction equal to

$$\Psi(\mathbf{r}) = \sqrt{\frac{\mu_{\text{TF}}}{g}\left(1 - \frac{x^2}{R_{\text{TF},x}^2} - \frac{y^2}{R_{\text{TF},y}^2} - \frac{z^2}{R_{\text{TF},z}^2}\right)}, \tag{2.11}$$

where $\mu_{\text{TF}} > V_{\text{ext}}(\mathbf{r})$ and zero elsewhere. The condensate wavefunction is an inverted parabola with three principal radii

$$\frac{1}{2} m \omega_i^2 R_{\text{TF},i}^2 = \mu_{\text{TF}}. \tag{2.12}$$

The Thomas-Fermi chemical potential μ_{TF} is fixed by the total number of atoms,

$$\mu_{\text{TF}} = \frac{\hbar \bar{\omega}}{2} \left(\frac{15 N a}{a_{\text{ho}}} \right)^{\frac{2}{5}} \tag{2.13}$$

We introduce also the healing length ξ_{int}. For a condensate in a box of volume V, see [147] , this is equal to:

$$\xi_{\text{int}} = \sqrt{\frac{\hbar^2}{2mgn}} \tag{2.14}$$

This is the length scale on which the condensate wavefunction heals from a perturbation.

[2]For the 3D geometry the atom number remains the same, but the trap frequencies are $\bar{\omega} = 2\pi \cdot 500\,\text{Hz}$: $Na/a_{\text{ho}} \approx 580$, the Thomas-Fermi approximation can still be applied.

2.1.4. Mean field approximation at $T > 0$

To extend our $T = 0$ theory for the condensate to $T > 0$, we present two approximations: the Bogoliubov and the Hartree-Fock approximations. The Bogoliubov approximation is valid only for very low temperatures, when the number of atoms in the condensate N_0 is approximately equal to the total number of atoms in the system; the gas is considered formed by the condensate plus a bath of non-interacting quasiparticles whose energy spectrum is modified by the interaction with the condensate atoms. The Hartree-Fock approximation, on the other side, is valid at higher temperatures, where we have a non negligible thermal part; it consists in neglecting all correlations between atoms and only consider the effect of interactions through a mean-field potential.

The Bogoliubov theory

We illustrate here the method, introduced by Bogoliubov in [20], to describe the low-energy excitations of weakly interacting condensate. We are more interested to define some basic concepts which we will use later on than to show the reader a way to compute Bogoliubov excitations for our particular system. Hence we limit ourself to an homogeneous system of volume V . For a complete discussion about excitations in trapped gases, we refer the reader to [140].
First of all, we rewrite the Hamiltonian (2.8) in terms of the operators that create and destroy a particle in momentum states (plane waves). These can be defined from $\hat{\Psi}(\mathbf{r})$ by

$$\hat{a}_{\mathbf{p}} = \frac{1}{\sqrt{V}} \int d\mathbf{r}\, \mathrm{e}^{-i\mathbf{p}\cdot\mathbf{r}/\hbar}\, \hat{\Psi}(\mathbf{r}). \tag{2.15}$$

If N_0 is the number of atoms in the state with $\mathbf{p} = 0$, in the thermodynamic limit, the action of the two operators $\hat{a}_{\mathbf{p}=0}$ and $\hat{a}^{\dagger}_{\mathbf{p}=0}$ on the state of the condensate is on the order of $\sqrt{N_0}$, much bigger than the commutator between the two operators of order 1. Hence, we can treat the two operators as c-numbers and approximate them as $\hat{a}_{\mathbf{p}=0} \approx \hat{a}^{\dagger}_{\mathbf{p}=0} \approx \sqrt{N_0}$. Following the Bogoliubov's approach, we divide the Hamiltonian in condensed and thermal part and we consider only terms at least quadratic in $\hat{a}_{\mathbf{p}=0}$ and $\hat{a}^{\dagger}_{\mathbf{p}=0}$. The linear terms disappear since the $T = 0$ state of the system, given by the GP equation, is stable. The resulting Hamiltonian can be diagonalised introducing the transformation

$$\hat{\alpha}_{\mathbf{p}} = u_{\mathbf{p}}\hat{a}_{\mathbf{p}} + v^{*}_{-\mathbf{p}}\hat{a}^{\dagger}_{-\mathbf{p}} \tag{2.16}$$

where $u_{\mathbf{p}}$ and $v_{\mathbf{p}}$ are amplitudes to determine. In the homogeneous case, $u_{\mathbf{p}}$ and $v_{\mathbf{p}}$ are plane waves and the diagonalised Hamiltonian has the form

$$\hat{H_{\mathrm{BOG}}} - \mu\hat{N} = E_0 - \mu N + \sum_{\mathbf{p}\neq 0} E_p \hat{\alpha}^{\dagger}_{\mathbf{p}}\hat{\alpha}_{\mathbf{p}} \tag{2.17}$$

with E_0 the energy of the ground state, $n_0 = N_0/V$ the density of particles in the zero momentum state and $\epsilon_p = p^2/2m$ the single particle's energy. The energy E_p, imposing $\mu = gn_0$, is the spectrum of the Bogoliubov's excitations

$$E_p = \sqrt{(\epsilon_p)^2 + 2\epsilon_p n_0 g} \tag{2.18}$$

To understand the nature of these excitations we consider the spectrum at high and low momenta. At low p values $p \ll mc_s$,where $c_s = \sqrt{\frac{n_0 g}{m}}$, the energy is equal to $\epsilon_p = c_s p$ and the excitations are phonon-like. At high values of p ($p \gg mc_s$), instead, the energy $\epsilon_p = \epsilon_p^0$ is equal to the energy of a single free particle. Looking more carefully at the wave vector $\frac{\hbar}{mc_s}$, we notice that it is the inverse of the healing length defined in (2.14). So the healing length is also the length associated with the wavevector below which the spectrum is phonon-like and above which it becomes free particle-like.
Since the Bogoliubov theory works at $T > 0$, we can use it to find the non-condensed density:

$$n_{\rm nc} = \frac{1}{V}\sum_{\mathbf{p}\neq 0}\langle \hat{a}^\dagger_{\mathbf{p}}\hat{a}_{\mathbf{p}}\rangle = \frac{1}{V}\sum_{\mathbf{p}\neq 0}|v_{\mathbf{p}}|^2 + \frac{1}{V}\sum_{\mathbf{p}\neq 0}(|u_{\mathbf{p}}|^2 + |v_{\mathbf{p}}|^2)\frac{1}{e^{E_p}-1} \tag{2.19}$$

where the first term accounts for the quantum depletion of the condensate[3], and the second for the thermal depletion; we call the latter $n_{\rm th}$. The Bogoliubov amplitudes are given by

$$|u_{\mathbf{p}}|^2 = \frac{1}{2}\left(\frac{\epsilon_p + gn_0}{E_p} + 1\right), \qquad |v_{\mathbf{p}}|^2 = \frac{1}{2}\left(\frac{\epsilon_p + gn_0}{E_p} - 1\right) \tag{2.20}$$

where we set $\mu = gn_0$. The thermal part of the non-condensed density can thus be written as

$$n_{\rm th} = \frac{1}{(2\pi)^3}\int d\mathbf{p}\,\frac{\epsilon_p + gn_0}{E_p}\frac{1}{e^{E_p}-1} = \frac{1}{\lambda^3_{th}} f_{\rm Bog}\left(\alpha = \frac{\mu}{k_B T}\right) \tag{2.21}$$

where

$$f_{\rm Bog}\left(\alpha = \frac{\mu}{k_B T}\right) = \frac{4}{\sqrt{\pi}}\int_0^{+\infty} dx\,\frac{x(x^2+\alpha)}{\sqrt{x^2+2\alpha}}\,\frac{1}{e^{x\sqrt{x^2+2\alpha}}-1} \tag{2.22}$$

where we introduced $x = p/_{\rm th}$. In the Bogoliubov approximation, we consider the non-condensed gas to be dilute enough to treat the excitations as an ideal gas.

The Hartree-Fock theory

The Hartree-Fock (HF) approximation was first applied to the study of trapped Bose gas by [54, 68]; it consists in considering only the average effect of interactions, neglecting all correlations. Also in this case we limit the discussion to a Bose gas trapped in a box of volume V. Replacing in the Hamiltonian (2.8), the Fourier components of the density operators, (2.15), by their thermal averages, the Hamiltonian is given by

$$\hat{H_{\rm HF}} - \mu\hat{N} = E_0 - \mu N + \sum_{\mathbf{p}\neq 0}(\epsilon_p - \mu + 2gn)\hat{a}^\dagger_{\mathbf{p}}\hat{a}_{\mathbf{p}}. \tag{2.23}$$

From the Hamiltonian, we can derive a formula for the density of thermal atoms

$$n_{\rm th} = \frac{1}{\lambda^3_{\rm th}} g_{3/2}(e^{\beta(\mu-2gn)}) \tag{2.24}$$

[3]We neglect it, since it is usually less than 10^{-2}.

where the chemical potential $\mu = 2gn - gn_0$. Eq. (2.24) must be solved self-consistently for n.
The Bogoliubov and the Hartree-Fock approximations give the same results in the regime $T \gg gn_0$. Looking at the Bogoliubov spectrum, this corresponds to the limit where the spectrum is dominated by single particle excitations. The difference between the two approximations arise at low temperatures, where the Bogoliubov spectrum is gapless ($\epsilon_p \to 0$ when $p \to 0$) and the Hartree-Fock spectrum has a gap, $\epsilon_p \to gn_0$ when $p \to 0$. In 3D, this difference can be neglected as long as $T \gtrsim \mu$.
Considering a quasi-condensate in a elongated harmonic trap, see Section 2.2, if the cloud temperature and chemical potential are of the order of the radial trapping potential, the Hartree-Fock approach fails due to the correlations in position that are not taken into account in the model. These correlations reduce the density fluctuations and allow the formation of a quasi-condensate, see [180].

The semi-ideal model

The extension of the two approximations discussed above to the case of a trapped Bose gas can be done easily thanks to the local density approximation. This applies to systems trapped in a sufficiently smooth potential V_{ext}, so that the density profile $n(r)$ is not uniform but varies sufficiently slowly in space. We can use the healing length ξ, given by (2.14), to divide the systems in cells of size d such that $1/\xi \ll d \ll R$. the density in each cell is then quasi-uniform and we can treat each cell as a quasi-uniform gas with local chemical potential $\mu_{\text{loc}}(r) = \mu - V_{\text{ext}}$.
Here we want to discuss a simple approximation, limit of both the HF and Bogoliubov theories in the regime where the mean-field due to the thermal component can be neglected. This is the semi-ideal model, introduced in [124]. It consists in treating the thermal atoms as a gas of non-interacting particles evolving in an effective potential given by the trap potential plus the mean-field potential exerted by the condensate $V_{\text{eff}} = V_{\text{ext}} + 2gn_0$. In this limit the thermal part can be written as:

$$n_{\text{th}} = \frac{1}{\lambda_{\text{th}}^3} \mathrm{g}_{3/2}\left(\mathrm{e}^{-\beta|V_{\text{ext}}(\mathbf{r})-\mu|}\right), \tag{2.25}$$

where no self-consistent calculation is needed, but we only need to solve for μ.
In Chapter 3 we use these different models to obtain the temperature and the condensed fraction of the condensate. In Figure 2.1 we show the difference between the Bogoliubov approximation and the semi-ideal model for a condensate at $T = 10\,\text{nK}$ and $\mu_{\text{TF}} = 120\,\text{Hz}$.

Phonon-like excitations and Hydrodynamic excitations

When discussing the Bogoliubov theory, we saw that low momentum excitations of the condensate are phonon-like. If we consider the condensate in the Thomas-Fermi limit these excitations are well described by the hydrodynamic theory of superfluids in the collisionless regime at zero temperature, see [33]. This formalism is needed to treat phase

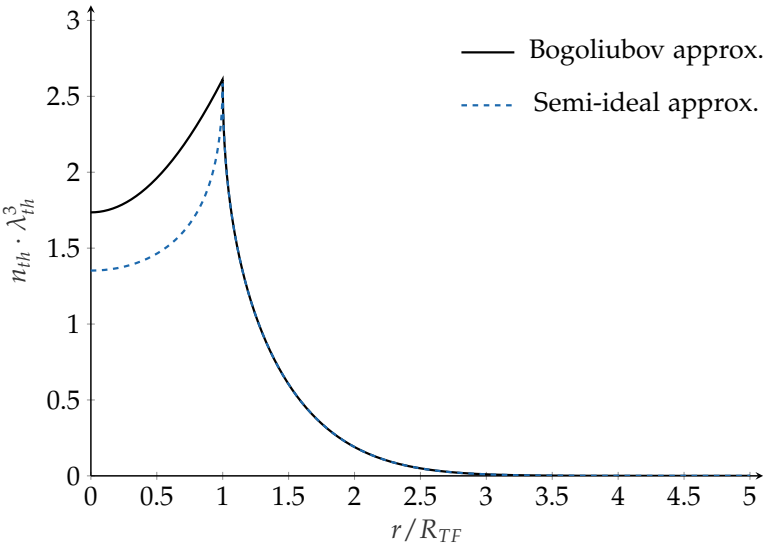

Figure 2.1.: Density profile of the thermal component in the Bogoliubov (solid black) and semi-ideal (dashed blue) approximations. The profiles have been calculated for a condensate at $T = 10\,\mathrm{nK}$ and $\mu_{\mathrm{TF}} = 120\,\mathrm{Hz}$.

fluctuations in the unidimensional condensate.
We start rewriting the condensate wavefunction as

$$\Psi = \mathrm{e}^{i\phi(\mathbf{r})}\sqrt{n_0(\mathbf{r})} \tag{2.26}$$

Introducing (2.26) in the Gross-Pitaevskii equation (2.9), we find the two hydrodynamic equations:

$$\frac{\partial}{\partial t}n + \frac{\hbar}{m}\nabla\cdot(\nabla\phi\, n) = 0 \tag{2.27}$$

and

$$\hbar\frac{\partial}{\partial t}\phi + V_{\mathrm{ext}} + gn - \frac{\hbar^2}{2m}\frac{\Delta\sqrt{n}}{\sqrt{n}} + \frac{\hbar^2}{2m}|\nabla\phi|^2 = 0 \tag{2.28}$$

The first equation is the continuity equation, the second one is the generalised Euler's equation for a perfect fluid. The fourth left-handed term in (2.28) gives the contribution of the kinetic energy and it is called quantum pressure term. In the Thomas-Fermi limit[4], we neglect the contribution of this quantum pressure term.
Linearising the two equations we find

$$\frac{\partial}{\partial t}\delta n = -\frac{\hbar}{m}\nabla\cdot(n_0\nabla\phi) \tag{2.29}$$

$$\hbar\frac{\partial}{\partial t}\phi = -g\,\delta n \tag{2.30}$$

[4]The validity of this approximation in the dynamic equations means that, for sufficiently large N, the restoring force of the collective mode is mostly due to external forces and to the interactions, the quantum pressure term playing a negligible role (see [176]).

The link between the density/phase picture of the excitations and the Bogoliubov's picture has been discussed in [142]. Writing the field operator $\hat{\Psi}(\mathbf{r})$ as a function of the density and phase operators

$$\hat{\Psi}(\mathbf{r}) = \sqrt{\hat{n}(\mathbf{r})}\, e^{i\hat{\phi}(\mathbf{r})}, \tag{2.31}$$

the authors have found that the phase and density operators obey operator equations similar to (2.27) and (2.28) . They expanded the density and phase operators in the terms of the Bogoliubov elementary excitations

$$\delta\hat{n}(\mathbf{r},t) = \sqrt{n_0(\mathbf{r})} \sum_{\mathbf{p}} f^-_{\mathbf{p}} \hat{\alpha}_{\mathbf{p}} e^{-i\omega_p t} + \text{h.c.} \tag{2.32}$$

$$\hat{\phi}(\mathbf{r},t) = \frac{1}{2i\sqrt{n_0(\mathbf{r})}} \sum_{\mathbf{p}} f^+_{\mathbf{p}} \hat{\alpha}_{\mathbf{p}} e^{-i\omega_p t} + \text{h.c.} \tag{2.33}$$

where the two eigenfunctions can be written as linear combinations of the Bogoliubov amplitudes $f^{\pm}_{\mathbf{p}} = u_{\mathbf{p}} \pm v_{\mathbf{p}}$ and are normalised by the condition

$$\frac{1}{2}\int \left(f^+_{\mathbf{p}}(\mathbf{r}) f^{-*}_{\mathbf{p}}(\mathbf{r}) + f^-_{\mathbf{p}}(\mathbf{r}) f^{+*}_{\mathbf{p}}(\mathbf{r}) \right) = 1. \tag{2.34}$$

To complete the link with the hydrodynamic picture of the excitations, it is then possible to rewrite δn and $\delta\phi$ of equations (2.27) and (2.28) as $\delta n_{\mathbf{p}} = \sqrt{n_0} f^-_{\mathbf{p}}$ and $\delta\phi_{\mathbf{p}} = (1/2i\sqrt{n_0}) f^+_{\mathbf{p}}$. We will use this formalism in the next section to predict the effect of density fluctuations on the density matrix of the condensate for a anisotropic dipole trap.

2.2. The scalar Bose gas in a 1D harmonic trap

In this section, we focus our attention on scalar Bose gases in 1D traps, see Figure 2.2. We are interested in anisotropic traps described by the potential

$$V_{\text{ext}}(\mathbf{r}_\perp, z) = \frac{1}{2} m(\omega_\perp^2 r_\perp^2 + \omega_z^2 z^2) \tag{2.35}$$

where $\omega_z \ll \omega_\perp$.

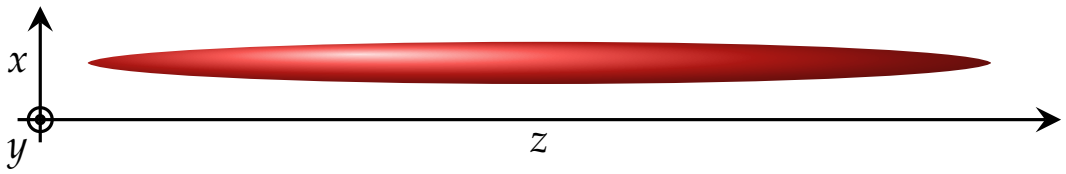

Figure 2.2.: Schematic of the density distribution of a BEC trapped in a cylindrically symmetric harmonic potential with $\omega_z \ll \omega_\perp$.

By effectively freezing two of the three spatial degrees of freedoms of the atoms moving inside the potential we engineer a system kinematically equivalent to a 1D system, [141].

Quantum 1D systems can not Bose-Einstein condense, but they present an occupation of the low energy excited states called quasi-condensate. Such systems can be described as composed by different condensates, each one with a well defined phase, but with very small correlations between the phases of adjacent condensates. In order to discuss BEC in an anisotropic harmonic potential, we start by discussing the non-interacting 1D Bose gas and the concept of quasi-condensate. As a second step, we introduce the 3D system with the anisotropic potential and we define some important quantities, such as the phase coherence length L_ϕ and the phase temperature T_ϕ. Finally, we discuss how we can experimentally observe these fluctuations with the time of flight techniques (TOF), see [86].

2.2.1. Bose gases in one dimension

We start by introducing the 1D ideal Bose gas. In the thermodynamic limit, there is no Bose-Einstein condensation, see [141]. This is due to the fact that density of states is constant for a single particle in a 1D harmonic potential, so that the number of atoms in the excited states never saturates. For finite systems, on the other hand, a phenomenon very similar to BEC is possible. In their works [87] and [184], the authors found that the population of the excited states saturate below a temperature

$$T_{c,1D} \approx \frac{N\hbar\omega}{k_{\mathrm{B}}\log(N)} \tag{2.36}$$

where N is the total atom number and ω is the harmonic oscillator frequency of the 1D harmonic potential.
As in the 3D case, interactions play a major role to describe a"quasi-condensate" gas. In the 3D geometry, phase and density fluctuations are small and the condensate has a well defined phase; this is not true for 1D systems, where phase fluctuations are large[5], due to the large occupancy of low energy excited states, [184]. In order to define properly these concepts, we introduce the density matrix of the system in the second quantisation formalism:

$$\rho(\mathbf{r},\mathbf{r}') = \left\langle \hat{\Psi}^\dagger(\mathbf{r})\hat{\Psi}(\mathbf{r}')\right\rangle \tag{2.37}$$

To study phase fluctuations, it is useful to rewrite the field operator (2.31) as a classical field $\Psi = \sqrt{n_0(\mathbf{r})}e^{i\phi(\mathbf{r})}$, where density fluctuations are neglected, such that $\sqrt{\hat{n}(\mathbf{r})} = \sqrt{n_0(\mathbf{r}) + \delta\hat{n}(\mathbf{r})} \simeq \sqrt{n_0(\mathbf{r})}$ and ϕ is a classical Gaussian random variable, such that $\frac{p^2}{2m}\left\langle \left|\phi_p\right|^2\right\rangle = \frac{k_B T}{2}$. The density matrix can then be rewritten as

$$\rho(\mathbf{r},\mathbf{r}') \simeq \sqrt{n_0(\mathbf{r})n_0(\mathbf{r}')}\left\langle e^{i(\hat{\phi}(\mathbf{r}')-\hat{\phi}(\mathbf{r}))}\right\rangle = \sqrt{n_0(\mathbf{r})n_0(\mathbf{r}')}e^{-\frac{1}{2}\left\langle[\hat{\phi}(\mathbf{r}')-\hat{\phi}(\mathbf{r})]^2\right\rangle}, \tag{2.38}$$

where we used the fact that ϕ obeys a Gaussian statistics. The squared difference between the phase fluctuations can be rewritten using (2.33) and approximating the operator $\alpha_{\mathbf{p}}$

[5] Density fluctuations remain small also in the 1D case, see [140].

with another Gaussian random variable α_p such that $\left\langle \left| \alpha_p \right|^2 \right\rangle = (\exp(\epsilon_p/k_BT) - 1)^{-1}$. We find

$$\left\langle (\Delta\phi)^2 \right\rangle = \left\langle [\phi(\mathbf{r}) - \phi(\mathbf{r}')]^2 \right\rangle = \frac{1}{4n_0(\mathbf{r})} \sum_p |f_{\mathbf{p}}^+(\mathbf{r})|^2 (2 \left\langle \left| \alpha_p \right|^2 \right\rangle + 1) \tag{2.39}$$

The sum in (2.39) is dominated by the low energy excitations with large excitation number, such that $\left\langle \left| \alpha_p \right|^2 \right\rangle \simeq k_BT/\epsilon_p$.
In the 1D case [140], it is possible to demonstrate that

$$\rho(z, z') \approx \sqrt{n_{1D}(z) n_{1D}(z')} \exp\left(- \frac{|z - z'|}{L_\phi} \right) \tag{2.40}$$

where $L_\phi = L\frac{T_\phi}{T} = \frac{n_{1D}\hbar^2}{mk_BT}$ defines a phase temperature such that $L > L_\phi$ if $T > T_\phi$. By lowering the temperature below $T_{c,1D}$, defined in (2.36), the phase is not well defined along the entire system. The density matrix decays on a length scale L_ϕ smaller than the condensate size. Therefore we define this state as a "quasi-condensate". Below T_ϕ, the phase is almost uniform across the cloud and the two extrema have a well defined phase relation.

2.2.2. Quasicondensation in 3D anisotropic trap

We discuss now the case of highly anisotropic harmonic traps with potentials given by (2.35), where $\omega_z \ll \omega_\perp$. These configurations are important because they are realised in our experiments. Figure 2.3 illustrates the different regimes accessible with ultracold atoms in optical potentials like (2.35). The critical temperature T_c for 3D condensation and the phase temperature T_ϕ divide the diagram in three different regions, see [142]:

> $\mathbf{T_c < T_\phi}$: in this case, as we lower the temperature, the 3D Bose gas condenses in a Bose-Einstein condensate;
>
> $\mathbf{T_c > T_\phi}$: in this second case the Bose gas, at $T = T_c$ exhibits a macroscopic occupation of the transverse ground state but the phase fluctuations along the z axis: it is a quasi-condensate. Then, at $T = T_\phi$, the phase fluctuations become negligible and the gas finally condenses.

The line $\mu = \hbar\omega_\perp$ separates the regime of 1D condensation from the regime of 3D condensation. For 1D condensation we want to prevent the promotion of atoms from the ground state to excited states of the harmonic oscillator in the radial direction, therefore it is necessary that $\mu \ll \hbar\omega_\perp$. A true 1D gas can be produced imposing much strict constraints: $k_BT \ll \hbar\omega_\perp$ together with $\mu \ll \hbar\omega_\perp$.
The optical dipole trap in our experiment allows us to prepare anisotropic harmonic oscillator traps with trap frequencies in the following ranges: $\omega_z = 2\pi[3 - 6]$ Hz, $\omega_\perp = 2\pi[250 - 400]$ Hz and $\mu = [100, 200]$ Hz. The green point in Figure 2.3 gives the resulting position in the diagram: we are at the edge between the 3D and the 1D regimes.

To describe properly the system, we have to redefine a coupling constant starting from the 3D one. In [133], the 3D scattering length has been rescaled to obtain an effective 1D coupling constants $g_{1D} = 2\hbar^2 a/ma_{\text{ho}}^2$ in the case of a BEC in the 1D regime $\mu \ll \hbar\omega_z$

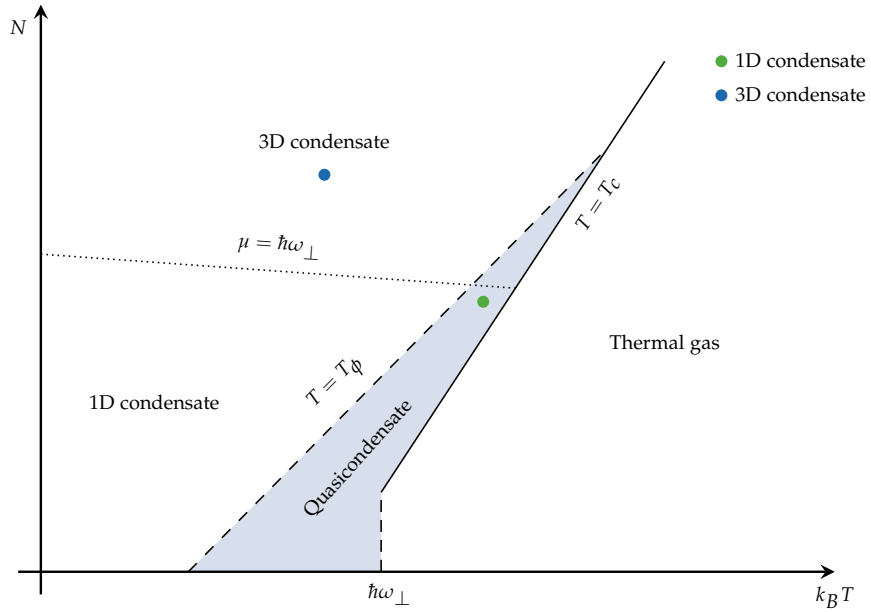

Figure 2.3.: Different regimes for a Bose gas trapped in an anisotropic trap. For high temperatures the gas is thermal. Cooling down the system, two regimes are present, defined by the two temperatures T_c and T_ϕ, respectively, the critical temperature for a 3D Bose gas and the phase temperature below which phase fluctuations are negligible. When $T_\phi > T_c$ the gas condenses in a 3D Bose-Einstein condensate. When $T_\phi < T_c$, a quasi-condensate regime region is present. Cooling a quasi-condensate at $T < T_\phi$, we obtain a Bose-Einstein condensate. The line which corresponds to $\mu = \hbar\omega_\perp$ separates the 3D from the 1D condensation regime. The green dot denotes the regime of the 1D condensate we study, the blue dot the regime of the 3D condensate.

When we consider a very anisotropic potential like (2.35), with $\omega_z \ll \omega_\perp$, the excitations of the 3D trapped condensate can be divided in: *i.*) low energy axial excitations, with $\epsilon_p < \hbar\omega_\perp$ and *ii.*) high energy excitations, with $\epsilon_p > \omega_\perp$. The axial excitations have wavelengths longer than the condensate radial size R and exhibit a 1D behaviour, so we expect these excitations to give the main contribution to phase fluctuations[6].
In order to compute the spectrum of these excitations and the wavefunctions corresponding to these modes, we can use the formalism introduced in Subsection 2.1.4, as done in [176] and [175].

[6]High energy excitations have wavelengths much smaller than the condensate dimensions. This is why they exhibit a 3D behaviour and they are not considered in the calculations for the phase fluctuations.

Solving the hydrodynamic equations for a BEC in a anisotropic harmonic trap, the author of [176] found the spectrum of these excitations:

$$\epsilon_j = \hbar\omega_z\sqrt{j(j+3)/4} \tag{2.41}$$

with j positive integer and the wavefunctions of these modes

$$f_j^+(\mathbf{r}) = \sqrt{\frac{(j+2)(2j+3)g\,n_0(\mathbf{r})}{4\pi(j+1)R^2L\,\epsilon_j}}P_j^{(1,1)}\Big(\frac{x}{L}\Big) \tag{2.42}$$

where $P_j^{(1,1)}\Big(\frac{x}{L}\Big)$ are Jacobi polynomials, $n_0(\mathbf{r})$ is the Thomas-Fermi distribution, R and L are the condensate sizes, respectively, along the radial and weak axial directions. These excitations are the low energy axial excitations whose give the major contribution to phase fluctuations.
The authors of [142] obtained a correlation very similar to (2.40) and, from the phase coherence length, they defined the phase temperature $T_\phi = \frac{L_\phi}{L}T$ equal to

$$T_\phi = \frac{15(\hbar\omega_z)^2N}{32\mu}, \tag{2.43}$$

For our condensate in the 1D trap, considering $\omega_z = 4\,\mathrm{Hz}$, $N = 20000$ and a chemical potential $\mu = 150\,\mathrm{Hz}$, we find a phase temperature $T_\phi \approx 50\,\mathrm{nK}$. This means that phase fluctuations can only be neglected by cooling the condensate below temperatures $T < 50\,\mathrm{nK}$.

2.2.3. Phase Fluctuations in TOF

Phase fluctuations cannot be identified with in situ absorption imaging, [86], but they can be detected in time of flight as density modulations along the 1D system, more simply: they resemble fringes perpendicular to the trap weak axis. To discuss this signature of phase fluctuations, we follow the work of [63].
The authors model the appearance of phase fluctuations as fringes on the condensate density profile in time of flight. They describe the time evolution of the Bose-Einstein condensation order parameter as done in [24], with the self-similar solution

$$\psi = \frac{\sqrt{n_0}}{b_\perp^2(t)}\mathrm{e}^{i\phi_0}, \tag{2.44}$$

where $b_\perp^2(t) = 1+\omega_\perp^2t^2$ comes[7] and $\phi_0 = \frac{m}{2\hbar}\frac{\dot{b}_\perp}{b_\perp}r_\perp^2$, $r_\perp$ is the radial coordinate and n_0 is the Thomas-Fermi density profile. Introducing (2.44) in the Gross-Pitaevskii equation (2.9), the authors of [63] obtain two equations similar to the hydrodynamic equations

[7] The scaling factor $b_\perp(t)$ from the assumption that the global density evolves following $n_0(\rho/b_\perp,t) = n_0(\rho,0)/b_\perp^2$ and that the time of flight consists in abruptly switching off the trapping potential. This way of describing TOF has been introduced in [24].

introduced before. Linearising these equations and expanding the phase density operators in Bogoliubov modes, they find the equation:

$$\hbar^2 \delta\ddot{n}_p + \epsilon_p^2(t)\delta n_p = 0, \tag{2.45}$$

where

$$\epsilon_p(t) = \sqrt{\epsilon_p^2 + \frac{2p\epsilon_p}{b_\perp^2(t)}}, \tag{2.46}$$

is an instantaneous Bogoliubov spectrum (2.18) in time of flight. Looking at the spectrum we see that, at short time of flight, the dominant excitations have a phononic nature and, at long time of flight, the excitations are dominated by the single-particle part of the spectrum.
Solving the problem at expansion times between these two limits, $\omega_\perp/\omega_x^2 \gg t \gg \omega_\perp^{-1}$, the authors of [63] provided an analytical solution for the evolution of density fluctuations in TOF:

$$\frac{\delta n_p}{n_0}(z,t) = 2\delta\phi_p(z,0)\tau^{-\left(\frac{\omega_p}{\omega_\perp}\right)^2}\sin(\omega_p t) \tag{2.47}$$

where $\omega_p = \epsilon_p/\hbar$, $\tau = \omega_\perp t$ and from which, using $\partial_t \delta n_k = -2\omega_k n_0 \delta\phi_k$, they obtained a solution also for the phase fluctuations:

$$\phi_k(z,t) \approx \phi_k(z,0)\tau^{-\left(\frac{\omega_k}{\omega_\perp}\right)^2}\cos(\omega_k t) \tag{2.48}$$

To give a more intuitive interpretation of how phase fluctuations become visible in TOF, we can make an analogy with speckle patterns in optics. As we have already pointed out, a quasi-condensate can be seen as an ensemble of condensates with different uncorrelated phases; a similar system is the random distribution of the phases for the components of a laser field diffused by a rough surface. As the interference between the different components with different phases creates the speckle pattern, the different condensates with different phases interfere in TOF creating the density fringes we observe in the condensate density profile.
Averaging $(\delta n/n_0)^2$ over many realisations, the authors of [63] find an approximated relation for the mean square density fluctuations, at the centre of the trap, as a function of temperature:

$$\left\langle \left(\frac{\delta n(0,t)}{n_0(0,t)}\right)^2 \right\rangle \simeq \frac{T}{\epsilon T_\phi}\sqrt{\frac{\log\tau}{\pi}}\left(\sqrt{1+\sqrt{1+\left(\frac{\hbar\omega_\perp\tau}{\mu\log\tau}\right)^2}} - \sqrt{2}\right). \tag{2.49}$$

For $\tau \to 0$, the mean square density fluctuations tends to $\langle(\delta n/n_0)^2\rangle \to 0$. For very long TOF, instead, the density fluctuations become bigger and bigger with $\langle(\delta n/n_0)^2\rangle \propto \sqrt{\tau}$. Eq. (2.49) has been proposed for thermometry of 1D gases, [63]. In Figure 2.4 we plotted the mean square density fluctuations as a function of T/μ for $N = 2\cdot 10^4$ atoms, $\omega_z = 2\pi\,4\,\mathrm{Hz}$ and $\omega_\perp = 2\pi\,400\,\mathrm{Hz}$.

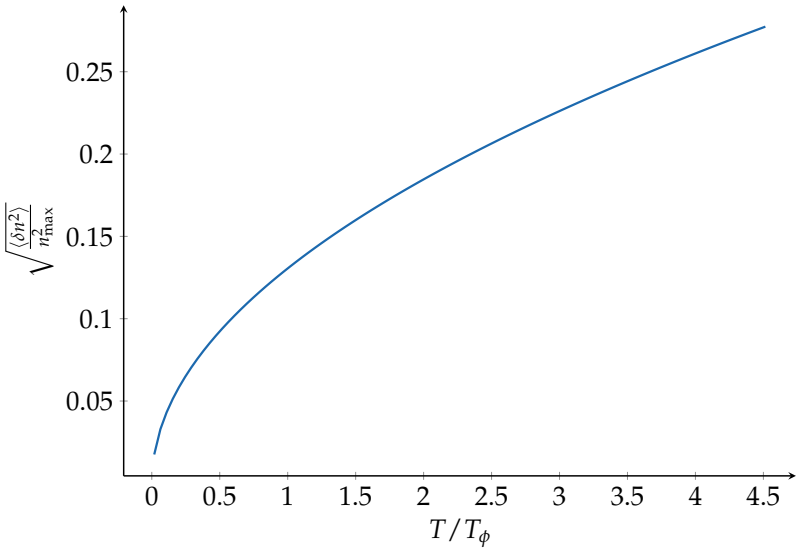

Figure 2.4.: Mean square density fluctuations as a function of T/T_ϕ computed from (2.49) for $N = 2 \cdot 10^4$ atoms, $\omega_z = 2\pi\, 4\,\mathrm{Hz}$ and $\omega_\perp = 2\pi\, 400\,\mathrm{Hz}$ and $t_{\mathrm{TOF}} = 3\,\mathrm{ms}$.

2.3. The spin-1 Bose Gas

Until now, we have discussed condensates with only one internal degree of freedom, also called scalar condensates. These were the first to be experimentally produced via evaporation in magnetic traps, [85, 31, 36]. When optical dipole traps became an accessible technology [170], it became easier to trap atoms with different hyperfine states in the same trap. This opened the possibility to study systems in which the interactions between different hyperfine components enrich the panorama. Degenerate Bose gases with a spin degree of freedom are called spinor condensates and we refer the reader to [84, 169] for a general exposition of the subject.
We start this section introducing the atomic structure of the Sodium atoms. From their properties, we construct the spinor Hamiltonian of the system and we find the ground state of this Hamiltonian based on a mean-field approach.

2.3.1. Hyperfine structure of Na atoms

The fine and hyperfine structures of Na atoms are sketched in Figure 2.5. The fine structure is the result of the coupling between the electron angular momentum $\mathbf{L}$ and the electron spin $\mathbf{S}$. We note the levels with the usual spectroscopic notation $N^{2S+1}L_J$, where the total angular momentum $\mathbf{J} = \mathbf{L} + \mathbf{S}$. In Figure 2.5, see [172], we can observe the ground state and the two first excited states. D_1 and D_2 are the name of the transitions between the ground state and the two excited states.

To obtain the hyperfine structure, the interaction between the total angular momentum $\mathbf{J}$ and the nuclear angular momentum $\mathbf{I}$, where $I = 3/2$ for ^{23}Na, is needed. At low

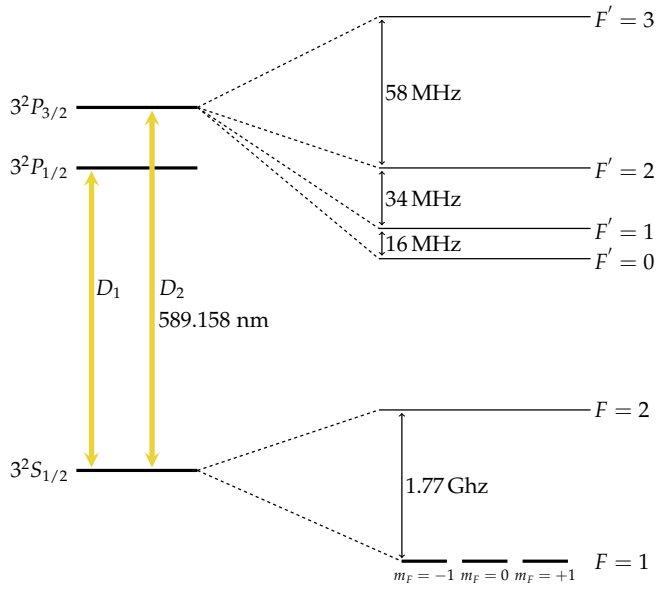

Figure 2.5.: Fine and hyperfine structure of the electronic ground state of a Na atom.

magnetic fields, the good quantum number is the total hyperfine angular momentum $\mathbf{F} = \mathbf{J} + \mathbf{I}$. As we can see in Figure 2.5, the ground state splits into two states with $F = 1$ and $F = 2$. The hyperfine splitting is $\Delta E_{hfs} \approx 1.77\,\text{GHz}$. The excited states $3^2P_{1/2}$ and $3^2P_{3/2}$ split in 2 and 4 hyperfine levels. Each hyperfine levels F can then be divided in $2F + 1$ Zeeman sublevels corresponding to the projection of the total angular momentum along the quantisation axis. These levels are degenerate for zero magnetic fields. In our experiment, we trap ^{23}Na atoms in an optical trap in the $F = 1$ ground state and we study the system composed by the three Zeeman sublevels $m_F = -1, 0$ and $+1$.

Optical dipole traps allow us to create the spin-independent potential we use to trap sodium atoms in the three Zeeman sublevels of $F = 1$. The red detuned[8] light of the laser induces an electric dipole moment. The interaction between the induced dipole moment and the electric field creates the trapping potential. In principle the atom polarisability is a rank-2 tensor that can be decomposed in a sum of three irreducible operators of rank 0, 1 and 2. The three terms produce, respectively, a scalar, a vector and a tensor light-shift, see [53]. In our case, if we use far red detuned, linear polarised light, only the scalar term is important and the potential is spin-independent, see [65].

2.3.2. Two-body scattering between Na atoms

We have already introduced interactions in the low energy limit in the first section of the chapter. The result was the definition of the pseudopotential (2.6) to describe two-

[8] Dipole trap can be blue detuned. In that case the laser light produce a repulsive potential for the neutral atoms.

body scattering. In the case of a spinor condensate, however, we have to consider also interactions between atoms in different internal degrees of freedom. In our case, we want to describe the scattering between two ^{23}Na atoms with $S = 1$.
First of all, the interaction potential is generated from the Coulomb repulsion between the electrons, so that it is invariant by spin rotations. This is an approximation, since magnetic dipole-dipole interactions break this symmetry. We neglect this contribution here and we justify this choice later. Also an applied magnetic field break the rotational symmetry, but the longitudinal spin projection S_z along the field direction is still conserved.
When two atoms with $S = 1$ collide, they combine their angular momenta in a total angular momentum $S = 0, 1$ or 2 with $m_S = -S, \dots, S$. Due to the rotational symmetry in angular momentum space, S is conserved during the collision. Therefore, we define a new interaction potential

$$\hat{V}(\mathbf{r}, \mathbf{r}') = \delta(\mathbf{r} - \mathbf{r}') \otimes \sum_S g_S \hat{P}_S \tag{2.50}$$

where $g_S = \frac{4\pi\hbar^2 a_S}{m}$ is the analogue of (2.7) for the S scattering channel and $\hat{P}_S = \sum_{m_S} |S, m_S\rangle \langle S, m_S|$ is the projection operator on the subspace with total angular momentum S.
We are discussing scattering events in the s-wave limit, hence the spatial part of the wave function is symmetric. The ^{23}Na atoms are bosons, therefore, also the spin part of the wave function must be symmetric. This means that only the $S = 0$ and 2 collisional channels are allowed. Thanks to the following two relations[9]:

$$\mathbb{1} = \hat{P}_0 + \hat{P}_2 \tag{2.51}$$

$$\hat{\mathbf{S}}_1 \cdot \hat{\mathbf{S}}_2 = \hat{P}_2 - 2\hat{P}_0 \tag{2.52}$$

we can rewrite the potential (2.50) in the form

$$\hat{V}(\mathbf{r}, \mathbf{r}') = \delta(\mathbf{r} - \mathbf{r}') \frac{\partial}{\partial r} r \otimes (\bar{g}\, \mathbb{1} + g_s \hat{\mathbf{S}}_1 \cdot \hat{\mathbf{S}}_2) \tag{2.53}$$

where there are two new coupling constant for the spin dependent and spin independent interactions:

$$\bar{g} = \frac{g_{S=0} + 2g_{S=2}}{3}, \tag{2.54}$$

$$g_s = \frac{g_{S=2} - g_{S=0}}{2}, \tag{2.55}$$

The scattering lengths for sodium atoms were measured in [93] combining Feshbach resonances and coupled-channels calculations. The authors found

$$\bar{a} = 2.8\,\mathrm{nm}, \tag{2.56}$$

$$a_s = 98\,\mathrm{pm}, \tag{2.57}$$

[9] The second relation can be derived using the expression of the total spin of the pair: $(\mathbf{S}_1 + \mathbf{S}_2)^2 = \mathbf{S}_1^2 + \mathbf{S}_2^2 + \mathbf{S}_1 \cdot \mathbf{S}_2 = \sum_S S(S+1)\hat{P}_S = 6\hat{P}_2$.

The positive sign of a_s means that the atoms minimise their energy anti-aligning their spins. Therefore, the ^{23}Na Bose gas exhibits an antiferromagnetic behaviour.
The ratio between the spin independent and spin dependent interaction is small:

$$\frac{a_s}{\bar{a}} \approx 0.036. \tag{2.58}$$

It is interesting to give also the ratio between magnetic dipole-dipole and spin dependent interactions. Considering two magnetic dipoles $\boldsymbol{\mu}_1$ and $\boldsymbol{\mu}_2$, the interaction energy between two permanent dipoles is equal to

$$U_{dd} = \frac{\mu_0}{4\pi r^3}\left[(\boldsymbol{\mu}_1 \cdot \boldsymbol{\mu}_2) - \frac{3}{r^2}(\boldsymbol{\mu}_1 \cdot \mathbf{r})(\boldsymbol{\mu}_2 \cdot \mathbf{r})\right] \tag{2.59}$$

where μ_0 is the vacuum permeability and, for atomic magnetic dipoles, we can write $\boldsymbol{\mu}_i = \mu_B g_j \mathbf{J}_i$, where g_j is the Landé factor and $\mathbf{J}_i$ is the total angular momentum. Therefore, for a polarised cloud with $|\langle \boldsymbol{S} \rangle| = 1$, the ratio between spin and dipole-dipole interactions is

$$\frac{g_{dd}}{g_s} \approx \frac{\mu_0 \mu_B^2 m}{16\pi\hbar^2 a_s} \approx 0.075 \tag{2.60}$$

From (2.60) it is clear that spin dependent interactions are much stronger than dipole-dipole interactions for ^{23}Na atoms therefore we are allowed to neglect them. This approximation is not valid for atomic species with much higher magnetic moment as, for example, Chromium [178, 16], Dysprosium [97] and Erbium [2].

2.3.3. The Zeeman shift

With interaction energy, another important energy scale for the system is provided by the magnetic field. Atoms are sensible to the application of an external magnetic field. In particular, ^{23}Na atoms have a magnetic dipole $\mu \approx \mu_B/2$. In the limit $\mu_B B/\Delta E_{hfs} \ll 1$, where the total angular momentum F is a good quantum number, the effect of an external magnetic field on a single atom can be obtained via an expansion of the Breit-Rabi formula, see [172],

$$\hat{H}^{(1)}_{\mathrm{mag}}(F, m_F) = (-1)^F \frac{m_F \mu_B B}{2} + (-1)^F \frac{(\mu_B B)^2}{4\,\Delta E_{hfs}}\left(1 - \frac{m_F^2}{4}\right) + \dots \tag{2.61}$$

where ΔE_{hfs} is the hyperfine energy splitting. The first term of (2.61) is the linear Zeeman energy; as we can see in Figure 2.6, it shifts the $m_F = +1$ and $m_F = -1$ levels, with respect to the $m_F = 0$ one, by $+p$ and $-p$, respectively, where

$$p = \frac{\mu_B B}{2} \approx h \cdot 696\,\frac{\mathrm{KHz}}{\mathrm{G}} \cdot B \tag{2.62}$$

The second term is the quadratic Zeeman energy, see Figure 2.6; it shifts both the $m_F = +1$ and the $m_F = -1$ levels, with respect to the $m_F = 0$ one, by $+q$, where

$$q = \frac{(\mu_B B)^2}{4\Delta E_{hfs}} \approx h \cdot 277\frac{\mathrm{Hz}}{\mathrm{G}^2} \cdot B^2. \tag{2.63}$$

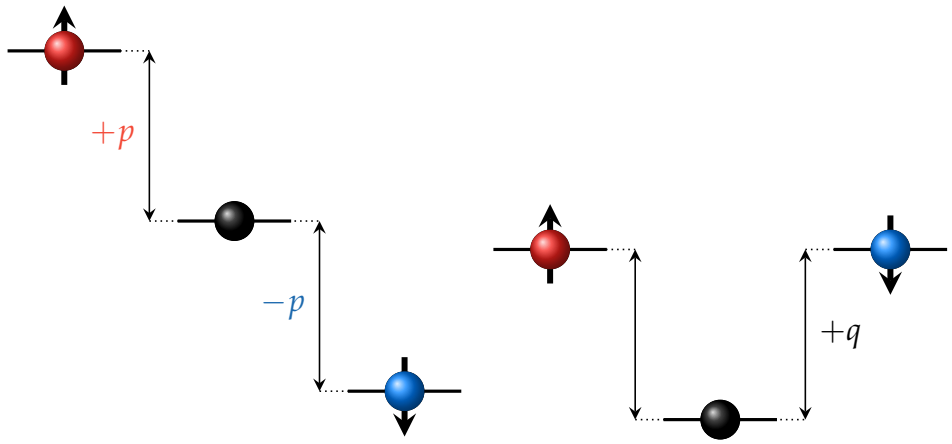

(a) Linear Zeeman shift (b) Quadratic Zeeman shift

Figure 2.6.: Effect of an external applied magnetic field on the Zeeman sub-levels of the $F = 1$ state of a ^{23}Na atom.

2.3.4. The Spinor Many-body Hamiltonian

The potential defined in (2.53) can be used to write the interaction many-body Hamiltonian for a systems of spin 1 bosons, see [169]:

$$\hat{H}_{\text{int}} = \frac{\bar{g}}{2}\int d\mathbf{r}\,\hat{n}(\mathbf{r})^2 + \frac{g_s}{2}\int d\mathbf{r}\,\hat{\mathbf{S}}^2 \tag{2.64}$$

where $\hat{n}(\mathbf{r})$ is the number operator and $\hat{\mathbf{S}} = (\hat{S}_x, \hat{S}_y, \hat{S}_z)$ is the spin density operator. Using the explicit expressions for the three spin density operators

$$\hat{S}_x = \frac{1}{\sqrt{2}}\Big(\hat{\Psi}^\dagger_{+1}\hat{\Psi}_0 + \hat{\Psi}^\dagger_{-1}\hat{\Psi}_0 + \text{h.c.}\Big) \tag{2.65}$$

$$\hat{S}_y = \frac{1}{\sqrt{2}}\Big(-i\hat{\Psi}^\dagger_{+1}\hat{\Psi}_0 + i\hat{\Psi}^\dagger_{-1}\hat{\Psi}_0 + \text{h.c.}\Big) \tag{2.66}$$

$$\hat{S}_z = \hat{\Psi}^\dagger_{+1}\hat{\Psi}_{+1} - \hat{\Psi}^\dagger_{-1}\hat{\Psi}_{-1} \tag{2.67}$$

and after some algebra, we can rewrite the interaction Hamiltonian as

$$\begin{aligned}\hat{H}_{\text{int}} = \int d\mathbf{r}\Bigg[&\frac{\bar{g}+g_s}{2}\hat{\Psi}^\dagger_{+1}\hat{\Psi}^\dagger_{+1}\hat{\Psi}_{+1}\hat{\Psi}_{+1} + \frac{\bar{g}}{2}\hat{\Psi}^\dagger_0\hat{\Psi}^\dagger_0\hat{\Psi}_0\hat{\Psi}_0 + \frac{\bar{g}+g_s}{2}\hat{\Psi}^\dagger_{-1}\hat{\Psi}^\dagger_{-1}\hat{\Psi}_{-1}\hat{\Psi}_{-1} \\ &+ \frac{(\bar{g}+g_s)}{2}\hat{\Psi}^\dagger_{+1}\hat{\Psi}^\dagger_0\hat{\Psi}_{+1}\hat{\Psi}_0 + \frac{(\bar{g}+g_s)}{2}\hat{\Psi}^\dagger_{-1}\hat{\Psi}^\dagger_0\hat{\Psi}_{-1}\hat{\Psi}_0 + \frac{(\bar{g}-g_s)}{2}\hat{\Psi}^\dagger_1\hat{\Psi}^\dagger_{-1}\hat{\Psi}_1\hat{\Psi}_{-1} \\ &+ g_s\Big(\hat{\Psi}^\dagger_{+1}\hat{\Psi}^\dagger_{-1}\hat{\Psi}_0\hat{\Psi}_0 + \hat{\Psi}^\dagger_0\hat{\Psi}^\dagger_0\hat{\Psi}_{+1}\hat{\Psi}_{-1}\Big)\Bigg]\end{aligned} \tag{2.68}$$

The first two lines of (2.68) give an energy shift due to the elastic collisions. The third line describes the only spin-flip collision allowed in the system. As we can see in Figure 2.7, two atoms in the Zeeman sub-levels $m_F = +1$ and $m_F = -1$ collide and come out as two atoms in the Zeeman sub-level $m_F = 0$. Since the Hamiltonian, by construction, is invariant over rotation in the angular momentum space, the projection of $\hat{\mathbf{S}}$ along the quantisation axis must be conserved. This conserved quantity is the longitudinal magnetisation of the system

$$M_z = \int d\mathbf{r}\, \hat{S}_z(\mathbf{r}) = N_{+1} - N_{-1} \tag{2.69}$$

Until now we have considered only interactions. The term of the many-body Hamiltonian corresponding to the magnetic field effect , using p and q, can be rewritten as:

$$\hat{H}_{\text{mag}} = p\hat{S}_z - q\left(\hat{N}_0 + 3\hat{N}\right) \tag{2.70}$$

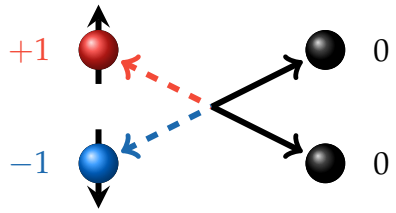

Figure 2.7.: Inelastic collision permitted for a system of spin 1 bosons. Two atoms, in the Zeeman states $m_F = +1$ and $m_F = -1$ become two atoms in $m_F = 0$. Since the Hamiltonian of the system is invariant over rotation in the total spin state, the projection of the total angular momentum along the quantisation axis, $M_z = N_{+1} - N_{-1}$, must be conserved in the scattering process.

2.3.5. Spinor BEC in the single spatial mode

We can now write the entire total many-body Hamiltonian $\hat{H}_{\text{tot}} = \hat{H}_{\text{sp}} + \hat{H}_{\text{int}} + \hat{H}_{\text{mag}}$, where $\hat{H}_{\text{int}}$ comes from (2.68), $\hat{H}_{\text{mag}}$ from (2.61) and

$$\hat{H}_{\text{sp}} = \sum_i \int d\mathbf{r}\, \hat{\Psi}_i^\dagger(\mathbf{r}) \left[-\frac{\hbar^2 \Delta}{2m} + \hat{V}_{\text{ext}}(\mathbf{r}) \right] \hat{\Psi}_i(\mathbf{r}) \tag{2.71}$$

In this section, we want to find its ground state making a mean-field approximation. This consists in choosing for all the atoms the same single-particle state $\boldsymbol{\phi}(r) = \left(\phi_{+1}(\mathbf{r}), \phi_0(\mathbf{r}), \phi_{-1}(\mathbf{r})\right)$. The mth component $\phi_m(\mathbf{r})$ of $\boldsymbol{\phi}(r)$, is the condensate wave function of the spin component m. The many-body state of the system with all the atoms occupying the state $\boldsymbol{\phi}$ can then be written as

$$|\boldsymbol{\Psi}\rangle_N = \frac{1}{\sqrt{N!}} \left(a_\phi^\dagger\right)^N |\mathbf{0}\rangle \tag{2.72}$$

Table 2.1.: Coupling constants for the possible interactions between neutral atoms in the $F = 1$ manifold defined from the Hamiltonian (2.68).

$2 \cdot g_{AB}$	$m_F = +1$	$m_F = 0$	$m_F = -1$
$m_F = +1$	$\bar{g} + g_s$	$\bar{g} + g_s$	$\bar{g} - g_s$
$m_F = 0$	$\bar{g} + g_s$	$\bar{g}$	$\bar{g} + g_s$
$m_F = -1$	$\bar{g} - g_s$	$\bar{g} + g_s$	$\bar{g} + g_s$

To find the ground state of the Hamiltonian, we use the many-body state to compute the expectation value of $G = \langle H_{\text{tot}} \rangle - \mu N$. Minimising the resulting functionals over the ϕ_m's, we obtain the three Gross-Pitaevskii equations for the three components wave functions $\phi_m(\mathbf{r})$:

$$i\hbar \frac{\partial}{\partial t}\phi_{+1} = \left(-\frac{\hbar^2}{2m}\Delta + V_{\text{ext}}(\mathbf{r}) + p \right)\phi_{+1} + \left(\bar{g}\rho + g_s\Big(\rho_0 + \rho_z\Big) \right)\phi_{+1} + g_s N \phi_0^2 \phi_{-1}^* \tag{2.73}$$

$$i\hbar \frac{\partial}{\partial t}\phi_{0} = \left(-\frac{\hbar^2}{2m}\Delta + V_{\text{ext}}(\mathbf{r}) - q \right)\phi_{0} + \left(\bar{g}\rho + g_s\Big(\rho_{+1} + \rho_{-1}\Big) \right)\phi_{0} + 2 g_s N \phi_{+1}\phi_{-1}\phi_0^* \tag{2.74}$$

$$i\hbar \frac{\partial}{\partial t}\phi_{-1} = \left(-\frac{\hbar^2}{2m}\Delta + V_{\text{ext}}(\mathbf{r}) - p \right)\phi_{-1} + \left(\bar{g}\rho + g_s\Big(\rho_0 - \rho_z\Big) \right)\phi_{-1} + g_s N \phi_0^2 \phi_{+1}^* \tag{2.75}$$

where $\rho_m(\mathbf{r}) = |\phi_m(\mathbf{r})|^2$ is the density of the spin component m and $\rho_z = \rho_{+1} - \rho_{-1}$ is the magnetisation density.

Another level of approximation, that is valid for our condensate in the 3D configuration, is based on the decoupling of the spatial and of the spin degrees of freedom by imposing, for the three components, the same spatial wave function. At first, we look at the miscibility and immiscibility of the different components of the spinor condensate. This will naturally bring us to introduce the Single Mode Approximation (SMA), which consists in the decoupling just described above.

Miscible and immiscible mixtures

Following the argument introduced in [168], we consider a mixture of two components in a box of volume V at $T = 0$. For simplicity, we restrict ourselves to a mixture of $m_F = +1$ and $m_F = 0$. Considering only the interaction energy of the condensed mixture,

$$E = \frac{1}{2}\Big(n_0^2 g_0 + n_{+1}^2 g_{+1} + 2 n_0 n_{+1} g_{0,+1} \Big), \tag{2.76}$$

where the coupling constants for the different interactions are defined from the Hamiltonian (2.68), see Table 2.1. To understand if the two components overlap or if they phase separate, we have to compare the energies of the two configurations. We follow the work [6]. We

consider the two components to have the same number of atoms N. The two energies are:

$$E_{\rm o} = \frac{N^2}{2V}\Big(g_0 + g_{+1} + 2g_{0,+1}\Big), \tag{2.77}$$

for the overlapped case, and

$$E_{\rm ps} = \frac{N^2}{2}\Big(\frac{g_0}{V_0} + \frac{g_{+1}}{V_{+1}}\Big), \tag{2.78}$$

for the phase separated case. In the latter case, the two volumes V_0 and V_{+1} are defined minimising the energy $E_{\rm ps}$ by varying V_0 with $V_{+1} = V - V_0$. This corresponds to have equal pressure in the two phases:

$$g_0\left(\frac{N}{V_0}\right)^2 = g_{+1}\left(\frac{N}{V_{+1}}\right)^2, \tag{2.79}$$

so that they can be rewritten as

$$V_0 = \frac{\sqrt{g_0 g_{+1}}}{g_{+1} + \sqrt{g_0 g_{+1}}}V \qquad \text{and} \qquad V_{+1} = \frac{g_{+1}}{g_{+1} + \sqrt{g_0 g_{+1}}}V. \tag{2.80}$$

The energy for the phase separated case takes the form

$$E_{\rm ps} = \frac{N^2}{2V}\Big(g_0 + g_{+1} + 2\sqrt{g_0 g_{+1}}\Big), \tag{2.81}$$

Comparing E_0 and $E_{\rm ps}$, we find that the two components $m_F = +1$ and $m_F = 0$ phase separate if

$$g_{0,+1} > \sqrt{g_0\, g_{+1}}. \tag{2.82}$$

For Sodium atoms, from Table 2.1, $\bar{g} + g_s > \sqrt{\bar{g}(\bar{g} + g_s)}$: the condition is true and the components phase separate. Considering the different mixtures we can produce with the three components, we see that the $m_F = +1$ and $m_F = -1$ components are miscible and the $m_F = 0$ component is not miscible with the other two.

The Single Mode Approximation

As we have just seen, the different components of the condensate separate and form domains in a trap. We focus now our attention on the 3D geometry; the 1D geometry is treated in details in Chapter 4. Making an analogy with the healing length (2.14), we can define the spin healing length

$$\xi_{\rm s} = \sqrt{\frac{\hbar^2}{2m g_s n}} \tag{2.83}$$

This is the length over which the spin wave function recover from a perturbation. If our condensate size is much smaller than this characteristic length ξ_s, it is not energetically favourable to form spin domains that would cost a tremendous amount of kinetic energy

$\sim \frac{\hbar^2}{md^2} \gg \mu$ with d the domain size. Therefore, for atom clouds small enough, we can consider the three Zeeman components to have the same spatial wave function: this approximation is called Single Mode approximation (SMA).
In the Thomas-Fermi regime, the condensate size R is given by (2.12), so the condition for the validity of SMA $R \ll \xi_s$, can be written as

$$\frac{\mu}{\hbar\omega} \ll \sqrt{\frac{\bar{g}}{g_s}} \quad \text{or} \quad g_s n \ll \sqrt{\frac{g_s}{\bar{g}}}\hbar\omega \tag{2.84}$$

In the case of $\mu \sim \hbar\omega$ the condensate size is $R \sim \sqrt{\frac{\hbar}{m\omega}}$ and from the condition $R \ll \xi_s$ we obtain

$$g_s n \ll \hbar\omega \tag{2.85}$$

These expressions set an upper limit on the number of atoms for the SMA approximation to hold. As we will see in Chapter 5, this condition can be valid along some trap axes and fails along others. For our system in the 3D trap, where densities are on the order $n = 10^{14}\,\mathrm{cm}^{-3}$, the spin healing length $\xi_s \sim 1\,\mu\mathrm{m}$, which is of the same order of the condensate length. Therefore, the SMA is a good approximation for our 3D system. For a more involved discussion about the validity of this approximation in our system, we refer the reader to [32]. In Figure 2.8, we can see an image of the three components after time of flight in a magnetic field gradient. The profiles, obtained integrating the optical density along a CCD axis, can be nicely fitted by three Thomas-Fermi distributions with the same radii.

Introducing the SMA approximation, we write the condensate wave function as

$$|\phi(\mathbf{r})\rangle = \phi(\mathbf{r}) \otimes |\xi\rangle \tag{2.86}$$

where the spatial wave function $\phi(\mathbf{r})$ is frozen and can be used to minimise $G = \langle H \rangle - \mu N$, where we consider only the Hamiltonian H_{sp} plus the first term of the interaction Hamiltonian (2.64) to obtain the Gross-Pitaesvkii equation

$$\left(-\frac{\hbar^2}{2m}\Delta + V_{\mathrm{ext}}(\mathbf{r}) + \bar{g}N|\phi(\mathbf{r})|^2 \phi(\mathbf{r}) \right) \phi(\mathbf{r}) = \mu\phi(\mathbf{r}), \tag{2.87}$$

We can parametrise the spin wave function in the following way, see [169]:

$$|\xi\rangle = \begin{pmatrix} \sqrt{n_{+1}}\, \mathrm{e}^{i\theta_{+1}} \\ \sqrt{n_0}\, \mathrm{e}^{i\theta_0} \\ \sqrt{n_{-1}}\, \mathrm{e}^{i\theta_{-1}} \end{pmatrix} = \mathrm{e}^{i\theta_0} \begin{pmatrix} \sqrt{\frac{x+mz}{2}}\, e^{i\frac{(\Theta+\alpha)}{2}} \\ \sqrt{1-x} \\ \sqrt{\frac{x-mz}{2}}\, \mathrm{e}^{i\frac{(\Theta-\alpha)}{2}} \end{pmatrix} \tag{2.88}$$

where we introduce the reduced quantities

$$n_m = \frac{N_m}{N}, \qquad x = n_{+1} + n_{-1}, \qquad \text{and} \qquad m_z = n_{+1} - n_{-1}, \tag{2.89}$$

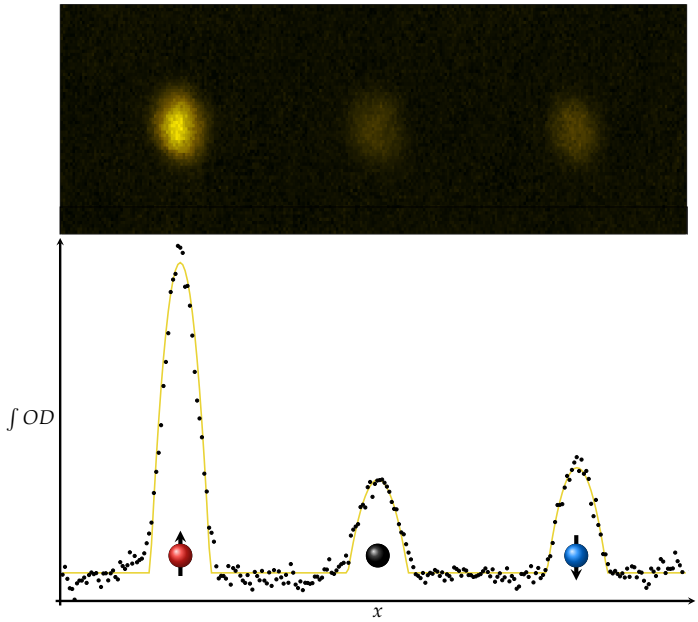

Figure 2.8.: Image of the three components after time of flight. The three profiles, obtained by integration of the optical density along one CCD axis, are well fitted by three Thomas-Fermi profiles with the same radii.

and the two relatives phases

$$\Theta = \theta_{+1} + \theta_{-1} - 2\theta_0 \qquad \text{and} \qquad \alpha = \theta_{+1} - \theta_{-1}. \tag{2.90}$$

We can use it to minimise the Hamiltonian $\hat{H}_{\text{tot}} = \frac{g_s}{2}\int d\mathbf{r}\,\hat{\mathbf{S}}^2 + \hat{H}_{\text{mag}}$ and obtain a spin energy

$$E_{\text{spin}} = \frac{U_s}{2N}\langle\hat{\mathbf{S}}\rangle^2 - q\hat{N}_0, \tag{2.91}$$

where

$$U_s = N g_s \int d\mathbf{r}\,|\phi(\mathbf{r})|^4, \tag{2.92}$$

is the spin interaction energy. For ^{23}Na, $g_s > 0$ and so also the interaction energy is positive. In the Hamiltonian there is no linear Zeeman energy. The latter is proportional to the longitudinal magnetisation m_z, which has a fixed value and it is a conserved quantity. Therefore, it only gives a constant shift of the energy that has been omitted. Only the quadratic Zeeman energy contributes to the spin dynamics of the system.

The equilibrium phase diagram

From the spin wavefunction (2.88) and the spin energy (2.91) we obtain an energy functional that can be minimised to find the system ground state:

$$E_{\text{spin}} = \frac{NU_s}{2}\left(m_z^2 + 2x(1-x) + 2\cos(\Theta)(1-x)\sqrt{x^2 - mz^2}\right) + NU_s qx. \tag{2.93}$$

All the different states are degenerate with respect to the relative phase α. Since $U_s > 0$, to minimise the energy the other phase Θ locks to $\Theta = \pi$, independently of the value of x and m_z. This locking of the relative phase enforces the presence of a nematic order in the system, as we experimentally demonstrated in [196].
The energy functional (2.93) can be minimised by varying the parameter x, with m_z and q imposed experimentally. The result is represented in Figure 2.9: a second-order phase transition appears as the magnetic field grows . This has been studied experimentally in [76].
For $m_z = 0$ and $q > 0$, we obtain a state with energy $E_{\text{spin}} = NU_s qx$. The energy minimum is at $x = 0$, i.e. the state is characterised by all the atoms in $m_F = 0$. In the case $q = 0$ we find a family of states called polar states $|\mathbf{\Omega}\rangle$ introduced in [65]. They can be written as:

$$|\mathbf{\Omega}\rangle = \boldsymbol{R}(\theta, \phi) \cdot \begin{pmatrix} 0 \\ 1 \\ 0 \end{pmatrix} = \begin{pmatrix} -\frac{1}{\sqrt{2}} \sin(\theta)\, \mathrm{e}^{-i\phi} \\ \cos(\theta) \\ \frac{1}{\sqrt{2}} \sin(\theta)\, \mathrm{e}^{i\phi} \end{pmatrix} \tag{2.94}$$

These are states for which all atoms are in the $m_F = 0$ state with respect to a quantisation axis $\mathbf{n}$, defined by the polar angles (θ, ϕ), and are all degenerate. A full quantum treatment of the case $m_z = 0$ and $q = 0$ can be found in [101].
Looking at the energy functional at $m_z > 0$, we can rewrite it as

$$\frac{E_{\text{spin}}}{N} = U_s(1 - x)\left(x - \sqrt{x^2 - m_z^2}\right) + qx \tag{2.95}$$

There are two contributions to the energy: *i.*) the interactions, presented in Figure 2.7, tend to minimise the energy locking $x = 1$; this is what we expect from an antiferromagnetic system as our gas of sodium atoms; *ii.*) the magnetic field, on the contrary, with the quadratic term q, tries to reduce the energy transfering as many atoms as it is possible[10] in $m_F = 0$. These two effects compete to determine the system equilibrium state. Looking at Figure 2.9, we see that, for each magnetisation, there is a critical value of q dividing the equilibrium phase diagram in two regions. This critical value is equal to

$$q_c = U_s(1 - \sqrt{1 - m_z^2}) \tag{2.96}$$

and it is sketched with a white line in the Figure.
For $q < q_c$, the magnetic field is not high enough to overcome the effect of the interactions and the ground state of the system is antiferromagnetic, with $n_{\pm 1} = (1 \pm m_z)/2$ and $n_0 = 0$. We call this state also quasi-spin nematic (qSN) state. Increasing the magnetic field, it is more and more energetically favourable for the system to transfer atoms in $m_F = 0$. For $q > q_c$, n_0 starts to grows with q until a maximum value fixed by the conservation of the magnetisation $m_z = n_{+1}$. We call this ground state transverse magnetised ($M_\perp$).

[10] The magnetisation is fixed, so there is a maximum number of atoms that can be transferred to the $m_F = 0$ state from $m_F = +1$ and $m_F = -1$.

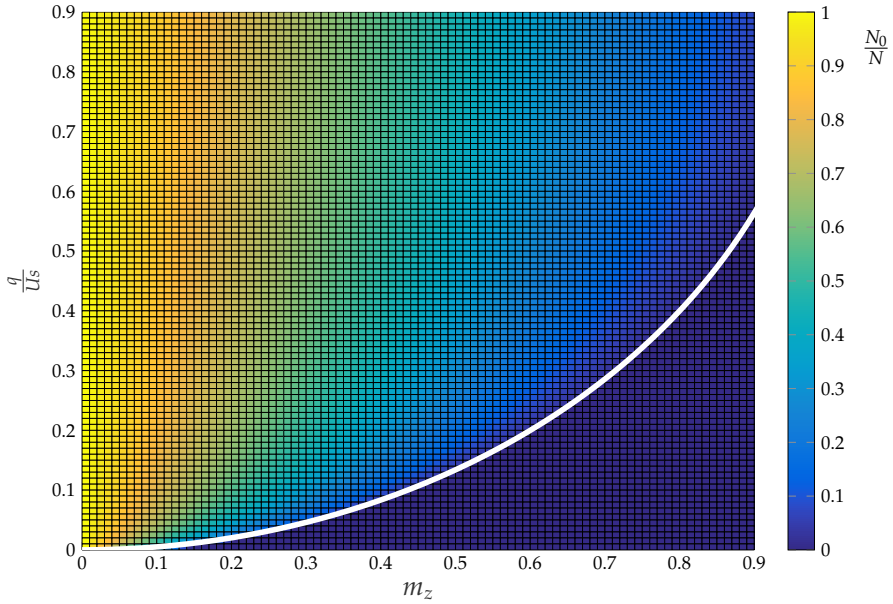

Figure 2.9.: Equilibrium phase diagram for a condensate of ^{23}Na atoms. The two axes correspond to the longitudinal magnetisation m_z and to the ratio between the quadratic Zeeman term and the interaction energy $\frac{q}{U_s}$. The color scale represents the population in the Zeeman state $m_F = 0$. The white line divides the diagram into two regions: for small magnetic fields, the system is in the antiferromagnetic state, with $n_{\pm 1} = (1 \pm m_z)/2$ and $n_0 = 0$. For high magnetic fields, the system is in the transverse magnetised ($M_\perp$) phase, where $m_F = 0$ becomes populated. Due to the conservation of the longitudinal magnetisation, there is a maximum number of atoms that can be transferred in this state.

3. Production and characterization of a spin-1 Bose-Einstein condensate of Sodium atoms

In this Chapter, we present in Section 3.1 and Section 3.5 the experimental recipe used to produce the 3D and the 1D condensate and to probe them. We present also in Section 3.2 the techniques used to manipulate the spin internal degrees of freedom of the spinor condensate.
The description of the experimental apparatus is reduced to the main parts needed to understand the experimental recipe. We refer the reader to the PhD Thesis [75, 118] for a comprehensive description of all the components.

3.1. Experimental Setup and cooling techniques

This section is devoted to the description of the experimental apparatus and the experimental sequence we use to reach quantum degeneracy from a dilute thermal gas of bosonic ^{23}Na atoms and obtain a Bose-Einstein condensate.

3.1.1. UHV chamber and atomic source

Spinor gases are very fragile with respect to stray magnetic fields [66, 8] and this is why our ultra high vacuum (UHV) chamber is made of Titanium, which has a low magnetic susceptibility. A schematic of the vacuum chamber is sketched in Figure 3.1.
All cold atoms experiments require an atom source, a magneto-optical trap (MOT) to collect hot atoms directly from this source and a second trap, where atoms can be cooled down to the quantum degeneracy by evaporation cooling techniques, see [86].
An efficient loading of the MOT requires an high background pressure, while the evaporative cooling of the trapped cloud requires UHV: the collisions between the trapped atoms and atoms of the background vapour can severely affect the evaporation process. These two opposite requirements are then matched using a dispenser as atomic source and light-induced atomic desorption (LIAD) to control the background pressure, see [119].

The dispensers mounted on our experiment contain a powder of sodium oxide which is inert at room temperature, but releases a vapour of Sodium when it is heated[1]. A few seconds after the Sodium starts to be released, the background pressure grows and atoms start to be adsorbed mostly at the windows of the chamber. In normal operation the dispensers are not powered. The partial sodium pressure is then very low, as the MOT loading rate. To enhance the background pressure during the MOT loading, we use the light–induced atomic desorption (LIAD) technique. It consists in illuminating with short-wavelength light the glass surfaces of the vacuum viewports, previously coated by Sodium atoms from the dispensers, to increase the desorption rate of sodium atoms. We use ultraviolet light (UV) light emitting diodes (LED) at a wavelength $\lambda \approx 375\,\mathrm{nm}$ to induce the desorption. The Sodium background pressure increases by a factor ~ 40 when the LEDs are on. Switching off the UV LEDs the initial background pressure is restored in less than 100 ms, see [119]. We also heat the dispensers on a weekly basis to maintain a consistent number of atoms in the chamber.

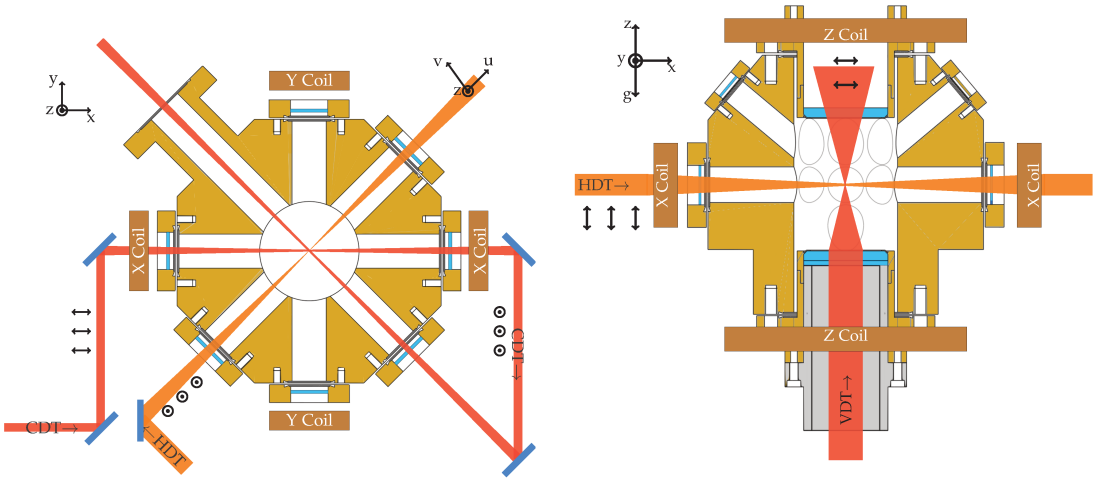

(a) Top view (b) Side view

Figure 3.1.: Sketch of our vacuum system. (a): vacuum system seen from above. The red line represents the cross dipole trap (CDT) used to capture atoms from the MOT and perform an initial stage of forced evaporation. In orange is sketched the horizontal dipole trap (HDT) beam, we use it to make the final evaporation step. Also shown are the coils we used to control the magnetic field at the atoms position. Along the Y axis, another pair of coils (not shown) is used to produce the MOT magnetic field. (b): vacuum system seen from the side. In orange we see the HDT, while in red the vertical dipole trap (VDT). The two lasers make the dimple trap.

[1] We heat the dispenser running an electric current (we use 3.5 A / 0.5 V to avoid large Sodium load in the chamber) through its metallic envelope.

3.1.2. Magneto-optical trap

The MOT is used to trap Sodium atoms from the background vapour and to cool them. The minimum temperature achievable is given by the Doppler limit $k_B T = \frac{\hbar\Gamma}{2} \approx 240\,\mu\text{K}$ for Sodium atoms and the D_2 transition, see [140]. The MOT is composed of a pair of coils in an anti-Helmholtz configuration and an optical field created at the intersection of 6 counter-propagating laser beams spanning 3 orthogonal directions. The beams cross at the zero of the magnetic field created by the pair of coils. The Sodium transition used for the cooling is the D_2 line between the $3^2S_{1/2}$ and the $3^2P_{3/2}$ levels and has a wavelength $\lambda_{D_2} = 589\,\text{nm}$, Figure 3.2. The spontaneous emission rate is equal to $\Gamma = 2\pi \cdot 9.8\,\text{MHz}$ and the saturation intensity for circularly polarised light is $I_{\text{sat}} = 9.4\,\text{mW/cm}^2$. The cooling beams are red detuned by 20 MHz from the $|F = 2\rangle \rightarrow |F' = 3\rangle$ transition and have an intensity $0.1\,I_{\text{sat}}$ per beam. Together with the 6 cooling beams, we use 6 repumper beams to bring back in the cooling cycle atoms felt in the hyperfine state $|F = 1\rangle$ after a non resonant transition $|F = 2\rangle \rightarrow |F' = 2\rangle$. The repumper beams are resonant with the $|F = 1\rangle \rightarrow |F' = 2\rangle$ transition and have an intensity $\sim 300\,\mu\text{W}$.

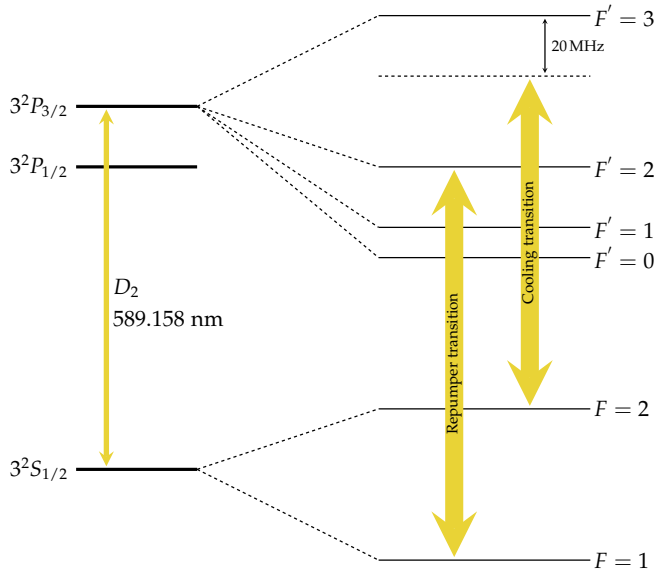

Figure 3.2.: Cooling scheme for the MOT phase. The cooling light drives the cooling transition between the $|F = 2\rangle$ and $|F' = 3\rangle$ levels. The light is detuned by 20 MHz from resonance. The repumper beam, used to bring back into the cooling cycle atoms felt in the hyperfine state $|F = 1\rangle$ after a non resonant transition $|F = 2\rangle \rightarrow |F' = 2\rangle$, is resonant.

Laser cooling light source

The light for the MOT beams come from an home-made solid state yellow laser. A complete description of the laser can be found in the thesis of E. Mimoun [118]. Here, we

limit ourselves to a brief description of its principal characteristics.
Two YAG lasers with wavelengths 1314 nm and 1064 nm are injected in a cavity that is resonant for both wavelengths, where they are combined inside a periodically-poled KTP crystal to produce ~ 600 mW of 589 nm laser light. The laser frequency is locked by modulation transfer spectroscopy, [162], to a molecular transition in a iodine cell, [81]. The cooling light is divided into three beams. One beam is used for the six MOT beams. S second beam, in combination with a high-frequency acousto-optic modulator (AOM) is used to produce the repumper beam. The third beam is used for imaging. Optical fibres guide all beams to the experimental chamber.

Loading of the crossed dipole trap

After the laser cooling stage, the atoms are loaded in the crossed dipole trap (CDT). The size of the atomic cloud in the MOT phase is ~ 1 mm, significantly larger than the waist of the dipole trap $\omega_0 \approx 40\,\mu$m. To maximise the mode matching and to make the loading as efficient as possible, the MOT is compressed and cooled down. The compression is obtained by lowering the repumper power: atoms start to occupy the hyperfine state $|F = 1\rangle$ and they are not resonant with the cooling light, hence the multiple atom-light scatterings inside the cloud are suppressed and the MOT size is reduced. This stage is called "Dark MOT", see [75, 77]. By further red-detuning the cooling beams to ~ 38 MHz we can then cool down the cloud to $T \approx 30\,\mu$K. This technique is called "Cold MOT", see [34].

3.1.3. The crossed dipole trap and the dimple optical traps

The crossed dipole trap is produced by a single laser beam from a $\lambda = 1070$ nm high power fibre laser (up to 40 W) with a linear polarisation assured by a Glan-Taylor polariser. The laser is focused at the centre of the chamber with a waist $\omega_0 \approx 40\,\mu$m and then folded and sent again back towards the atoms at an angle $\theta = 45°$ with respect to the initial direction, see Figure 3.1(a). To produce a crossed dipole trap, we rotate the light polarisation by $\frac{\pi}{2}$ between the two crossing arms to suppress interferences.

The power of the laser is controlled by a servo loop on the pump diode current in combination with a motorised $\lambda/2$ wave-plate and a Glan-Taylor polariser. The motorised wave-plate + Glan-Taylor polariser can change the laser power without any distortion of the beam[2] profile and allow us to have powers below the lasing threshold; the drawback of this method is the low bandwidth of 10 Hz limited by the rotation speed of the wave-plate. The faster servo loop on the pump diode current is used to stabilise the laser power around a value given by the rotating wave-plate and, thanks to a bandwidth of a few KHz, it can corrects high frequency fluctuations of the laser power. A thorough description of

[2] In high power lasers the emitted spatial mode can change with the emitted power, which is not good for evaporative cooling. The motorised wave-plate allows us to change power without changing the laser emitted power and solve this problem.

our stabilisation system for the laser power can be found in the PhD thesis [160].

To continue in our description of the sequence and explain the need for a second cross dipole trap, we recall here the potential felt by neutral atoms given by a laser beam propagating along the direction z [57]

$$V_{\mathrm{Dip}}(z,x,y) = V^0_{\mathrm{Dip}}\left(\frac{\omega_0}{w(z)}\right)^2 \exp\left(-2\frac{x^2+y^2}{w^2(z)}\right), \tag{3.1}$$

where $V^0_{\mathrm{CDT}} \propto \frac{I_0}{I_{\mathrm{sat}}} = 2P_0/\pi\omega_0^2$.
The potential felt by the atoms due to the CDT is given by the sum of two laser beams propagating as sketched Figure 3.1(a). We also need to account for the gravitational potential if we want to compute the effective trap depth. The trap frequencies are proportional to $\omega_{i\epsilon\{x,y,z\}} \propto \sqrt{V^0_{\mathrm{CDT}}} \propto \sqrt{P}$. At the loading of the CDT trap, the laser power is $P = 25\,\mathrm{W}$, which corresponds to $V^0_{\mathrm{CDT}} = 1\,\mathrm{mK}$.
In this trap we perform evaporative cooling by lowering the laser power, the trap depth is diminished and the most energetic atoms can escape from the trap. The remaining atoms can thermalise to a lower temperature due to the lower average thermal energy per atom, see [88].
Evaporative cooling is efficient only if the collision rate is high enough to let the atoms rethermalise each time the trap depth is lowered. When we lower the laser power we also lower the trap frequencies, since $\omega_i \propto \sqrt{P}$, therefore reducing the density and the collision rate. With the CDT laser alone it is not possible to reach quantum degeneracy, because the collision rate becomes too low and the cloud cannot thermalise anymore at the end of the evaporation ramp.

Different techniques have been implemented trying to solve this issue. In [89], the authors increase the atomic density by dynamically reducing the trap size, while the atoms are evaporatively cooled by reducing the light intensity. In [67], the trap depth of the dipole trap is controlled thanks to a magnetic gradient, leaving the trap frequencies unchanged. In [28], the authors used a crossed dipole trap composed by two crossed beams with different waist: the smaller one is the real trap, while the other is used to remove the most energetic atoms from the smaller arm. More recently, an AOM has been used to shape the trap potential of a crossed dipole trap and obtain a condensate in less than 2 s, [154]. In our experiment, the problem was solved by adding a second crossed dipole trap, as done in [186]. The second "dimple" dipole trap is composed by two beams with smaller waists with respect to the CDT trap; hence the trap can have the same trap depth with higher trap frequencies. In our experiments the "dimple" dipole trap is composed by an horizontal beam (HDT) and a vertical beam (VDT), see Figure 3.1(b), both coming from a $\lambda = 1064\,\mathrm{nm}$ and red-shifted in frequency by a relative frequency $\sim 200\,\mathrm{MHz}$ thanks to 2 acousto-optic modulators. The different AOMs allow us to control and servo the power of the two beams independently. In this trap we perform the final evaporation cooling to reach quantum degeneracy.
Figure 3.3 shows the atom number N, temperature T and longitudinal magnetisation m_z

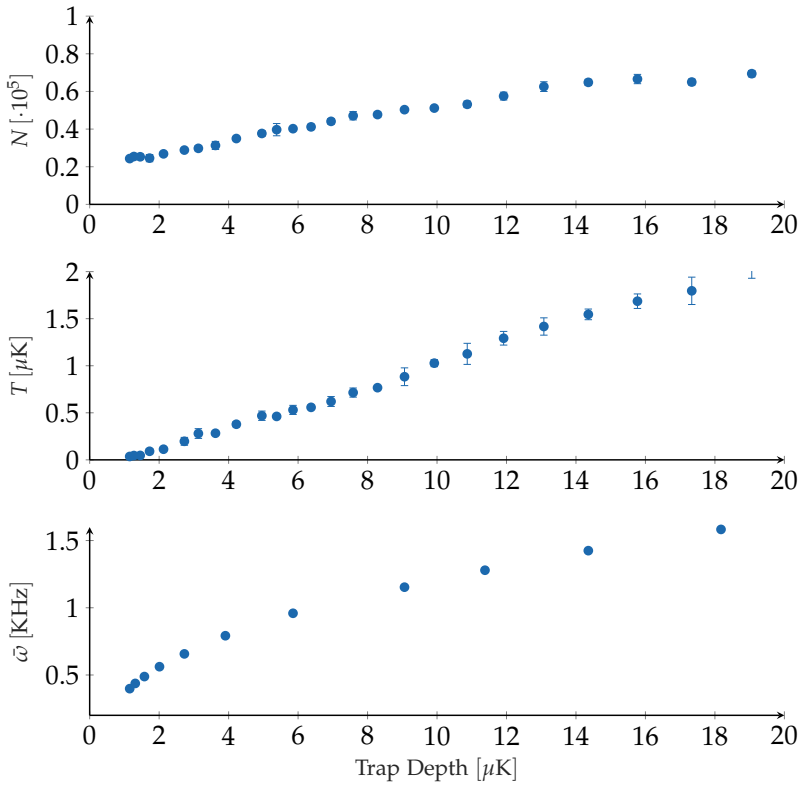

Figure 3.3.: Atom number N, temperature T and magnetisation m_z of the Bose gas trapped in the dimple trap at different steps of the evaporation ramp.

for different trap depths during the evaporation ramp performed in the dimple trap.

Figure 3.4 summarises a typical experimental sequence used to produce the condensate in the 3D geometry. After the MOT phase and the loading of the CDT, the evaporation happens in two steps. At first the atoms are trapped only in the CDT trap, since they are too hot to be trapped in the "dimple" trap. Here we perform the first evaporative cooling step. At the end of the evaporation, the atoms are loaded in the "dimple" trap, where their collision rate increases thanks to higher trapping frequencies. Finally, the evaporative cooling in the final trap leads to the quantum degeneracy.

3.1.4. Stern-Gerlach time of flight

As described in Chapter 1, we actually reach degeneracy in a spin-1 system. To probe our spinor system we need a spin dependent imaging technique. We implemented a Stern-Gerlach (SG) imaging technique, see[51, 144], which consists in applying a spin dependent force during the ballistic expansion.

We have a total of 4 pairs of coils to generate magnetic fields to manipulate our spinor

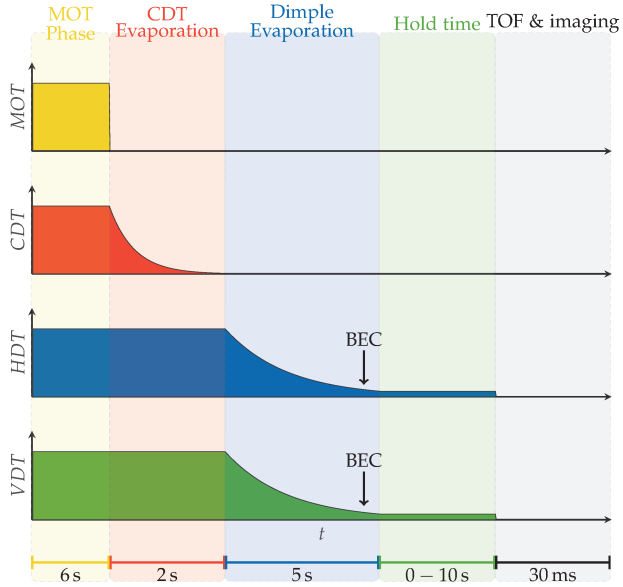

Figure 3.4.: Typical experimental sequence used to produce the 3D condensate. After the MOT phase and the loading into the crossed dipole trap (CDT), a first evaporation is performed. The atoms are then loaded into the dimple trap, composed by an horizontal and a vertical dimple beams, HDT and VDT. A final evaporation step allows us to reach the quantum degeneracy. After a hold time, the trap is switched off and the atoms expand ballistically during 3 – 8 ms time of flight (TOF), after which they are detected by absorption imaging.

system, see Figure 3.1. Three of them in the Helmholtz configuration are used to produce uniform magnetic fields along the 3 orthogonal axes. The fourth pair of coils along the y axis, in the anti-Helmoltz configuration, is used to produce the quadrupole magnetic field for the MOT. We have also another small coil along the vertical axis that we use to manipulate the atoms spin state via RF pulses, see Section 3.2.

To perform the Stern-Gerlach experiment, we use the MOT coils to produce a magnetic field gradient $\mathbf{B'} = \left(b'x, 2b'y, b'z\right)$ at the atom position. If the fields are ramped up matching the adiabaticity criterium, see Section 3.2, the potential felt by an atom in the Zeeman state m_F is equal to

$$V_{\text{mag}} = \mu_B g_F m_F |\mathbf{B}|. \tag{3.2}$$

We add a strong bias field $\mathbf{B_0} = \left(B_{0,x}, B_{0,y}, B_{0,z}\right)$ which moves away the zero of the quadrupole field from the atom position and we obtain a magnetic field gradient along the direction of the bias field. The force acting on the centre of mass of each Zeeman

component is given by $\mathbf{F}_{\text{mag}} = -\nabla V_{\text{mag}}$ and can be written as

$$\mathbf{F}_{\text{mag}} = -\frac{\mu_B g_F m_F b'}{2|\mathbf{B}|}\begin{pmatrix} B_{0,x} \\ 2B_{0,y} \\ B_{0,z} \end{pmatrix} \tag{3.3}$$

The atoms in the Zeeman sub-levels $m_F = \pm 1$ feel a force with the same modulus, but opposite direction; the atoms in $m_F = 0$ do not feel any force. So, when the atoms are released from the trap and we perform the SG experiment, the three atomic species will separate allowing us to image all of them at the same time.
To maximise the separation of the atomic clouds during time of flight, we use a bias field along the y direction, which is the MOT coils axis. Imperfections on the coils, such as asymmetries in their construction (geometrical or in their number of turns), lead to small gradients that modify the effective direction of the magnetic force given in (3.3). This effect becomes more visible in the 1D trap, because of the more relaxed confinement, see Chapter 5. To compensate any deviation from the desired direction of the force, we fine tune the current applied to the bias coils.

The two trap geometries studied during these thesis work, the 1D and the 3D geometries, require two different implementations of the SG experiment.

The study of stepwise Bose-Einstein condensation in a spinor gas, presented in Chapter 4, required a maximum separation between the different spin components. Our experiments, ranging from thermal gases at $T = 5\,\mu$K to BECs at $T = 40\,$nK, required the careful study of thermal wings, which expand to up to $\sim 200\,\mu$m in the typical 3 ms expansion time. Therefore, maximum separation is very critical to obtain the thermodynamic properties of the gas. We used a discharge capacitor to implement a fast pulse of current through the MOT coils during SG imaging. This method is described in the PhD thesis [47].
To study the 1D geometry, we have chosen to use another SG modality, described in [32, 75] and sketched in Figure 3.5. It consists in reducing the gradient strength used to separate the atoms with respect to the previous implementation, and in attenuating the dimple power before time of flight to slow down the cloud expansion. Thanks to this reduced expansion, we are able to image the atoms at longer time of flights.

3.1.5. Imaging after TOF

To image the atoms after TOF, we use the absorption imaging technique, see [86]. It consists in illuminating the atoms with resonant light recording the cloud absorption.
We introduce in this Subsection the optical system used to image the condensate and the absorption technique from which we obtain the condensate column density.

The imaging system

The imaging system is composed by a couple of microscope objective + lens systems, aligned to work in an afocal configuration. The first microscope has an high numerical aperture $N.A. \sim 0.33$ and an effective focal length $f \sim 40\,$mm and it is followed by an

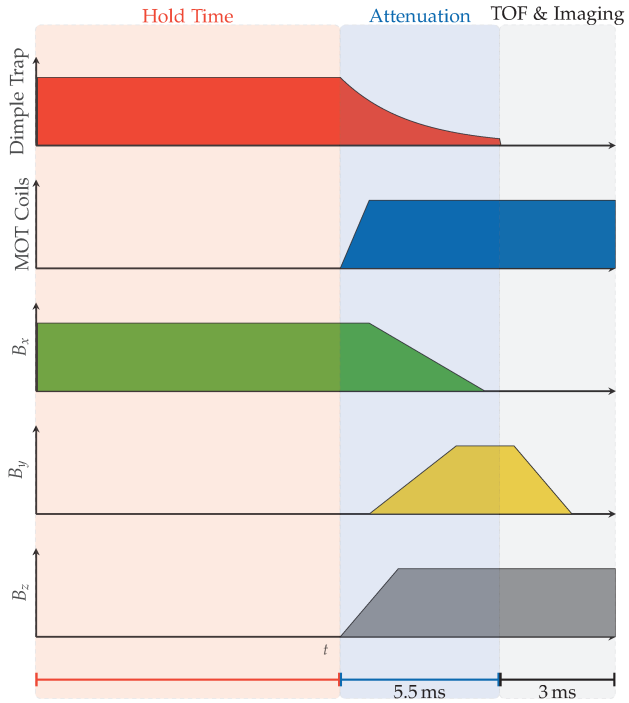

Figure 3.5.: Typical experimental sequence to perform a Stern-Gerlach experiment and image the three different Zeeman sub-levels of the $F = 1$ state of ^{23}Na in time of flight. To obtain a separation of the three clouds along the y direction, we ramp a gradient with the MOT coils and a bias field along the y direction. Just before the imaging, the field is rotated along the vertical direction to image the cloud with the correct polarisation (the imaging beam propagates along z). To slow down the cloud expansion, before the TOF the dipole trap potential depth is lowered with an exponential ramp.

achromat of $f \sim 80\,\text{mm}$. These two lenses produce an image of the atoms with a theoretical magnification of 1.5. A razor blade is placed near the atoms image to mask part of the final sensor from light. A second microscope objective with effective focal length $f \sim 18\,\text{mm}$ and an achromat with $f \sim 100\,\text{mm}$ produce the final image on the charge coupled device (CCD) camera. The theoretical magnification of this second imaging system is equal to 5. The resolution of the imaging system is characterised by imaging the smallest cloud possible. We can detect clouds with RMS size $> 2\,\mu\text{m}$.
The masked part of the CCD sensor is used for the frame transfer technique. This consists in hiding part of the camera sensor and allow us to take two successive images. The first image is taken on the exposed part of the CCD, then the image is shifted on the hidden part of the sensor and the second image can be taken. Only after this process the CCD is completely read out and the data acquired. The frame transfer technique allows a shorter time between the two images with respect to the readout time. This is important for minimising the imaging noise, as we will discuss in the following. In the

sequence, after a 20 μs repumper pulse, we send two pulses of resonant light lasting both 10 μs and separated by 5 ms.
We use light resonant with the transition $3S_{1/2}\,F = 2 \rightarrow 3P_{3/2}\,F' = 3$ to image the atoms. The imaging pulse propagates along the z axis and it is σ_+ polarised. Before the imaging pulse, a first pulse of light, coming from the repumper laser and propagating along the 6 MOT axes, repumps atoms from $3S_{1/2}\,F = 1$ to $3S_{1/2}\,F = 2$.

Absorption imaging

To obtain an image of the atomic cloud by absorption imaging we have to take two images: a first image I_1 with the atoms, and a second image I_2 without atoms, see [86]. An example of the two images can be seen in Figure 3.6(a).

We can model the absorption of the first imaging pulse by the atomic cloud via the Lambert-Beer law:

$$\frac{\partial I}{\partial z} = -\sigma n I, \tag{3.4}$$

where n is the atomic density, σ is the atomic cross-section for the atom absorption and I is the incoming pulse intensity. We can model in a simple way the atom-light interaction using a 2-level atom model. In this case the cross-section can be written as

$$\sigma = \frac{\sigma_0}{1 + \frac{I}{I_{\text{sat}}} + \left(\frac{2\delta}{\Gamma}\right)^2}, \tag{3.5}$$

where $\sigma_0 = \frac{3\lambda^2}{2\pi}$ is the resonant scattering cross section for circularly polarised light, λ is the resonant wavelength, δ is the detuning of the probe frequency with respect to the transition and Γ is the transition natural line width. With this expression, we can solve the differential equation (3.4) and following the authors of [151], we find

$$OD(x,y) = \sigma \int dz\, n(x,y,z) = f(x,y) \tag{3.6}$$

where the function $f(x,y)$ is equal to:

$$f(x,y) = -\log\left(\frac{I_1(x,y)}{I_2(x,y)}\right) + \frac{I_2(x,y) - I_1(x,y)}{I_{\text{sat}}}, \tag{3.7}$$

$OD(x,y)$ is the optical density and $I_i(x,y)$ refer to the spatial distribution of the probe beam captured in image $i = 1, 2$.
The model we have just described can be used only if the optical density is lower than unity. At higher OD, indeed, phenomena like multiple scatterings change the cloud response to the light impulse, thanks to the high density inside the cloud, and the Lambert-Beer law is not valid anymore. This problem makes the *in situ* imaging difficult [151]. To solve this issue, before imaging the cloud, we release it from the trapping potential. This free expansion, that we call time of flight (TOF), reduces the cloud optical density to $OD \leq 2$. Using it with the Stern-Gerlach experiment, we can image the atomic density of the 3 Zeeman sub-levels at the same time.

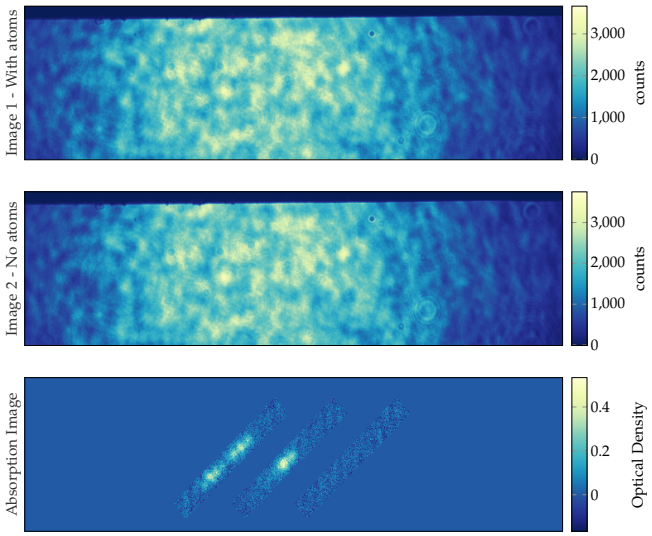

(a) Absorption images

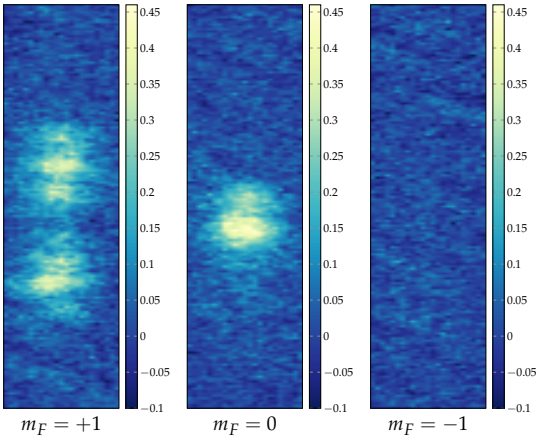

(b) Extracted and rotated atomic clouds

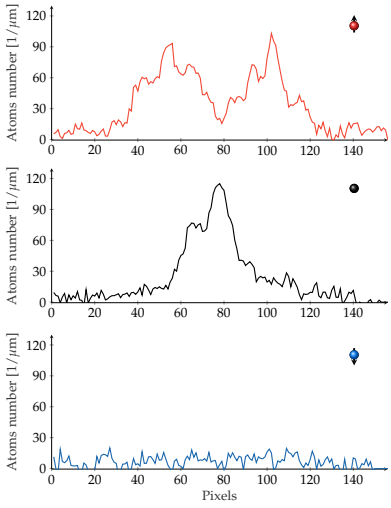

(c) Integrated profiles

Figure 3.6.: Process to obtain the clouds density profiles. In (a) we see the sequence of images taken during the imaging phase to reconstruct the absorption imaging signal. **Upper**: probe intensity profile, taken in presence of the atomic cloud. **Middle**: probe intensity profile, taken without atom cloud. The colormap represents the digital scale (counts) coming from the CCD analogical to digital converter (ADC). **Lower**: OD, obtained by taking the logarithm of the ratio between the first two and multiplied by a mask to select the atomic regions. In (b) we have the three clouds extracted from the initial image and rotated. In (c) we have the 3 profiles obtained by integration of the clouds of image (b).

3.2. Manipulating internal states with spin degrees of freedom

The study of a spinor condensate requires a very good control on the spin degrees of freedom of the trapped atoms. In particular the applied magnetic field, which defines the energy difference between the Zeeman sub-levels of our spin-1 system, must be very well controlled. In this section, we introduce the methods we use to characterise the ambient magnetic fields as well as the bias magnetic field generated by our coils. We then present the methods we use to set the magnetisation of the spinor gas and to change the spin state of the system.

3.2.1. Magnetic field control

The control of external magnetic field is of paramount importance in spinor condensate physics. External magnetic fields determine the ground state of the system and a good control on them is required to prepare the system in any desired configuration. During the experimental sequence, we need to change magnitude and orientation of the external magnetic field to perform different tasks; for example, apply a field along x with a certain magnitude and then rotate it towards z to image. This section is divided into two parts: in the first one we derive an adiabaticity criterium for any magnetic field variation and then we illustrate the spectroscopy method we use to characterise the external and applied magnetic fields.

Adiabaticity and Majorana transitions

We consider a single ^{23}Na atom plunged in a magnetic field $\mathbf{B}$ aligned along z. We use a semi-classical description of the atom, for which its internal degrees of freedom are described with quantum mechanics and the external degrees of freedom, $(\mathbf{r}, \mathbf{p})$, are described with classical mechanics. Therefore, the internal state of the atom will see a magnetic field moving with $\mathbf{B}(\mathbf{r}) \to \mathbf{B}(\mathbf{r}_0 + \frac{\mathbf{p}t}{m})$ and we can describe the system of an atom moving in a set magnetic field like a fixed atom plunged in a magnetic field changing in modulus and orientation in time . We suppose the atom to be in the spin eigenstate $m_F = +1$ at time $t = 0$. If the magnetic field, at $t > 0$, starts to rotate in space, the atom will try to remain in the same eigenstate while the latter will try to follow the magnetic field movement rotating in spin space. To remain in the same state, the atom must follow the magnetic field adiabatically.
To obtain a criterium for the adiabaticity, we can confront the velocity at which the atomic spin can rotate in a magnetic field $\mathbf{B}$, expressed by the Larmor frequency $\omega_L = \frac{p}{\hbar}$, where p is the linear Zeeman shift (2.62), with the magnetic field rate of change $\dot{\theta}$. The atom follows adiabatically the magnetic field if $\omega_L \gg \dot{\theta}$, or equivalently, if

$$\frac{|\dot{B}|}{||\mathbf{B}||} \ll \frac{\mu_B B}{\hbar} \tag{3.8}$$

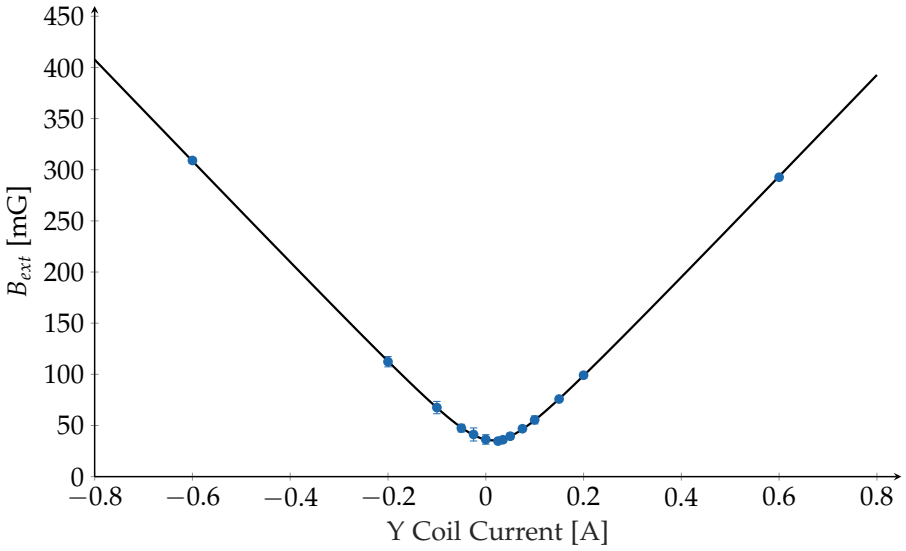

Figure 3.7.: Resonant magnetic field as a function of the current feed to the bias coils along the Y direction. The resonance was found looking at the depolarisation of a polarised $m_F = +1$ sample plunged in a RF magnetic field. A small bias field of $\sim 30\,\mathrm{mG}$ was applied along X to obtain a finite resonance frequency at the current compensation value.

If the condition is not fulfilled, the atom will change its spin state during the evolution. In a magnetic trap, this usually means loosing the atom. In our dipole trap, where all the spin degree of freedom are trapped, this translates in a unpredictable variation of the magnetisation m_z. From (3.8), it is clear that for low magnitude of the magnetic field the criterium is more and more difficult to be satisfied. Indeed in quadrupolar traps, where a zero of the magnetic field is present, these type of losses are well known, [86], and we refer to them as to Majorana transitions.
In our experiment we use linear ramps to change the magnetic field and we have to be careful about the bias field to avoid the field to change at maximum rate when the bias field is too low for the atoms spin degree of freedom to follow adiabatically.

Calibration of the magnetic fields

As we have already explained in Chapter 2, the magnitude of the external magnetic field changes the ground state of our system. A precise calibration of the magnetic field produced by the bias coils and of the environmental magnetic field is then important to study the state of the system and, as we have just pointed out in the section above, to change the magnetic field on the atoms without changing the magnetisation.

We perform RF-spectroscopy to calibrate the magnetic environment. During the evaporation step in the CDT trap, see Figure 3.4, we use the three pairs of bias coils, see Figure 3.1, along the three directions to apply a uniform magnetic field. The magnetic field

splits the three Zeeman sublevels accordingly to the Linear Zeeman shift (the quadratic term is negligible in this case). At the same time, we send an RF field towards the atoms, via a coil placed on the top of the vacuum chamber. This field is in resonance with the energy difference between the different Zeeman sub-levels and induces Rabi oscillations between these levels. We send a pulse of 5 ms duration at low intensity. If we prepare the system with all the atoms in $m_F = +1$, we can look at the depolarisation as a function of the RF frequency. We calibrate one axis at a time, considering that the three pairs of coils produce a magnetic field only along its own direction[3]. Chosen an axis, we apply a small transverse field $\mathbf{B}_\perp$ with the coils along the other 2 directions and we measure the resonance frequency f as a function of the current feed to the coils of the chosen axis. We successfully measure $|\mathbf{B}|$ varying the current value I_i along one direction, the other two being fixed, see Figure 3.7,

$$|\mathbf{B}| = \sqrt{\sum_i (B_{\mathrm{env},i} + b_i I_{\mathrm{coils},i})^2}, \tag{3.9}$$

where b_i, with $i \in \{x, y, z\}$, are the magnetic field current parameters of the coils pair. The minimum of the function is found at $I_{\mathrm{coils},i} = B_{\mathrm{env},\perp}/b_i$, which corresponds to the currents we have to feed to the coils to compensate the environment magnetic field $\mathbf{B}_{\mathrm{env}} = (B_{\mathrm{env},x}, B_{\mathrm{env},y}, B_{\mathrm{env},z})$. The results of this calibration are reported in Table 3.1.

Table 3.1.: Magnetic field-current characteristics α_i of the three pairs of coils along the axis $i \in \{x, y, z\}$ and bias magnetic fields $B_{\mathrm{env},i}$ obtained by the characterisation method explained in 3.2.1.

i	x	y	z
b_i $[mG/A]$	1.429(3)	0.498(3)	1.809(3)
$B_{\mathrm{env},i}[mG]$	157(2)	15(2)	318(2)

3.2.2. Rabi Oscillations

One of the techniques we use to prepare the system in a chosen spin state is spin rotations. The basic idea behind this method is to couple to the system an oscillating field, resonant with some transition, in order to drive it into a precise evolution and stop this evolution at a specific time, when the system is in the desired state. We discuss here the Rabi oscillations we induce in our spin 1 system via a sequence like the one sketched in Figure 3.8. An example of the resulting oscillation is represented in Figure 3.9.
To induce the rotation we apply an oscillating magnetic field along the z axis, see Figure 3.1, using a coil placed on the flange of the upper microscope in the vacuum system. Via this coil, we feed to the atoms an RF pulse $\mathbf{B}_{\mathrm{RF}} = B_{\mathrm{RF}} e^{i\omega_{\mathrm{RF}} t} \hat{\mathbf{e}}_z$, resonant with the energy

[3] Later, in Chapter 5, we see this is just an approximation and we need to compensate for the non perfect alignment of the three pairs of bias coils.

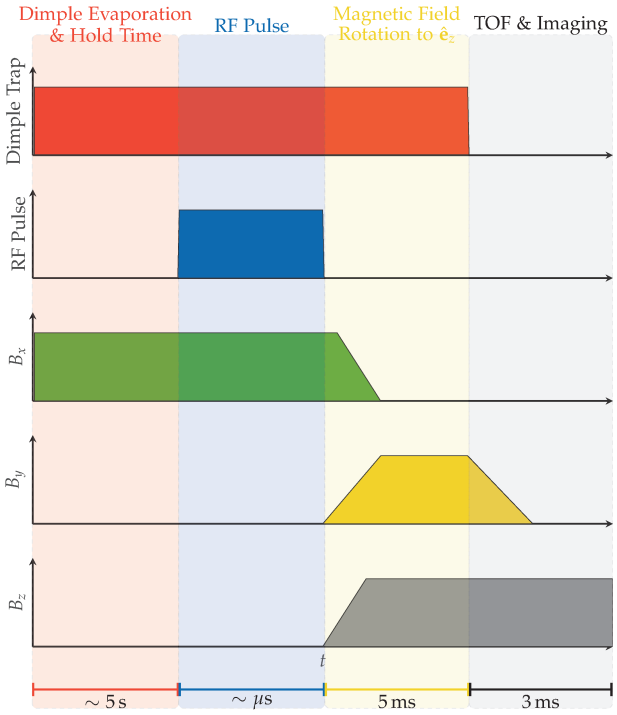

Figure 3.8.: Sketch of the experimental sequence used to observe Rabi oscillations. The magnetic bias field is initially aligned along the x axis to favour the coupling between the atoms and the RF pulse coming from a coil placed along the vertical axis. To image the atoms, we use a resonant beam circularly polarised σ_+ coming from the vertical upper window, hence we need to rotate the bias field along the z axis before taking the picture.

difference between the Zeeman sub-levels $m_F = 0, \pm 1$ due to the bias field $\mathbf{B}_{\text{Bias}} = B_{\text{Bias}}\hat{\mathbf{e}}_x$. The coupling Hamiltonian can be written as:

$$\hat{H}_{\text{RF}} = \mu_B g_F B_{\text{RF}} \cos(\omega_{\text{RF}} t)\hat{S}_z, \tag{3.10}$$

where the g_F is the Landé factor. Using the Dirac picture to rewrite the Hamiltonian in the referential frame rotating at ω_{RF} along the x axis and making the rotating wave approximation, see [30], the Hamiltonian can rewritten as

$$\hat{H}'_{\text{RF}} = \begin{pmatrix} -\delta & \Omega_{\text{RF}}/2 & 0 \\ \Omega_{\text{RF}}/2 & -q & \Omega_{\text{RF}}/2 \\ 0 & \Omega_{\text{RF}}/2 & \delta \end{pmatrix}, \tag{3.11}$$

where $p \approx 696\,\frac{\text{KHz}}{\text{G}}$ and $q \approx 277\,\frac{\text{Hz}}{\text{G}^2}$ are, respectively, the linear and quadratic Zeeman energies defined in Subsection 2.3.3 and where $\delta = \omega_{\text{RF}} - p$ is the detuning of the RF field, the Rabi frequency $\Omega_{\text{RF}} = -\frac{1}{4}\mu_B B_{\text{RF}}$ and q is the quadratic Zeeman energy. The primed

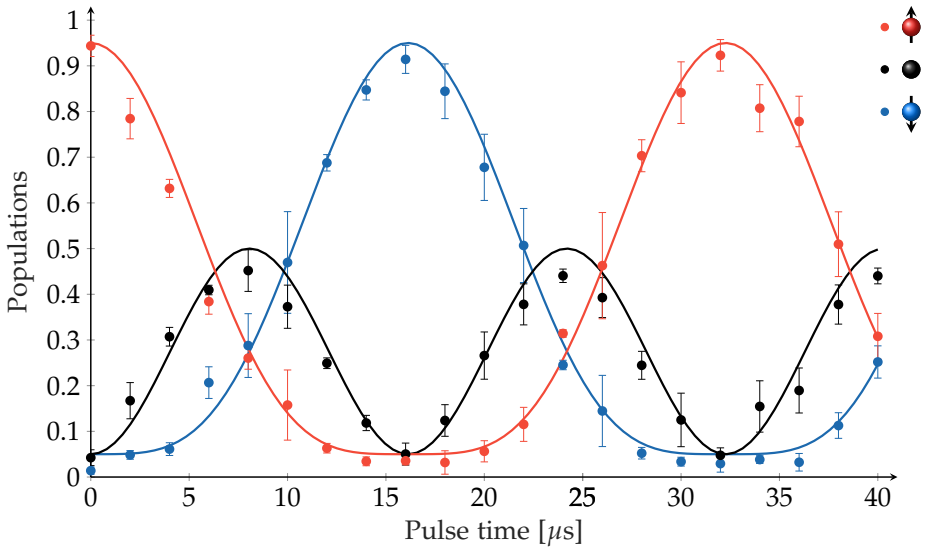

Figure 3.9.: Rabi oscillations starting from the polarised state $\xi = (1, 0, 0)$. The solid lines are a fit to the data with the theory curves of (3.14).

sign indicates the rotated Hamiltonian. In the case $\delta = 0$ the evolution of the system is described by the rotation

$$R_y = \mathrm{e}^{-i\Omega_{\mathrm{RF}} t \hat{S}_y}. \tag{3.12}$$

In the more general case of non-zero detuning, the calculations are more involved. We refer the reader to the PhD thesis [32] for a more complete discussion of the subject.
We can resolve spin oscillations up to 10 ms. However, a good control of the magnetic field bias, see 3.2.1, and a control over the magnetic noise are required to obtain reliable population measurements after a Rabi oscillation. Our main source of "noise" was 50 Hz AC field coming from the electronics surrounding the experiment. This spurious signal, indeed, acts as a noise on the applied field and then on the Zeeman sub-levels detuning δ with $\delta\omega_{50\,\mathrm{Hz}}$ amplitude and $\phi_{50\,\mathrm{Hz}}$ phase.

$$\delta = p - \omega_{\mathrm{RF}} + \delta\omega_{50\,\mathrm{Hz}} \cos(2\pi\, 50\, t + \phi_{50\,\mathrm{Hz}}) \tag{3.13}$$

To address this issue we modified our experimental sequence to start the RF pulse at a chosen phase of the 50 Hz signal. To synchronise the RF pulse starting time with a chosen value of $\phi_{50\,\mathrm{Hz}}$, we use a Schmitt trigger. The trigger reads a signal synchronised with the main one and provides a rising edge for the chosen value of the phase. Thanks to the synchronisation on the phase value $\phi_{50\,\mathrm{Hz}}$, we obtained reproducible Rabi oscillations for times much shorter than the mains period. The AC field is still present and its effect on Rabi oscillations is observable for $t \sim 10$ ms.
In Figure 3.9, there is an example of Rabi oscillations of our spin 1 system starting from

the state $\xi = (1, 0, 0)$. Using (3.12), we obtain the evolution of this state as

$$|\xi'|^2 = \begin{pmatrix} n'_{+1} \\ n'_0 \\ n'_{-1} \end{pmatrix} = \begin{pmatrix} \cos^4(\Omega_{\mathrm{RF}} t) \\ \sin^2(2\Omega_{\mathrm{RF}} t)/2 \\ \sin^4(\Omega_{\mathrm{RF}} t) \end{pmatrix} \tag{3.14}$$

where the primed symbol indicates the rotated states at $t > 0$.

3.2.3. Adiabatic rapid passage

The adiabatic rapid passage (ARP), see [30], is another well known technique in NMR with which we can transfer our atoms from a completely polarised state $m_F = +1$ to a completely polarised state in $m_F = -1$. The technique consists in dressing the atoms with a field, an RF field in our case, and making a ramp from one side of the transition to the other. We used a magnetic field ramp keeping ω_{rf} constant. This passage must be slow enough to be adiabatic with respect to the RF coupling, but faster than the relaxation processes. To describe the system evolution during the ramp, we can diagonalise the Hamiltonian (3.11); the eigenvalues of the system are roots of the characteristic polynomial:

$$\lambda^3 + q\lambda^2 + \left(\delta^2 + \frac{\Omega_{\mathrm{RF}}}{2}\right) - q\delta^2 = 0. \tag{3.15}$$

We show the three roots in Figure 3.10(b). At $\delta \ll 0$, the eigenvalues are equal to the eigenvalues of the Hamiltonian without coupling RF field $E \approx -q, \pm\delta$. We start with a polarised system with all the atoms in $m_F = +1$, that is the state with lower energy in Figure 3.10(b); following adiabatically the evolution of the eigenenergy, we end up with all the atoms in $m_F = -1$ for $\delta \gg 0$.
Experimentally, we implemented the ARP as follows. We prepare a polarised condensate with all the atoms in $m_F = +1$. We abruptly switch on the RF dressing and we set the RF frequency ω_{RF} at a constant value. Then, a sweep on the magnetic field is responsible for the populations transfer. In Figure 3.10(a), we can see how the populations change during the passage. The experimental procedure we used to implement the ARP is very similar to the one for the Rabi Oscillations and it is sketched in Figure 3.11.

3.2.4. Magnetization preparation

Loading the CDT trap and performing the evaporation in the CDT and dimple trap leads to a cloud of magnetisation $m_z \sim 0.7$. As we have already pointed out in sub-Section 2.3.4, this is a conserved quantity in our system; hence, to study our system at different magnetisation, we need some techniques to modify m_z in a reliable way. Two techniques have been implemented: the spin-mixing and the spin-distillation techniques. Here we discuss briefly the physical ideas behind these two methods and we refer the reader to the PhD thesis [161, 32, 75] and to the ref. [76] for a more involved presentation.

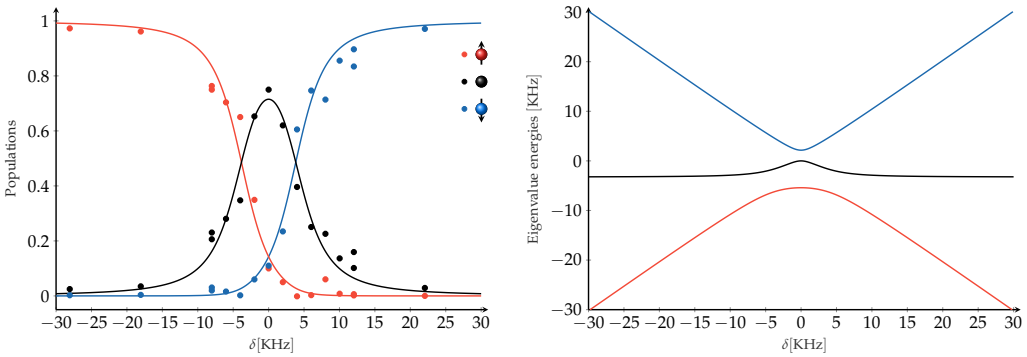

(a) (b)

Figure 3.10.: Typical adiabatic rapid passage implemented on the experiment. We start from all the atoms in the $m_F = +1$ and, maintaining a constant coupling Ω_{RF}, we ramp the magnetic in order to change the detuning of the RF field from $\delta < 0$ to $\delta > 0$. We end up with all the atoms in $m_F = -1$. In Figure 3.10(a) we can see how the three populations change during the magnetic ramp. In Figure 3.10(b), the three eigenenergies of the Hamiltonian (3.11) are sketched. We use the lowest one to perform the ARP.

Spin mixing

This method is based on the dephasing of Rabi oscillations to lower the ensemble magnetisation, from its "natural" value $m_z \sim 0.7$ to zero. We call this technique spin distillation. During the evaporation in the CDT trap, we set a bias magnetic field $\mathbf{B} = B_x \hat{\mathbf{e}}_x$ along the x axis to break the degeneracy of the Zeeman sub-levels and to have an energy difference between the levels corresponding to $\sim 200\,\mathrm{KHz}$. We set also a small magnetic gradient, to have a inhomogeneous magnetic field inside the atomic cloud. With the antenna placed on the top of the vacuum chamber, we send a long ($\sim 200\,\mathrm{ms}$) pulse with an artificially broadenend $\sim 10\,\mathrm{KHz}$-wide spectrum at resonance. The atoms undergo Rabi oscillations that dephase rapidly due to the inhomogeneities of the Rabi frequencies at different position inside the cloud and to the spin diffusion due to spin interactions. For high power, we obtain a randomised sample with the three Zeeman sub-levels equally populated. Lowering the RF power, ss we can see in Figure 3.12, we can control the magnetisation from $m_z = 0.7$ down to 0.

Spin distillation

The spin distillation technique is used to produce high polarised samples. The idea behind this method is to use a magnetic gradient to change the trapping potential for the three Zeeman sub-levels during the evaporation in the CDT trap. The magnetic gradient, produced by the MOT coils and by a bias field which determines the gradient direction, see Subsection 3.1.4, affects the $m_F = \pm 1$ components trapping potential and leave the

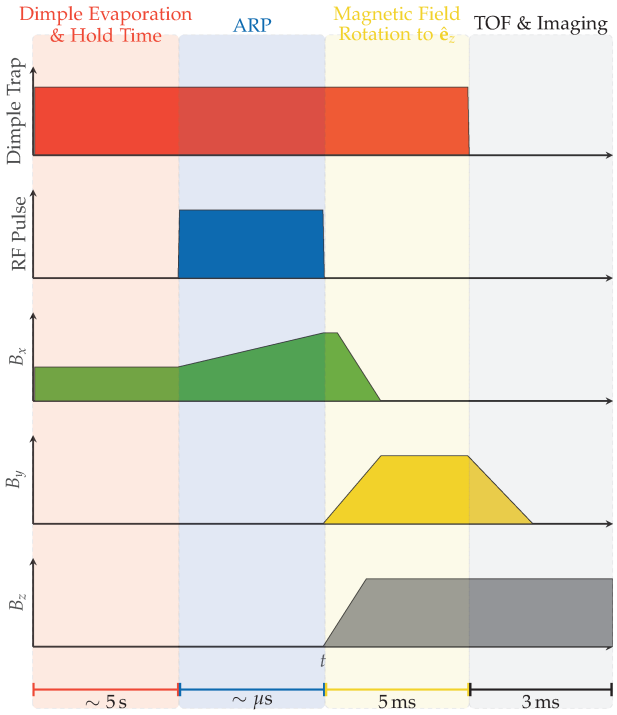

Figure 3.11.: Sketch of the typical experimental procedure used to implement the ARP. During the RF pulse, we ramp the magnetic field along the vertical direction to transfer the atoms from $m_F = +1$ to $m_F = -1$. Afterwards, we have to rotate the field along the z axis to image the atoms.

$m_F = 0$ trapping potential unchanged. If we set the magnetic gradient along the vertical direction, the potential felt by the atoms $m_F = \pm 1$ is the sum of the dipole potential given by (3.1), of the gravitational potential and of the potential given by the magnetic gradient. Depending on the sign of the magnetic gradient, it can favours the trapping of the $m_F = +1 (m_F = -1)$atoms and have the opposite effect on the $m_F = -1 (m_F = +1)$ atoms. If now we start the evaporation, the more confined atomic species is less favourably evaporated with respect to the less confined one; this effect allows us to produce high polarisation clouds with $m_z \sim 1$. The final polarisation can be controlled changing the gradient strenght.

3.3. Image characterisation

In Subsection 3.1.5 we described our imaging system and the concepts behind absorption imaging. We describe now how we calibrate this imaging system and the absorption cross-sections.

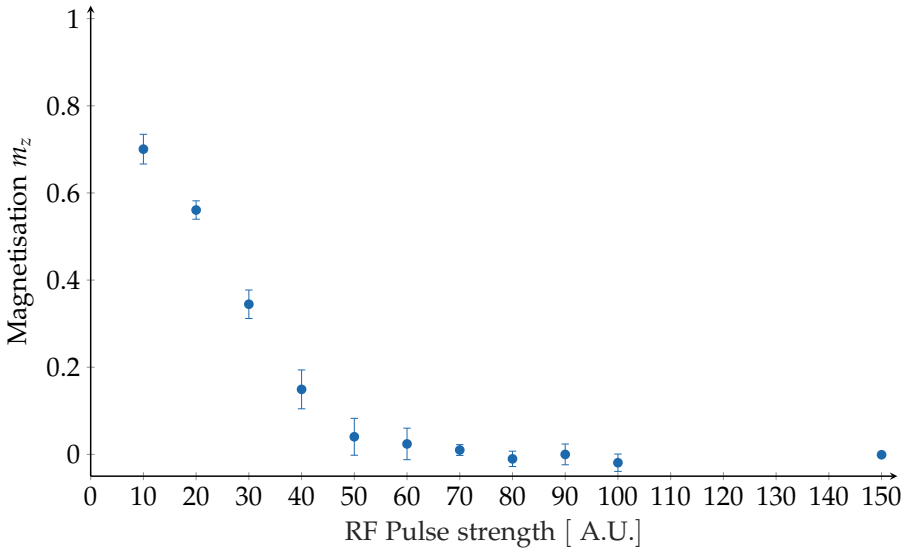

Figure 3.12.: Magnetisation obtained with different RF pulse strength during the evaporation in the CDT trap. This Spin mixing technique allow us to control the magnetisation from $m_z = 0.7 \rightarrow 0$.

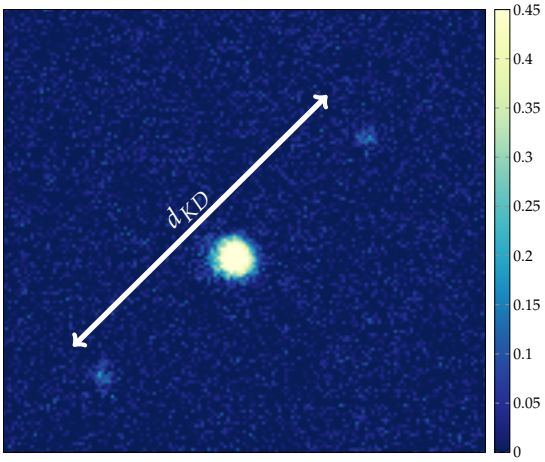

Figure 3.13.: Kapitza-Dirac diffraction observed on the 3D condensate via a 1D lattice installed on the HDT axis. From the distance d_{KD} between the two peaks we can characterise the magnification of the imaging system $M = 7.64 \pm 0.01$.

3.3.1. Magnification characterisation

The magnification of the imaging system is an important parameter if we want to measure precisely the thermodynamics quantities of our atomic cloud, as the temperature, and the size of spin domains forming in 1D. To characterise it, we installed along the HDT axis a 1D lattice with $\lambda_L = 1064\,\text{nm}$, see Figure 3.1. Thanks to the standing wave of light, the atoms of the 3D condensate in the ground state feel a potential

$$U(z) = U_0 \cos^2(kz) \tag{3.16}$$

where $U_0 = -\hbar\Omega_0^2/\Delta$, Ω_0 is the travelling wave Rabi frequency and Δ is the lattice frequency detuning from the resonance.
For a sufficiently short pulse duration $\tau \ll 1/\mu$ the effect of the potential on the atom wavefunction can be described as a phase modulation given by $\phi(z) = U(z)\tau/\hbar = \phi_0 \cos^2(kz)$, where $\phi_0 = \Omega_0^2\tau/\Delta$ is the peak amplitude. The atoms with zero momenta along z will therefore be split by the lattice into multiple components of momenta $p_n = 2\hbar k n$, with $n = 0, \pm1, \pm2\ldots$ This diffraction is known as the Kapitza-Dirac effect and it has already been observed for the first time on neutral atoms in [134] and on BECs in [55]. Figure 3.13 shows the ±1 diffraction orders from a 1D lattice obtained with a $10\,\mu$m pulse. After a TOF of $t_{\text{TOF}} = 3\,\text{ms}$, the two peaks are separated by a distance

$$d_{\text{KD}} = \frac{4h}{\lambda_L m} t_{\text{TOF}} \tag{3.17}$$

Measuring the distance between the two peaks we obtain a magnification $M = 7.64 \pm 0.01$. This compares well with the expected value of $M = 7.5$.

3.3.2. Calibration of spin-dependent cross sections

Sodium atoms present a complex electronic structure with different ground and excited levels that can be coupled by light, see [172]. A two level atom model is correct only in particular configurations as, for example, when all the atoms are in the ground state $|F = 2, m_F = +2\rangle$, we send σ_+ polarised light to couple only the $|F = 2, m_F = +2\rangle$ and the $|F' = 3, m_F = +3\rangle$ state and we neglect the possible excitations of atoms to the state $|F' = 2, m_F = +2\rangle$, from where they emit a photon to decay into the state $|F = 1, m_F = +1\rangle$. In our system, we work with cold atoms prepared in the $|F = 1\rangle$ ground state manifold of ^{23}Na and we image them by illuminating them with light resonant on the cooling transition $|F = 2\rangle \rightarrow |F' = 3\rangle$. Before imaging the atomic cloud, we have to transfer the atoms to the $|F = 2\rangle$ state. We use a pulse of $10\,\mu$s of repumping light to do that. The repumper light we use is the same used for the MOT phase: it propagates along the 6 axis and a priori all the polarisations components are present. After this pulse, we don't transfer all the atoms in the $m_F = +2$ state; hence, optical pumping effects become important to determine the density of the atomic cloud from absorption imaging.
To take in consideration all these effects, we model the effective cross-section $\sigma_{0,i}$ equal to $\sigma_{0,i} = \sigma_0/\alpha_i$ and a saturation intensity $I_{\text{sat},i}$ per each Zeeman state $i = 0, \pm1$. The total

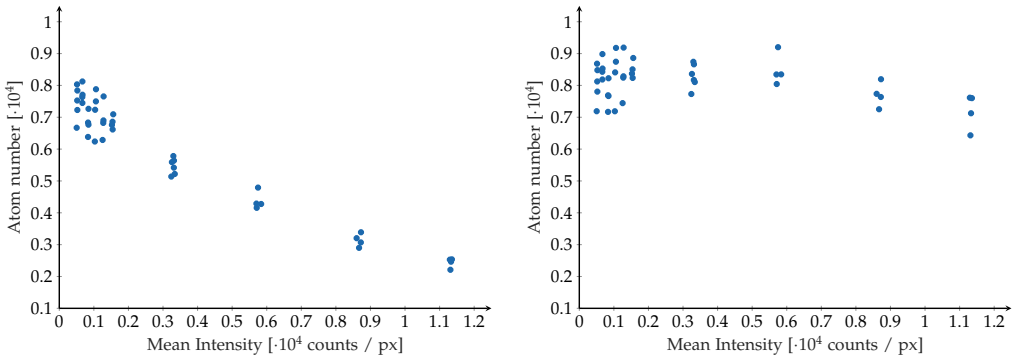

(a) (b)

Figure 3.14.: Results of the measurements used to obtain the saturation intensity for the $m_F = +1$ Zeeman state. In (a), we plot the atom number, integrated over a box of area 60×60 pixels, as a function of the imaging probe intensity. In (b), we plot the integrated atom number after we have minimised the change of the atom number with the probe intensity by changing the $I_{\mathrm{sat},+1}$ value. From these data, we obtained $I_{\mathrm{sat},+1} = 5057 \pm 171$. The number of counts are linked to the intensity via $I = \frac{\hbar\omega}{A\tau}\eta \cdot \mathrm{counts}$, where A is the pixels area, η is the CCD detectivity and τ is the imaging pulse duration. See Section 3.4.

cross-section (3.5) becomes then

$$\sigma = \sum_i \frac{\sigma_0}{\alpha_i} \frac{1}{1 + \frac{I}{I_{\mathrm{sat},i}} + \left(\frac{2\delta}{\Gamma}\right)^2}, \tag{3.18}$$

where α_i and $I_{\mathrm{sat},i}$ are effective parameters adjusted from the data.
Since we implemented a Stern-Gerlach imaging, see 3.1.4, from now on we consider the three Zeeman states separately and we consider their analysis in three separated regions[4]. Therefore, for each Zeeman state, we obtain from the Lambert-Beer law a density

$$n_i = -\frac{\alpha_i}{\sigma_0} \log\left(\frac{I_1^i}{I_2^i}\right) + \frac{I_2^i - I_1^i}{I_{\mathrm{sat},i}/\alpha_i} \tag{3.19}$$

where the 3 α's and the 3 saturation intensities have to be characterised experimentally. In the following we present how we measure these parameters.

The saturation intensities

Following the method presented in [151], we measure the atom number at different imaging probe intensities. A typical result of this measurement is presented in Figure 3.14(a). To obtain the saturation intensities we look at (3.19). At low probe intensities, the

[4] In Chapter 4 we analyse the case of overlapping atomic clouds.

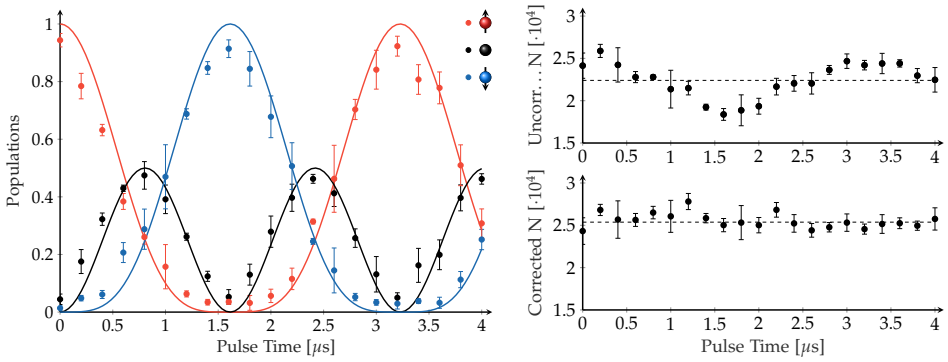

(a) (b)

Figure 3.15.: (a) Rabi oscillations used to determine the spin-dependent imaging cross-sections; (b) the unweighted spin populations sum to a total atom number that varies with time and (c) by properly weighting the spin-components by the spin-dependent imaging cross sections we obtain a total atom number that is nearly constant. We found the values of the ratios $\alpha_{+1}/\alpha_0 = 0.88(4)$ and $\alpha_{-1}/\alpha_{+1} = 1.39(5)$ we obtain the lower figure.

logarithmic part of (3.19) dominates, at high intensities the atomic density becomes $n_i \approx \alpha_i(I_2^i - I_1^i)/I_{\mathrm{sat},i}$. Hence, since the atom number must be constant with respect to the probe intensity, if (3.19) describes well the atoms density[5] , we identify the saturation intensity $I_{\mathrm{sat},i}$ as the value at which the atomic density determined by (3.19) gives a constant atom number as a function of probe intensity . In Figure 3.14(b) we can see the result of this process on the data for a cloud in $m_F = +1$. We repeat for $m_F = -1, 0$.

The spin-dependent cross-sections

To determine the spin dependent imaging cross-sections we take advantage of RF-driven Rabi oscillations. During the spin rotation, the relative spin populations vary as described in Subsection 3.2.2. However the total number of atoms, defined as the sum of atoms in the three Zeeman sub-levels, remains constant.
Being a total number-conserving process, Rabi oscillations allow us to evaluate the spin-dependent cross-sections in a straight-froward way. We can set the values of the ratio between different α's to have a constant number of atoms over time. In Figure 3.15(a) we present an example of this kind of measurement. In Figure 3.15(b), the total number of atoms is plotted before and after the correction via the ratios α_{+1}/α_0 and α_{-1}/α_{+1}.

The Absolute atom number

The final step consists in the calibration of the absolute atom number. To do that, we need a quantity that we can measure absolutely with the absorption imaging. In our

[5] We obtain the atom number by simple integration of the measured atomic density.

experiment we use the Thomas-Fermi radius of the cloud, which depends on atom number as $R_{\mathrm{TF}} \propto N^{1/5}$. Typical atom numbers in our experiment are not sufficiently high to truly reach the Thomas-Fermi regime and therefore we rely on a full 3D Gross-Pitaevskii (GP) simulation of the density distribution of a pure condensate. Using the imaginary-time spectral-splitting method, we compute the ground state of the condensate in the trap; afterwards we use real time evolution to simulate the TOF expansion of the density distribution. We run the simulation for different atom numbers and we fit the synthetic data with a Thomas-Fermi distribution.
In the experiment, we produce condensates with different atom numbers by changing the MOT loading time and we fit the density profile with the same distribution used for the simulated data.
To make the comparison between the two curves, we fit the simulated Thomas-Fermi radius as a function of atom number with a power law of equation

$$R_{\mathrm{GP}} = \sqrt{a^2 + b^2(\alpha_0 N)^c}. \tag{3.20}$$

The parameters b and c take into account the mean field potential, while the parameter a takes into account the quantum pressure which is not negligible for the small atom number we have in the BEC. In the Thomas-Fermi limit, we have $a = 0$, $b = \frac{2\mu_{\mathrm{TF}}}{m\omega^2}$ and $c = 2/5$. We set the parameter α_0 , the same can be done for $\alpha_{\pm 1}$, by adjusting the measured curve to the power law fitted on the synthetic data. In Figure 3.16 we can see a measurement to calibrate α_0. In Figure 3.16(a) we can see the data obtained from the GP simulation fitted by the power law (3.20); the two curves correspond to the Thomas-Fermi radius along two perpendicular axis on the imaging plane. In Figure 3.16(b), we see the measured Thomas-Fermi radius after the adjustment of the α_0 parameter.

3.4. Image analysis

Imaging the atoms with laser light allow us to obtain absolute measurements of several thermodynamic quantities. However, the high spatial coherence of the light entails diffraction and interference effects that we observe as intensity patterns (fringes) on the CCD images. Static intensity patterns are directly eliminated by our imaging analysis; non-static intensity patterns remain visible on the optical density images and represent a noise source we need to minimise. Taking the two images with the shortest delay possible helps in reducing the noise on the final images. In this section we model the noise observed on the absorption images and we present the two methods used to reduce it when analysing the images.
We write the intensities in counts, such that $I = \frac{\hbar\omega}{A\tau}\eta \cdot \mathrm{counts}$, where A is the pixels area, η is the CCD detectivity, τ is the imaging pulse duration and $\hbar\omega$ is the photon energy. Therefore, the counts are the number of photons arrived on a certain pixel detected by the CCD divided by η.

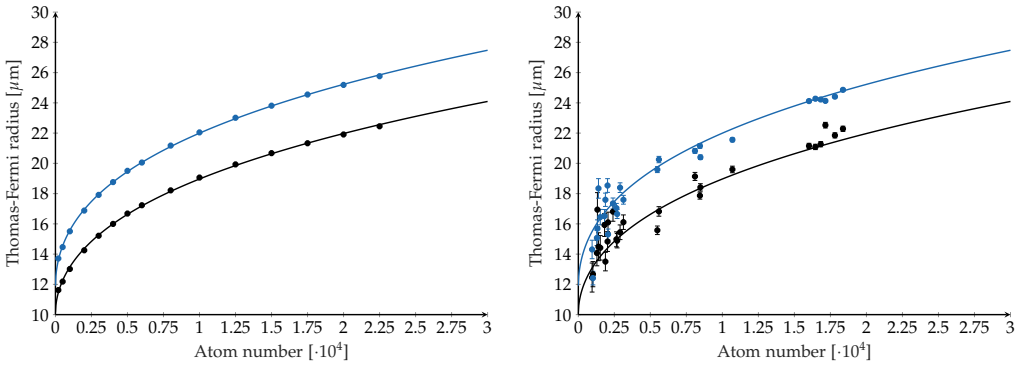

(a) (b)

Figure 3.16.: Comparison between the synthetic and measured data for the Thomas-Fermi radius as a function of atom number. In (a) we can see the data generated via a GP simulation and fitted with the *adhoc* function (3.20). In (b), the measured Thomas-Fermi radius are compared to the result of the synthetic data fit to obtain a value for $\alpha_0 = 2.44(22)$. The blue and black curve corresponds to the radii along the X and Y direction of our experiment. See Figure 3.1.

3.4.1. Noise modelisation

Looking at the absorption images, we observe two noise typologies: the shot noise, which comes from the intensity fluctuations of the laser light intensity, and fluctuations of the intensity profile. The major source of noise comes from a global scaling of the intensity pattern. This change of probe intensity can be due to several technical sources, as, for example, fluctuations in the probe fibre coupling efficiency or fluctuations of the probe polarisation.
We model the probe intensity pattern as:

$$I_i(\mathbf{r}) = f_i(\mathbf{r})\Big[I_0 + \delta I_i(\mathbf{r})\Big], \tag{3.21}$$

where $i \in \{1, 2\}$ labels the first and second image for the absorption imaging, I_0 is the average intensity, where the intensity has been averaged over the CCD area considered and the different realisations, $f_i(\mathbf{r})$ are random variables describing the probe light pattern and $\delta I_i(\mathbf{r})$ is taking into account the shot noise.
We model the shot noise defining for each pixel $\mathbf{r}$ a Poisson distribution of standard deviation $\sqrt{I_0 \langle f_i(\mathbf{r})\rangle}$.
The random variables $f_i(\mathbf{r})$ are more difficult to model because their properties depend on the experimental conditions of the moment at which the images have been taken.
Considering a static pattern in which the noise comes from a global scaling of the intensity pattern, we can set $f_1(\mathbf{r}) = f(\mathbf{r})$ and $f_2(\mathbf{r}) = (1 + \alpha) f(\mathbf{r})$ where α is another random variable which describe these intensity fluctuations. From (3.6), at the first order , we

obtain the fluctuations of the measured column density

$$\Delta n(\mathbf{r}) = \frac{\alpha}{\sigma}\left(1 + f(\mathbf{r})\,\frac{I_0}{I_{\text{sat}}}\right) + \frac{\delta I_1 - \delta I_2}{I_0\,\sigma}\,\frac{1}{f(\mathbf{r})}\left(1 + f(\mathbf{r})\,\frac{I_0}{I_{\text{sat}}}\right). \tag{3.22}$$

We now compute the associated error on the atom number. We select on the CCD three areas corresponding to the three atomic clouds divided in TOF by the Stern-Gerlach TOF, see Subsection 3.1.4. These rectangular boxes RB have sizes $\sim 30 \times 180$ pixels for the 1D trap. In this case[6]

$$\langle N\rangle_{RB} \approx W \times H\,\frac{\langle\alpha\rangle}{\sigma}\left(1 + \frac{I_0}{I_{\text{sat}}}\right) \approx 2640\,\text{atoms} \tag{3.23}$$

where we have taken $\langle\alpha\rangle \sim 0.01$, $RB = 30 \times 180$ pixels, $I_0 = 704$ counts and σ is the cross-section for the $m_F = +1$ Zeeman sub-levels. This spurious offset (which changes from one pixel to the next) is already comparable to the mean atom number.
We compute the variance of (3.22) paying attention to divide shot noise and speckle pattern noise; indeed, while shot noise is uncorrelated from pixel to pixel, the speckle pattern is correlated. Considering the rectangular box RB, we obtain

$$(\Delta N_{RB})^2 = (W \times H)^2\,\frac{(\Delta\alpha)^2}{\sigma^2}\left(1 + \frac{I_0}{I_{\text{sat}}}\right)^2 + (W \times H)\,\frac{1}{\sigma^2}\,\frac{2}{I_0}\left(1 + \frac{I_0}{I_{\text{sat}}}\right)^2. \tag{3.24}$$

where the first term takes into account the speckle pattern fluctuations and the second one the shot noise. From the previous equation it is clear that, while the speckle pattern noise variance scales as $(\Delta N_{RB,\text{speckle}})^2 \propto N^2$, the shot noise scales as $(\Delta N_{RB,\text{Sn}})^2 \propto N$. In Figure 3.17, the standard deviation of the noise on the atomic density is presented as a function of the RB rectangular box size. We changed RB size by setting $H = 30$ pixels and changing the box width W. On the x axis, we plot the area divided by 30. In blue is plotted the noise coming from the integration of the absorption images, it scales linearly with the area, indicating that the correlated noise is dominant. In red and green we have the same data corrected in two ways we describe in the next Subsection. The Upper black line represents the noise we expect from (3.24), the lower black line represents the shot noise.

3.4.2. Noise reduction

In order to reduce the noise coming from the shot noise and the intensity pattern noise we use two either of two algorithms: the *rescaling* algorithm and the best reference picture algorithm.

The rescaling algorithm is based on the assumption that, during the time between the two pictures I_1 and I_2 are taken, the intensity pattern do not change and the main

[6] We have taken $\langle f(\mathbf{r})\rangle = 1$, since the average of the intensity over the considered CCD area for the different realisations is equal to I_0 and since the considered box is large enough. It has been verified this is true for boxes down to 60 pixels area, see [47].

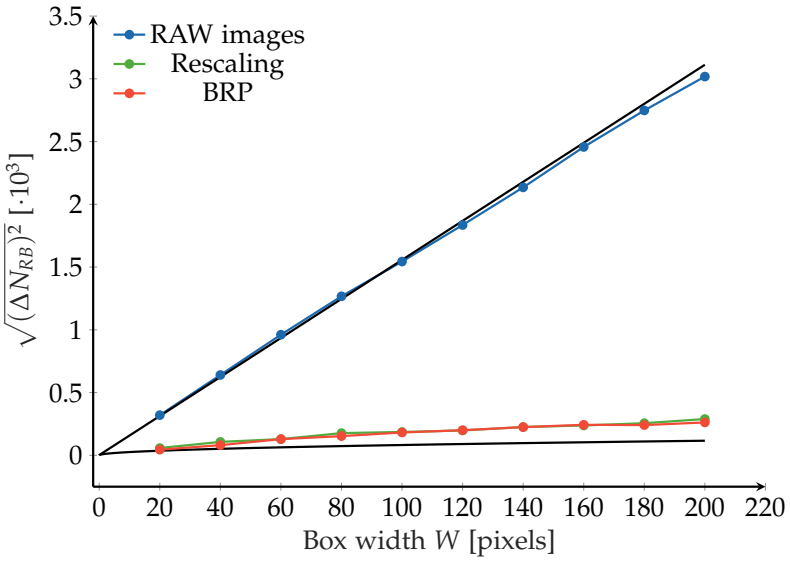

Figure 3.17.: Standard deviation of the noise on the atomic density measured on empty images as a function of the rectangular box RB area. The box size $W \times H$ has been changed keeping the $H = 30$ pixels constant and varying the box width W. The data were taken at $I \sim 0.1\, I_{\mathrm{sat}}$. In blue we can see the noise obtained by integrating the absorption images, in red the same data analysed with the best reference picture algorithm and in green with the rescaling method[7]. The upper black lines indicates the noise expected from (3.24), the lower one the shot noise.

contribution to the noise comes, as in the previous Subsection, from a variation of the global intensity. This variation can be described by the parameter $\alpha, definedas\alpha = \frac{\sum_{i,j} I_{1,i,j}}{\sum_{i,j} I_{2,i,j}} - 1.$(3.25)To obtain the optical density from a couple of images I_1 and I_2, we compute α in the region showed in Figure 3.18 and we rescale the intensity of the first image accordingly. In Figure 3.17 we see that the algorithm reduces down to values comparable with the shot noise. This is true also for big boxes, where we expect the correlated part of the noise to be more important and the rescaling algorithm to be less efficient. This is due to the low imaging intensity at which these data have been taken, $I \sim 0.1\, I_{\mathrm{sat}}$. In Figure 3.19 we see the algorithm works well at low intensities, where the shot noise is important, but become less and less effective as the intensity increases and the correlated noise becomes more important. The rescaling algorithm works better for low intensities, where the shot noise is dominant and the optical density (3.6) is described by the $\sim \log$ part.

We implemented the best reference picture algorithm, based on the works [103, 129, 128], to reduce the noise coming from the intensity pattern variation. The method consists in constructing a best second image I_2 from all the second images composing a particular

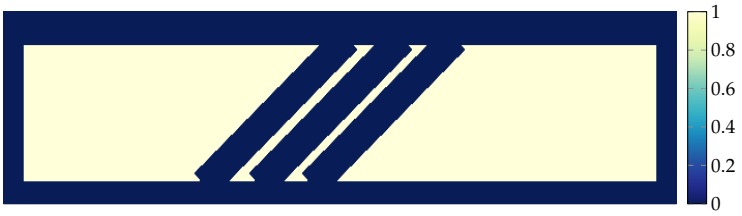

Figure 3.18.: Example of a typical image with the areas considered for the noise reduction algorithms. The continuous blue region following the image edges and in the centre of the image represents the area we don't consider because it contains the atomic clouds and some unwanted features as diffraction from the razor blade we use for the frame transfer technique.

data set:

$$I_{2,\mathrm{best}} = \sum_k c_k I_{2,k}. \tag{3.26}$$

The c_k coefficients are obtained by minimising the quantity $\sum(I_1 - \sum_k c_k I_{2,k})^2$, where the first sum is over the area showed in Figure 3.18. If there is a correlation between the intensity pattern inside and the outside the analysed regions, the algorithm is able to reduce it. In Figure 3.17 we see the algorithm reduces the noise efficiently also increasing the box size. In Figure 3.19 we see that it works well also at high intensities, where the optical density (3.6) is described by the $I_2 - I_1$ part.
In Figure 3.19 we see a minimum of the noise at $I \sim I_{\mathrm{sat}}$. The study of the 3D condensate presented in Chapter 4 is done at $I \sim 0.1\, I_{\mathrm{sat}}$, to minimise the noise coming from the $I_2 - I_1$ part of the optical density and use a fitting procedure to extract temperatures and atoms numbers. To study the 1D configuration, as presented in Chapter 5 and Chapter 6, we used instead a $I \sim 0.3\, I_{\mathrm{sat}}$ to work with an higher signal-to-noise ratio.

3.5. From the 3d to the 1d geometry

To produce the 1D condensate, we start from the 3D condensate produced following the sequence sketched in Figure 3.4. Then, we trap the cloud in a single red detuned laser propagating along the horizontal direction (HDT beam, see Figure 3.1) switching off the CDT laser. In this Section we describe how we implemented this transfer.

3.5.1. The adiabatic transfer

The transfer from the 3D to the 1D trap is a crucial passage in our experimental sequence and it has required some effort to produce a 1D condensate with a negligible breathing motion and low phase fluctuations (low T).
Breathing modes are easily excited in a quasi-1D trap with trapping frequency $\omega_z = 2\pi\, 4.6\,\mathrm{Hz}$. Therefore, to reduce their excitations as much as possible, we need to align the two beams (HDT and VDT) to have their focus at the same position and we need to

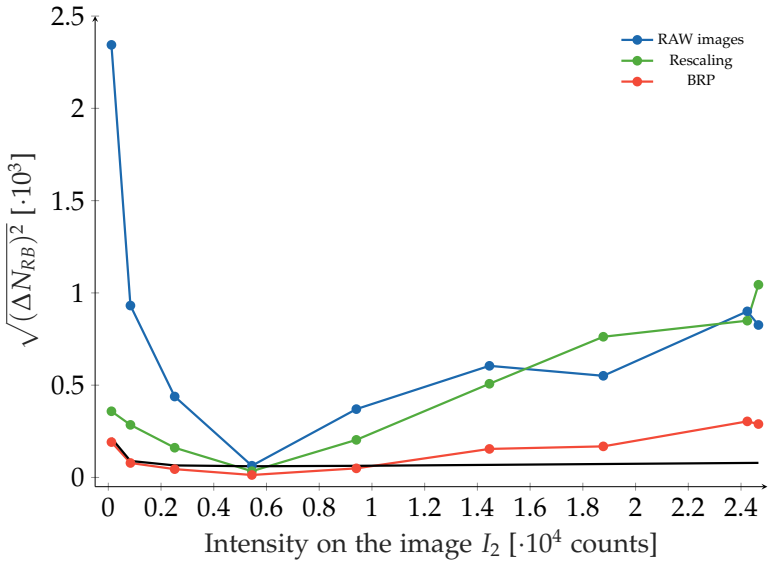

Figure 3.19.: Standard deviation of the noise on the atomic density measured on void images as a function of the probe imaging intensity. In blue we see the noise obtained by integration of the absorption imaging, in red the same data analysed with the best reference picture algorithm and in green with the rescaling method. The black line represents the shot noise. We can see a minimum of the noise at $I_{\text{sat}} = 5000$ counts, see Figure 3.14.

switch off the VDT laser as smoothly as possible. In this way, making the transfer as smooth as possible, we reduce the possible heating of the cloud and therefore we reduce also the phase fluctuations after TOF.
Our intensity lock allows us to control the VDT laser power down to $\sim 2.4\,\mu$W. At this power, the VDT beam produces on the atoms a trapping potential with frequency ~ 4 Hz along the weak axis. This trapping frequency is near to the one due to the HDT laser. Therefore, if we lower the laser power until this lower bound value and then we switch it off abruptly, the atoms feel an important sudden change in the trapping potential which excites breathing modes and heat up the cloud.
There are different techniques we could use to solve this problem: in the work [152], the authors implemented an adiabatic short cut to freeze the cloud dynamic in a 1D system. An alternative method to switch off the VDT laser as adiabatically as possible is to lock the laser power with two photodiodes; one photodiode working at high powers and the second one at low powers.
We decided to solve the problem in another way, implementing the system sketched in Figure 3.20. The laser power is controlled by an AOM. The laser lock reads the photodiode signal and controls the AOM via an AOM driver. We put an attenuator[8] after the AOM Driver and a Sample&Hold circuit between the laser lock and the AOM Driver. In this

[8] Mini-circuits ZX73-2500-S+

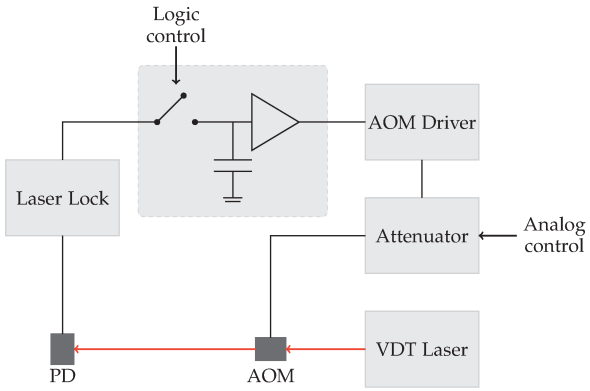

Figure 3.20.: Sketch of the circuit implemented for the atom transfer from the 3D to the 1D trap geometries. The power laser lock reads the photodiode (PD) signal and regulates the laser power via an AOM driver and the AOM. The Sample&Hold circuit between the laser lock and the AOM driver is used to keep the signal fed to the AOM driver constant to value coming from laser lock when the switch is opened. Thanks to it we can prevent erratic behaviour of the laser lock when the power becomes low. From that moment, the RF power fed to the AOM is controlled by the attenuator.

way, when the Laser lock arrives at the lowest value at which it can lock, we use the Sample&Hold system to prevent the lock from changing the laser power. Then, we control the AOM via the attenuator.
In Figure 3.21 is sketched the experimental sequence we use to transfer the atoms from the 3D to the 1D trap geometries.

Varying the time during which we lower the VDT power with the attenuator we tried to minimise the excitations of breathing modes and the cloud heating up due to the transfer. In Figure 3.22 and Figure 3.23 we can see, respectively, the dynamics of the cloud and the mean square density fluctuations after TOF for different VDT attenuation times.
As we can see from Figure 3.22, after and attenuation time of 50 ms, blue in the picture, the cloud presents a clear breathing mode; a fit of the curve gives as oscillating frequency $\omega = 2\pi\, 7.3\,\mathrm{Hz}$, which is consistent with the frequency of the first breathing mode at $\omega_B = \sqrt{5/2}\,\omega_z$, see [175]. After 500 ms and 5 s there is no clear sign of dynamics. Moreover, when we measure the position of the cloud centre from shot to shot, we see fluctuations of $\sim 8.5\,\mu$m, which is near to the fluctuations on the cloud position that we observe for 500 ms and 5 s attenuation time.
The mean square density fluctuations plotted in Figure 3.23 have been determined by fitting the cloud with a Thomas-fermi profile and then computing the standard deviation in a region centred on the cloud centre and of length half a Thomas-Fermi radius. The error bars correspond to the standard deviation of the averages. In red is shown the standard deviations of the profiles obtained from void images (images without atoms):

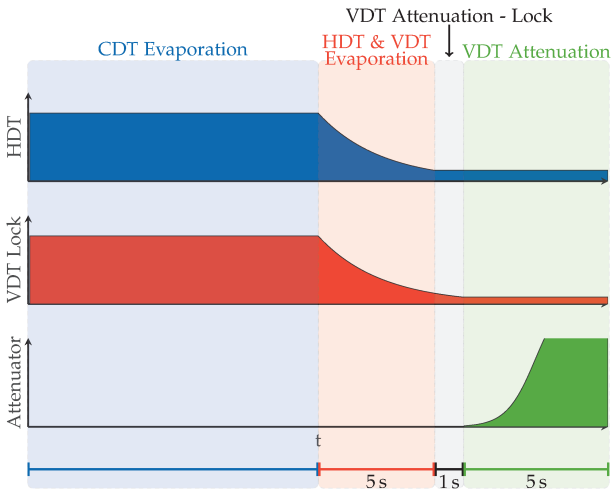

Figure 3.21.: Sketch of the experimental sequence we use to transfer the atomic cloud from the 3D to the 1D trap geometries. The sequence is divide in 3 steps: *i.*) we produce the 3D condensate, *ii.*) we keep the HDT power constant and we reduce further the VDT power via the lock, *iii.*) we isolate the lock with the Sample&Hold circuit and we attenuate to zero the VDT power via the attenuator.

every point correspond to the standard deviation of the optical density (computed in atoms number using (3.6)) , divided by the peak density of the average profile measured at each attenuation time. It represents the limit at which we can not divide phase fluctuations fringes on the profiles from the fringes coming from the imaging. At attenuation times lower than 1 s there is a clear signal. Then, at attenuation times longer then 4 s, we reach the lower bound.
Thanks to these measurements we have chosen to set the attenuation time at 5 s. In Appendix A we discuss what we expect from this kind of transfer supposing it adiabatic. We make an estimate for a BEC in a box for simplicity. For our experimental parameter we obtain a final temperature $T/gn \approx 3.4$ and $\mu/gn \sim 1$, which corresponds to $T \sim 21\,\mathrm{nK}$ for a chemical potential $\mu = h \cdot 130\,\mathrm{Hz}$. For $N = 2 \cdot 10^4$ atoms and $\omega_z = 2\pi\, 4.6\,\mathrm{Hz}$ the phase temperature $T_\phi = 73\,nK$, then $T/T_\phi \approx 0.3$.
After the transfer, we end up with a condensate of $N \sim 2 \cdot 10^4$ atoms when $\omega_z \sim 2\pi\, 4.6\,\mathrm{Hz}$.

3.5.2. Characterisation of the trap frequencies

Since the atoms are trapped in a single beam, the ratio between the radial and the axial trapping frequencies $\omega_\perp$ and ω_z is fixed by the beam wavelength and waist and remains constant as we change the laser power.

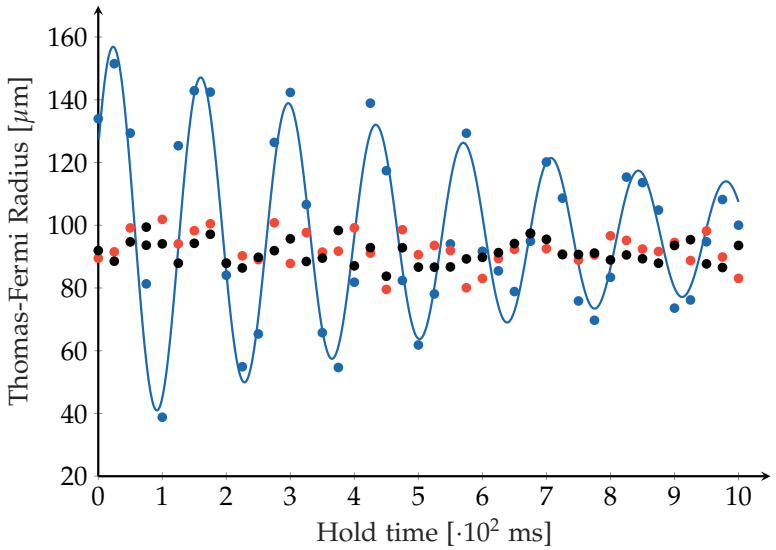

Figure 3.22.: Cloud dynamic after the attenuation. In blue is represented the breathing we obtain at 50 ms attenuation time. In red and black, respectively, the dynamic after 500 ms and 5000 ms. In blue there is also a fit of the breathing mode by a sinusoidal function multiplied by an exponential. We obtain an oscillation frequency $\omega_b = 2\pi\, 7.3\,\text{Hz}$ and a characteristic time for the decaying exponential of $\tau = 1048\,\text{ms}$.

Considering a trapping potential similar to (3.1),

$$V_{\text{HDT}} = V^0_{\text{HDT}} \left(\frac{\omega_0}{\omega(z)} \right)^2 \exp\left(-2\frac{x^2+y^2}{\omega^2(z)} \right) \tag{3.27}$$

where V^0_{HDT} is equal to V^0_{CDT}, see (3.1), for the HDT laser. The ratio between the two trapping frequencies is given by

$$\frac{\omega_z}{\omega_\perp} = \frac{\lambda}{\pi\sqrt{2}\omega_0} \approx 0.012 \tag{3.28}$$

considering $\lambda = 1064\,\mu$m and $\omega_0 = 20.3\,\mu$m. Therefore, if we assume a gaussian mode without imperfections, to characterise our single beam dipole trap, it suffices to measure the trapping frequencies only along the axial direction. Figure 3.24 shows the results of the measurements of the trap frequency along **z**. To measure them, we produce the 1D condensate and we use a magnetic field gradient along the cloud weak axis to excite dipole oscillations. We measured also the trap frequencies along the radial direction finding good agreement with the frequencies calculated from (3.28). Typical axial frequencies are $\omega_z = 2\pi\, 4.6\,\text{Hz}$ and $\omega_\perp = 2\pi\, 383.3\,\text{Hz}$.

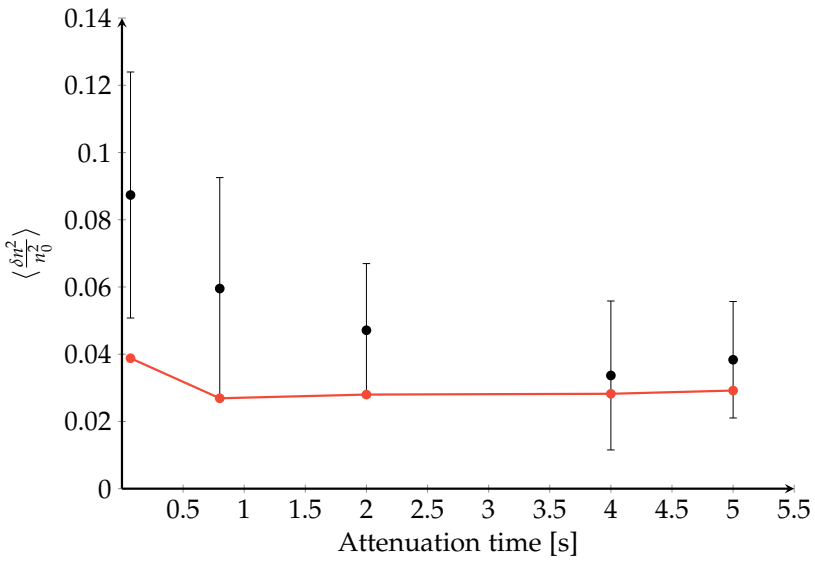

Figure 3.23.: Mean square density fluctuations after TOF as a function of the attenuation time. In red we show $\langle \delta n^2 \rangle$ computed from empty images, divided by the peak density of the average profile measured at each attenuation time.

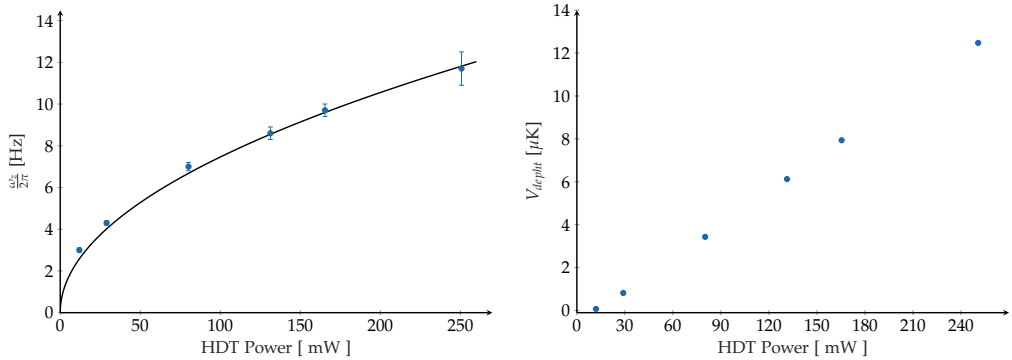

Figure 3.24.: Measured trap frequencies and computed trap depth. In (a) we presented the trap frequencies measured inducing a dipole oscillation of the condensate along the **z** axis. Fitting the data, we are able to measure the beam waist $\omega_0 = 20.3\,\mu$m. In (b) we sketched the trap depth computed from the measured trap frequencies and the waist. The gravitational potential is taken into account.

4. Stepwise Bose-Einstein Condensation in a Spinor Gas

This third chapter is devoted to the presentation of the article "Stepwise Bose-Einstein Condensation in a Spinor Gas", [48], published during my thesis. Since the work is already presented in a exhaustive way in the article and since more details can be found in the PhD thesis [47], we decided here to report the article without modifications, including the supplementary materials.

4.1. Article

Multi-component quantum fluids described by a vector or tensor order parameter are often richer than their scalar counterparts. Examples in condensed matter are superfluid ^{3}He [185] or some unconventional superconductors with spin-triplet Cooper pairing [127]. In atomic physics, spinor Bose-Einstein condensates (BEC) with several Zeeman components m_F inside a given hyperfine spin F manifold can display non-trivial spin order at low temperatures [65, 131, 173, 169]. The macroscopic population of the condensate enhances the role of small energy scales that are negligible for normal gases. This mechanism (sometimes termed *Bose-enhanced magnetism* [169]) highlights the deep connection between Bose-Einstein condensation and magnetism in bosonic gases, and raises the question of the stability of spin order against temperature.

In simple cases, magnetic order appears as soon as a BEC forms. Siggia and Ruckenstein [163] pointed out for two-component BECs [163] that a well-defined relative phase between the two components implies a macroscopic transverse spin. BEC and ferromagnetism then occur simultaneously, provided the relative populations can adjust freely. A recent experiment confirmed this scenario for bosons with spin-orbit coupling [79]. This conclusion was later generalized to spin-F bosons without [188] or with *spin-independent* [40] interactions. These results indicate that without additional constraints, bosonic statistics favors ferromagnetism.

In atomic quantum gases with $F > 1/2$, this type of ferromagnetism competes with

spin-exchange interactions, which may favor other spin orders such as spin-nematics [169]. Spin-exchange collisions can redistribute populations among the Zeeman states [26, 159, 96], but are also invariant under spin rotations. The allowed redistribution processes are therefore those preserving the total spin, such as $2 \times (m_F = 0) \leftrightarrow (m_F = +1) + (m_F = -1)$. For an isolated system driven to equilibrium only by binary collisions (in contrast with solid-state magnetic materials [102]), and where magnetic dipole-dipole interactions are negligible (in contrast with dipolar atoms [138]), the longitudinal magnetisation m_z is then a conserved quantity. This conservation law has deep consequences on the thermodynamic phase diagram.

The thermodynamics of spinor gases with conserved magnetisation has been extensively studied theoretically using various assumptions and methods [73, 192, 82, 100, 182, 145, 83]. A generic conclusion is that Bose-Einstein condensation occurs in steps, where BEC occurs first in one specific component and magnetic order appears at lower temperatures when two or more components condense. Natural questions are the number of steps that can be expected, and the nature of the magnetic phases realized at different temperatures.

In this Letter, we report on the observation of multi-step condensation in an antiferromagnetic $F = 1$ condensate of sodium atoms. Fig. 4.1 illustrates four situations that occur when lowering the temperature starting from a normal Bose gas. Without loss of generality, we focus in this work on the case of positive magnetisation, given that the case of $m_z < 0$ can be deduced by symmetry. In all cases with $m_z \neq 0$, we find a sequence of transitions where different Zeeman components condense at different temperatures. Depending on the applied magnetic field B and on the magnetisation, we find either two or three condensation temperatures. The purpose of this paper is to explore this rich landscape of transitions in a bosonic spinor system and to elucidate the role of atomic interactions.

The present work is to the best of our knowledge the first comprehensive measurement of thermodynamic properties of spinor condensates with conserved magnetisation. Previous experimental works exploring finite temperatures in spinor gases mostly studied spin dynamics in thermal gases [139, 62, 41, 125], or demonstrated cooling of a majority Zeeman component by selective evaporation of the minority components [132, 126]. The realisation of dipolar spinor gases with free magnetisation [138] was limited to the study of spin-polarised condensed phases in equilibrium due to dipolar relaxation. More recently, a gas of spin excitations in a spin-polarised ($m_z \approx 1$) ferromagnetic Bose-Einstein condensate was observed to equilibrate and even condense at sufficiently low temperatures [42].

Our experiments are performed with ultracold ^{23}Na atoms confined in a crossed optical dipole trap (ODT). The longitudinal magnetisation $m_z = (N_{+1} - N_{-1})/N$ acts as an external control parameter independent of the externally applied magnetic field B. Here, N_{m_F} is the reduced population in Zeeman state m_F and N the total atom number. We vary m_z between unmagnetised ($m_z \approx 0$) and fully magnetised samples ($m_z \approx 1$) using a preparation sequence performed far above T_c [76]. An applied magnetic field B shifts the single-atom energy by $\Delta E_{m_F} = pm_F + q(m_F^2 - 1)$. The conservation of magnetisation makes the linear Zeeman effect $\propto p$ irrelevant in the equilibrium state. The quadratic Zeeman energy (QZE), which lowers the energy of $m_F = 0$ with respect to $m_F = \pm 1$, is

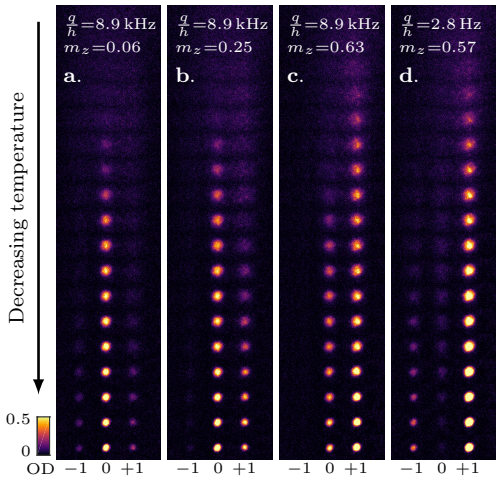

Figure 4.1.: Illustration of stepwise Bose-Einstein condensation in antiferromagnetic spin 1 gases. Each column is formed by juxtaposing absorption images of spin distributions with monotonically decreasing temperature T from top to bottom. The quadratic Zeeman energy q and low-T magnetisation m_z are indicated at the top of each column. **a.** Only $m_F = 0$ condenses ($m_F = 0, \pm 1$ are the three Zeeman states). **b.** (**c.**) For low (high) magnetisations, $m_F = 0$ ($m_F = +1$) condenses first followed by $m_F = +1$ ($m_F = 0$). **d.** For small q and high m_z, $m_F = +1$ condenses first followed by $m_F = -1$, while $m_F = 0$ does not condense.

the relevant term, and is given by $q = \alpha_q B^2$ with $\alpha_q/h \approx 277\,\mathrm{Hz/G^2}$ for sodium atoms.

The depth V_0 of the ODT determines the temperature T and total atom number N for a given V_0. We find that the magnetisation m_z also varies with V_0 (by up to 15 %), a byproduct of evaporative cooling. Once a condensate forms in one of the Zeeman components, evaporation tends to eliminate preferentially atoms in the other Zeeman states. The evaporative cooling dynamics is very slow compared to the microscopic thermalisation time on which the gas returns to thermal equilibrium. As a result, the kinetic equilibrium state for the quantum gases studied in this work is still determined by a magnetisation-conserving Hamiltonian. Furthermore, the ODT is tight enough such that a condensate forms in the so-called single-mode regime [191], where the spatial shape of the condensate wavefunction is independent of the Zeeman state. In the following, we characterise our data for a given value of q by an evaporation "trajectory" $(N, T, m_z)_{V_0}$, taking four experimental realisations for each point in the trajectory.

Absorption images as shown in Fig. 4.1 are recorded after 3 ms of expansion in an applied magnetic field gradient (Supplementary Materials 4.2). We perform a fit to a bimodal distribution for each component to extract the temperature, the populations N_{m_F}, and the condensed fraction f_{c,m_F} per component (Supplementary Materials 4.2). We found that low condensed fractions $< 5\%$ are difficult to detect with the fit algorithm due to a

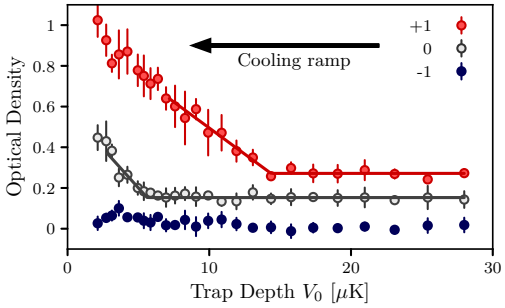

Figure 4.2.: Evolution of peak optical density with trap depth for a particular evaporation trajectory with $q/h \approx 69\,\mathrm{Hz}$ and $m_z \approx 0.3$ at the highest temperature. For these parameters, the $m_F = +1$ component condenses first (at a temperature $T_{c,1} \approx 1.8\,\mu\mathrm{K}$), followed by the $m_F = 0$ component (at a temperature $T_{c,2} \approx 560\,\mathrm{nK}$). No condensate was detected in the $m_F = -1$ component. The curves for $m_F = +1$ and $m_F = 0$ have been shifted vertically by 0.2 and 0.1 for clarity. The error bars denote statistical uncertainties at a 66 % confidence level. The solid lines indicate the piece-wise linear fits used to determine the critical trap depths.

combination of low signal-to-noise ratio and the complexity of fitting the three Zeeman components simultaneously. The signature of BEC, the appearance of a dense, narrow peak near the centre of the atomic distribution, can instead be tracked by monitoring the peak optical density (OD) taken as a proxy for the condensed fraction [181]. This procedure avoids relying on bimodal fits or other indirect analyses with uncontrolled systematic biases.

Fig. 4.2 shows such a measurement for a particular evaporation trajectory. The peak OD increases sharply when Bose-Einstein condensation is reached, demonstrating in this particular example a two-step condensation where $m_F = +1$ condenses first, followed by $m_F = 0$. For a given evaporation trajectory, we identify the critical trap depth $V_{0,\mathrm{c}}$ where condensation is reached by a piece-wise linear fit to the data, taking the intercept point as the experimentally determined $V_{0,\mathrm{c}}$ (see Fig. 4.2). We interpolate numerically the atom number, magnetisation and temperature to obtain the critical values N_c, T_c, $m_{z,\mathrm{c}}$ from $V_{0,\mathrm{c}}$.

Fig. 4.3 summarses the results of this work. We show the peak optical density for each Zeeman component and each value of q in a $(T - m_z)$ plane (Fig. 4.3 a-c, e-g and i-k). In this plot, all data taken at a given QZE q are binned with respect to magnetisation and temperature. The domains where condensation occurs appear in light colours. For convenience, the temperature is scaled to the critical temperature of a *single-component* ideal gas $k_B T_{c,\mathrm{id}} = \hbar\overline{\omega}[N/\zeta(3)]^{1/3}$, with $\overline{\omega}$ the geometric average of the trap frequencies and ζ the Riemann zeta function [33]. The same plot also shows the measured critical temperatures (Fig. 4.3 d, h, l)[1]. The phenomenon of sequential condensation is always

[1]In one case, $m_F = 0$ when $m_z \approx 0.3$ and $q/h = 2.8\,\mathrm{Hz}$, the lowest temperature images do show a

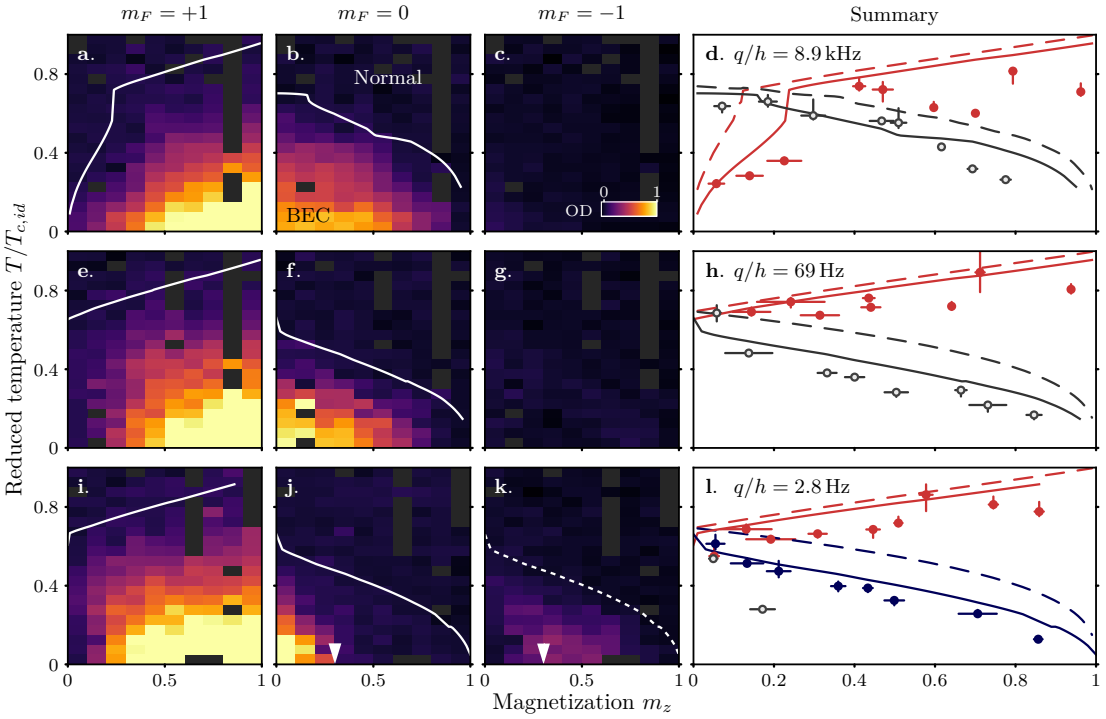

Figure 4.3.: Thermodynamic phase diagram of an antiferromagnetic spin $F = 1$ Bose gas. The peak optical density of each Zeeman component is reported for the entire set of data at each value of the QZE – $q/h = 8.9\,\mathrm{kHz}$ (**a-c**), $69\,\mathrm{Hz}$ (**e-g**) and $q = 2.8\,\mathrm{Hz}$ (**i-k**). The temperature is normalised to $T_{c,\mathrm{id}}$, the critical temperature of a *single-component* ideal Bose gas with the same number of atoms. The grayed areas indicate the absence of data in the corresponding regions. The right column (**d,h,l**) shows the measured critical temperatures of the $m_F = +1, 0, -1$ Zeeman components (red, gray, and blue markers, respectively). The solid (dashed) lines are the predictions of a Hartree-Fock (HF) model with spin-independent interactions (ideal gas theory). The dotted line in **k** shows the expected $T_{c,2}$ where $m_F = 0$ condenses according to the HF model.

observed for $m_z \neq 0$, but the overall behaviour changes drastically with q.

We first discuss the cases with largest QZE, $q/h \approx 8.9\,\mathrm{kHz}$ (Fig. 4.3 a-d) and $q/h \approx 69\,\mathrm{Hz}$ (Fig. 4.3 e-h). For $q/h \approx 8.9\,\mathrm{kHz}$ and highly magnetised samples, the majority component $m_F = +1$ condenses first at a critical temperature $T_{c,1}$, followed by the $m_F = 0$ component at a lower temperature $T_{c,2}$. For low magnetisations, the condensation sequence is reversed. For $q/h \approx 69\,\mathrm{Hz}$, we observe only one sequence, a two-step condensation with $m_F = +1$ first and $m_F = 0$ second.

This behaviour can be understood qualitatively from ideal gas theory, taking the QZE and the conservation of magnetisation into account [100]. For ideal gases, BEC occurs when the chemical potential μ equals the energy of the lowest single-particle state [33]. The same criterion holds for a spin 1 gas with $\mu_0 = \mu$ and $\mu_{\pm 1} = \mu \pm \lambda$, where λ is a Lagrange multiplier enforcing the conservation of m_z. For $m_z = 0$ ($\lambda = 0$) and $q > 0$, the QZE lowers the energy of $m_F = 0$, which is therefore the first component to condense when $\mu = -q$. For $m_z > 0$, λ is positive and increases with m_z. The energetic advantage of $m_F = 0$ is in balance with the statistical trend favouring the most populated component $m_F = +1$. Eventually, this trend takes over at a "critical" value m_z^* (where $\lambda = q$). For $m_z > m_z^*$, the $m_F = +1$ component condenses first.

Coexisting $m_F = 0$ and $m_F = \pm 1$ components with a well-defined phase relation correspond to a non-zero transverse spin $\langle \hat{S}_x + i\hat{S}_y \rangle \neq 0$ ("transverse magnetised" phase – $M_\perp$). For large q, the condensate is reduced to an effective two-component system $m_F = 0, +1$ with $m_F = -1$ mostly spectator. The case $m_z = m_z^*$ ($\mu_0 = \mu_{+1}$) realises the Siggia-Ruckenstein (S-R) scenario, where condensation and ferromagnetic behaviour appear simultaneously. Away from that point, the S-R picture breaks down ($\mu_0 \neq \mu_{+1}$) and sequential condensation takes place.

Figure 4.3 d-h show the critical temperatures and compare them to ideal gas theory. Although the general trends in the theory are the same as in the experiment, we observe a systematic shift of $T_{c,1}$ and $T_{c,2}$ towards lower temperatures, and an experimental "critical" $m_z^* \sim 0.3$ larger than the ideal gas prediction. The behaviour for $q/h \approx 69\,\mathrm{Hz}$ (Fig. 4.3 e-h) is qualitatively similar to the largest q case, but with a small m_z^* that cannot be resolved experimentally (the ideal gas theory predicts ≈ 0.002).

Repulsive interactions between the atoms can be expected to lower the critical temperatures as in single-component gases [52], with an enhanced shift of $T_{c,2}$ due to the presence of a condensate. We use a simplified version of Hartree-Fock (HF) theory to make quantitative predictions [83]. Our self-consistent calculations include the trap potential in a semi-classical approximation, and treat the interactions as spin-independent. These approximations are valid only above $T_{c,2}$, where at most one component condenses (Supplementary Materials 4.2). As a result, the HF model cannot make any prediction for the low-temperature behaviour below $T_{c,2}$. The results of the HF calculations, performed for atom numbers and trap frequencies matching the experimental values (Supplementary Materials 4.2), are shown in Figure 4.3. The HF model qualitatively accounts for the experimental data, explaining in particular the strong downwards shift of $T_{c,2}$ for all q and

condensed component but the critical temperature could not be extracted reliably from the fitting procedure due to sparse sampling. This particular point is not reported in Fig. 4.3l.

the shift of $m_z^\star$ to higher values for $q/h \approx 8.9\,\mathrm{kHz}$. The residual discrepancy around $7-8\,\%$ could be partially explained by finite-size and trap anharmonicity effects not included in the Hartree-Fock calculation (Supplementary Materials 4.2).

At the lowest field we studied, $q/h \approx 2.8\,\mathrm{Hz}$ (Fig. 4.3 i-l), we observe a change in the *nature* of $T_{\mathrm{c},2}$. For high values of m_z, $T_{\mathrm{c},2}$ corresponds to condensation into $m_F = -1$ while $m_F = 0$ remains uncondensed. This phenomenon is incompatible with ideal gas theory [73, 100] *and* with our HF model with spin-independent interactions. It corresponds to a change of the magnetic ordering appearing below $T_{\mathrm{c},2}$. While coexisting $m_F = 0$ and $m_F = +1$ components form a $M_\perp$ phase with $\langle \hat{S}_x + i\hat{S}_y \rangle \neq 0$, coexisting $m_F = \pm 1$ components correspond to a phase with $\langle \hat{S}_x + i\hat{S}_y \rangle = 0$ but where the spin-rotational symmetry around z is broken by a non-zero spin-quadrupole tensor ("quasi-spin nematic" phase -qSN). At $T = 0$ and in the single-mode regime, the $M_\perp$- qSN transition occurs at a critical magnetisation $m_{z,c} = \sqrt{1-[1-(q/U_s)]^2}$, with $U_s \leq q$ the spin-dependent interaction energy [193]. When $q > U_s$, there is no phase transition and only the $M_\perp$ phase is present. This explains the qualitative difference between the data for $q/h = 2.8\,\mathrm{Hz}$ and the other two values. We estimate $U_s/h \lesssim 50\,\mathrm{Hz}$ and $m_{z,\mathrm{crit}} \approx 0.3$ for a BEC without thermal fraction [75]. This agrees well with the lowest temperature measurements reported in Fig. 4.3j-k.

In the experimental data in Fig. 4.3 i-l, the region of the phase diagram occupied by the $M_\perp$ phase shrinks with increasing temperature. In fact, we find that $m_F = -1$ condenses at $T_{c,2}$ for all parameters we have explored, with $m_F = 0$ condensing at a third, lower critical temperature (except for $m_z \approx 0$, where all components appear to condense together within the accuracy of our measurement). Finally, the dashed line in Fig. 4.3k shows $T_{\mathrm{c},2}$ predicted by the HF model with spin-independent interactions. Although the model incorrectly predicts that $m_F = 0$ should condense below $T_{\mathrm{c},2}$, the predicted transition closely matches the observed boundary between single-component $m_F = +1$ BEC and qSN $m_F = \pm 1$ BEC. This indicates that the transition line itself (but not the magnetic order below it) is determined by the thermal component alone.

In conclusion, we have studied the finite-T phase diagram of a spin-1 Bose gas with antiferromagnetic interactions. For condensates in the single-mode regime, we observed a sequence of transitions, two for high QZE and three for low QZE, with the lower two leading to different magnetic orders. We have found that a simplified HF model reproduces the trends observed in the variations of the critical temperatures $T_{\mathrm{c},1}$ and $T_{\mathrm{c},2}$ with magnetisation and QZE. A more complete theoretical analysis accounting for all experimental features –in particular the harmonic trap, which is crucial to stabilise an antiferromagnetic condensate in a single spatial mode [191]– and elucidating the exact nature of the low-temperature transitions for low QZE remains open. A natural extension of this work would be to study the critical properties of the observed finite-T transitions, in particular near $m_z = m_z^\star$ and between the $M_\perp$ and qSN phases at very low q. Two-dimensional systems provide another intriguing direction to explore. Several Berezinskii-Kosterlitz-Thouless transitions mediated either by vortices or spin textures have been predicted [121, 78]. We expect that such topological features will further enrich the already complex phase diagram observed in three dimensions.

4.2. Supplementary Materials

4.2.1. Experimental sequence

Trap geometry

Our experiments start with a thermal gas of $\sim 10^5$ ^{23}Na atoms in a crossed dipole trap, at a temperature around $T \approx 4\,\mu$K. We set the normalised magnetisation of the cloud m_z between 0 and 1 using the same procedure as in [76], and perform evaporative cooling by decreasing the power of the optical dipole trap. We found that the magnetisation varies during the evaporation ramp, typically by $10-15\,\%$ (see Subsection 4.2.2 below). Once the desired final trap depth is reached, we hold the atoms in the trap for 4 seconds to ensure thermalisation. We apply a constant bias magnetic field B during the evaporation. For the data sets with $B = 0.1\,$G and $B = 0.5\,$G (resp. $B = 5.6\,$G), the bias field is along the $\mathbf{x}$ (resp. $\mathbf{x}+\mathbf{y}+\mathbf{z}$) direction (see Fig. 4.4).

Stern-Gerlach Imaging

We detect the atoms using absorption imaging after a period of expansion in a magnetic field gradient to spatially separate the Zeeman components (Stern-Gerlach – SG – imaging). We use in this work a slightly different SG sequence than in [76, 196]. A quadrupole magnetic field (created by the pair of coils used to operate the magneto-optical trap) together with a strong bias magnetic field parallel to the y axis produces a magnetic force along y. We pulse this magnetic force after the trap has been switched off. We trigger a $\sim 1\,$ms-long pulse by discharging a large capacitor into the coils. A power diode and a semiconductor switch limit the current pulse to one half period of the resulting L-C oscillation. After a time of flight of 3 ms, we repump the atoms to the $F = 2$ hyperfine manifold and take an absorption image using light resonant on the $F = 2 \rightarrow F' = 3$ transition.

The magnification of the imaging system is calibrated directly by imaging the Kapitza-Dirac diffraction pattern from a pulsed optical lattice with known wavelength, and indirectly by comparison to an orthogonal imaging system calibrated against gravity. Both methods agree within their uncertainty, on the order of $1\,\%$.

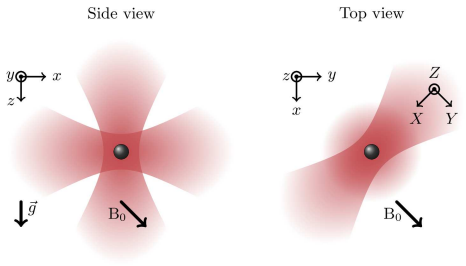

Figure 4.4.: Crossed dipole trap geometry.

Trap Calibrations

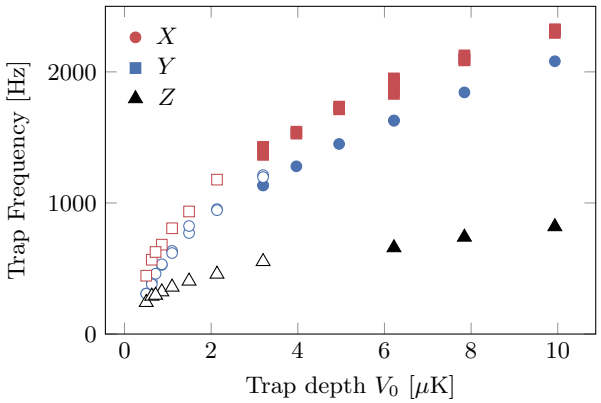

Figure 4.5.: Evolution of trap frequencies in an evaporation trajectory. Filled symbols indicate frequencies measured with parametric heating, open symbols indicate frequencies measured with dipole oscillations.

Evaporative cooling in optical traps is performed by lowering the optical power of the trap laser, which reduces the trap depth but also the trap frequencies [130]. In our experiments, they change from around 2 kHz for the highest power to a few hundred Hz for the lowest. We calibrate the trap frequencies using two methods, (i) centre-of-mass oscillations, and (ii) parametric excitation (see Fig. 4.5). For method (i), we use a gas of atoms polarised in the $m_F = +1$ Zeeman sub-level ($m_z \approx 1$). We slowly ramp up a magnetic field gradient that displaces the cloud centre to a new equilibrium position, and then switch off the gradient to induce oscillations at the trap frequencies. For method (ii), we modulate the dipole trap optical power to induce parametric heating. When interactions can be neglected, resonant excitation is obtained when the modulation frequency coincides with the second harmonic of one of the trap frequencies.

Method (i) is best suited for trap frequencies below approximately 1 kHz, and method (ii) above. In our experiment, we cannot switch off the magnetic field gradient faster than approximately a millisecond, which is long compared to the typical oscillation period for the highest trap depths. Consequently, the switch-off becomes almost adiabatic, and the induced oscillations of the centre-of-mass are hardly detectable. While the parametric heating method (ii) should in principle work at all temperatures, once a condensate is formed the relation between the measured resonant frequencies and the bare trap frequencies is no longer straightforward. To avoid complicated modelling involving finite temperature theories of Bose-Einstein condensed gases [146], we restrict method (ii) to normal gases above the critical temperature, which corresponds typically to trap frequencies $\gtrsim 1$ kHz.

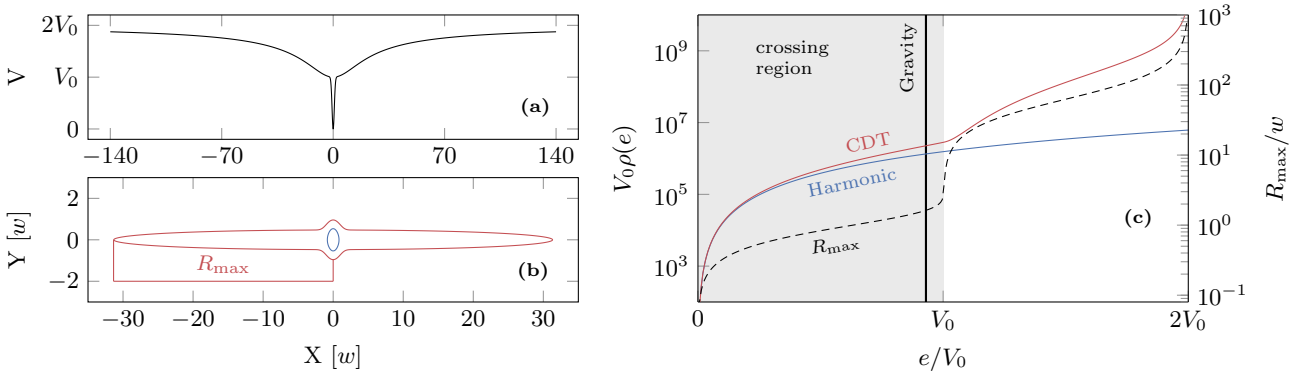

Figure 4.6.: **a**: Potential V of a crossed optical dipole trap (CDT) formed by two Gaussian traps of waist w and trap depth V_0. **b**: Classical isopotential contours $V(\boldsymbol{r}) = E$ for energies $E < V_0$ (blue solid line) and $V_0 < E < 2V_0$ (red solid line). **c**: Density of state $\rho(e)$ (red solid line) and maximum radius of classical trajectory (dashed line). The blue solid line shows the density of states of the harmonic potential closest to the CDT potential $V(\boldsymbol{r})$. The grayed area correspond to classical trajectories bounded within the crossing region. The vertical solid line shows the energy cutoff due gravity for vertical trajectories, slightly lower than the energy V_0 where the atoms escape from the crossing region.

4.2.2. Evaporation dynamics

Trap Depth

In this Subection, we discuss how we extract a trap depth for a crossed dipole trap geometry involving two Gaussian beams, as sketched in Fig. 4.4. For simplicity we consider here two identical, mutually incoherent beams. The dipole potential for a single beam is [57] $V(\boldsymbol{x}) \approx -V_0 e^{-2(x_1^2+x_2^2)/w^2}/[1+(x_3/z_R)^2]$, with V_0 the single-beam trap depth, proportional to laser power, with w the beam waist and with $z_R = \pi w^2/\lambda_L$ the Rayleigh length. For the geometry we consider, we have $x_1 = X, x_2 = Y$ and $x_3 = Z$ for the vertical beam 1 and $x_1 = Y, x_2 = Z$ and and $x_3 = X$ for the horizontal beam 2 (see Fig. 4.6a). For atoms with energies much lower than V_0, this leads to an approximately harmonic trap with frequencies $\omega_{\{X,Y,Z\}} = \{1, \sqrt{2}, 1\}\sqrt{4V_0/mw^2}$. In general, we distinguish two different energetic regimes based on the shape of the isopotential curves $V(\boldsymbol{r}) = E$ (Fig. 4.6b). For atoms with low energies $E < V_0$, the classical trajectories are bounded within the crossing region of size $\sim w \times w$. Atoms with energies $V_0 < E < 2V_0$, on the other hand, experience classical trajectories extending far in the arms of the CDT, over distances $\sim R_{\max}$ many times greater than the size of the trapped gas in the crossing region (typically $\ll w$ for cold clouds with $k_B T \ll V_0$). The high-energy atoms populating the arms of the CDT thus form a very dilute cloud, not necessarily in equilibrium with the majority of atoms in the crossing regions. From this simple picture, the trap depth relevant for evaporative

cooling is on the order of V_0, the energy where the isopotential maximum radius and the density of states $\rho(E)$ (calculated semiclassically) both increase dramatically (see Fig. 4.6c). Including gravity, classical trajectories with energies $\sim V_0 - mgw$ can escape along Z, as indicated by the vertical line in Fig. 4.6c.

It is difficult to make more precise statements about the value of V_0, since it depends on evaporation dynamics, and on the ergodicity of classical trajectories. We did not carry a detailed kinetic calculation of evaporative cooling in the CDT potential $V(\boldsymbol{r})$ (as done in [187] for a truncated harmonic trap), a task that goes well beyond the scope of this work. We assume here that we can take V_0 as the relevant trap depth determining the evaporative cooling dynamics. This has no impact on our experimental results, as V_0 is merely used as a label for each point on a given evaporation trajectory.

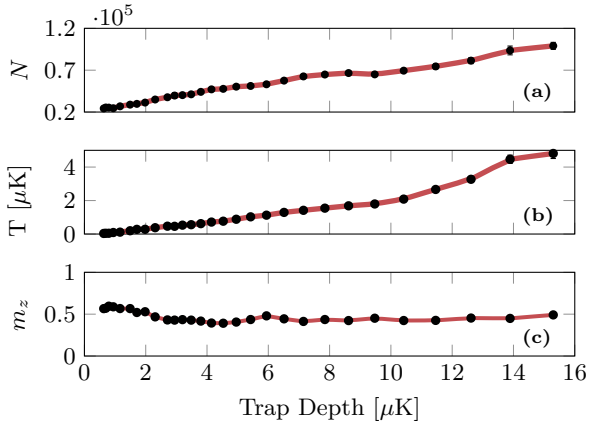

Figure 4.7.: Evaporation trajectory showing atom number, magnetisation and temperature versus trap depth. The solid line shows a numerical interpolation which we use to extract the critical values for each quantity from the critical trap depth (see Subsection 4.2.3).

Discussion on the conservation of magnetisation

A typical evaporation trajectory is shown in Fig. 4.7. The behaviour of the total atom number and temperature are expected, but one can also notice a variation of the magnetisation m_z with trap depth. This behaviour seems at first glance incompatible with the announced conservation law of m_z. However, the argument that microscopic binary collisions driving the system to thermal equilibrium conserve m_z disregards the dynamics of evaporative cooling. Once a condensate forms in one of the Zeeman components, evaporation tends to eliminate preferentially atoms in the other Zeeman states.

In spite of this variation, the conservation of magnetisation is still relevant to determine the state of kinetic equilibrium reached by the system. The evaporative cooling dynamics is very slow compared to the microscopic thermalisation time on which the gas returns to thermal equilibrium. The thermalisation time can be estimated from the classical collision time $1/(n\sigma v_{\mathrm{th}})$ (here, n is the spatial density of the thermal component, σ the

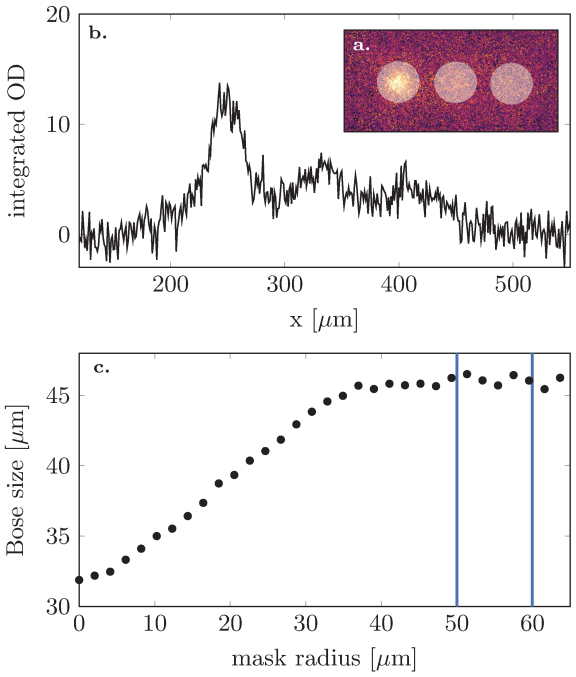

Figure 4.8.: Extraction of the temperature by fitting thermal density profiles to images with a varying mask sizes. **a**: Typical single shot image with a mask of radius 30 μm. **b**: Integrated density profile from image **a**. **c**: Size of the fitted Bose distributions versus mask size. The final thermal size is obtained by an average over the "plateau" delimited by the vertical blue lines. For mask sizes larger than ≥ 70 μm, the fit fails because imaging noise overtakes the atomic signal. For mask sizes below 40 μm, condensed atoms still contribute to the masked image.

$s-$wave scattering cross section, $v_{\mathrm{th}} = \sqrt{k_B T/\pi m}$ the thermal velocity and m the mass of a sodium atom). For typical parameters in our experiment, one finds a thermalisation time on the order of a ms while typical evaporation times range are around 1 s. As a result, the quantum gases studied in this work can be considered to follow the slowly changing magnetisation, with the relevant kinetic equilibrium state at each time determined by a magnetisation-conserving Hamiltonian. We note that the same conclusion follows naturally from a classical model of evaporative cooling [106], where the evaporation rate scales as $\tau_{\mathrm{ev}}^{-1} \sim n\sigma v_{\mathrm{th}} e^{-\eta}$, with $\eta = V_0/k_B T$ the evaporation parameter. Since $\eta \sim 8$ in typical experiments, the separation of scales between the microscopic thermalisation time and the evaporation time always holds.

4.2.3. Extracting T_c

Bimodal fits

We model the measured column densities using the standard parametrisation, *i.e.* by the sum of a Bose-Einstein distribution describing the thermal component and a Thomas-Fermi profile describing the condensate [86]. We fit the three Zeeman components simultaneously, with a few assumptions to reduce the number of fitting parameters. We assume in particular a fugacity $z = 1$, equal temperatures for all three thermal clouds, and equal condensate sizes in accordance with the single-mode approximation. From the fit parameters, one can obtain in principle the temperature, the total population and the condensate fraction of each component. However, the parametrization is heuristic and prone to systematic errors. The bimodal fit is sensitive to image noise when the condensate fraction is below 5 %. Additionnally, systematic deviations from the Thomas-Fermi profile due to the tight confinement become problematic when the condensate fraction is higher than approximately 50 % [76]. For this reason, we only use the bimodal fits to obtain the total populations of each component and the geometric centre of each cloud, and use other methods which we believe more reliable to determine the temperature and the critical point.

Determination of the temperature from the thermal tails of the atomic distribution

We extract the temperature from the wings of the thermal components. The basic assumption is that the wings of the time-of-flight distribution are determined by the wings of the in-trap momentum distribution, which is well approximated by an ideal Bose-Einstein distribution for large enough momenta. To determine the range of momenta where this description applies, we apply circular masks at the centre of each cloud, as shown in Fig. 4.8 a, and fit the outer atomic distribution with a Bose-Einstein distribution $\propto g_2\left[e^{-r^2/R_{\mathrm{th}}^2}\right]$, where $g_n(x) = \sum_{k=1}^{\infty} x^k/k^n$ is a Bose-Einstein function. The fitted size varies when the size of the mask increases, and eventually reaches a plateau (Fig. 4.8 c). We identify this plateau with the dilute wings of the cloud, well reproduced by an ideal Bose-Einstein distribution. We extract the temperature from $k_B T = m R_{\mathrm{plateau}}^2/t^2$, with t the time of flight and where R_{plateau} is the average of R_{th} for five mask sizes between 50 μm and 60 μm.

Determination of the threshold for Bose-Einstein condensation from the peak density

The critical point is detected by a sudden change in the peak value of the optical density $OD_{m_F} = \sigma_0 \tilde{n}_{m_F}$ of each Zeeman component m_F. We choose a square integration zone of side 3×3 pixels near the centre of each component to evaluate the peak optical density. The evolution of OD_{+1} as a function of evaporation time is shown in Fig. 4.9, and shows an abrupt change at a particular trap depth which we identify as critical point. We extract the critical trap depth from a piece-wise linear fit to the data near the critical

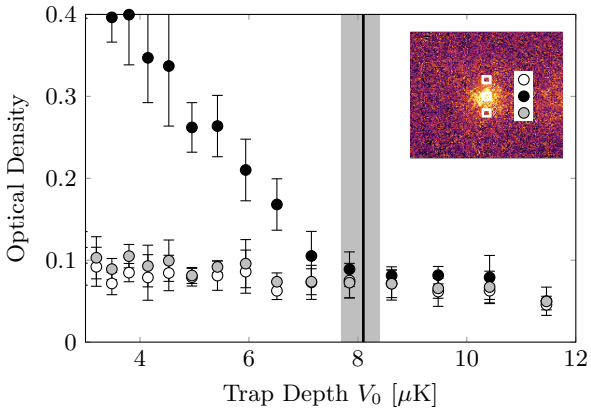

Figure 4.9.: Optical density as a function of evaporation time, showing the increase of optical density at the BEC transition happens only in the centre of the momentum distribution. The inset shows the correspondence between plot symbols and integration regions. The black line shows the Bose-Einstein transition extracted from a fit to the data, and the gray area the 66 % confidence interval.

point. Finally, we use the critical trap depth determined to evaluate the atom number, temperature, magnetisation and trap frequency (see Fig. 4.7) at the critical point.

We have verified that the sudden increase of the optical density is observed only in the centre of the distribution. Choosing other off-centred regions is compatible with the behaviour of a slowly cooling thermal gas (see Figure 4.9).

4.2.4. Theoretical models of spinor gases at finite temperatures

Ideal spin 1 gas

We first calculate the BEC critical temperature of a spin 1 Bose gas with fixed magnetisation M_z and atom number N [73, 192, 100]. The gas is trapped in a harmonic potential with frequencies ω_i $(i = x, y, z)$. The Gibbs free energy is written as

$$G = H_{\mathrm{sp}} - \sum_{m_F=0,\pm1} \mu_{m_F} N_{m_F}, \tag{4.1}$$

with H_{sp} the sum of the kinetic and potential energies, N_{m_F} the population of Zeeman state m_F, and q the quadratic Zeeman energy. The chemical potentials for each Zeeman component are given by $\mu_{\pm1} = \mu \pm \lambda$ and $\mu_0 = \mu + q$, where the Lagrange multipliers μ and λ ensure conservation of N and M_z on average.

Following the usual method [146], we write the Zeeman population $N_{m_F} = N_{c,m_F} + N'_{m_F}$ as the sum of the population of the trap ground state N_{c,m_F} and of all excited state N'_{m_F}. Here and in the following, the prime subscript denotes quantities related to non condensed atoms. We calculate N'_{m_F} from the semi-classical formula dalfovo1999theory,

Condensation order	$m_F = +1$ first	$m_F = 0$ first
T_{c1}	$\mu_{+1} = 0$	$\mu_{+1} = \lambda - q$
	$\mu_0 = q - \lambda$	$\mu_0 = 0$
	$\mu_{-1} = 0$	$\mu_{-1} = -\lambda - q$
T_{c2}	$\mu_{+1} = 0$	$\mu_{+1} = 0$
	$\mu_0 = 0$	$\mu_0 = 0$
	$\mu_{-1} = -2q$	$\mu_{-1} = -2q$

Table 4.1.: Summary of the conditions of condensation in the ideal case. Here $T_{c1/2}$ denotes the first/second critical temperature, μ_{m_F} is the effective chemical potential for the Zeeman component m_F, λ is a Lagrange multiplier enforcing a given magnetisation and q is the quadratic Zeeman energy. Note that $\lambda > 0$ when $m_z > 0$.

$N'_{m_F} = (k_B T/\hbar\overline{\omega})^3 \, g_3\left(e^{\beta\mu_{m_F}}\right)$, with $\overline{\omega} = \left(\prod_{i=x,y,z} \omega_i\right)^{1/3}$. For a given T, m_z and q, we find numerically the chemical potential μ and λ by solving the set of equations $\sum_{m_F} N_{m_F} = N$ and $N_{+1} - N_{-1} = M_z$.

The BEC transition takes place in the Zeeman component m_F when $\mu_{m_F} = 0$. As the temperature is lowered, the Zeeman components condense sequentially. Ideal gas theory predicts critical temperatures shown as dashed lines in Fig. 4.10. For $q > 0$, there are two regimes depending on the magnetisation. For low m_z, the $m_F = 0$ component condenses first at a critical temperature T_{c1}, and the $m_F = +1$ component condenses second at a lower critical temperature $T_{c2} \leq T_{c1}$. For high m_z, the sequence is reversed. We remark that the $m_F = -1$ component never condenses, except in the limiting case $q = 0$ where it condenses simultaneously with $m_F = 0$. The conditions on the chemical potentials for each condensation temperature are summarised in Table 4.1.

Hartree-Fock model

We now consider the effect of interactions, described by the Hamiltonian [169]

$$\hat{H}_{\text{int}} = \frac{\overline{g}}{2} \int d^3\boldsymbol{r} \; \hat{n}^2(\boldsymbol{r}) + \frac{g_s}{2} \int d^3\boldsymbol{r} \; \hat{\boldsymbol{\mathcal{S}}}^2(\boldsymbol{r}). \tag{4.2}$$

Here $\hat{n}_{m_F}(\boldsymbol{r})$ denotes the spatial density of the m_F component, $\hat{n}(\boldsymbol{r}) = \sum_{m_F} \hat{n}_{m_F}(\boldsymbol{r})$ the total density, and $\hat{\boldsymbol{\mathcal{S}}}$ the spin density. In the following we also note $n'_{m_F}(\boldsymbol{r})$ the density of non-condensed atoms in state m_F, and the total non-condensed density $n'(\boldsymbol{r}) = \sum_{m_F} n_{m_F}(\boldsymbol{r})$.

We make a series of approximations to simplify the problem and compute the thermodynamic properties:

1. We treat the interactions in the Hartree-Fock approximation [52, 95, 83],
2. We neglect the spin-dependent interaction term $\propto g_s$ in comparison with the spin-independent interactions $\propto \overline{g}$,

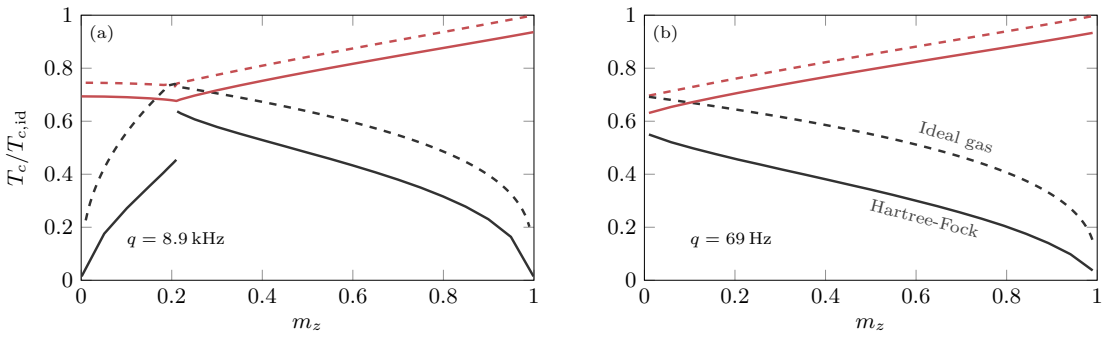

Figure 4.10.: **a**. Critical temperatures for $q/h = 8.9\,\mathrm{kHz}$ for $N = 5 \cdot 10^4$, $\omega = 2\pi \times 1200\,\mathrm{s}^{-1}$. The red and blue lines show T_{c1} and T_{c2}, respectively. The solid lines are calculated using the Hartree-Fock model and the dashed lines using ideal gas theory. The and $q/h = 69\,\mathrm{Hz}$ **b**. Close-up view of the region near m_z^* where $T_{c,1}$ and $T_{c,2}$ cross for the ideal gas. The dashed line show the prediction of a so-called "semi-ideal" model intermediate between the ideal gas and the complete Hartree-Fock treatment.

3. We assume that a semi-classical approximation (for the condensate and for the excited atoms) is valid.

We restrict ourselves to a regime where at most one Zeeman component condenses. This component is identified by the label c in the following.

Under these assumptions, the density profile of the condensate is determined by

$$n_c(\boldsymbol{r}) = \frac{1}{\overline{g}} \max\left\{ \mu_c - V(\boldsymbol{r}) - \overline{g}\left[n'(\boldsymbol{r}) + n'_c(\boldsymbol{r})\right], 0 \right\}, \tag{4.3}$$

with a BEC index c corresponding to 0 or +1 depending on the particular case under consideration. The last term describe interactions between condensed and non-condensed atoms, with a strength $2\overline{g}$ for atoms in the same Zeeman component c as the condensate and $\overline{g}$ otherwise. The density profiles of the thermal components are determined by the set of non-linear equations,

$$n'_{m_F}(\boldsymbol{r}) = \frac{1}{\lambda_T^3} g_{3/2}\left\{ e^{\beta\left[\mu_{m_F} - W_{m_F}(\boldsymbol{r})\right]} \right\}. \tag{4.4}$$

Here W_{m_F} denotes a self-consistent mean-field potential for non-condensed atoms in the Zeeman state m_F,

$$W_{m_F} = \overline{g}\left[(1 + \delta_{m_F,c})n_c + n' + n'_{m_F}\right] + V. \tag{4.5}$$

Eqs. (4.3,4.4) must be solved self-consistently for the thermodynamic potentials parameters μ, η, imposing the constraints of total atom number and magnetisation.

At first sight, it may seem straightforward to extend the model discussed above to include more than one condensed component and spin-dependent interactions terms $\propto g_s$.

However, antiferromagnetic interactions tend to induce phase separation when $m_F = 0$ and $m_F = \pm 1$ are simultaneously condensed [73, 191]. In the experiment, this trend is penalized by the high energetic cost of domain walls in a tight trap, stabilizing a condensate in a single spatial mode. This effect is due to the so-called "quantum pressure" term neglected in the semi-classical approximation. To include it in a consistent manner, one would need to solve the complete Gross-Pitaevskii equation as well as Schrödinger-like equations for the excited modes in a self-consistent manner. We did not attempt to do such a calculation, which promises to be numerically taxing in three dimensions.

Scaling properties of the Hartree-Fock model

The simplified Hartree-Fock model of Subsection 4.2.4 admits a scaling form. We introduce the critical temperature of a single component ideal gas, $k_B T_{\mathrm{c,id}} = \hbar\overline{\omega}\,(N/\zeta(3))^{1/3}$, and two associated spatial scales, the thermal De Broglie wavelength $\lambda_{\mathrm{c,id}} = (2\pi\hbar^2/mk_B T_{\mathrm{c,id}})^{1/2}$ and the thermal cloud radius $R_{\mathrm{c,id}} = (k_B T_{\mathrm{c,id}}/m\omega^2)^{1/2}$. We now introduce dimensionless variables denoted with a tilde symbol. Energies are scaled by $T_{\mathrm{c,id}}$, and densities by $1/\lambda^3_{\mathrm{c,id}}$.With these notations, any thermodynamic state function can be rewritten as universal functions of the scaled temperature $\tilde{T}$, chemical potentials $\tilde{\mu}, \tilde{\eta}$ and quadratic Zeeman energy $\tilde{q}$, and of the dimensionless strength of interactions γ

$$\gamma = \frac{\overline{g}}{\lambda^3_{\mathrm{c,id}} k_B T_{\mathrm{c,id}}} = \frac{2\overline{a}}{\lambda_{\mathrm{c,id}}}. \tag{4.6}$$

This is a natural extension of the scaling behaviour noted for single-component Bose gases [33]. In three dimensions, this behaviour holds because of the semi-classical approximation. Including the kinetic energy in the theory would break the universality.

Example of results from the Hartree-Fock model

As an example, the calculated critical temperature for $q/h = 8.9\,\mathrm{kHz}$ is shown in Fig. 4.10a for fixed atom number and trap frequencies. One observes a significant shift downwards of the interacting model from the non-interacting one, as expected for repulsive interactions [52].

In the ideal gas model, the critical temperature curves $T_{c,1}$ and $T_{c,2}$ are continuous and cross at a particular point labeled as m_z^*. In contrast, the Hartree-Fock model shows a discontinuity of the second critical temperature near m_z^*. To understand this feature, we turn to a "semi-ideal model", which is simpler to discuss but preserves the discontinuity (Fig. 4.10b). In the semi-ideal model [123], one retains only terms proportional to $\overline{g}n_c$ and neglects terms proportional to $\overline{g}n'_{m_F}$ in Eqs. (4.3,4.4). Uncondensed atoms experience a mean-field potential which differs from the harmonic trapping potential only within the volume of the condensate, and depends on their internal state : either a $W-$shaped potential for atoms in the same Zeeman state the condensate (similar to the single-component case [123]) or a "flat-bottom" potential for atoms in other Zeeman states [42, 91].

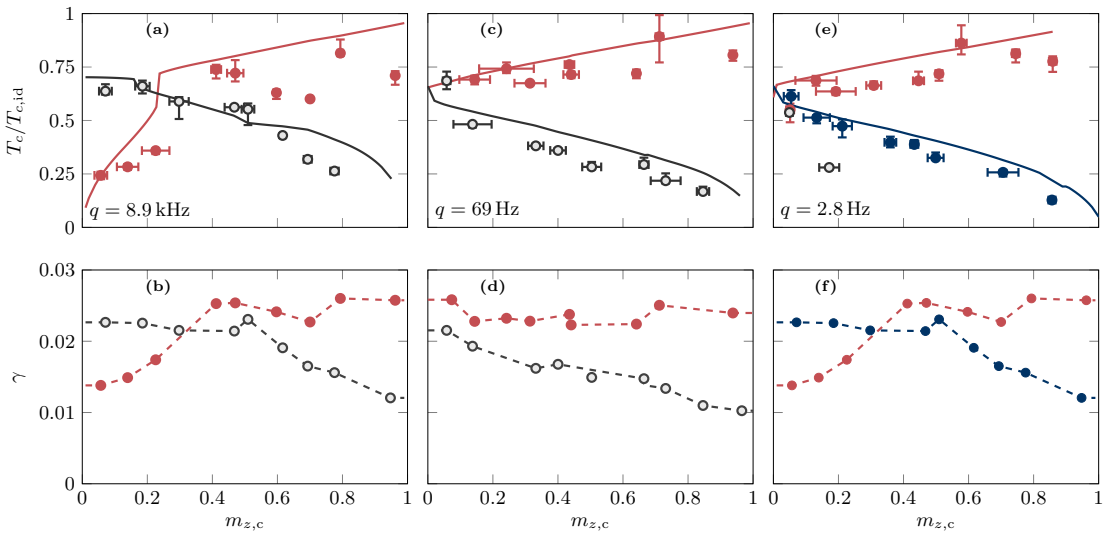

Figure 4.11.: Comparison between the experimental data and the Hartree Fock model for $q/h = 8.9\,\mathrm{kHz}$ (**a,b**), $q/h = 69\,\mathrm{Hz}$ (**c,d**), and $q/h = 2.8\,\mathrm{Hz}$ (**e,f**). For each column, the top panel shows the critical temperatures. The bottom panel shows the value of the interaction parameter γ for each measured critical temperature (circles), as well as the interpolated curves $\gamma(m_z)$ used as input for the Hartree-Fock calculation (dashed lines). In each panel, red, gray and dark blue colors correspond to $m_F = +1$, $m_F = 0$ and $m_F = -1$, respectively.

To explain the discontinuity of $T_{c,2}$, we consider the temperature regime $T_{c,1} > T > T_{c,2}$, and the case $m_z < m_z^*$ first. The condensate forms in $m_F = 0$, and the magnetisation is entirely carried by the thermal component ($N'_{+1} - N'_{-1} = M_z$). The condition for second condensation is $\mu_{+1} = \mu + \lambda = \overline{g} n_c(\mathbf{0})$, with $n_c(\mathbf{0})$ the condensate density in the centre of the trap. Since $\mu_0 = \mu + q = \overline{g} n_c(\mathbf{0})$, this leads to the same condensation criterion $\lambda = q$ as for an ideal gas. Lowering the temperature leads to both a decrease of the total thermal population $N' = N'_0 + N'_{+1} + N'_{-1}$ and an increase in the degree of polarization of the thermal component, $P'_z = (N'_{+1} - N'_{-1})/N'$. Note that mean-field interactions compared to the one of an ideal gas at the same temperature T and chemical potential $\lambda < q$. For "high" temperatures $T \lesssim T_{c,1}$, when the condensate population is small ($N' \sim N$), the conservation of magnetisation amounts to $m_z \approx P'_z$. The flattening of the mean-field potential for uncondensed $m_F = \pm 1$ atoms leads to a slight increase of the atom number N_{c,m_F} at which these Zeeman components can condense. Equivalently, the chemical potential λ must adjust to a value $< q$ in order to maintain a given magnetisation. This effect prevents condensation in $m_F = +1$ in a wide temperature range, until the condensate population becomes sufficiently large. In that regime, the conservation law $m_z = P'_z \times N'/N$ is fulfilled if the decrease of N'/N is compensated by an increase of P'_z. This corresponds to an increase of λ which eventually reaches the critical value $\lambda = q$. As a consequence, the formation of a condensate in the minority component $m_F = +1$ is delayed to low

temperatures, when the condensed fraction in $m_F = 0$ is large enough.

In the other case $m_z \gtrsim m_z^*$, the BEC first appears in the $m_F = +1$ component. The magnetisation is now shared between the condensate and the thermal component, and $m_z = N_c/N + P'_z \times N'/N$. As the temperature decreases and the condensate population in $m_F = +1$ increases, the conservation of m_z is ensured by decreasing N'_{+1} and increasing N'_0. As a result, the condensation in $m_F = 0$ is not merely shifted to lower values by the mean-field potential. The shift depends on the condensate population at $T_{c,2}$ and vanishes for $m_z = m_z^*$ in the semi-ideal model.

The explanation of the discontinuity in the more complete Hartree-Fock theory is qualitatively the same in the semi-ideal model.

Comparison with experimental data

In order to make a comparison of the Hartree-Fock model with the experimental data, we need to account for the variations of the parameters N, ω across all data. These parameters naturally decrease while the evaporation ramp proceeds to lower temperatures. As a result, for a given evaporation trajectory N, ω are smaller at the second critical temperature than at the first. Additionally, the magnetisation varies as well as evaporation proceeds (see Sec. 4.2.2). Instead of a couple of critical temperatures T_{c1}, T_{c2} for given m_z, N, ω, we have in fact two sets of parameters $(T_{c1}, m_{z1}, N_1, \omega_1)$ and $(T_{c2}, m_{z2}, N_2, \omega_2)$.

One possibility is to do a point-by-point comparison. This results in a sparsely sampled curve that does not reflect the full behaviour of the critical temperatures. To cure this, we have performed an interpolation of the experimental parameters to use as input in the calculation. We used the scaling properties of the thermodynamic functions discussed in Sec. 4.2.4. We perform a numerical interpolation of the experimentally determined values of γ calculated from Eq. (4.6), the measured T_{c1} and $\overline{g} = 4\pi\hbar^2\overline{a}/m_{\mathrm{Na}}$. The s-wave scattering length $\overline{a}$ is measured in [94] and m_{Na} is the mass of a sodium atom. We plot the final results in reduced units. The critical temperature curves shown in the main article are reproduced in Fig. 4.11, together with the measured values of γ and their interpolations.

Further corrections to the ideal gas critical temperature

Finite-size effects : The ideal gas theory is computed with the semi-classical formula, valid in the thermodynamic limit for trapped gases dalfovo1999theory, *e.g.* when $N \to \infty$ and $\omega \to 0$ keeping $N\omega^3$ constant. For finite N and ω, corrections to the thermodynamic limit decrease the critical temperature by $\delta T_c/T_{c,\mathrm{id}} \simeq -0.73N^{-1/3}$. This correction is between -1% ($N_c = 10^5$) and -4% ($N_c = 10^4$) for our experimental parameters.

Trap anharmonicity : The CDT is only harmonic near its minimum and has a finite trap depth. The most energetic atoms are sensitive to the non-harmonic shape of the CDT potential and also to the finite trap depth (see Fig. 4.6). The evaporation parameter $\eta = V_0/k_B T$ remains large ($\eta > 7$) during the evaporation ramp, so that the fraction of atoms affected by these effects is small.

The critical atom number and temperature are affected by two separate effects. First, the finite trap depth introduces an energy cutoff that reduces the critical atom number and increases T_c (this effect is likely to be enhanced when gravity is taken into account). Second, the anharmonic part of the CDT potential tend to increase N_c and thus to reduce of T_c (Gaussian traps are "looser" than pure harmonic traps near their edges). The second effect becomes more important for high values of η.

We have estimated the two effects by evaluating numerically the critical atom number in a CDT potential, using

$$N_c = \int_0^{V_0} \rho(\epsilon) f_{\mathrm{BE}}(\epsilon) d\epsilon, \tag{4.7}$$

with $f_{\mathrm{BE}}(\epsilon) = (e^{\beta\epsilon} - 1)^{-1}$ the critical Bose-Einstein distribution and $\rho(\epsilon)$ the density of states. We have taken a potential of the form given in Subsection 4.2.2, with beam sizes $21\,\mu$m and $25\,\mu$m for the two arms of the CDT. For an evaporation parameter $7 < \eta < 10$ as in our experiments, the effect of the anharmonicity is dominant, and we evaluate a reduction of the critical temperature around -3% for $\eta = 8$. We did not consider in this calculation atoms possibly trapped in the arm region, which would slightly further the magnitude of the shift.

Combined effect of the finite-size and anharmonicity corrections: To summarize this Subsection, the combination of finite-size effects and of the deviation of the CDT potential from an harmonic one can lower the critical temperature of a non-interacting gas by $\sim -5\,\%$ compared to the semi-classical prediction in a harmonic trap. The finite-size effects are not easily incorporated in the Hartree-Fock model. Trap anharmonicity effects are difficult to evaluate rigorously due to the ambiguity in the precise definition of the trap depth and of the role of a small, high energy population in the arms of the dipole trap. As a result, we did not include these effects in the comparison between theory and experiments. However, the order-of-magnitude estimate presented here show that they could well explain most of the residual shift between the experimental data and the Hartree-Fock model.

5. Spin-1 BEC in 1D: Spin domains and phase transition

In Chapter 2 we saw that, depending on the trap geometry, the single-mode approximation can hold in some trap directions and not in others. In the 3D regime, the trap frequencies along the three axes are of the same order and the SMA holds along the three directions. This is not true, in general, for the 1D geometry, where one of the trap frequencies is much lower than the other two. The spin healing length $\xi_s = \sqrt{\frac{\hbar^2}{2mg_sn}}$ gives the length scale for the formation of spin structures in a spinor condensate. In the regime where the spin-healing length is smaller than the size of the condensate, it becomes energetically favourable for the system to form spin domains that can be spatially redistributed to minimise interaction energy. The spinor components can therefore exhibit different spatial wave functions and form spin structures depending on their miscibility, as we have already introduced in Section 2.3. For our experimental parameters, we have $\xi_s = 5.3\,\mu$m for a density $n = 100\,\mu\text{m}^{-1}$, a length $L_z \approx 90\,\mu$m along the axial direction and $R_\perp \approx 1\,\mu$m along the radial direction. Therefore spin domains are expected to form along the weak axis. Figure 5.1 shows typical spin domains observed in our spinor condensate of ^{23}Na, see [112]. As we can see in Figure 5.1(a), $m_F = 0$ and $m_F = +1$ components are not miscible, so they phase separate. The $m_F = 0$ components stays in the middle, where the density is higher, because interactions between $m_F = 0$ atoms are less energetic than between $m_F = +1$ atoms. The $m_F = +1$ and $m_F = -1$ components are miscible and overlap with each other Figure 5.1(b).

The study of the behaviour of a ^{23}Na $F = 1$ antiferromagnetic spinor condensate in an elongated harmonic trap in the presence of a magnetic field began with the work [173], where the formation of spin domains was reported for the first time. However, the spin structures were strongly influenced by the presence of a gradient of magnetic field intentionally applied along the weak axis of the trap. The only reported configuration without a magnetic gradient was found to be free of spin domains because it was composed of atoms in the $m_F = +1$ and $m_F = -1$ states, which are miscible. In following works [117, 171] the same authors investigate how a system of spin domains equilibrates and the

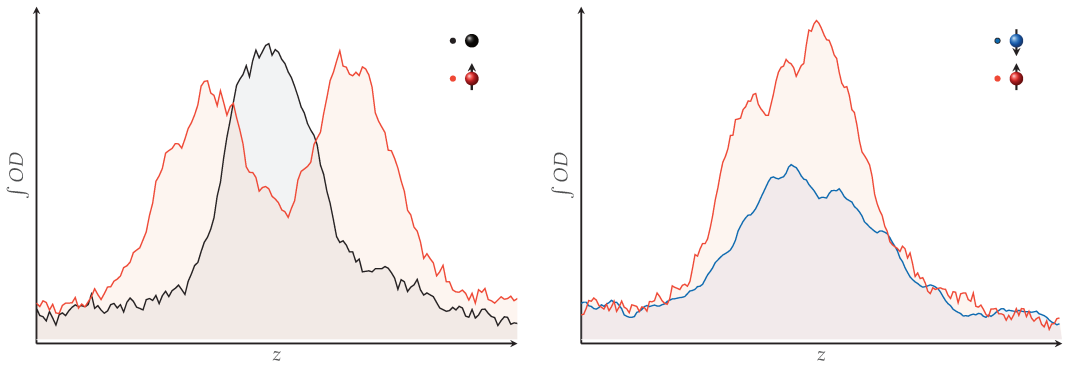

Figure 5.1.: Integrated density profiles along the weak axis. The immiscibility of the $m_F = 0$ and the $m_F = +1$ components leads to the formation of a spin domain of $m_F = 0$ atoms in the trap centre, surrounded by $m_F = +1$ atoms, Figure (a). The $m_F = +1$ and $m_F = -1$ are miscible, as a consequence, their spatial distribution overlap almost perfectly, Figure (b).

tunnelling processes involved in this equilibration. In [117], spin domains were treated as metastable states in a strong magnetic field gradient and observed to relax to an equilibrium configuration in a long time (several seconds). This relaxation was attributed to quantum tunnelling.
In early theoretical work [74, 193], spin domains in presence of an applied magnetic field gradient were theoretically studied. In several follow-up works [195, 17], it has been assumed that the SMA would hold in zero magnetic field gradient. However it was realised in [112] that antiferromagnetic spin-1 systems, in an elongated harmonic trap, can develop spin domains if the condensate size along the longitudinal axis is larger than the spin healing length. Our observations confirm this prediction.

The purpose of this Chapter is the investigation of these spin structures experimentally in a quasi-1D system. We experimentally produced these spin structures in an antiferromagnetic spinor condensate of ^{23}Na atoms, and we characterised them by fitting each spin component independently after Stern-Gerlach TOF, see Section 3.1. We observed also a second order transition, from an antiferromagnetic miscible system to a transverse magnetised immiscible system, with the n_0 population as order parameter. This transition is analogous to the one observed for the 3D case (SMA valid), see Section 2.3.

5.1. Stable phases of a 1D Spin-1 antiferromagnetic BEC

Here we present a quantitative description of the formation of spin domains in an elongated trap, summarising the results of references [112, 111, 113]. We assume for now a purely 1D system, where the radial motion is frozen ($\mu \ll \hbar\omega_\perp$).

At $T = 0$, the equilibrium state is determined by the minimisation of the Gibbs free energy $G = \langle H_{\rm tot}\rangle - \mu N - \eta \mathrm{M}_z = \int d\mathbf{r}\, G(\mathbf{r})$, where the Hamiltonian $\hat{H}_{\rm tot}$ is defined in Section 2.3 as $\hat{H}_{\rm tot} = \hat{H}_{\rm sp} + \hat{H}_{\rm int} + \hat{H}_{\rm mag}$. We have introduced two Lagrange multipliers: the chemical potential μ ensures conservation of atom number while the "magnetic potential" η ensures the conservation of magnetisation. As in the 3D case, the linear Zeeman term is just an energy shift and does not contribute to the determination of the ground state. Due to the breakdown of the SMA in the 1D regime, we cannot decouple the spatial and spin degrees of freedom, as done in Chapter 2. Instead, the system is described by three coupled Gross-Pitaevskii equations, one per Zeeman component:

$$(\mu \pm \eta)\phi_{\pm1} = \left[-\frac{\hbar^2}{2m}\Delta + V_{\rm ext} + \bar{g}_{1D}\rho + g_{s,1D}(\rho_0 \pm \rho_z)\right]\phi_{\pm1} + g_{s,1D}\phi_0^2\phi_{\mp1}^* \tag{5.1}$$

$$(\mu + q)\phi_0 = \left[-\frac{\hbar^2}{2m}\Delta + V_{\rm ext} + \bar{g}_{1D}\rho + g_{s,1D}(\rho_{+1} + \rho_{-1})\right]\phi_0 + 2g_{s,1D}\phi_{+1}\phi_{-1}\phi_0^* \tag{5.2}$$

where q denotes the quadratic Zeeman energy, $\rho = \rho_{+1} + \rho_{-1} + \rho_0$ is the total density and $\rho_z = \rho_{+1} - \rho_{-1}$ is the longitudinal magnetisation density. The coupling constants $\bar{g}_{1D}$ and $g_{s,1D}$ are effective 1D coupling constants introduced in Section 2.2 as $\bar{g}_{1D} = 2\hbar\omega_\perp a$ and $g_{s,1D} = 2\hbar\omega_\perp a_s$. Equations (5.1) and (5.2) need to be solved under the constraints

$$\int d\mathbf{r}\, \rho(\mathbf{r}) = N, \tag{5.3}$$

$$\int d\mathbf{r}\, \rho_z(\mathbf{r}) = M_z, \tag{5.4}$$

where N is the total atom number and M_z is the total magnetisation. The two constraints determine implicitly the chemical and magnetic potentials.

5.1.1. The uniform case

We start by considering the homogeneous case. This will be useful when we introduce the Bose gas in an harmonic potential in the LDA approximation. Considering a spinor gas trapped in a unidimensional box of length L, with constant density $\rho = N/L$. In the thermodynamic limit there are 4 different stable phases, see [113]:

I) **transverse quasi-nematic phase**, atoms are distributed in the $m_F = +1$ and $m_F = -1$ states, depending on the system magnetisation. The magnetisation profile is uniform along the box, with $0 \le \rho_z \le \rho$:

$$\begin{aligned} \mu_I &= \bar{g}_{1D}\rho, \\ \eta_I &= g_{s,1D}\rho_z = \text{const}, \\ \epsilon_I &= \frac{\bar{g}_{1D}}{2}\rho^2 + \frac{g_{s,1D}}{2}\rho_z^2 \end{aligned} \tag{5.5}$$

II) **demixed "phase"**, atoms in $m_F = 0$ and $m_F = \pm1$. The two atomic species phase separate and domains of **Phase I** and **Phase III** are simultaneously present in the trap. The longitudinal magnetisation m_z is conserved.

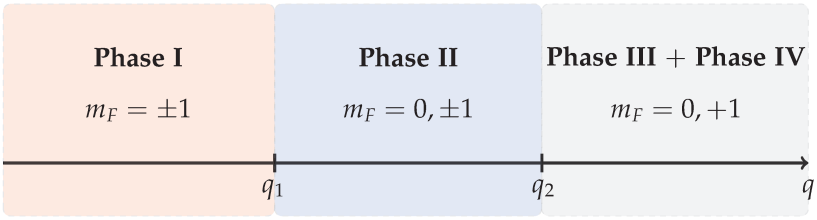

Figure 5.2.: Sketch of the Phase Diagram for the uniform system for $0 < m_z < 1$.

III) **z-nematic phase**, all the atoms are in the $m_F = 0$ state, $\rho_z = 0$ and $\rho_0 = \rho$. Chemical potential and energy density of this phase are equal to:

$$\begin{aligned} \mu_{III} &= \bar{g}_{1D}\rho - q, \\ \epsilon_{III} &= -q\rho + \frac{\bar{g}_{1D}}{2}\rho^2 \end{aligned} \tag{5.6}$$

IV) **z-polarised phase**, all the atoms occupy the $m_F = +1$ state, $\rho_z = \rho$ and $\rho_0 = 0$. We can write:

$$\begin{aligned} \mu_{IV} &= (\bar{g}_{1D} + g_{s,1D})\rho - \eta, \\ \epsilon_{IV} &= \frac{\bar{g}_{1D} + g_{s,1D}}{2}\rho^2 \end{aligned} \tag{5.7}$$

In Section 2.3 we introduced that the longitudinal magnetisation m_z is a conserved quantity in our system. Depending on m_z, the system can organise itself one or more phases among the ones described above. For $m_z = 0$, the system is in **Phase III**. For $m_z = +1$, on the contrary, the system is in **Phase IV**. It is interesting now to discuss in which phase the system organises itself when $0 < m_z < 1$, see Figure 5.2.
We consider a uniform system like the one sketched in Figure 5.3. The energy of the demixed phase (**Phase II**) E_{demix} is equal to the energy of **Phase I** over the length $L(1 - f_0)$ plus the energy of **Phase III**, over the length Lf_0:

$$E_{\text{demix}} \simeq \frac{\bar{g}_{1D}}{2}\frac{N^2}{L} + \frac{g_{s,1D}M_z^2}{2L(1-f_0)} - qNf_0, \tag{5.8}$$

where f_0 is the fraction of atoms in **Phase III** and q is the quadratic Zeeman energy. We assumed the density of the two phases to be equal to ρ. This is valid only to the lowest order in $g_{s,1D}/\bar{g}_{1D}$, see Chapter 2.
The difference between the energy of **Phase I** and **Phase II** for a uniform density is equal to

$$E_{\text{demix}} - E_{\pm 1} \simeq Nf_0\left(\frac{g_{s,1D}\rho m_z^2}{2}\frac{1}{1-f_0} - q\right). \tag{5.9}$$

From eq. (5.9) we see that quadratic Zeeman energy and interactions are competing to form, respectively, an immiscible or miscible system. A critical field q_1 can be defined looking at the expression inside the parenthesis. A miscible system ($q < q_1$) in **Phase I**

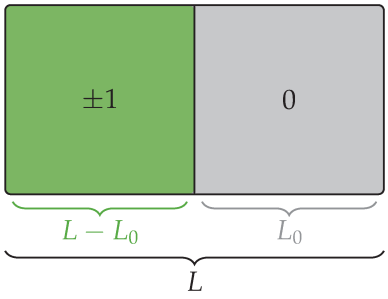

Figure 5.3.: Sketch of the spin-1 uniform Bose gas in a demixed phase.

can indeed undergo a phase transition to an immiscible system ($q > q_1$) in **Phase II** when the quadratic Zeeman energy is increased until it reaches the critical value q_1, defined as the value for $f_0 = 0$ at which $E_{\text{demix}} = E_{\pm 1}$:

$$q_1 = \frac{g_{s,1D}\rho m_z^2}{2}. \tag{5.10}$$

Increasing further the magnetic field, thanks to the spin-changing collisions described in Chapter 2, the $m_F = 0$ spin domain starts to grow.
This process ends because of the conservation of the longitudinal magnetisation m_z, when there are no atoms in $m_F = -1$ and the atoms remaining in state $m_F = +1$ are required to conserve the magnetisation.
To find the critical field at which there are no more $m_F = -1$ atoms in the system, we look at the fraction of atoms in the $m_F = 0$ state, f_0, which minimise the energy E_{demix}. We find

$$f_0 = 1 - \sqrt{\frac{q_1}{q}}. \tag{5.11}$$

When there are no more $m_F = -1$ atoms, we can write $f_0 = 1 - m_z$ and, from the equation above, we find the critical value q_2 for this second phase transition

$$q_2 = \frac{g_{s,1D}\rho}{2} \tag{5.12}$$

These two phase transitions exist in the uniform case, but also persist in presence of a trap potential. The spatial arrangement of the spin is influenced by the trap, although their existence is not.

5.1.2. Adding an harmonic potential in the LDA approximation

We consider now the Bose gas to be trapped in a cigar shaped potential given by (2.35), where $\omega_z \ll \omega_\perp$. As a first approach, we make the local density approximation neglecting the kinetic energy terms from the Gross-Pitaevskii equations.
We start considering the system in the immiscible phase. Since the density is not constant along the trap, **Phase II** do not exist for a harmonically trapped condensate and the

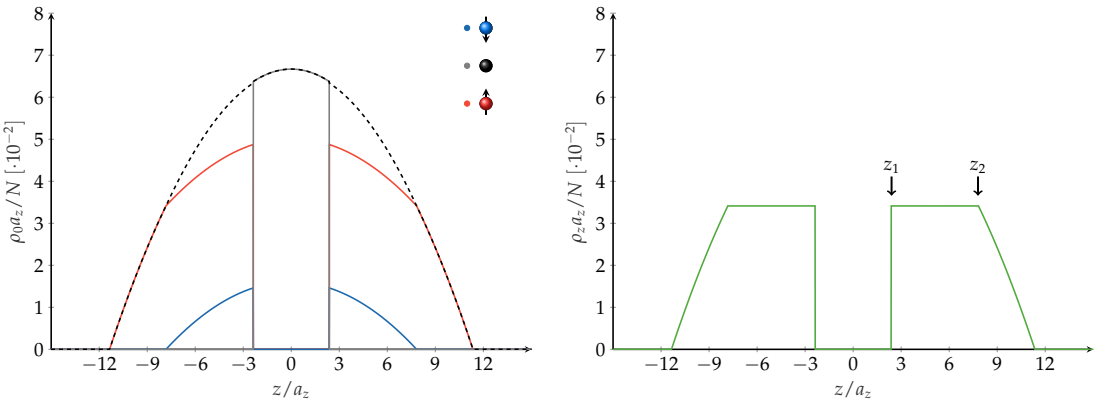

(a) Density profile (b) Magnetisation profile

Figure 5.4.: Density and magnetisation profiles for a Bose-Einstein condensate trapped in a 1D harmonic trap in the LDA approximation. The density are in harmonic oscillator unit; $q = 0.35\hbar\omega_z$ and $m_z = 0.5$.

system divides into two spin domains of inhomogeneous density corresponding to **Phase I** and **Phase III**. This means that, at each point of the trap $\mathbf{r}$, we can consider the system to be in **Phase I - III** or **IV**.
We consider now a position $\mathbf{r}$ with density $\rho(\mathbf{r})$. For $g_s > 0$ the following inequality gives an energy hierarchy between the energy densities of the phases **Phase III**, **Phase I** and **Phase IV**

$$\frac{\bar{g}}{2}\rho^2 - q\rho \leq \frac{\bar{g}_{1D}}{2}\rho^2 + \frac{g_{s,1D}}{2}\rho_z^2 \leq \frac{\bar{g}_{1D} + g_{s,1D}}{2}\rho^2, \tag{5.13}$$

where $0 \leq \rho_z \leq \rho$. This density-dependent energy hierarchy determines the spatial order of the different phases along the trap axis, starting from the centre. Since the $m_F = 0$ component has the smallest interspecies scattering length, it is generally localised in the centre of the trap, where the density is the highest. The $m_F = \pm 1$ components phase separate from the $m_F = 0$ and, when $m_z > 0$, there is always a magnetised shell of $m_F = +1$ atoms at the edges of the cloud.

Replacing the global chemical potential μ with its local counterpart $\mu - V_{\text{ext}}$, we can write the density profile as

$$\rho(z) = \begin{cases} \frac{\mu+q-V_{\text{ext}}(z)}{\bar{g}_{1D}}, & z \leq z_1, \\ \frac{\mu-V_{\text{ext}}(z)}{\bar{g}_{1D}}, & z_1 \leq z \leq z_2, \\ \frac{\mu+\eta-V_{\text{ext}}(z)}{\bar{g}_{1D}+g_{s,1D}}, & z_2 \leq z \leq L. \end{cases} \tag{5.14}$$

and the magnetisation profile as

$$\rho_z(z) = \begin{cases} 0, & z \le z_1, \\ \frac{\eta}{g_{s,1D}}, & z_1 \le z \le z_2, \\ \rho(z), & z_2 \le z \le L. \end{cases} \tag{5.15}$$

where z_1 and z_2 are, respectively, the boundaries between **Phase III - Phase I** and **Phase I - Phase IV** and L is the spatial extent of the system in the LDA approximation. The profiles for the three components separately are given by

$$\rho_0(z) = \begin{cases} \rho(z), & z \le z_1, \\ 0, & z \ge z_1. \end{cases} \qquad \rho_{\pm1}(z) = \begin{cases} 0, & z \le z_1, \\ \frac{\rho(z) \pm \rho_z(z)}{2}, & z \ge z_1. \end{cases} \tag{5.16}$$

In Figure 5.4, we present dimensionless density profiles showing the coexistence of **Phase I - Phase III - Phase IV** in the harmonic trap [1].
The boundaries between the different domains are usually defined as the surfaces where the pressures inside the different components are equal. In a 1D system, pressure is replaced by the density of energy[2]. Considering now the boundary at z_1 between two components 1 and 2, we can write

$$\frac{g_{11}}{2}\rho_1^2(z_1) = \frac{g_{22}}{2}\rho_2^2(z_1) \quad \rightarrow \quad \frac{\rho_1(z_1)}{\rho_2(z_1)} = \sqrt{\frac{g_{22}}{g_{11}}} > 1. \tag{5.17}$$

Eq. (5.17) implies that there is a density step at the boundary between the two components. This effect is visible also in our system, where the profiles of the three Zeeman component do not sum up to give an overall smooth Thomas-Fermi profile. Looking at (5.14) indeed, the $m_F = 0$ spin domain is higher than the profile formed by the sum of the $m_F = \pm 1$ domains. Experimentally however, we are not able to resolve this feature of the density profile, which is $\propto \sqrt{g_{00}/g_{+1,+1}} \sim 0.98$, because of the noise on the imaging. Therefore, in analysing the profiles, we model the domains to form a Thomas-Fermi profile when summed together.

The boundaries between the different phases can be found by imposing the energy densities to be equal:

III - I Phases boundary, we find $q\rho_I = \frac{g_{s,1D}\rho_z^2}{2} = \frac{\eta^2}{2g_{s,1D}}$.
The density in Phase I is given by $\rho_I(z) = \frac{\mu - V_{\text{ext}}(z)}{\bar{g}_{1D}}$, hence the boundary between these two phases is at:

$$V_{\text{ext}}(z_1) = \mu - \frac{\bar{g}_{1D}\eta^2}{2g_{s,1D}q}, \tag{5.18}$$

[1] Here we work in harmonic oscillator units: lengths are in units of a_z, defined in (2.3), energies are in units of $\hbar\omega_z$ and coupling constants are in units of $\bar{g}(g_s) = N\bar{g}(g_s)/(a_z\hbar\omega_z)$.
[2] For a 1D system we have $dE = P\,dx$, such that the density of energy $\epsilon(x)$, defined by $E = \int \epsilon(x)\,dx$, is identical to the pressure.

I - IV Phases boundary, we find $\rho_{IV} = \rho_z$.
In this case, the boundary can be obtained from

$$V_{\text{ext}}(z_2) = \mu - \bar{g}_{1D}\rho_z = \mu - \frac{\bar{g}_{1D}\eta}{g_{s,1D}} \tag{5.19}$$

Cloud edge, can be found for $\rho_{IV} = 0$.
This is true for

$$V_{\text{ext}}(L) = \mu + \eta. \tag{5.20}$$

We remind that the two Lagrange multipliers μ and η are defined by the conservation, respectively, of atom number, (5.3), and magnetisation, (5.4).

When the system is in the miscible phase, only **Phase I** and **Phase IV** are present. The formula for the density and magnetisation profiles remain the same as before, with $z_1 = 0$.

5.1.3. The phase transition

To find the Zeeman quadratic energy critical value at which the system undergo the phase transition from miscible to immiscible, we can use the boundary z_1 between **Phase III** and **Phase I**. Imposing $z_1 = 0$ we find

$$q_1(m_z) = \frac{g_{s,1D}\rho_z(0)^2}{2\rho(0)}. \tag{5.21}$$

Since ρ_z is defined only implicitly by eq.(5.15), it is not possible to find an analytical formula for $q_1 = q_1(m_z)$ without making any further approximation.
When $q < q_1$, therefore when only **Phase I** and **Phase IV** are present, since $\bar{g}_{1D} \ll g_{s,1D}$ for ^{23}Na atoms, we approximate the density profile as $\rho(z) \approx (\mu - V_{\text{ext}})/\bar{g}_{1D}$ all along the density profile. The atom number constraints gives

$$N = \frac{4}{3}\frac{\mu}{\bar{g}_{1D}}L, \tag{5.22}$$

where we approximated the cloud Thomas-Fermi radius $L \approx \sqrt{2\mu/M\omega_z^2}$. And the magnetisation constraint gives

$$N_{-1} = \frac{N - M_z}{2} = \int_{-z_2}^{z_2} dz\, \frac{\rho(z) - \rho_z(z)}{2}. \tag{5.23}$$

From (5.19) follows, when$(q \le q_1)$,

$$\left(\frac{z_2}{L}\right)^2 \approx 1 - \frac{\bar{g}_{1D}\eta}{g_{s,1D}\mu}. \tag{5.24}$$

Therefore, from (5.23) and (5.24) we obtain, when$(q \leq q_1)$,

$$z_2 \simeq L(1 - m_z)^{1/3}. \tag{5.25}$$

From (5.24) and (5.25), recalling that $\rho_z(0) = \eta/g_{s,1D}$, we can write the magnetisation density in the centre, when$(q \leq q_1)$, as

$$\rho_z \approx \rho(0)\left[1 - (1 - m_z)^{2/3}\right] \tag{5.26}$$

and from (5.26) we can finally obtain a formula for q_1:

$$q_1 \approx \frac{g_{s,1D}\mu}{2\bar{g}_{1D}}\left[1 - (1 - m_z)^{2/3}\right]^2 \tag{5.27}$$

For $q < q_1$ only **Phase I** and **Phase IV** are present in the condensate, so that we have a profile like the one in Figure 5.1(b). Increasing the magnetic field to $q > q_1$, a domain of $m_F = 0$ atoms appears in the centre of the trap. The profile will be like the one in Figure 5.1(a).
To find the critical field for the second phase transition, we increase q further: the central $m_F = 0$ domain grows. To maintain a fixed magnetisation, the **Phase I** shell where $m_F = +1$ and $m_F = -1$ are present is reduced accordingly. This means that the boundary z_2 approaches z_1 and, at a certain value q_2, the boundaries will coincide and **Phase I** disappears. This happens when

$$q \geq q_2 = \frac{g_{s,1D}\mu}{2\bar{g}_{1D}}. \tag{5.28}$$

Figure 5.5 shows the phase diagram at $m_z = 0.5$ for our systems of ^{23}Na atoms in terms of the density in the $m_F = 0$ component, Figure 5.5(a), as well as the longitudinal magnetisation, Figure 5.5(b), both as a function of q. We obtained it numerically by using the profiles (5.14) and (5.15) to satisfy the two constraints (5.3) and (5.4), without making the approximation $g_{s,1D} \ll \bar{g}_{1D}$, for $N = 20000$, $\omega_z = 2\pi\,4\,\mathrm{Hz}$ and $\omega_\perp = 2\pi\,400\,\mathrm{Hz}$. In Figure 5.5(a) the ρ_0 density profile, in units of the harmonic oscillator, is plotted as a function of the quadratic Zeeman energy $q/\hbar\omega_z$. The dashed white line corresponds to the critical field computed from (5.27). In Figure 5.5(b), instead, we plotted the longitudinal magnetisation profile as a function of $q/\hbar\omega_z$. The dashed line denotes, another time, the critical field q_1; the solid white line corresponds to z_1 and the solid yellow line to z_2. We found a critical field $q_1 \approx 0.18\,\hbar\omega_z$.

5.1.4. GP simulation vs LDA solution

In this section we compare the results of the LDA model described above with the numerical solutions of the GP equations (5.1, 5.2) . In Appendix B, the reader can find a description of the algorithm used to solve the GP equation numerically. Figure 5.6(a), 5.6(b) and 5.6(c) show three comparisons between solutions to the GP equations and the

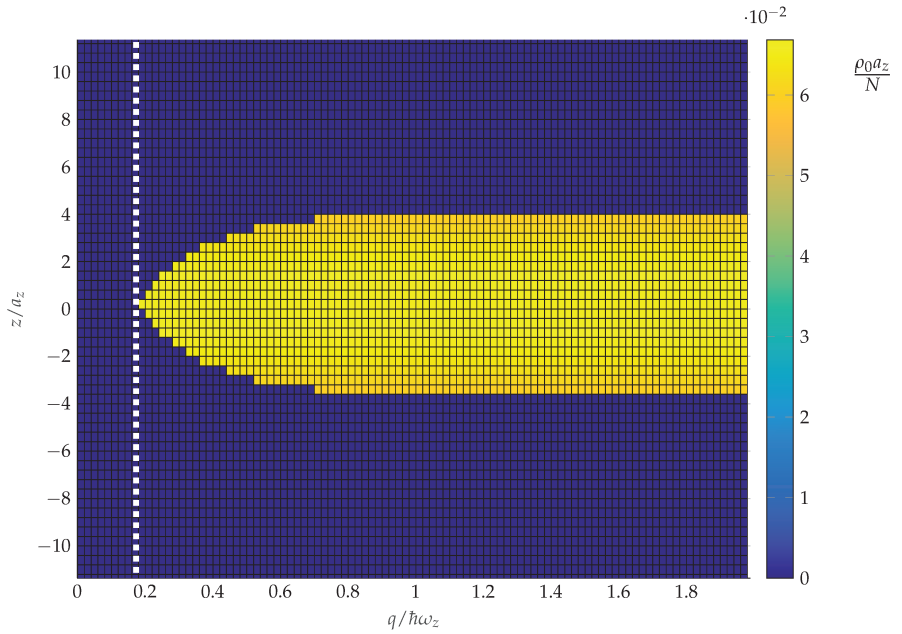

(a) Density profile

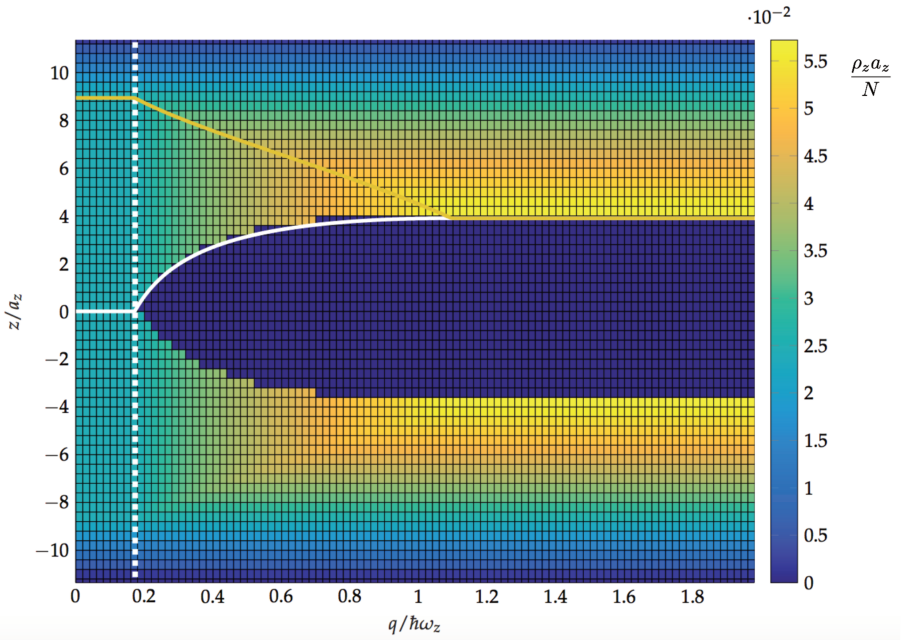

(b) Longitudinal magnetisation profile

Figure 5.5.: Phase diagram of the transition under the LDA approximation. Figure (a) represents the ρ_0 density profile, in units of the harmonic oscillator, as a function of $q/\hbar\omega_z$. The white dashed line corresponds to the critical field q_1 for the appearance of spin domains, computed using (5.27). In Figure (b), the magnetisation profile is represented. The dashed white line denotes the same as in the Figure above; the solid white line corresponds to the values of z_1 while the solid yellow line corresponds to z_2.

LDA approximation for q values $q = 0.15\hbar\omega_z$, $q = 0.41\hbar\omega_z$ and $q = 1\hbar\omega_z$, respectively.
The GP simulation results are in good agreement with the LDA ones, apart from an expected smoothing of the profiles in the GP solutions due to the kinetic energy.
The transition happens at higher values of q in the numerical GP with respect to the LDA. This is due to the kinetic energy cost we have to pay to form a **Phase I** domain in the centre of the trap. We can roughly estimate the cost of this domain to be equal to the difference between the energy cost for the $E_{0,\pm}$ configuration minus the energy cost for the $E_{\pm}$ configuration at which we add an estimation of the kinetic energy cost to form the $m_F = 0$ domain:

$$E_{0,\pm} - E_{\pm} \approx \left(-q\rho(0) + \frac{g_{s,1D}}{2}\rho_z^2 \right) z_1 + \frac{\hbar^2\rho(0)}{2m\xi_s} \tag{5.29}$$

The formation of the **Phase I** domain occurs when z_1 becomes large enough, delaying the transition to $q_1^* > q_1$. In the example we considered numerically, we have found that $q_1 \approx 0.18\,\hbar\omega_z$ for the LDA approximation becomes $q_1^* \approx 0.4\,\hbar\omega_z$ with the GP. In Figure 5.6 we show the 3 Zeeman components profiles at $q < q_1^*$, $q > q_1^*$ and $q \gg q_1^*$.

5.2. 1D-3D crossover

In Section 5.1 we presented the theory that models the spatial distribution of spin domains in the harmonic trap. However, to make the comparison between the theory and our experimental data, we need to be more careful when describing our system. While the theory presented so far is unidimensional, our experimental system consists of a Bose-Einstein condensate with chemical potential $\mu \in [100, 150]\,\mathrm{Hz}$, trapped in an anisotropic harmonic trap with $\omega_z = 2\pi\,4.6\,\mathrm{Hz}$ and $\omega_\perp = 2\pi\,383.3\,\mathrm{Hz}$. A truly 1D quasi-condensate can be observed only if $\mu \ll \hbar\omega_\perp$, a condition not perfectly fulfilled given our parameters: our condensate is in an intermediate regime between the 3D and 1D.
To describe this crossover from the one-dimensional to the three-dimensional regime, a waveguide model with uniform axial density has been developed for a gas of ultra-cold bosons in [35]. The impact of the axial trapping on the density profile was then studied in [115]. In the work [50], an analytical approximation for the "equation of state" of the quasi-1D gas has been introduced. The approximated equation of state smoothly connects, in the LDA approximation, the 3D to the 1D mean field regime and gives a formula for the atomic density in the crossover regime.
The authors of [50] start from a 3D Bose-Einstein condensate trapped in a cylindrical harmonic trap. The 1D density is defined as the 3D density integrated along the transverse direction, $n_{1D}(z) = \int d^2\rho\, n_{3D}(\rho, z)$ and the radial mode $f_\perp$ is defined as $n_{3D}(\rho, z) = |f_\perp(\rho, z)|^2 n_{1D}(z)$. Neglecting the density derivatives along the weak axis, the Gross-Pitaevskii equation is given in cylindrical coordinates:

$$-\frac{\hbar^2}{2m}\frac{\Delta_\perp f_\perp}{f_\perp} + \frac{1}{2}m\omega_\perp^2\rho^2 + g n_{1D}(z)|f_\perp|^2 = \mu_{\mathrm{l.e.}}[n_{1D}(z)]. \tag{5.30}$$

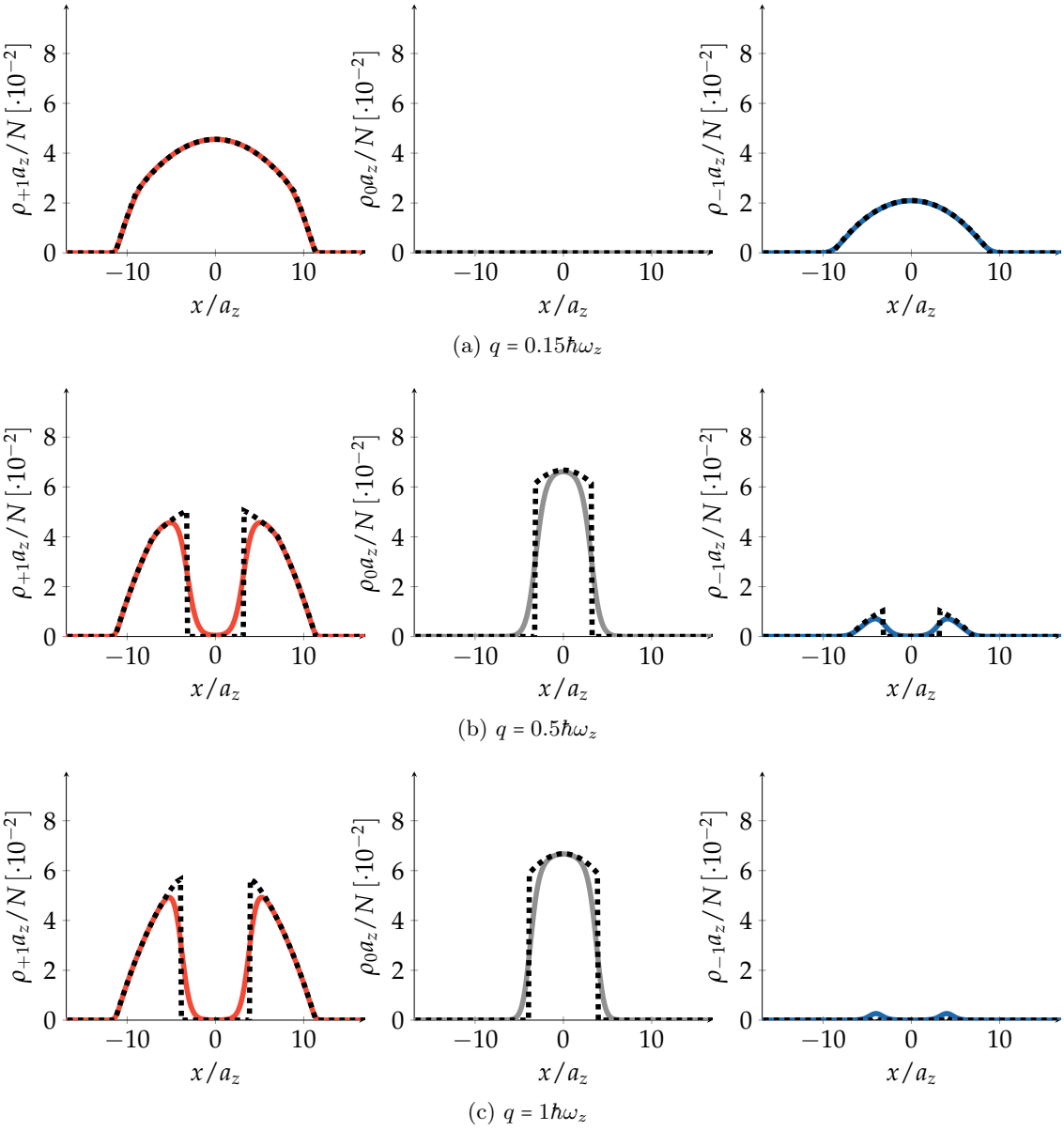

(a) $q = 0.15\hbar\omega_z$

(b) $q = 0.5\hbar\omega_z$

(c) $q = 1\hbar\omega_z$

Figure 5.6.: Results of the GP simulation for $m_z = 0.5$. In dashed black are sketched the results of the LDA model for the same parameters. In (a) $q = 0.15\hbar\omega_z$; (b) $q = 0.5\hbar\omega_z$ and (c) $q = 1\hbar\omega_z$.

Using the LDA a potential $V(z)$ along the axial direction can be taken into account. The local equilibrium chemical potential $\mu_{\text{l.e.}}$ depends on z through

$$\mu_{\text{l.e.}}[n_{1D}(z)] + V(z) = \mu, \tag{5.31}$$

The effective equation of state for the quasi-1D gas is then obtained making a gaussian *ansatz* for the radial mode $f_\perp$ and minimising the chemical potential $\mu_{\text{l.e.}}$. This variational method is not the usual one in which the energy is minimised, but it works well considering that in the two limits, $1D$ and $3D$, we recover the two correct solutions. The authors obtained

$$\mu_{\text{l.e.}}[n_{1D}(z)] = \hbar\omega_\perp\sqrt{1 + 4an_{1D}}. \tag{5.32}$$

Introducing as axial trapping potential $V(z) = \frac{1}{2}m\omega_z^2 z^2$, from the local equilibrium condition (5.31) and the equation of state (5.32), one finds

$$n_{1D}(z) = \frac{\alpha}{16a}(1 - \tilde{z}^2)\Big[\alpha(1 - \tilde{z}^2) + 4\Big], \tag{5.33}$$

where $\alpha = 2(\mu/\hbar\omega_\perp - 1)$, $\tilde{z} = z/L$, $L = \frac{a_z^2}{a_\perp}\sqrt{\alpha}$ and a_z and $a_\perp$ are the harmonic oscillator lengths for, respectively, the axial and transverse directions. The α parameter gives a measure of how much 1D or 3D is the system. Using the condition $\int n_{1D}(z) = N$, one can show that it obeys

$$\alpha^3(\alpha + 5)^2 = (15\chi)^2, \tag{5.34}$$

where the parameter $\chi = Naa_\perp/a_z^2$ gives approximately the ratio between the interaction energy and the radial zero-point energy. In the limit $\alpha \gg 5$, mean field interactions dominates over the transverse confinement strength: the system is 3D, the parameter α is equal to $\alpha \approx \alpha_{3D} = (15\chi)^{2/5}$ and the density profiles is the 3D Thomas-Fermi profile integrated along the transverse direction. For $\alpha \ll 5$ the transverse confinement is high enough to freeze the motion along that direction and the system is 1D. The parameter α is equal to $\alpha \approx \alpha_{1D} = (3\chi)^{2/3}$ and the density profile is the 1D Thomas-Fermi profile.

5.3. Preparation and study of spin domains

In order to produce spin domains as the ones in Figure 5.1, we prepare a condensate in the 1D trap, as discussed in Chapter 3, with a longitudinal magnetisation $m \in [0, 1]$.
We want to observe the ground state of the system in the presence of a uniform magnetic field. Therefore, we have to get rid of magnetic field gradients. In our system we identify environmental gradients as well as gradients that we directly produce with the experimental apparatus during the sequence. Environmental magnetic field gradients can come from the electrical components of the experimental apparatus, as photodiode power supplies, see [47], vacuum gauges and ionic pumps, but also from sources external to the lab.
Other magnetic field gradients come from the imperfect alignment of the coils system we use to produce the magnetic field at the position of the atoms.
In this section we describe how we get rid of these stray magnetic field gradients and we introduce the techniques used to characterise them.

5.3.1. Minimisation of magnetic field gradients

In Chapter 3 Subsection 3.1.4 we considered the effect of a magnetic field during the Stern-Gerlach TOF. However, to describe the magnetic field gradient, we considered the gradient eigenaxes to correspond to the coil axes. We want now to be more general, therefore we write a magnetic field gradient in the most general form

$$\mathbf{B} = \mathbf{B_0} + \bar{\bar{b}}' \cdot \mathbf{x} + O(\mathbf{x}^2), \tag{5.35}$$

where, from $\nabla \cdot \mathbf{B} = 0$, we know that $\mathrm{Tr}\,\bar{\bar{b}}' = 0$ and from $\nabla \times \mathbf{B} = 0$, we know that $b'_{ij} = b'_{ji}$. Then, the modulus of the magnetic field is written as

$$|\mathbf{B}| \simeq |\mathbf{B_0}| \left(1 + \frac{\bar{\bar{b}}' \cdot \mathbf{x}}{|\mathbf{B_0}|} \cdot \mathbf{B_0}\right) \tag{5.36}$$

and the potential felt by the atoms due to the magnetic field gradient is equal to

$$V_{\mathrm{mag}} = \mu_B g_F m_F |\mathbf{B}| = -\frac{\mu_B m_F}{2}|\mathbf{B_0}| - \frac{\mu_B m_F}{2}\frac{\mathbf{B_0}}{|\mathbf{B_0}|} \cdot (\bar{\bar{b}}' \cdot \mathbf{x}). \tag{5.37}$$

If we consider the potential felt by the atoms along the trap weak axis z, we can write

$$V_{m_F}(z) = \frac{1}{2}m\omega^2 x^2 - \frac{\mu_B m_F}{2}\left(\sum_\alpha \frac{B_{0\alpha} b'_{\alpha z}}{|\mathbf{B_0}|}\right) z = \frac{1}{2}m\omega^2 z^2 - m_F \tilde{\lambda} z, \tag{5.38}$$

where $\tilde{\lambda} = \frac{\mu_B}{2}\left(\sum_\alpha \frac{B_{0\alpha} b'_{\alpha z}}{|\mathbf{B_0}|}\right)$. In experiments, we chose $\mathbf{B_0}$ to lie in the horizontal plane. Using the coordinate system recalled in Figure 5.7, this corresponds to $\mathbf{B_0} = B_{0z}\mathbf{e_z} + B_{0x}\mathbf{e_x}$. The gradient component $b'_{\alpha z}$ has two contributions: stray magnetic field gradients and parasitic gradients produced by the bias coils used to produce the uniform component $\mathbf{B_0}$. Therefore we can write

$$b'_{\alpha z} = b'^{(\mathrm{stray})}_{\alpha z} + \sum_{\mu=z,u} \gamma^\mu_{\alpha z} B_{0,\mu}. \tag{5.39}$$

We did not attempt to characterise all the $b'^{(\mathrm{stray})}_{\alpha z}$ and $\gamma^\mu_{\alpha z}$ coefficients, but we determined the orientation of $\mathbf{B_0}$, for a given $|\mathbf{B_0}|$, that cancels $\tilde{\lambda}$.

From (5.38), we can write the potential felt by the atom along a generic direction u as

$$V_m(u) = \frac{1}{2}m\omega^2 u^2 - m_F \tilde{\lambda} u \approx \frac{1}{2}m\omega^2 (u - u_0)^2, \tag{5.40}$$

where we have defined $u_0 = \tilde{\lambda}/m\omega^2$. The magnetic field gradient changes the harmonic potential shifting the potential minimum of a quantity u_0 along the considered axis.
For our experimental parameters, with magnetic field gradients $b' \sim 10\,\mathrm{mG{\cdot}cm^{-1}}$, we obtain a shift of $z_0 \approx 15\,\mu\mathrm{m}$ along the weak axis ($\mathbf{u} = \mathbf{z}$) and and a shift $x_0 \approx 2\,\mathrm{nm}$ along

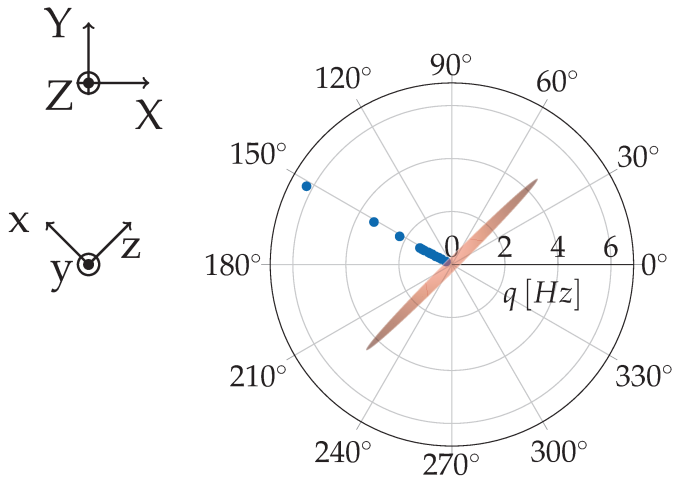

Figure 5.7.: Measurement to establish the bias magnetic field direction that cancels magnetic forces along the trap weak axis. The polar plots has the quadratic Zeeman shift as radial coordinate. The condensate orientation is represented by the sketch of the red atomic cloud.

the radial direction ($\mathbf{u} = \mathbf{x} = \mathbf{y}$). If u_0 is very small with respect to the cloud dimension along the considered axis, the effect of the magnetic field gradient is negligible. Therefore the effect of $|\nabla \mathbf{B}|$ along the radial direction is negligible. On the weak axis, on the contrary, this effect can be observed in our experiment. From now on we consider only the effect of the magnetic field gradient along the weak trap axis $\mathbf{z}$.

To describe the method we use to calibrate the orientation of $\mathbf{B_0}$ we focus on (5.38). The force felt by the atoms due to a magnetic gradient can be derived from (5.38) and it is equal to $F_{\text{mag}} = m_F \tilde{\lambda}$.
If we consider a condensate where the three atomic species are present, arranged like in Figure 5.4, and the gradient along the z direction is not zero, we expect the $m_F = +1$ component to feel a force directed along the same direction as the gradient, the $m_F = -1$ to feel the same force, but along the opposite direction and the $m_F = 0$ component to not feel any "direct" force. However, interactions with the other components will force it to move and respond to a magnetic gradient as well.
Considering now a condensate where only the $m_F = 0$ and $m_F = +1$ components are present, the position of the $m_F = 0$ spin domain with respect to trap centre can then be used as a probe for the presence of a magnetic field gradient along the direction of the trap weak axis. When the domain is in the trap centre, there is no magnetic gradient[3].
To cancel $\tilde{\lambda}$, we changed the orientation of the bias field $\mathbf{B_0} = |B_0|\Big(\cos\theta\, \mathbf{e_X} + \sin\theta\, \mathbf{e_Y}\Big)$,

[3] In Chapter 6 we present a characterisation of the response of the system to magnetic gradients and we show the appearance of a large spin-dipole polarisability depending on the longitudinal magnetisation m_z.

see Figure 5.7 for the axes definition, for a given value of $|B_0|$ looking at the $m_F = 0$ domain position.
In Figure 5.7 we can see the results of such a measurement. In the polar plot, the red cloud represents the cloud position. The blue points represent the angles (in the (X, Y) plane) at which the $m_F = 0$ domain is in the trap centre. Each point has a different radial coordinate, corresponding to the quadratic Zeeman energy at which that measurement was performed.
The measured angles do not correspond to the axis x perpendicular to the weak axis of the trap and additionally depend on the quadratic Zeeman shift q. This effect is due to the fact that, changing the magnetic field bias, we introduce a magnetic field gradient due to the imperfection of the bias coils alignment, the $\gamma^{\mu}_{\alpha z}$ terms. The compensation angle is constant for very weak ($b'^{(\mathrm{stray})}_{\alpha z}$ dominant) or very strong ($\gamma^{\mu}_{\alpha z}$ dominant) applied magnetic fields.

5.3.2. Fitting the Spin Domains

In this section we introduce the functions used to fit the spin domains and we present the results of this study. We have already explained in Section 5.2 that our atomic cloud is in an intermediate regime between the 1D and the 3D regimes. Therefore to fit the overall profiles $n_{1D}(z)$, sum of the three Zeeman components profiles, we use the equation (5.33). To sum them without introducing any alignment error, we separately measured the positions of the clouds with all the atoms in $m_F = \pm 1$ or 0 to calibrate the different cloud centres after TOF. We then use this calibration to recenter all components to $m_F = 0$.

To fit the spin domains composing the overall profile, we use the function sketched in Figure 5.8. To fit the $m_F = 0$ domain, we multiply the profile (5.33), in the left of Figure 5.8, by a smoothed step function

$$s_0(z; z_c, \Delta, \xi) = \frac{1}{2}\tanh\left(\frac{z - z_c + \frac{\Delta}{2}}{\xi}\right) - \frac{1}{2}\tanh\left(\frac{z - z_c - \frac{\Delta}{2}}{\xi}\right) \tag{5.41}$$

which can account for the domain structure predicted by the LDA theory plus the smoothing expected when we consider the kinetic energy. The parameter z_c is the $m_F = 0$ domain centre, Δ is the width of the domain $m_F = 0$ and ξ describes the width of the boundary between the two species. To fit the $m_F = +1$ profile, instead, we multiply the overall profile (5.33) with a function $s_{+1}(z) = 1 - s_0(z)$. The final fitting functions can be written as

$$n_{1D,0} = n_{1D}(z) \cdot s_0(z; z_c, \Delta, \xi), \tag{5.42}$$

$$n_{1D,+1} = n_{1D}(z) \cdot \Big[1 - s_0(z; z_c, \Delta, \xi)\Big], \tag{5.43}$$

and are sketched in Figure 5.8. Two examples of the resulting fit on averages profiles are presented in Figure 5.9. Both profiles result from the average of 4 images. They have longitudinal magnetisation $m_z = 0.45(5)$ and $N \sim 10^4$ atoms. From the fit, we obtained

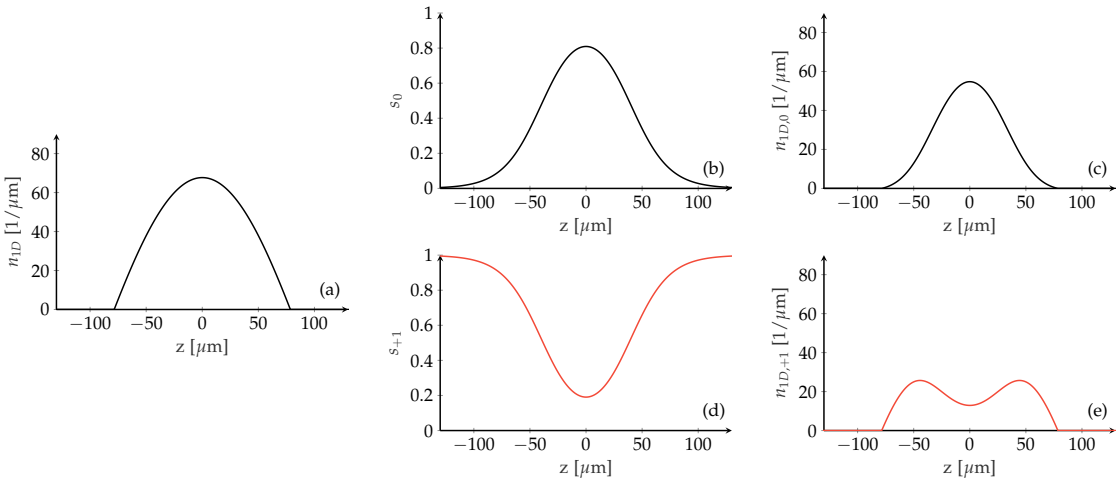

Figure 5.8.: Sketch of the functions we use to fit the spin domain profiles. (a) Overall profile given by (5.33); (b) smooth box function $s_0(x)$ given by (5.41); (c) fit function for the $m_F = 0$ domain, obtained by the multiplication of the profile (a) by $s_0(x)$; (d) smooth box function $s_{+1}(x) = 1 - s_0(x)$; (d) fit function for the $m_F = +1$ domain, obtained multiplying the profile (a) by $s_{+1}(x)$.

Table 5.1.: Results of the fit of the two averaged domains sketched in Figure 5.9 with the fitting functions sketched in Figure 5.8.

Profile	a.	b.
α	0.66(2)	0.67(2)
μ [Hz]	126(6)	128(5)
Δ [μm]	46(3)	65(3)
ξ [μm]	20(1)	18(1)

the value listed in Table 5.1. The parameter α is much lower than 5, hence our system is closer to the 1D regime than to the 3D one. The profile sketched in Figure 5.9(a) is close to the ground state in a uniform magnetic field. This is not true for the profile of Figure 5.9(b), which is in the ground state in presence of a magnetic field gradient. It is interesting to observe how the domain width Δ changes from one profile to the other. This is due to the fact that, when the $m_F = 0$ domain forms in the centre, the density is higher and it has to form two boundaries with the $m_F = +1$ domain.

The boundary width ξ is bigger than the one expected. We use the GP theory developed in Subsection 5.1.4 to simulate the spin domains with the same parameters of the profiles of Figure 5.9 and we fit them with the same program: we obtain $\xi \approx 9\,\mu$m. We recall that, at the beginning of the chapter, we computed the spin healing length $\xi_s = 5.3\,\mu$m. We believe that the difference between the ξ obtained from the real data and the one obtained from the synthetic data is due to the presence of the thermal part. In Figure 5.10 we show

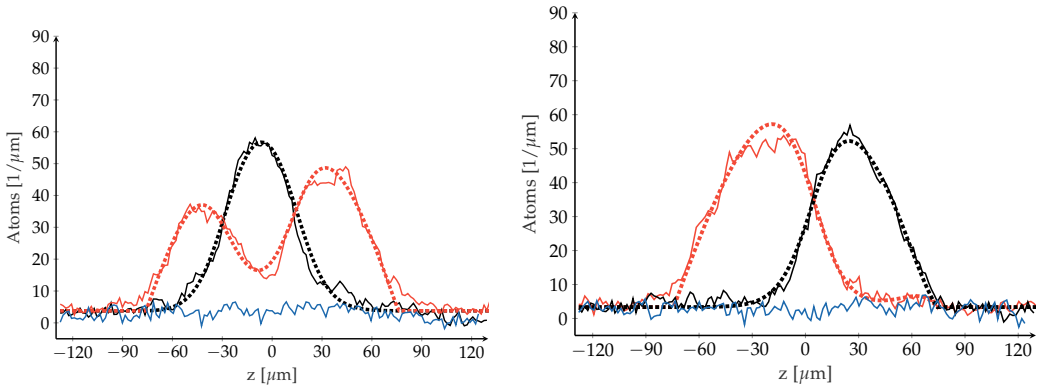

Figure 5.9.: Profiles obtained averaging 4 images each. In the figures are also sketched the result of the fit via the functions sketched in Figure 5.8. The results of the fit are listed in Table 5.1.

the profile for a $m_F = +1$ domain, obtained from the GP simulations for $N = 2 \cdot 10^4$ atoms and $\omega_z = 2\pi\, 4.6\,\text{Hz}$. In the same figure we also show the self-consistent mean-field potential for the $m_F = +1$ thermal atoms due to the presence of the condensed atoms and to the trapping potential, as it has been presented in Section 4.2. The red ellipses highlight the regions where the thermal atoms sit. It is clear that, as we increase the temperature from $T = 0$, the thermal part starts to accumulate in the centre between the two parts of the $m_F = +1$ domain and at the edges. This increases the penetration depth of the two condensates one into the other. We expect this effect to be also dependent on the longitudinal magnetisation m_z. At a given temperature and atom number, indeed, as we increase the magnetisation, we reduce the number of atoms in the $m_F = 0$ domain. As we have seen in Chapter 4, this reduces the $m_F = 0$ critical temperature for the condensation and increases the number of thermal $m_F = 0$ atoms. The penetration depth of the two domains one into the other, as a consequence, increases.

Before fitting the data, we also have to consider the effects of the free expansion in TOF. Since our anisotropic trap, along the weak axis, has a very low trapping frequency, we expect the cloud to not expand much during TOF and then to be able to measure the *in situ* density distribution. To be sure about the validity of this approximation, we prepared a cloud as the one in Figure 5.1(a) and we measured the atomic cloud size and the size of the central $m_F = 0$ domain in TOF. The results of this measurement are presented in Figure 5.11. The cloud size (in blue), the domain size (in green) and the boundary width (in red) are plotted for different TOFs. It was not possible to measure the domain size at TOFs lower than 2 ms because, at these short TOFs, the different Zeeman components are not yet separated enough to fit them separately.

As we can see from the Figure 5.11, the condensate is not expanding and the domain

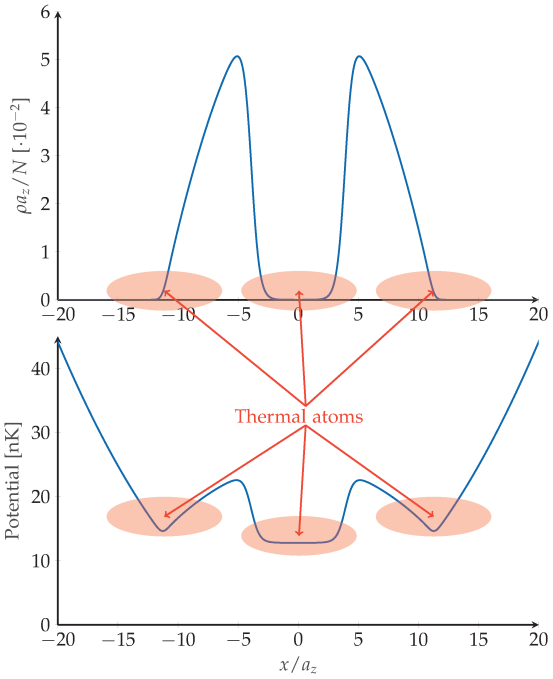

Figure 5.10.: *Top:* Profile of a $m_F = +1$ spin domain obtained from the GP simulations for $N = 2 \cdot 10^4$ atoms and $\omega_z = 2\pi\, 4.6\,\text{Hz}$ and *bottom:* Hartree-Fock potential, see Section 4.2, for the $m_F = +1$ thermal atoms due to the presence of the condensed atoms and to the trapping potential. The red ellipses indicate where the $m_F = +1$ atoms sit as we increase the temperature.

width Δ and penetration length ξ are both stable. Therefore we are confident that the spin structure we observe is close to the *in situ* one.

5.3.3. Equation of State and temperature

The determination of the temperature of a quasi-1D cloud is more difficult than in 3D. We have tried to perform temperature measurements by analysing the thermal component of our quasi-1D system in different regimes. This has proven difficult due to low signal to noise ratio of the thermal wings and its behaviour near to the Thomas-fermi radius [180] . In the literature two specific methods have been used to extract the temperature of quasi-1D, namely: thermometry by phase fluctuations and thermometry by equation of state.

We have already presented in Subsection 2.2.3 the work [63] in which the authors have found a relation between the phase fluctuations observed in TOF and the quasi-condensate temperature, $\langle(\delta n/n_0)^2\rangle \propto \sqrt{T/T_\phi}$. The measurement of the mean square density fluctuations can then be used for thermometry.

In their work [71], the authors present a variant of this thermometry scheme based on

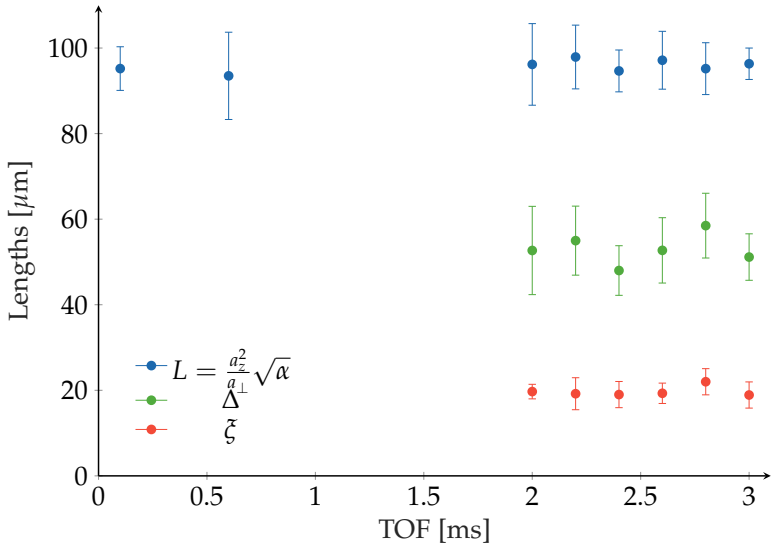

Figure 5.11.: Cloud size (blue), $m_F = 0$ domain size Δ (green) and boundary width ξ (red) as a function of TOF ofr $m_z = 0.5$. Since no clear expansion is visible, we model the profiles as the ones we expect *in situ*.

the analysis of density correlations in free expansion. The density correlation function is measured and the "spectrum of density ripples" $\left\langle \left| \rho(q) \right|^2 \right\rangle$ is obtained by Fourier transformation. This spectrum presents maxima with amplitude strongly dependent on TOF and initial temperature. Therefore, the spectrum gives a measurement of the gas temperature before free expansion. This method cannot be used in our experiment because, how we described in Section 3.5, we minimised the phase fluctuations fringes to be of the same order of the imaging fringes.
Another thermometry method is based on the comparison of the *in situ* profiles with the one derived in the LDA from a model for Equation of State (EOS) $n[\mu]$, see[3, 7, 180]. The authors of [3, 180] considered also that the system is only 1D in an approximate sense. More precisely, they took into account the fact that the chemical potential μ and the transverse trapping $\hbar\omega_\perp$ are comparable, so that the radial excited states of the trap are occupied.
To obtain an estimate of our gas temperature we decided to measure the EOS and fit the thermal part to obtain a temperature. A review of a number of theories that can be used to model the different EOS regimes can be found in the work [64].

Measuring the potential

In order to measure the EOS we need the exact shape of the potential felt by the atoms. The first step is the calibration of the trapping frequency along the trap weak axis ω_z. In Section 3.5, we have already presented this calibration. The typical value for ω_z is $\omega_z = 2\pi 4.6(2)$ Hz. To measure the deviations of the exact potential from the harmonic

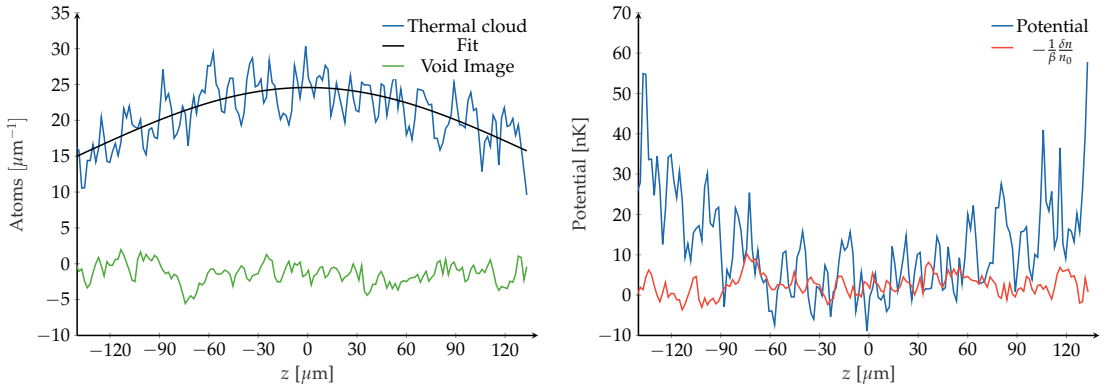

(a) Thermal cloud profile (b) Potential

Figure 5.12.: Thermal cloud profile trapped in the HDT trap and the resulting potential.

one, we can use thermal atoms whose distribution can be approximated by the Boltzmann (high T) prediction, $n \propto e^{-\beta V}$. If the Boltzmann approximation is valid, their thermal distribution allow to directly measure the potential through the following formula:

$$V(z) = -\frac{1}{\beta}\log\left(\frac{n(z) - n_{\text{bkg}}}{n_0}\right), \tag{5.44}$$

where n_{bkg} represents an average profile taken without atoms, subtracted to the potential in order to remove possible structures and the temperature of the atoms is determined fitting the thermal atoms density profile by $n(z) = \exp\big(-\beta m\omega_z^2 z^2\big)$ after coarse graining. We experimentally loaded into the anisotropic trap $N \approx 1\cdot 10^4$ thermal atoms at T ~ 80 nK.

Table 5.2.: Results of the fit of the potential shown in Figure 5.13.

A [nK]	d [μm $\cdot 10^2$]	ϕ	C [nK]
2.5(5)	2.0(2)(1)	9.6(5)	1.6(6)

Figure 5.12 shows an example of this measurement. In Figure 5.12(a) we plot the thermal distribution profile (blue), the gaussian fit (black) and an average profile of 20 images taken without atoms (green). Fitting the density with an integrated Bose distribution $g_{\frac{3}{2}}$, we obtain a fugacity $z = 3\cdot 10^{-4}$, therefore the Boltzmann approximation is valid in the considered regime. In Figure 5.12(b) we plot the potential curve obtained from (5.44) (blue) and the error on the potential given by the imaging profile (red). The error $-\frac{1}{\beta}\frac{\delta n}{n_0}$ comes from the linearisation of (5.44), taking $n(z) = n_0(z) + \delta n$. Here δn models deviations of the measured density from its actual value, for instance because of fringes in the image. From the average of 35 potential profiles, we obtained the potential which is plotted in Figure 5.13. In black we can see an harmonic fit of the potential, which does

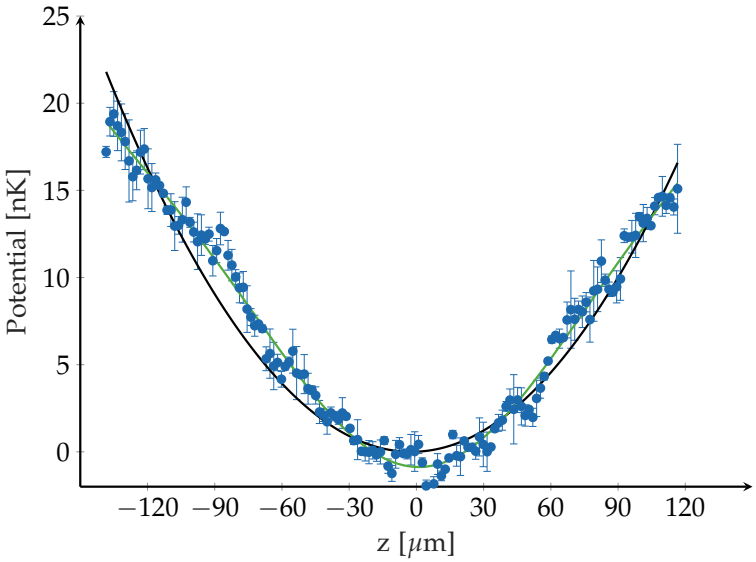

Figure 5.13.: Potential along the weak axis felt by the atoms. It has been measured loading into the dipole trap thermal atoms and measuring their density distribution. The potential profile is then obtained using (5.44).

not captures some deviations on both the potential arms. Plotting the residual of this harmonic fit we obtained Figure 5.14. It presents a clear sinusoidal shape. The green fit in Figure 5.13 is the sum of the sinus and the harmonic potential. The final fitting function can be written as

$$V(z) = \frac{1}{2}m\omega_z^2 z^2 + A \cdot \sin\left(\frac{2\pi z}{d} + \phi\right) + C \tag{5.45}$$

The fit gives the results listed in Table 5.2. Figure 5.13 has been re-centred, but we fitted also the centre of the potential, on which we have an uncertainty of 1 μm. We were not able to determine precisely the source of the sinusoidal modulation of the potential profile. It can be due to some light reflection or to some structure on the imaging we are not able to remove by subtracting the averaged background profile (without atoms). However the residuals, obtained subtracting to the potential profile the fit, have a standard deviation of ~ 0.7 nK. Recalling that the chemical potential we measure for the quasi-condensate is $\mu \sim 10$ nK, we have a $\leq 10\,\%$ systematic error on the determination of the chemical potentials along the profile.

The Equation of State

We know the exact potential shape and, in particular, its deviations from the harmonic potential at $V(z) \approx k_B T$. The following step is the determination of the EOS by using this potential. We make the LDA approximation, so that $\mu = \mu_0 - V(z)$. To associate at each point along the profile a chemical potential, we need a method to measure μ_0.

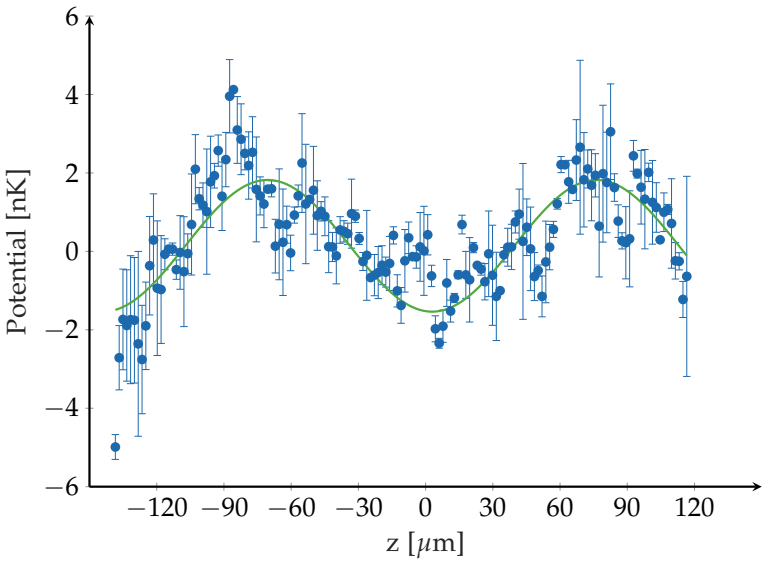

Figure 5.14.: Residual of the harmonic fit on the potential profile plotted in Figure 5.13. The sinusoidal modulation can be due to the imaging or to some light reflection inside the vacuum chamber.

Usually, the low density part is fitted to obtain the value of the chemical potential, see [189]. We decided to measure μ_0 fitting the profiles as described in Subsection 5.3.2. Plotting the cloud density as a function of the local chemical potential μ, we obtain the Equation of state (EOS)

$$n = n(\mu) \tag{5.46}$$

In Figure 5.15 we can see the EOS of a polarised cloud with all the atoms in $m_F = +1$ produced with the typical sequence described in Chapter 3.

The quasi-condensate part and the thermal part join together at $\mu = 0$. As we can see in Figure 5.16(b), we fitted the condensed part with the EOS formula given by the 1D-3D crossover theory (5.32) (black). We obtained a value for the scattering length $a = 2.6(1)\,\text{nm}$, which compares well with the known value $\bar{a} + a_s \simeq 2.55\,\text{nm}$: our 1D-3D crossover model works well in the degenerate part of the cloud. We make also the comparison in Figure 5.16(b) with the purely 1D Thomas-Fermi prediction, $n \simeq \mu/g_{1D,m}$. We obtain a value for the 1D coupling constant $g_{1D,m} = 0.86(3) \cdot [2\hbar\omega_\perp(\bar{a} + a_s)]$.
We recall the 1D-3D crossover formula for the profile density (5.33) and we recall the typical value that we find for the fitting parameter $\alpha = 2\left(\mu/\hbar\omega_\perp - 1\right) \approx 0.6$. There is a $\sim 15\%$ difference between the peak density of the 1D Thomas-Fermi model and the peak density of the 1D-3D crossover theory. We see this difference also in the two different values for the coupling constant that we find fitting the EOS with the two different models.

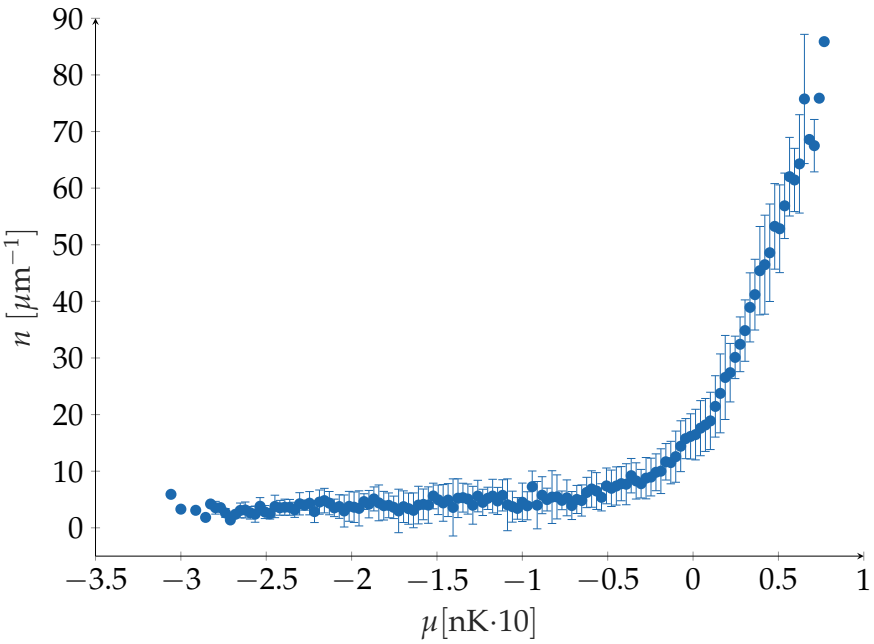

Figure 5.15.: Equation of State of a polarised cloud with all the atoms in $m_F = +1$ at $T \simeq 44\,\mathrm{nK}$, see Figure 5.16(a). The cloud is produced with the typical procedure described in Chapter 3.

Determining the temperature

The part of the EOS for negative chemical potentials can be used to determine the cloud temperature, [3, 7]. We are using the wings of the measured potential $V(z)$ to determine the temperature of the degenerate cloud. Different models can be used to capture the EOS behaviour in different regimes, [64]. If we suppose our system to be purely 1D, we can use two models to fit the EOS: the ideal 1D model, for which the EOS is given by

$$n_{1D,\mathrm{ideal}} = \frac{1}{\lambda_{\mathrm{th}}} g_{\frac{1}{2}}\left(\mathrm{e}^{\beta\mu}\right), \tag{5.47}$$

where the Bose function $g_{\frac{1}{2}}(z)$ diverges at $z = 1$, and 1D Hartree-Fock model, for which the EOS is given by

$$n_{1D,\mathrm{HF}} = \frac{1}{\lambda_{\mathrm{th}}} g_{\frac{1}{2}}\left(\mathrm{e}^{\beta\mu - 2g_{1D}n_{1D,\mathrm{HF}}}\right). \tag{5.48}$$

In Figure 5.16(a), we reported the fit used to study the thermal part and obtain a temperature measurement. The temperature we obtain from the 1D ideal model and from the Hartree-Fock models are, respectively, $T = 140(3)\,\mathrm{nK}$ and $T = 152(2)\,\mathrm{nK}$. This temperature T is higher than the radial confinement $T \gg \hbar\omega_\perp \approx 20\,\mathrm{nK}$. Therefore, our initial 1D hypothesis is not valid and we need to take into account the occupation of the transverse radial excited states, [3, 7].

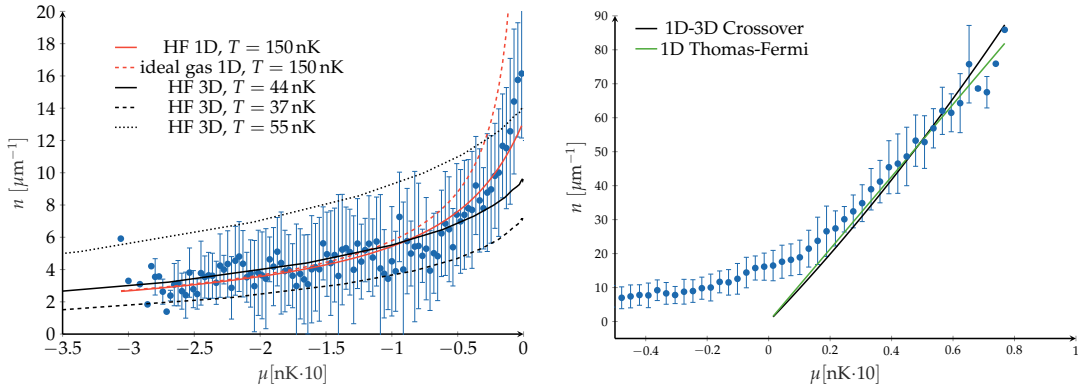

(a) EOS Thermal Part (b) EOS Quasi-condensate part

Figure 5.16.: Equation of State of a polarised cloud with all the atoms in $m_F = +1$ at $T \simeq 44\,\mathrm{nK}$. In (a) the thermal part is shown, together with the results of the different models used to obtain the cloud temperature. In (b) the condensed part is shown with two fits corresponding to the 1D-3D crossover and the purely 1D Thomas-Fermi theories.

Hartree-Fock for the 1D gas in the crossover regime

We want here to discuss the Hartree-Fock (HF) model, presented in [180], to fit the EOS of a non-degenerate, quasi-1D bosonic gas. We have very briefly introduced the HF model in Chapter 2, Subsection 2.1.4. In the HF approximation, we consider the motion of atoms in a self-consistent potential given by the sum of the trap potential V and of a mean-field potential

$$V_{\mathrm{eff}} = V(\mathbf{r}) + 2gn(\mathbf{r}), \tag{5.49}$$

where $g = 4\pi\hbar^2 a/m$ is the coupling constant and the factor 2 takes into account both direct and exchange scattering processes [140]. In our case, the potential $V(\mathbf{r})$ is harmonic with $\omega_z \ll \omega_\perp$. Since $k_B T \sim \hbar\omega_\perp$, we can neither use the semi-classical approximation along the three axis, nor consider the thermal gas frozen in the transverse ground state. An appropriate way to implement the HF approximation is to treat the axial direction in the semiclassical approximation and to take into account a discrete set of excited modes in the transverse direction in a self consistent way [3, 180].
We start modelling the system with the waveguide model, as we have done before in describing the $T = 0$ theory of the quasi-1D Bose gas. In particular, we consider a system of bosons with uniform axial density in the potential $V_\perp(\rho) = \frac{1}{2}m\omega_\perp^2\rho^2$, with $\rho = (x, y)$ the radial coordinate vector.
Because of the cylindrical symmetry and of the separability of the potential, the average density depends only on ρ. We introduce the transverse eigenstates as the solutions of

the HF equations,

$$\left[-\frac{\hbar^2}{2m}\Delta_\perp + V_\perp(\rho) + 2gn(\rho) \right]\phi_\nu = E_\nu \phi_\phi. \tag{5.50}$$

The wave functions ϕ_ν are normalised as $\int d^2\,\rho|\phi_\nu(\rho)|^2 = 1$. The eigenstates of the full HF $(\mathbf{p}^2/2m + V_\perp)$ are then products of a plane wave along z and of a transverse eigenstate, with energy $E_\nu + \frac{\hbar^2 k_z^2}{2m}$. The 3D density of a gas at temperature T and chemical potential μ is then given by

$$n(\rho) = \frac{1}{\lambda_{\rm th}} \sum_\nu |\phi_\nu(\rho)|^2\, g_{1/2}\Big[\mathrm{e}^{\beta(\mu - E_\nu)} \Big]. \tag{5.51}$$

To obtain a measurement of the temperature from the EOS using (5.51), we solve the Hartree-Fock problem numerically in an iterative way. We calculate the eigenstates of (5.50) numerically, starting with $n = 0$ and we use (5.51) to compute the density and iterate the procedure. We use a convergence criterion

$$\int d^2\rho \Big[n_i(\rho) - n_{i-1}(\rho) \Big]^2 < \epsilon \left[\int d^2\rho\, n_i(\rho) \right]^2, \tag{5.52}$$

to terminate the iteration, where i denote the iteration step and $\epsilon = 10^{-4}$. In Figure 5.16(a) we show three curves obtained with this model. The curve at $T = 44\,\mathrm{nK}$ reproduce well our experimental data. The two curves at $T = 37\,\mathrm{nK}$ and $55\,\mathrm{nK}$ are, respectively, too low or too high with respect to the data. Therefore, our atomic cloud has a temperature around $T = 44\,\mathrm{nK}$ with a conservative error bar of $\pm 10\,\mathrm{nK}$. This result is in marked contrast with the pure 1D prediction of $T = 150\,\mathrm{nK}$. The reason for this difference lies in the number of available modes, which is much smaller in 1D than when accounting for the transverse excited modes. To obtain a certain distribution of thermal atoms at a given chemical potential μ in the 1D model, it is then necessary to artificially increase T quite a lot to compensate for the "missing" modes.

5.4. 1D Transition

In order to observe the phase transition predicted in Section **??** we prepare the 1D condensate at different magnetic fields keeping the longitudinal magnetisation m_z constant. We have determined, for each magnetic field value, the angle which minimise $\tilde{\lambda}$ along the trap weak axis, as shown in Figure 5.7. A not-compensated gradient, indeed, not only spoils the spin domain structure of the ground state at that value of the magnetic field, but also shifts the critical magnetic field value for the transition.
To understand this effect we can make the comparison between the cloud in presence and in absence of the magnetic gradient. Figure 5.18 shows the results of two GP simulations for a system with $N = 1 \cdot 10^4$, $m_z = 0.5$ and a quadratic Zeeman energy $q = 0.1\,\hbar\omega_z$. In Figure 5.18(a) there is no gradient, in Figure 5.18(b), instead, there is a gradient $\lambda = g_F \mu_B b' a_z/\hbar\omega_z = 0.5$. For each gradient value are plotted, in this order, the two profiles for the $m_F = +1$ (red) and $m_F = -1$ (blue) profiles, the longitudinal magnetisation profile

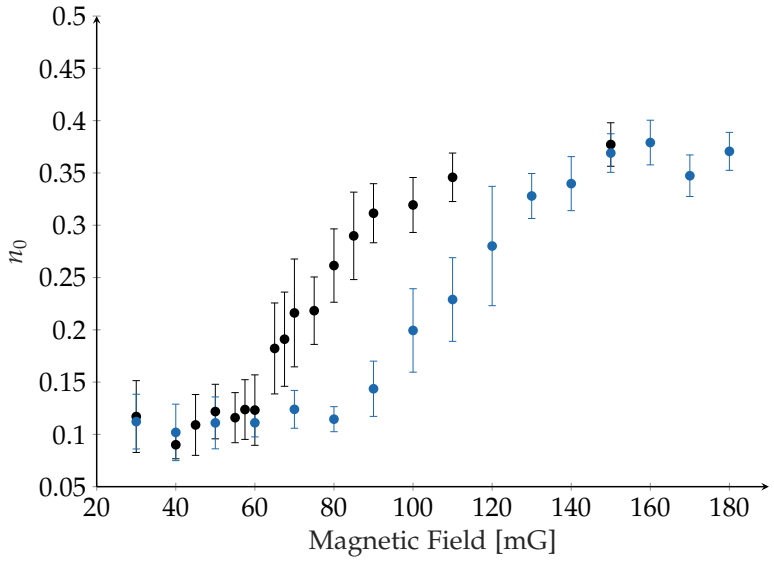

Figure 5.17.: Magnetic transition in 1D for $m_z = 0.55(5)$. The relative number of atoms in the $m_F = 0$ Zeeman state $n_0 = N_0/N_{\text{tot}}$ is plotted as a function of the modulus of the magnetic field. In black are sketched the data taken with the compensated magnetic field gradient. In blue are plotted the data taken with a gradient of $|\nabla \mathbf{B}| = 12\,\text{mG/cm}$ along the trap weak axis.

and the ρ_z^2. We focus our attention on these last two profiles. The two systems are in the miscible phase and their interaction energy, at each point along the profile, is given by the energy of **Phase I**, which is $\propto \rho_z^2$. It is clear from Figure 5.18 that the interaction energy of the gradient configuration is bigger than the one without gradient.
As we have already explained in Section 2.3, the transition arises from the competition between two terms in the spin energy functional (2.95): the quadratic Zeeman energy and the interaction energy. Therefore, a higher interaction energy shifts the critical magnetic field to higher values. This effect can be seen experimentally in Figure 5.17, where is shown a transition at $m_z = 0.55(5)$. The black dots corresponds to the data point taken when the gradient is compensated, while the blue dots correspond to the data taken when a gradient of $|\nabla \mathbf{B}| = 12\,\text{mG/cm}$ is applied along the trap weak axis.

We show in Figure 5.19 a measurement of the transition at $m_z = 0.45(5)$. The relative populations for the atoms in $m_F = 0$ (black), $m_F = +1$ (red) and $m_F = -1$ (blue) are plotted as a function of the magnetic field. The relative number of atoms $n_0 = N_0/N_{\text{tot}}$ is fitted with a function of the form

$$n_0 = \begin{cases} A_0 & B < B_c \\ A_0 + A_1 \frac{B-B_c}{B-B_c+\Delta B} & B \geq B_c \end{cases} \tag{5.53}$$

as done in [76] to obtain a value for the critical magnetic field $B_c = 57(3)\,\text{mG}$. We can compare the critical field values obtained experimentally with the ones expected from the

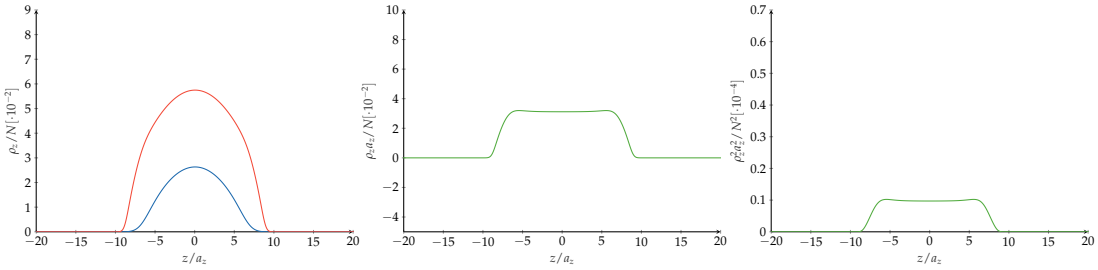

(a) No gradient

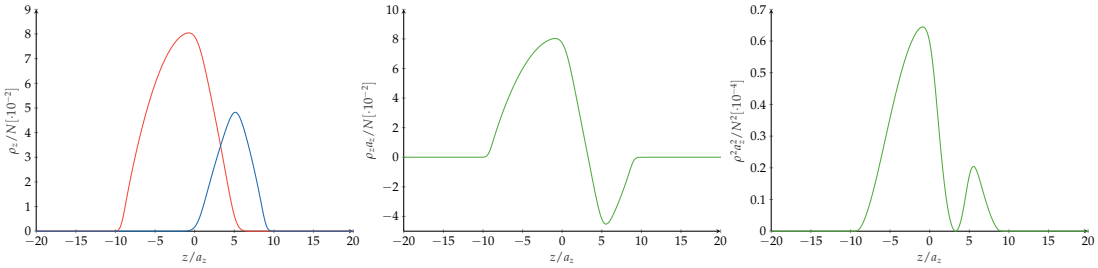

(b) $\lambda = 0.5$

Figure 5.18.: Density, magnetisation and ρ_z^2 profiles for a system with $N = 1 \cdot 10^4$, $m_z = 0.5$ and a quadratic Zeeman energy $q = 0.1\,\hbar\omega_z$. In (a) there is no gradient; in (b) there is a gradient $\lambda = g_F \mu_B b' a_z / \hbar\omega_z = 0.5$.

theory. Using the LDA theory, eq. (5.27) gives a critical magnetic field $B_{c,LDA} = 31\,\text{mG}$. Using the GP theory developed in this Subsection 5.1.4 to simulate the transition for a system of $N = 1.5 \cdot 10^4$ atoms and $m_z = 0.55(5)$ in a 1D harmonic trap with $\omega_z = 4.6\,\text{Hz}$, we obtain a critical field $B_{c,GP} = 56.8\,\text{mG}$. The critical field obtained from the LDA theory is lower than the measured one; this is expected since in the LDA approximation the energetic cost of producing the two domain boundaries of the $m_F = 0$ domain are not taken into account. The GP model, instead, gives a value which is in good agreement with the measured one.

In Figure 5.20 we plot averaged profiles of the measurement shown in Figure 5.19. At low magnetic field ($B < B_c$), we have only the $m_F = +1$ and $m_F = -1$ components condensed. Since they are miscible, there is no phase separation. At higher magnetic fields, the $m_F = 0$ domain appears and the $m_F = +1$ starts to divide into two parts. In Figure 5.20(c) we don't observe the structure expected from the LDA and GP theory. This can be due to the presence of the thermal part, which can mask the double structure of the $m_F = -1$ component, or can be due to the interaction between the condensed and thermal part as explained in the work [153].

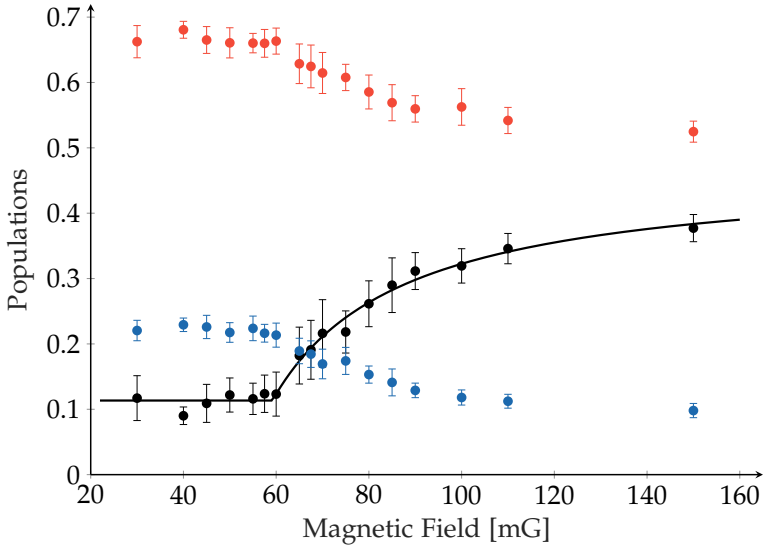

Figure 5.19.: Transition measurement at $m_z = 0.45(5)$. The relative populations of the atoms in the Zeeman states, $m_F = +1$ (red), $m_F = -1$ (blue) and $m_F = 0$ (black) are plotted as a function of the modulus of the magnetic field. The solid line is the results of the fit of the $n_0 = N_0/N_{\text{tot}}$ relative population with the function (5.53), which gives a critical magnetic field $B_c = 57(3)\,\text{mG}$.

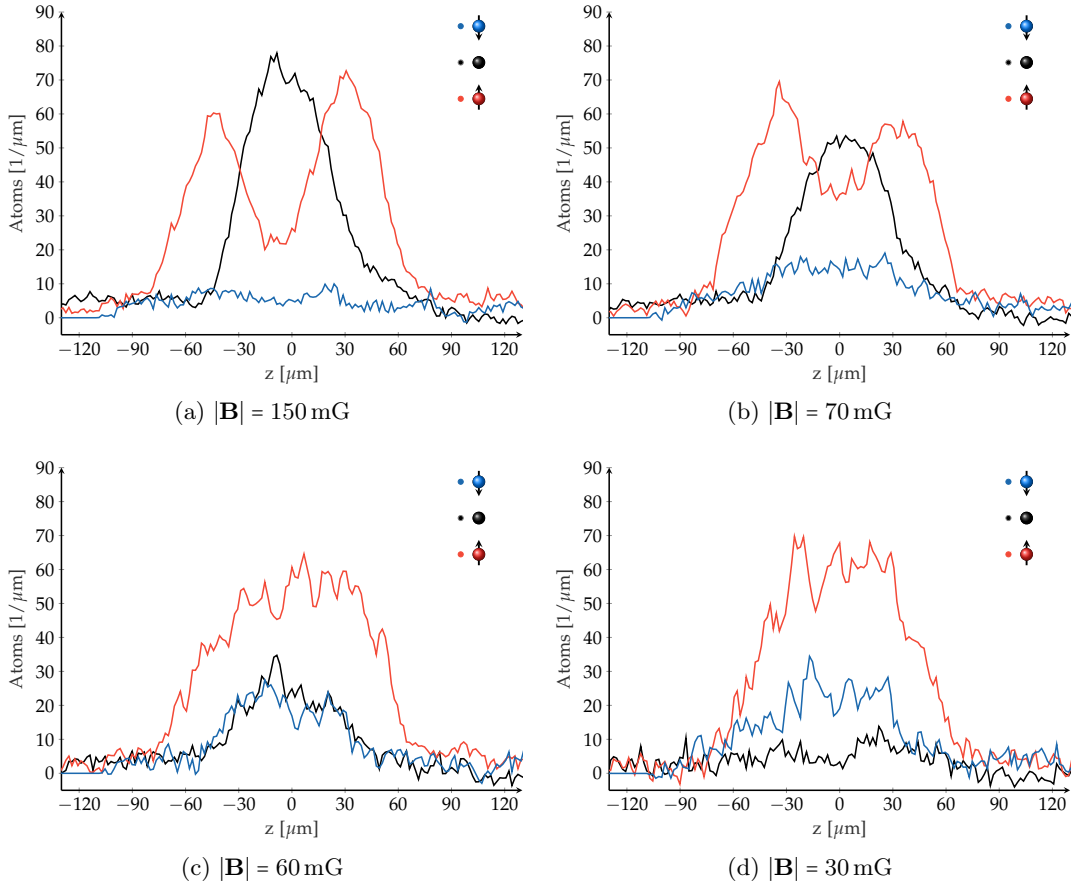

(a) $|\mathbf{B}| = 150\,\mathrm{mG}$ (b) $|\mathbf{B}| = 70\,\mathrm{mG}$

(c) $|\mathbf{B}| = 60\,\mathrm{mG}$ (d) $|\mathbf{B}| = 30\,\mathrm{mG}$

Figure 5.20.: Averaged integrated profiles with $m_z = 0.45(5)$. The profiles at $|\mathbf{B}| = 60\,\mathrm{mG}$ and $|\mathbf{B}| = 30\,\mathrm{mG}$ are averaged over 5 images. The profiles at $|\mathbf{B}| = 150\,\mathrm{mG}$ and $|\mathbf{B}| = 70\,\mathrm{mG}$ over 10 images. The profiles come from the measurement shown in Figure 5.19.

6. Binary mixtures

Chapter 5 was devoted to the characterisation of the spin-1 ^{23}Na gas in an anisotropic harmonic trap. The arrangement of the three Zeeman components along the trap as well as their presence as a function of the quadratic Zeeman energy in a uniform magnetic field were characterised.
In this chapter we want to consider the immiscible phase in which essentially only the $m_F = 0$ and $m_F = +1$ domains are present in the system. More precisely, a small but detectable population of $m_F = -1$ atoms is present, but they remain purely thermal in the experiments presented in this chapter. To be sure that this is the case, we set the magnetic field at $|\mathbf{B_0}| = 600\,\mathrm{mG}$, corresponding to a quadratic Zeeman shift $q = \hbar \cdot 99.7\,\mathrm{Hz} = 21.7 \cdot \hbar\omega_z$. This value is far above both the critical values for all the explored magnetisations, as explained in Section 5.1. Therefore, our system can be described as a binary mixture of quasi-condensates in $m_F = +1$ and $m_F = 0$.

The first binary mixture was formed by two different hyperfine spin states of ^{87}Rb atoms, [122]. The two-component condensate was produced by cooling one component via sympathetic cooling through interactions with the second one, cooled via evaporation. Many others binary mixtures were produced using Bose gases, mixing two different hyperfine states of ^{87}Rb, as in [37, 107], or of ^{23}Na, as in [117]; mixing different isotopes of the same atomic species, as in [135], where ^{85}Rb and ^{87}Rb were used together and mixing different atomic species, as K and Rb in [45] and Ca and Rb in [114]. Binary mixtures have been studied also using Fermi gases, as in the recent work [183], where mixtures of ^{6}Li atoms have been used to explore the possibility of itinerant ferromagnetism, or in [157], and using Bose-Fermi superfluid mixtures, as in [46] and in [155].
Two components systems have already been studied extensively both theoretically and experimentally. The relative phase coherence properties of the two components have been investigated, [164], as their dynamics [116, 107, 148, 23, 165]. Also the boundaries between different components have been studied theoretically, [6, 10]. Furthermore, binary systems can be used to measure external forces, [12]. The sensibility to external forces typical of BEC, [61], can be enhanced by the interspecies interactions present in binary systems, making these latter good systems to quantitatively measure these external forces.

Focusing on the mixtures composed by two weakly interacting BEC, their ground state can be in a miscible, or immiscible phase, [135], depending on the trap and on the intra et interspecies interactions, as introduced in Section 2.3. In their two works [149] and [148], the authors described the ground state and the collective excitations of a Bose-Bose binary system.

The spin-dipole (SD) polarisability of a spin mixture is the response of the system to a displacement of the trapping potentials of the two components in opposite directions. This quantity can be used to characterise the system response to an external field. In the recent works [13] and [44], the authors measured the spin-dipole (SD) polarisability of a miscible $m_F = \pm 1$ mixture of ^{23}Na atoms as well as the difference between the response of the thermal and of the condensed parts. In this chapter we present a detailed experimental characterisation of the SD polarisability in the opposite case of immiscible components, $m_F = 0, +1$. Following the proposal in [12], the high measured SD polarisability could be used to implement a very accurate sensor to magnetic field gradients or more generally, magnetic forces. As discussed in Section 5.3, we have already used this configuration to reduce the effects of uncontrolled magnetic fields on the spin domains arrangement.

6.1. Spin-dipole polarisability

We consider a spin-1 Bose gas trapped in a harmonic anisotropic trap. The quasi-condensate is in the immiscible phase and only the $m_F = 0$ and $m_F = +1$ components are present. The atoms in the $m_F = -1$ state are purely thermal and we neglect them in our modelisation of the system. The two components feel an harmonic potential $V(\rho, z) = \frac{1}{2}m\left(\omega_\perp^2\rho^2 + \omega_z^2 z^2\right)$. We want to describe what happens to the system when a magnetic field gradient is applied. Recalling Section 5.3, we know that a magnetic field gradient changes the potential $V(\rho, z)$ by shifting its centre for the $m_F = +1$ and $m_F = -1$ components in opposite directions. Moreover, if the magnetic field gradient is small enough, we can consider its effect only along the weak trap axis, see Section 5.3. In the following, we neglect the radial direction and describe the system as purely 1D for simplicity.
The potential felt by the atoms in the Zeeman state m_F is then equal to

$$V_{m_F}(z) = \frac{1}{2}m\omega_z^2 z^2 - m_F\tilde{\lambda}z \approx \frac{1}{2}m\omega_z^2(z - z_0)^2 - \frac{1}{2}m\omega_z^2 z_0^2, \tag{6.1}$$

where $\tilde{\lambda} = \frac{\mu_B}{2}b'$, b' is the applied magnetic field gradient and

$$z_0 = \frac{m_F\tilde{\lambda}}{m\omega_z^2}. \tag{6.2}$$

Since we consider only the $m_F = 0$ and $m_F = +1$ components, the potentials felt by the two components are shifted by z_0 one with respect to the other.
As introduced above, the SD polarisability of a binary mixture is the ability of the system

to reorganise when the potentials felt by the two components are displaced in opposite directions. Following the definition of SD polarisability given in the recent work [13][1], we define it as

$$P_{SD} = \frac{SD}{z_0} = \frac{1}{z_0}\left(\bar{z}_{+1} - \bar{z}_0\right) \tag{6.3}$$

where

$$\bar{z}_\alpha = \frac{1}{N_\alpha}\int dz\, z\, n_\alpha(z) \tag{6.4}$$

To measure the SD polarisability for the $m_F = 0, +1$ configuration, we have to apply a magnetic field gradient along the weak trap axis and measure the position of the centres of mass (COM) of the two components. In the following we present some preliminary results on these measurements.

6.1.1. Polarised cloud response: z_0

If we consider a polarised gas in $m_F = +1$ and we apply a magnetic field gradient, only its centre of mass will move. Therefore, we expect $SD = z_0$, and $P_{SD} = 1$. Experimentally we can change $\tilde{\lambda}$ by changing the current fed to a pair of coils in the anti-Helmholtz configuration placed along the HDT axis, as explained is Section 5.3. In the following we measure z_0 directly. We prepare a polarised condensate, all atoms in $m_F = +1$, in a uniform magnetic field pointing along the direction that minimises uncontrolled magnetic field gradients, as described in Section 5.3. During the entire sequence, we apply a constant magnetic field gradient using the coils along the HDT ($\mathbf{z}$) direction and we record the final cloud position. We repeat this measurement for several values of the magnetic field gradient.
Figure 6.1 shows the COM of the $m_F = +1$ cloud divided by the cloud size as a function of the applied magnetic field gradient. We found a response $\mathrm{d}z_0/\mathrm{d}I = -31.3(7)\,\mu\mathrm{m\,A^{-1}}$.

6.1.2. Spin-dipole polarisability vs magnetisation

We show now the measurements of the SD polarisability for the $m_F = 0, +1$ spin domain configuration for different magnetisations m_z. All the experimental data we present are taken at $B = 600\,\mathrm{mG}$. For a given value of the magnetisation m_z, we repeat the exact same experimental sequence as in the polarised case described above, the only difference being the initial system magnetisation.
In Figure 6.3 we show three profiles obtained at a magnetisation $m_z = 0.47$ for different values of the magnetic field gradient. Figure 6.3(c) shows the ground state of the $m_F = 0, +1$ configuration in a uniform magnetic field, with the central $m_F = 0$ domain and two $m_F = +1$ domains at the edges. The $m_F = +1$ distribution is not perfectly symmetric with respect to the centre of the overall profile, which signal the fact that the uncontrolled magnetic field gradients were not completely negligible during the data

[1] There is a difference of a factor 2 between our definition and the definition of SD polarisability given in [13]. Indeed, in our system, only one component ($m_F = +1$) is affected by the magnetic field gradient.

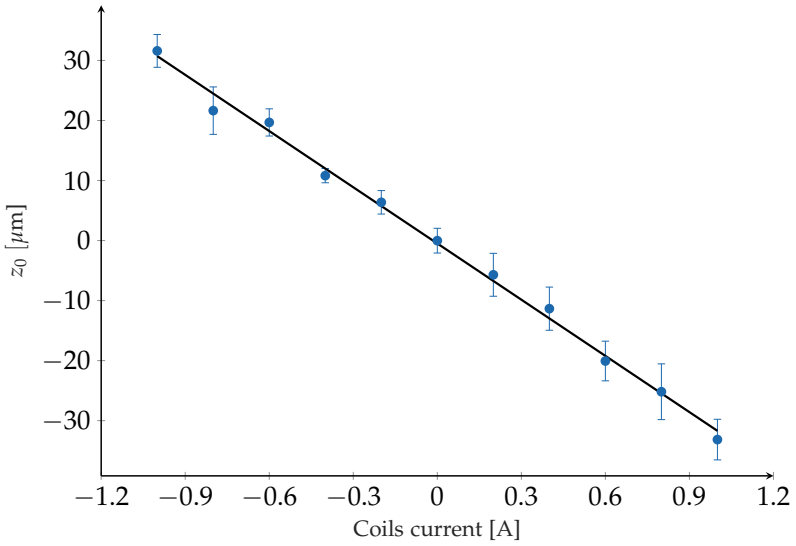

Figure 6.1.: Response of a polarised cloud with all the atoms in the state $m_F = +1$ at a magnetic field gradient generated by a pair of coils placed on the HDT axis. From the linear fit we found $z_0 = -31.3(7)\,\mu\mathrm{m\,A^{-1}}$.

taking. Figure 6.3(a) and Figure 6.3(b) show the two opposite situations in which the gradient changes the spin domain arrangement. The $m_F = +1$ component feels the potential shift due to the magnetic field gradient and follows it. The $m_F = 0$ domain does not feel any direct force due to the gradient, however the interactions between the two components push the two domains further away.

For each value of the applied magnetic field we use the fitting method presented in Section 5.3 to obtain the two domain's centre of mass and cloud size, then we record the distance between the COMs of the $m_F = 0$ and $m_F = +1$ components: the SD.
Figure 6.3 shows the results of these measurements at $m_z = 0.37, 0.47, 0.68$ and 0.79. The error bars represent the standard deviations obtained from 4 shots per each magnetic field gradient. It is already visible from Figure 6.3 that the steepness of the curves increases with the magnetisation.
Figure 6.4 shows the resulting SD polarisability, obtained by dividing SD by the single atom response z_0.

We want now to measure the response of the domains to the applied magnetic field gradient at $z_0 = 0$. From Figure 6.4, it is clear that the response is not linear for all z_0 values. In the neighbourhood of $z_0 = 0$, where the response is approximately linear, we define it as R_{SD}:

$$R_{SD} = \left.\frac{\mathrm{d}SD}{\mathrm{d}z_0}\right|_{z_0=0}. \tag{6.5}$$

This quantity gives the $m_F = 0, +1$ domains response in unit of the polarised $m_F = +1$

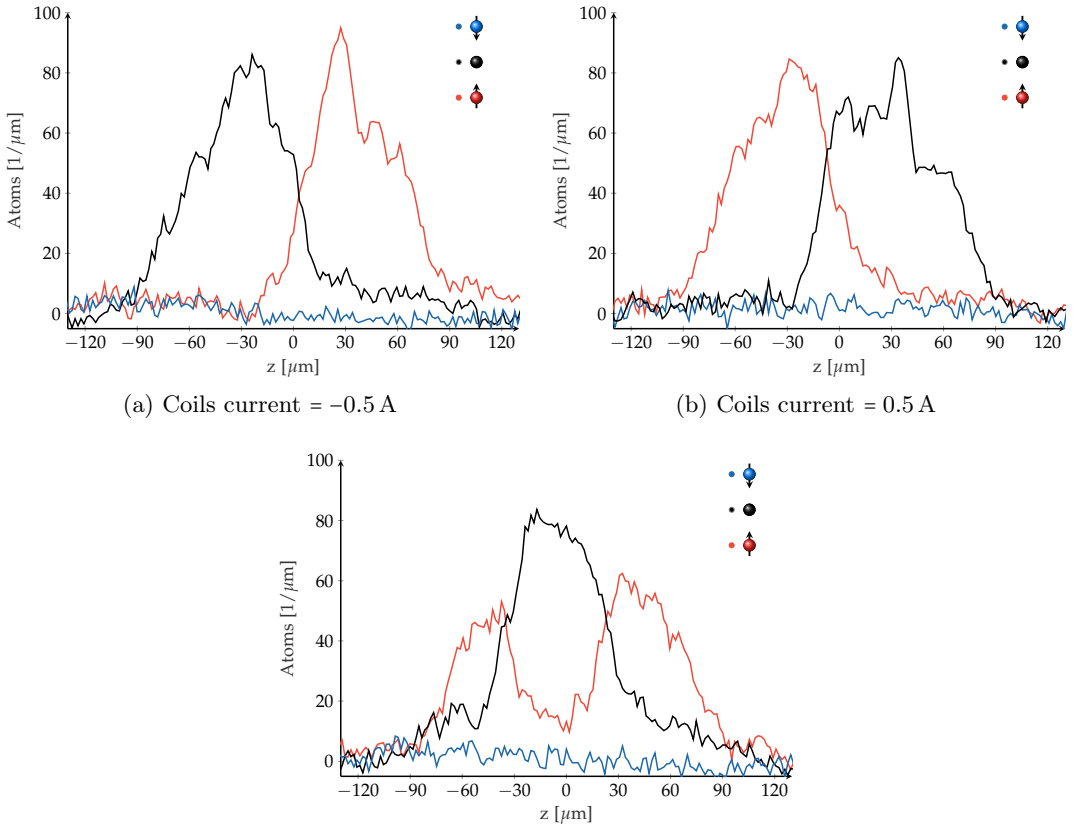

(a) Coils current = −0.5 A

(b) Coils current = 0.5 A

(c) Coils current = 0 A

Figure 6.2.: Profiles of the $m_F = 0, +1$ mixture for different gradients applied along the HDT axis. The magnetic field gradient is reported in Amperes, corresponding to the current fed to the coils pair to produce a given $|\nabla \mathbf{B}|$. We have characterised the gradient produced by the coils: $|\nabla \mathbf{B}| = 21.4(5)\,\mathrm{mG\,cm^{-1}\,A^{-1}}$.

cloud response.
The R_{SD} can be obtained from the data shown Figure 6.3 by fitting the experimental curves with the empirical following function

$$SD(I) = a + b \cdot (I - I_c) + d \cdot \tanh\left(\frac{I - I_c}{d}\right), \tag{6.6}$$

where I stands for the current fed to the coils. The black curves in Figure 6.3 are the results of the fits. Then, to obtain the response of the $m_F = 0, +1$ spin domain configuration in the curve centre, we compute the derivative of the fitted curve at $I = I_c$:

$$\left.\frac{\mathrm{d}SD(I)}{\mathrm{d}I}\right|_{I=I_c} = b + \frac{d}{c}. \tag{6.7}$$

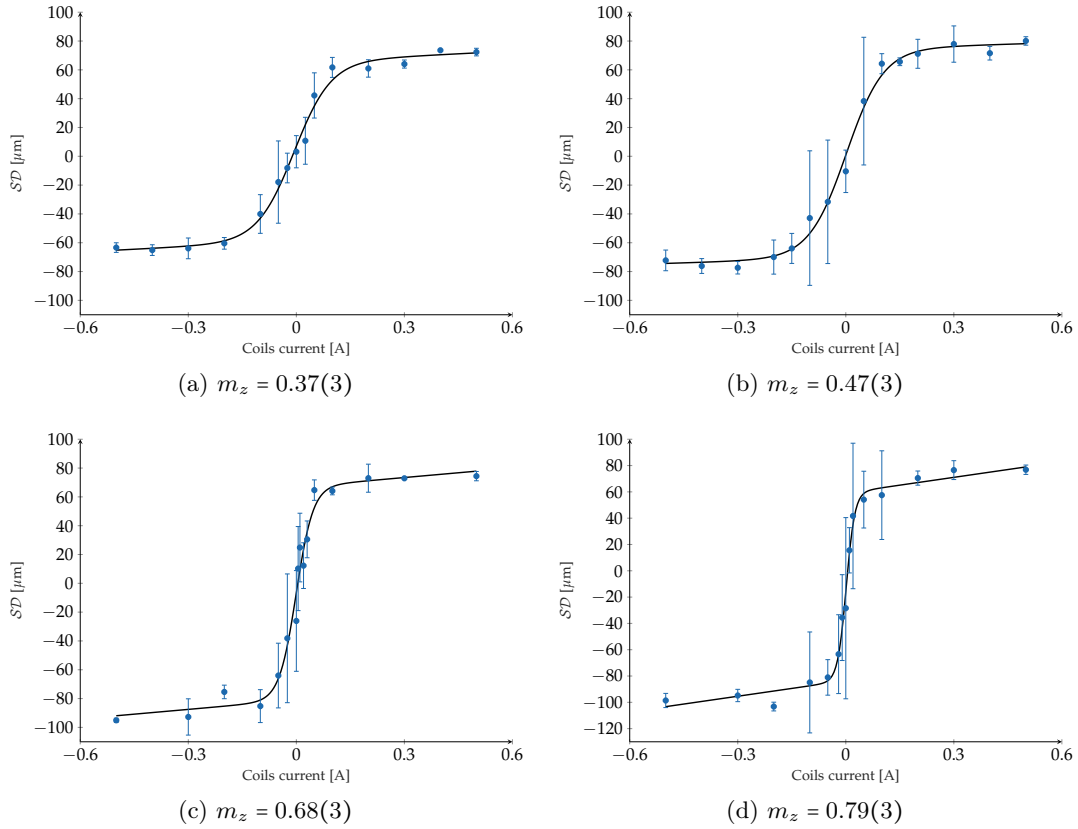

(a) $m_z = 0.37(3)$ (b) $m_z = 0.47(3)$

(c) $m_z = 0.68(3)$ (d) $m_z = 0.79(3)$

Figure 6.3.: Response of the $m_F = 0, +1$ spin domains configuration to an external magnetic field gradient applied along the weak trap axis. The plots correspond to different longitudinal magnetisation m_z and show the difference of COM, $SD = (\bar{z}_{+1} - \bar{z}_0)$ as a function of the current fed to the coils to produce the gradient. In black are sketched the results of the fit of the curves with the an hyperbolic function, (6.6).

Figure 6.5 shows the $m_F = 0, +1$ response R_{SD} obtained by dividing $\left.\frac{\mathrm{d}SD(I)}{\mathrm{d}I}\right|_{I=I_c}$ by $\mathrm{d}z_0(I)/\mathrm{d}I$. The y error bars come from the fit while the x error bars represent the standard deviation of the longitudinal magnetisation of the shots considered for that point.

There are no points at low magnetisation, $m_z < 0.2$, because at these low m_z values the $m_F = +1$ component is almost completely thermal. This is true at high magnetisation for $m_F = 0$.

We expect the curve to increase at low magnetisation as it does at high magnetisations. This is due to the fact that one of the two domains, at high and low m_z, becomes smaller than the other one, so that it becomes more and more easy to push it toward the cloud

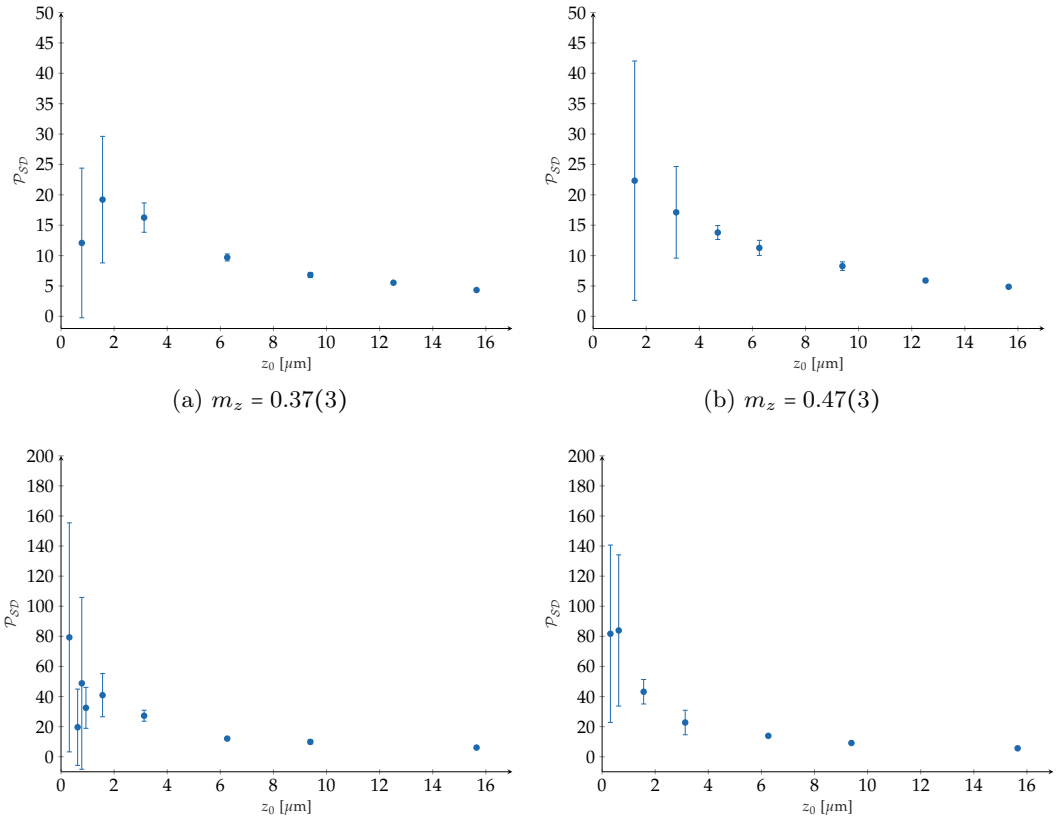

(a) $m_z = 0.37(3)$ (b) $m_z = 0.47(3)$

(c) $m_z = 0.68(3)$ (d) $m_z = 0.79(3)$

Figure 6.4.: Spin-dipole polarisability measured for different magnetisations.

edge. We do not observe this increase at low magnetisation. We are currently trying to measure the cloud temperature as a function of m_z to see if this effect is temperature-related.

We defined the response R_{SD} to be in unit of the polarised cloud response. Figure 6.5 shows that the measured response is much larger with respect to the single atom's one. This point is currently under investigation, in particular we are implementing T=0, 1D and a 1D-3D crossover models, based on the spin-1 GP equations (5.1) and (5.2) to make a first comparison with the experimental data, [156, 109].

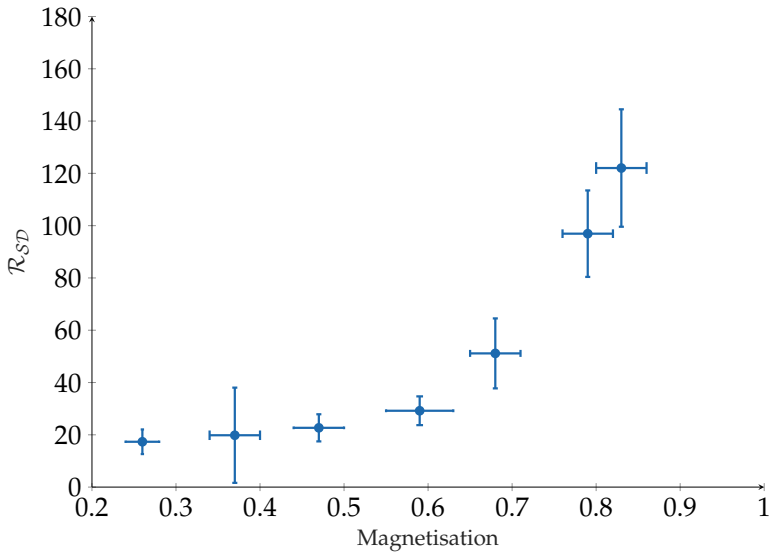

Figure 6.5.: Spin-dipole polarisability of the $m_F = 0, +1$ spin domain configuration as a function of magnetisation.

7. Conclusions and perspectives

In this manuscript we have studied the thermodynamic of a system of spin-1 ^{23}Na atoms in a 3D trap, where the SMA approximation is valid, and the magnetic ordering in a 1D trap, where the SMA is broken along the weak trap axis.

In Chapter 2 and Chapter 3 we presented the basics theoretical notions needed to understand the thesis work and we described the experimental apparatus, the techniques used to manipulate the spin internal degrees of freedom of the atoms and the analysis of the absorption images.
In particular, in Chapter 3 we described the characterisation of the atoms' transfer from the 3D to the 1D trap. In the Appendix A we studied the transfer supposing it adiabatic and the traps to be box-like. We have found that, starting from a 3D condensate in a cross dipole trap with trapping potential depth $V_{\mathrm{td}} = 1.6\,\mu$K, we would obtain a 1D condensate at a temperature $T \approx 20\,$nK.

In Chapter 4 we reported the experimental observations of stepwise condensation of our Bose gas in a 3D trap, where the SMA approximation is valid. We presented the methods used to obtain the temperature of the clouds, through a simultaneous fit of the three thermal components masking the condensed parts, and the critical temperatures for the condensation, using the peak density as a probe. The major result of this study is the representation of the peak density varying the longitudinal magnetisation m_z and the temperature T. In particular, we explored 3 different regimes corresponding to a quadratic Zeeman shift q: $q \gg U_s$ (U_s spin interaction energy), $q > U_s$ and $q < U_s$. For $q \gg U_s$ we observed the $m_F = 0$ or $m_F = +1$ component to condense first, for low and high magnetisations, respectively. Lowering further the system temperature, the $m_F = +1$ or $m_F = 0$ component condenses, respectively. The $m_F = -1$ component does not condense, in accordance with the ideal gas theory. In the intermediate case the $m_F = +1$ component is always condensing first, except for m_z close to zero, where the $m_F = 0$ component is the only one to condense. For $q < U_s$ the results are completely different. The system is indeed in the antiferromagnetic phase, for this low value of the Zeeman quadratic shift, and the production of $m_F = 0$ atoms is not energetically favourable in the system. As a result, the

$m_F = +1$ is still the component which condenses first, but, depending on m_z, we have 2 or 1 more critical temperatures. The $m_F = 0$ component condenses only at low m_z, while the $m_z = -1$ component condenses at all m_z, with a critical temperature similar to the $m_F = 0$ one for the intermediate q case. This is the most striking difference between the experimental data and the ideal model system. For the latter, indeed, the $m_F = -1$ should never condense. In order to predict the condensation of the $m_F = -1$ component, we used an Hartree-Fock model. The model has 3 assumptions: i) spin independent interactions are negligible, since $g_s \ll \bar{g}$; ii) the condensate is in the Thomas-fermi regime and iii) we use the semiclassical approximation to obtain the condensed and thermal fractions. The model is in good agreement with the experimental data. The remaining $\sim 10\,\%$ difference that we observe for all the data point could be explained by effects such as finite atom number and trap anharmonicities.

Chapter 5 is devoted to the experimental characterisation of a spin-1 Bose gas in a 1D harmonic trap. For this system the SMA approximation breaks along the weak trap axis. At first, we discussed the theory of a spin-1 Bose gas in a box potential: we expect a phase transition from an antiferromagnetic to a transverse magnetised phase which correspond to a transition from a miscible to an immiscible phase, respectively. This is due to the different behaviour of the $m_F = \pm 1$ mixture (antiferromagnetic and miscible phase) with respect to the $m_F = 0, \pm 1$ one (now an immiscible phase). A second phase transition is expected at high q, when the $m_F = -1$ components disappears from the system.
Using the LDA approximation, we extended the uniform results to the harmonic trap case. The ground state of the spin-1 Bose gas in an harmonic 1D trap in a uniform magnetic field depends on the magnetic phase: in the antiferromagnetic phase we have two miscible spin domains, corresponding to the two components $m_F = \pm 1$. In the transverse magnetised phase we have a central spin domain ($m_F = 0$) and the $m_F = \pm 1$ components form symmetric spin domains at the two edges. Thanks to the very low trap frequency along the trap weak axis, we were able to experimentally observe after time of flight the *in situ* profile of these two phases. We experimentally observed the system ground state for a uniform magnetic field as well as the phase transition from a miscible to an immiscible system. In particular, we developed a method to minimise the influence of uncontrolled magnetic field gradients along the trap weak axis. The domains are indeed very sensible to magnetic field gradients to which they respond re-organising themselves in the trap.
We fitted the spin domains in the $m_F = 0, +1$ configuration, obtaining their sizes as well as the penetration depth of one spin domain in the other one. We think that the temperature affects strongly the penetration depth, since thermal atoms are miscible with the atoms of all components. We also used a 1D-3D crossover model to fit the domains: this allow to take into account the possible occupation of radially excited levels by the quasi-condensate atoms. We have found that the system is very close to the 1D limit.
In order to obtain the system temperature, we measured the equation of state of a polarised cloud (all the atoms in $m_F = +1$). We measured the trapping potential loading thermal atoms into the dipole trap. Then, for a given profile we ordered the atomic density as a function of the chemical potential μ, obtaining $n = n(\mu)$. To obtain a temperature

from the Equation of State, we fitted the $\mu < 0$ part with a model for the thermal atoms density, taking into account the occupation of the radial excited states.

Finally, in Chapter 6, we presented the experimental observation of the spin-dipole polarisability of the $m_F = 0, +1$ configuration. We measured the spin-dipole polarisability for different magnetisations m_z, finding that it is bigger than the single atom response of a factor ~ 100. The major result presented in the chapter is the curve presenting the spin-dipole polarisability vs longitudinal magnetisation.

Perspectives

As already stated above, the short term goal of the experiment is to gain further understanding on the spin-dipole polarisability results presented in Chapter 6. We are currently implementing two T=0 models, 1D and 1D-3D crossover, to make a first comparison with the experimental results. We are also measuring the system temperature as a function of the magnetisation, to understand why the measured spin-dipole polarisability at low m_z is lower than the one at high m_z. In order to understand why the non-zero temperature can play an important role, we consider the energy associated to the different configurations of the $m_F = 0, +1$ domains in the trap. The configuration with the $m_F = 0$ domain in the centre and the $m_F = +1$ component at the two edges, for example, or the configuration with the $m_F = 0$ slightly de-centred and two asymmetric $m_F = +1$ side lobes. If the energy difference between these two configurations is smaller than $k_B T$, then thermal fluctuations can hide the $T = 0$ behaviour, preventing us from measuring the expected spin-dipole polarisability.

As a long term goal of the experiment, the installation of the 1D lattice along the HDT arm allows the study of the spin-1 system in a 1D lattice. We can observe the Superfluid-Mott insulator transition in 1D and, in the limiting case of a deep Mott insulator with negligible tunnelling, the step-like nature of the equation of state. In this Mott phase, we can explore insulating phases with different magnetic properties due to the filling [70, 69]. For $m_z = 0$, we expect to see (fluctuating) spin-nematic states for odd fillings and spin-singlet, [101], states for even fillings. These insulating phases are visible only at very low magnetic fields, such that the quadratic Zeeman energy $q \ll U_s$ is way smaller than the spin interaction energy. Increasing the quadratic Zeeman energy, the spin-singlet states become polar states and the spin-nematic states do not fluctuate anymore, because they are pinned to the quantisation axis defined by the magnetic field. For $m_z > 0$, we expect to observe magnetisation plateau depending on the filling: for even filling we expect $\rho_z = 0$ magnetisation, since the atoms are in singlet states, and for odd filling we expect $\rho_z > 0$.

Appendices

A. Adiabatic Transfer of a quasi-condensate in 1D

In this appendix we present a theoretical study of the transfer from the 3D geometry to the 1D geometry presented in Chapter 3. We assume that the transfer from the crossed dipole trap to the single beam trap is adiabatic and we compute its final temperature, starting from an initial temperature and condensed fraction. To simplify the problem, we model the two traps with a box potential with volumes corresponding to the Thomas-Fermi volumes measured in the experiment, see Figure A.1. The results are based on the work on quasi-condensates [120].

Figure A.1.: Sketch of the model considered in this appendix. The adiabatic transfer of a condensate from a 3D box trap to a 1D box trap.

A.1. Theory of quasi-condensate

We have already introduced the concept of quasi-condensate and the phase fluctuations typical of this state in Chapter 2. Here we reintroduce it very briefly with the Bogoliubov approach presented in [120].
We start writing the atom field operator in the density-phase representation, as we have done for the condensate wavefunction in 2.1.4:

$$\hat{\Psi} = \mathrm{e}^{i\hat{\phi}}\sqrt{n_0 + \delta\hat{n}} \tag{A.1}$$

where n_0 is the density of atoms occupying the ground state and $\delta\hat{n}$ and $\hat{\phi}$ are operators describing, respectively, the density and phase fluctuations. As usual for uniform systems,

we decompose the fluctuations in plane wave modes

$$\delta\hat{n} = \sum_k \delta n_k \hat{b}_k + \text{h.c.} \qquad \hat{\phi} = \sum_k \phi_k \hat{b}_k + \text{h.c.}, \tag{A.2}$$

where the $\hat{b}_k$'s are the annihilation operators for the quasiparticles of momentum $\hbar k$. The coefficients of the two expansions can be written as functions of the Bogoliubov amplitudes u_k and v_k by

$$\delta n_k = \sqrt{n_0}(u_k - v_k)\frac{e^{ikx}}{\sqrt{L}} \qquad \delta\phi_k = \frac{u_k + v_k}{2i\sqrt{n_0}}\cdot\frac{e^{ikx}}{\sqrt{L}} \tag{A.3}$$

In the Bogoliubov theory, as we have seen in Chapter 2 the Hamiltonian is written as the sum of these independent Bogoliubov modes, see (2.17),

$$\hat{H} = \sum_{k\neq 0} E_k \hat{b}_k^\dagger \hat{b}_k + E_0, \tag{A.4}$$

where E_0 is the ground state energy, $E_k = \sqrt{\epsilon_k(\epsilon_k + 2\mu)}$ is the Bogoliubov excitations spectrum for each plane wave k, μ is the chemical potential and $\epsilon_k = \frac{\hbar^2 k^2}{2m}$ is the free energy per particle. We recall also the definition of healing length ξ given in (2.14), $\xi_{\text{int}} = \sqrt{\frac{\hbar^2}{2mgn}}$. Thanks to the healing length, we can define a characteristic wavevector ξ^{-1} below which the Bogoliuobov modes represent collective excitations of the 1D quasicondensate.

As done by the authors of [120], we can write the equation of state including fluctuation corrections to n:

$$\frac{\mu}{gn} = 1 + \sqrt{2\gamma}\,F(\tau,\alpha), \tag{A.5}$$

where the function $F(\tau,\alpha)$[1] is equal to

$$F(\tau,\alpha) = \frac{1}{\pi}\int_0^\infty du\left[\frac{u}{\sqrt{u^2+2\alpha}}\,\frac{1}{\exp\left(\frac{u\sqrt{u^2+2\alpha}}{\tau}\right)-1} + \frac{1}{2}\left(\frac{u}{\sqrt{u^2+2\alpha}} - 1\right)\right], \tag{A.6}$$

and where we have introduced the reduced variables

$$\tau = \frac{k_B T}{gn}, \qquad \alpha = \frac{\mu}{gn}, \tag{A.7}$$

and the dimensionless interacting parameter

$$\gamma = \frac{mg}{\hbar^2 n}. \tag{A.8}$$

For our experiment we estimate $\gamma \approx 5\cdot 10^{-5}$, with $n = 100\,\mu\text{m}^{-1}$. The equation (A.5) must be solved self-consistently for μ, given the total density n and the temperature T.

[1] To write the chemical potential as in (A.5), we write the Bogoliubov amplitudes in a box as $u_k^2 = \frac{1}{2}\left(\frac{\epsilon_k+\mu}{E_k} + 1\right)$ and $v_k^2 = \frac{1}{2}\left(\frac{\epsilon_k+\mu}{E_k} - 1\right)$.

The entropy can be evaluated from $S/k_B = \frac{U-T-\mu N}{k_B T}$. The entropy per particle, using the same reduced variables as before, can then be written as

$$\frac{S}{Nk_B} = \sqrt{2\gamma}\, G(\tau, \alpha) \tag{A.9}$$

where

$$G(\tau,\alpha) = \frac{1}{\pi}\int_0^\infty du \left[\frac{u\sqrt{u^2+2\alpha}}{\exp\left(\frac{u\sqrt{u^2+2\alpha}}{\tau}\right)-1} - \ln\left(1-\mathrm{e}^{-\frac{u\sqrt{u^2+2\alpha}}{\tau}}\right)\right] \tag{A.10}$$

In Figure A.2 we represent the chemical potential and the entropy per particle as a function of t for $\gamma = 5\cdot 10^{-5}$.

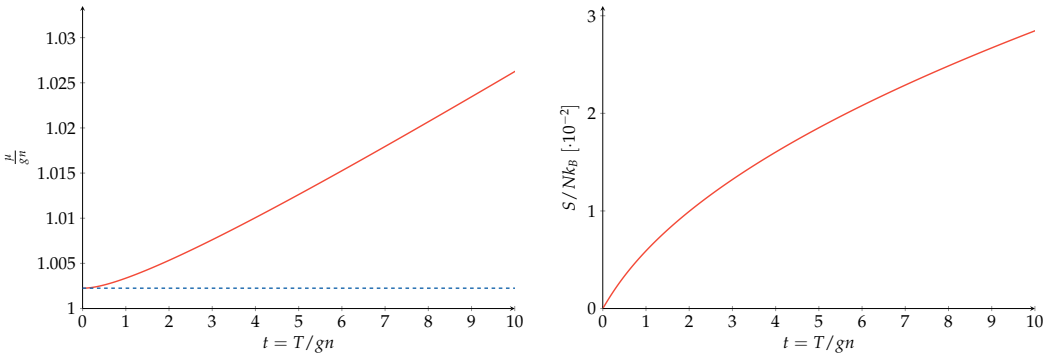

(a) (b)

Figure A.2.: Chemical potential μ/gn and entropy per particle S/Nk_B for $\gamma = 5\cdot 10^{-5}$. In Figure A.2(a), the blue dashed line represents the $T = 0$ limit.

A.2. The adiabatic transfer

To model the adiabatic transfer, we need to model the initial state of the 3D condensate. We suppose the latter to be well described by an ideal gas trapped in a box potential of volume V. The volume V= $\frac{4}{3}\pi \cdot R_{\mathrm{TF},x}\cdot R_{\mathrm{TF},y}\cdot R_{\mathrm{TF},z}$ is defined such that $N = n\cdot V$ where n is the 3D gas density and the three radii $R_{\mathrm{TF},i}$ are the cloud Thomas-fermi radii along the three trap axes. Thanks to the volume V and to the formula for the critical temperature in a uniform system

$$k_B T_{c,3D} = \frac{2\pi\hbar^2}{m}\left(\frac{n}{\xi(3/2)}\right)^{\frac{2}{3}}, \tag{A.11}$$

we can compute the entropy per atom, that for an ideal gas in a uniform system is equal to

$$\frac{S}{Nk_B} = \frac{5\xi(5/2)}{2\xi(3/2)}\left(\frac{T}{T_{c,3D}}\right)^{\frac{3}{2}} \tag{A.12}$$

where ξ is the Riemann zeta function. If the transfer is adiabatic, the entropy is conserved and we can find the final thermodynamic state of the system by equating the initial and final entropies. Looking at Figure A.3, we can visually obtain the result of this procedure. The upper figure shows the trap depth of the starting 3D trap. The lower figure shows instead the temperature and the chemical potential, in units of gn, for the condensate in the 1D trap. All the quantities are plotted as functions of the entropy per particle S/Nk_B, which is a conserved quantity in the transfer. Therefore, we can choose a value for the initial trap depth of the 3D condensate and directly look, after the transfer, at the temperature and chemical potential we obtain.
Starting from a trapping depth of $V_{\mathrm{td}} = 1.6\,\mu\mathrm{K}$, which is the typical value we start from in the 3D trap, we end up with a temperature which is equal to $T \approx 3.4\,gn$. Considering that we measure $gn \approx 130\,\mathrm{Hz}$ for the 1D condensate, this means we expect temperatures $T \sim 21\,\mathrm{nK}$ from the construction of Figure A.3. In the experiment, we measure temperatures $T \approx 44\,\mathrm{nK}$, see Chapter 5 Subsection 5.3.3. Both values are compatible up to a numerical factor, which is not too surprising since we don't take the trap potential into account.

It is worth to notice that this model is strictly 1D, but, as we have already pointed out in Chapter 5, our system is quasi-1D. This because the temperature of the cloud is of the same order of the radial confinement, $k_B T \sim \hbar\omega_\perp$. Therefore, to model the system in a proper way, we should consider the occupation of the radial excited states. In this case, atoms have more energy states that they can occupy at a lower temperature. Therefore, at a given temperature, the entropy is higher in this case than in the 1D case. Figure A.3 shows that, taking this effect into account, we expect a lower temperature from the transfer with respect to the one obtained with the 1D model.

It is interesting to see if the evaporation plays or not an important role in determining the final temperature of the cloud. Evaporation cooling relies on the elimination of the atoms with energy higher than the trap depth V_{td} and thermalisation of the atoms remaining in the trap via binary collisions. Only a few collisions are required to the atoms to thermalise and rearrange themselves in an equilibrium distribution, see [88, 166]. A thermalisation rate Γ_{th} can defined as $\Gamma_{\mathrm{th}} = n\sigma\bar{v}$, where n is the 3D gas density, σ is the cross-section, $\sigma = 8\pi^2$, and $\bar{v}$ is the average thermal velocity, $\bar{v} = \sqrt{8k_BT/\pi m}$. For our system in the anisotropic harmonic trap, taking $n = \frac{100}{\pi a_\perp^2}\,\mu\mathrm{m}^{-1}$ and $T = 44\,\mathrm{nK}$, we have $\Gamma_{\mathrm{th}} \approx 37\,\mathrm{s}^{-1}$. We define now the evaporation parameter $\eta = V_{\mathrm{td}}/k_BT$. For value $\eta \gg 1$, we can use the formula for the evaporation rate from [88] that is equal to $\Gamma_{\mathrm{ev}} = n\sigma\bar{v}\eta\mathrm{e}^{-\eta}$. For the 1D anisotropic trap we compute $V_{\mathrm{td}} = 0.94\,\mu\mathrm{K}$, from which we obtain $\eta = 21.5$ and a very small value for $\Gamma_{\mathrm{ev}} = 4 \cdot 10^{-7}\,\mathrm{s}^{-1}$.
This means that the evaporation cooling is not working from the gas in the 1D trap and that the temperature is mostly determined by the transfer process. The difference in temperature could be due to our crude modelling ignoring the trap, but also to heating (due to technical reasons) occurring during the transfer process.

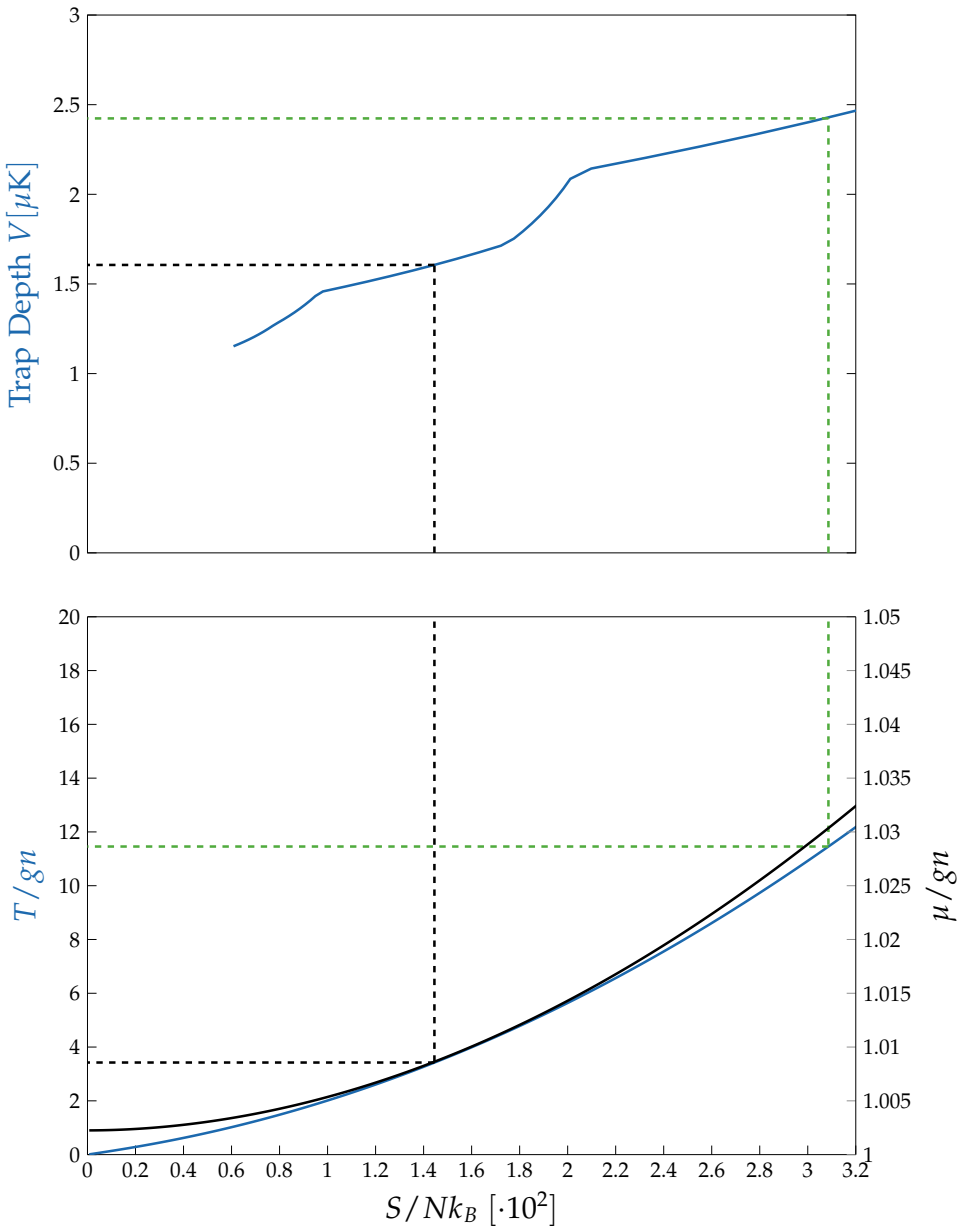

Figure A.3.: Construction to determine the temperature of the condensate in the 1D geometry, after the transfer from the 3D to the 1D trap discussed above. **Upper**: Plot to choose the 3D condensate initial conditions. The trap depth V_{td} of the 3D trap is plotted as a function of the entropy per particle S/Nk_B. **Lower**: Plot to obtain the final temperature of the 1D condensate. On the same graph are plotted temperature and chemical potential of the 1D condensate, in units of gn, as a function of the entropy per particle S/Nk_B. If the transfer from the 3D to the 1D geometry is adiabatic, the entropy is conserved. The black dashed line on the two graphs indicates the final entropy per particle for such an adiabatic process starting from a typical trap depth $V_{\mathrm{td}} = 1.6\,\mu$K. The green dashed line indicates T_ϕ.

B. Numerical solution of the spin 1 Gross-Pitaevskii equations

In this appendix we want to briefly present the algorithm we use to solve the three Gross-Pitaevskii equations (2.73, 2.74, 2.75) for the spin-1 spinor condensate.
We focus our attention on 1 dimensional system with trapping potential $V(z) = \frac{1}{2}M\omega_z^2 z^2$.
We use harmonic oscillator units, therefore time and lengths are rescaled according to

$$t \to \tilde{t} = \omega_z t, \tag{B.1}$$

$$z \to \tilde{z} = \frac{z}{\sigma}, \tag{B.2}$$

$$g \to \tilde{g} = \frac{N\bar{g}}{\sigma_z \hbar\omega_z}, \tag{B.3}$$

$$\rho \to \tilde{\rho} = \frac{\rho\sigma_z}{N}, \tag{B.4}$$

$$S_z \to \tilde{S}_z = \frac{S_z\sigma_z}{N} \tag{B.5}$$

where $\sigma = \sqrt{\hbar/M\omega_z}$ is the oscillator length and the wavefunctions $\mathbf{\Psi}$ are normalised. We rewrite the Gross-Pitaevskii equations (2.73, 2.74, 2.75) in a vectorial form

$$i\frac{\partial\mathbf{\Psi}}{\partial\tilde{t}} = L[\mathbf{\Psi}]\cdot\mathbf{\Psi}, \tag{B.6}$$

where L is a differential operator defined as $L = K + U$, with[1]

$$K = -\frac{1}{2}\frac{\partial\cdot}{\partial z^2}, \tag{B.7}$$

$$U = \frac{1}{2}z^2 + g\,\rho + g_s\begin{pmatrix} \rho_0 + S_z & \mathbf{\Psi}_0\mathbf{\Psi}_{-1}^* & 0 \\ \mathbf{\Psi}_0^*\mathbf{\Psi}_{-1} & \rho_{+1} + \rho_{-1} & \mathbf{\Psi}_0^*\mathbf{\Psi}_{+1} \\ 0 & \mathbf{\Psi}_0\mathbf{\Psi}_{+1}^* & \rho_0 - S_z \end{pmatrix} \tag{B.8}$$

[1] We drop from now on the tilde notation for the sake of readability.

The ground state is computed using imaginary time evolution, *i. e.* we look for solutions of

$$\frac{\partial \mathbf{\Psi}}{\partial \tau} = -L[\mathbf{\Psi}] \cdot \mathbf{\Psi}, \tag{B.9}$$

where $\tau = i\tilde{t}$. This is done numerically, discretising time in steps $\Delta\tau$ and evolving the wavefunction at each step. Considering infinitesimal evolutions between τ_n and $\tau_{n+1} = \tau_n + \Delta\tau$, we can identify the GP solutions with the solution of the Schrödinger equation

$$\mathbf{\Psi}(\tau_{n+1}) = \mathrm{e}^{-(K+V)\Delta\tau}\mathbf{\Psi}(\tau_n), \tag{B.10}$$

with a potential energy $V_n = V[\mathbf{\Psi}(\tau_n)]$. The evolution operator is further approximated by

$$\mathrm{e}^{-(K+V_n)\Delta\tau} = \mathrm{e}^{-K\Delta\tau}\,\mathrm{e}^{-V_n\Delta\tau}\,\mathrm{e}^{-\frac{1}{2}[K,V]\Delta\tau^2} \approx \mathrm{e}^{-K\Delta\tau(1-V_n\Delta\tau)} \tag{B.11}$$

where we used the Baker-Campbell-Hausdorff (BCH) formula in the first step and we neglected the commutator and performed a Taylor expansion of the potential term in the second step. The last term is the one used to propagate the GP equations. The potential term is propagated in real space, the kinetic term, instead, is propagated in momentum space using a fast Fourier transform.
In the literature we can found alternative schemes where momentum and potential part are propagated separately, see [9, 179].
At the end of each propagation step, the components of $\mathbf{\Psi}$ are renormalised to ensure the conservation of total norm and magnetisation, which are not conserved in imaginary time evolution.The normalisation constants are equal to

$$A_0^2 = \frac{1 - m_z^2}{||\mathbf{\Psi}_0||^2 + \sqrt{4(1-m_z^2)||\mathbf{\Psi}_{+1}||^2||\mathbf{\Psi}_{-1}||^2 + m_z^2||\mathbf{\Psi}_0||^2}} \tag{B.12}$$

$$A_\pm^2 = \frac{1 \pm m_z - A_0^2||\mathbf{\Psi}_0||^2}{2||\mathbf{\Psi}_{+1}||^2} \tag{B.13}$$

The choice of step size for the evolution is of capital importance, while implementing these algorithm. The step should be chosen in such a way that all the steps correspond to a small change of the wave function.
The Taylor expansion of the potential term implies

$$z^2\Delta\tau \ll 1 \rightarrow \Delta\tau \ll \frac{1}{(N_z\Delta z)^2}, \tag{B.14}$$

where is the grid size and N_z is the number of grid points. In the second equation we choose the grid size as typical distance. A more natural and less restrictive choice would have been the cloud size. Neglecting the commutator implies

$$\tilde{x}k_{\max}\Delta\tau^2 \ll 1 \rightarrow \Delta\tau \ll \sqrt{\frac{1}{2\pi N_z}}, \tag{B.15}$$

where $k_{\max} = 2\pi/\Delta z$ is the maximum wavevector used in the momentum space propagation. For the simulations described in Chapter 5, we used $\Delta_z \approx 0.025$ ($N_z = 2000$ points on a

grid from −25 to +25) and $\delta\tau = 10^{-3}$.
If we used also the Taylor expansion of the kinetic term, we would have an additional criterion

$$k_{\max}^2 \Delta\tau \ll 1 \rightarrow \Delta\tau \ll \frac{\Delta z^2}{2\pi^2}. \tag{B.16}$$

which is more restrictive than the previous one.

Bibliography

[1] JR Abo-Shaeer et al. “Observation of vortex lattices in Bose-Einstein condensates”. In: *Science* 292.5516 (2001), pp. 476–479.

[2] K Aikawa et al. “Bose-Einstein condensation of erbium”. In: *Physical review letters* 108.21 (2012), p. 210401.

[3] A. H. van Amerongen". “Yang-Yang Thermodynamics on an Atom Chip”. In: *Physical Review Letters* 100.9 (2008). DOI: 10.1103/PhysRevLett.100.090402.

[4] Mike H Anderson et al. “Observation of Bose-Einstein condensation in a dilute atomic vapor”. In: *science* 269.5221 (1995), p. 198.

[5] MR Andrews et al. “Observation of interference between two Bose condensates”. In: *Science* 275.5300 (1997), pp. 637–641.

[6] P Ao and ST Chui. “Binary Bose-Einstein condensate mixtures in weakly and strongly segregated phases”. In: *Physical Review A* 58.6 (1998), p. 4836.

[7] Julien Armijo et al. “Mapping out the quasicondensate transition through the dimensional crossover from one to three dimensions”. In: *Physical Review A* 83.2 (2011), p. 021605.

[8] S Ashhab and AJ Leggett. “Measurement theory and interference of spinor Bose-Einstein condensates”. In: *Physical Review A* 65.2 (2002), p. 023604.

[9] Weizhu Bao, I-Liang Chern, and Yanzhi Zhang. “Efficient numerical methods for computing ground states of spin-1 Bose–Einstein condensates based on their characterizations”. In: *Journal of Computational Physics* 253 (2013), pp. 189–208.

[10] RA Barankov. “Boundary of two mixed Bose-Einstein condensates”. In: *Physical Review A* 66.1 (2002), p. 013612.

[11] M Bartenstein et al. “Crossover from a molecular Bose-Einstein condensate to a degenerate Fermi gas”. In: *Physical review letters* 92.12 (2004), p. 120401.

[12] SG Bhongale and Eddy Timmermans. “Phase separated BEC for high-sensitivity force measurement”. In: *Physical review letters* 100.18 (2008), p. 185301.

[13] Tom Bienaimé et al. “Spin-dipole oscillation and polarizability of a binary Bose-Einstein condensate near the miscible-immiscible phase transition”. In: *Physical Review A* 94.6 (2016), p. 063652.

[14] Juliette Billy et al. “Direct observation of Anderson localization of matter-waves in a controlled disorder”. In: *arXiv preprint arXiv:0804.1621* (2008).

[15] G Bismut et al. “Anisotropic excitation spectrum of a dipolar quantum bose gas”. In: *Physical review letters* 109.15 (2012), p. 155302.

[16] G Bismut et al. "Collective excitations of a dipolar Bose-Einstein condensate". In: *Physical review letters* 105.4 (2010), p. 040404.

[17] Adam T Black et al. "Spinor dynamics in an antiferromagnetic spin-1 condensate". In: *Physical review letters* 99.7 (2007), p. 070403.

[18] I Bloch, TW Hansch, and T Esslinger. "Measurement of the spatial coherence of a trapped Bose gas at the phase transition". In: *Nature* 403.6766 (2000), p. 166.

[19] Immanuel Bloch, Theodor W Hänsch, and Tilman Esslinger. "Atom laser with a cw output coupler". In: *Physical Review Letters* 82.15 (1999), p. 3008.

[20] N Bogoliubov. "On the theory of superfluidity". In: *J. Phys* 11.1 (1947), p. 23.

[21] Satyendra Nath Bose. *Plancks gesetz und lichtquantenhypothese*. Springer, 1924.

[22] Thomas Bourdel et al. "Experimental study of the BEC-BCS crossover region in lithium 6". In: *Physical Review Letters* 93.5 (2004), p. 050401.

[23] Th Busch et al. "Stability and collective excitations of a two-component Bose-Einstein condensed gas: A moment approach". In: *Physical Review A* 56.4 (1997), p. 2978.

[24] Y Castin and R Dum. "Bose-Einstein condensates in time dependent traps". In: *Physical Review Letters* 77.27 (1996), p. 5315.

[25] Ming-Shien Chang et al. "Coherent spinor dynamics in a spin-1 Bose condensate". In: *arXiv preprint cond-mat/0509341* (2005).

[26] M.-S. Chang et al. "Observation of spinor dynamics in optically trapped ^{87}Rb Bose-Einstein Condensates". In: *Phys. Rev. Lett.* 92 (14 Apr. 2004), p. 140403.

[27] Steven Chu. "Nobel Lecture: The manipulation of neutral particles". In: *Reviews of Modern Physics* 70.3 (1998), p. 685.

[28] J-F Clément et al. "All-optical runaway evaporation to Bose-Einstein condensation". In: *Physical Review A* 79.6 (2009), p. 061406.

[29] Claude N Cohen-Tannoudji. "Nobel Lecture: Manipulating atoms with photons". In: *Reviews of Modern Physics* 70.3 (1998), p. 707.

[30] Claude Cohen-Tannoudji, Jacques Dupont-Roc, and Gilbert Grynberg. *Processus d'interaction entre photons et atomes*. Edp Sciences, 2012.

[31] Eric A Cornell and Carl E Wieman. "Nobel Lecture: Bose-Einstein condensation in a dilute gas, the first 70 years and some recent experiments". In: *Reviews of Modern Physics* 74.3 (2002), p. 875.

[32] Vincent Corre. "Magnetism in spin-1 Bose-Einstein condensates with antiferromagnetic interactions". PhD thesis. Ecole normale supérieure-ENS PARIS, 2014.

[33] Franco Dalfovo et al. "Theory of Bose-Einstein condensation in trapped gases". In: *Reviews of Modern Physics* 71.3 (1999), p. 463.

[34] J. Dalibard. "Une brève histoire des atomes froids". In: Cours du Collège de France, 2015.

[35] Kunal K Das, MD Girardeau, and EM Wright. "Crossover from one to three dimensions for a gas of hard-core bosons". In: *Physical review letters* 89.11 (2002), p. 110402.

[36] Kendall B Davis et al. "Bose-Einstein condensation in a gas of sodium atoms". In: *Physical review letters* 75.22 (1995), p. 3969.

[37] Guillaume Delannoy et al. "Understanding the production of dual Bose-Einstein condensation with sympathetic cooling". In: *Physical Review A* 63.5 (2001), p. 051602.

[38] Brian DeMarco and Deborah S Jin. "Onset of Fermi degeneracy in a trapped atomic gas". In: *Science* 285.5434 (1999), pp. 1703–1706.

[39] Albert Einstein. *Quantentheorie des einatomigen idealen Gases*. Akademie der Wissenshaften, in Kommission bei W. de Gruyter, 1924.

[40] E. Eisenberg and E. H. Lieb. "Polarization of Interacting Bosons with Spin". In: *Phys. Rev. Lett.* 89 (22 Nov. 2002), p. 220403.

[41] M. Erhard et al. "Bose-Einstein condensation at constant temperature". In: *Phys. Rev. A* 70 (3 Sept. 2004), p. 031602.

[42] F. Fang et al. "Condensing Magnons in a Degenerate Ferromagnetic Spinor Bose Gas". In: *Phys. Rev. Lett.* 116 (9 Mar. 2016), p. 095301.

[43] M Fattori et al. "Damagnetization cooling of a gas". In: *arXiv preprint cond-mat/0610498* (2006).

[44] Eleonora Fava et al. "Spin Superfluidity of a Bose Gas Mixture at Finite Temperature". In: *arXiv preprint arXiv:1708.03923* (2017).

[45] G Ferrari et al. "Collisional properties of ultracold K-Rb mixtures". In: *Physical review letters* 89.5 (2002), p. 053202.

[46] Igor Ferrier-Barbut et al. "A mixture of Bose and Fermi superfluids". In: *Science* 345.6200 (2014), pp. 1035–1038.

[47] Camille Frapolli. "Thermodynamics and magnetism of antiferromagnetic spinor Bose-Einstein condensates". PhD thesis. Paris Sciences et Lettres, 2017.

[48] C Frapolli et al. "Stepwise Bose-Einstein condensation in a spinor gas". In: *arXiv preprint arXiv:1702.08265* (2017).

[49] Alexander L Gaunt et al. "Bose-Einstein condensation of atoms in a uniform potential". In: *Physical review letters* 110.20 (2013), p. 200406.

[50] Fabrice Gerbier. "Quasi-1D Bose-Einstein condensates in the dimensional crossover regime". In: *EPL (Europhysics Letters)* 66.6 (2004), p. 771.

[51] Walther Gerlach and Otto Stern. "Der experimentelle nachweis der richtungsquantelung im magnetfeld". In: *Zeitschrift für Physik A Hadrons and Nuclei* 9.1 (1922), pp. 349–352.

[52] S Giorgini, LP Pitaevskii, and S Stringari. "Condensate fraction and critical temperature of a trapped interacting Bose gas". In: *Physical Review A* 54.6 (1996), R4633.

[53] Nathan Goldman et al. "Light-induced gauge fields for ultracold atoms". In: *Reports on Progress in Physics* 77.12 (2014), p. 126401.

[54] Victor V Goldman, Isaac F Silvera, and Anthony J Leggett. "Atomic hydrogen in an inhomogeneous magnetic field: Density profile and Bose-Einstein condensation". In: *Physical Review B* 24.5 (1981), p. 2870.

[55] Phillip L Gould, George A Ruff, and David E Pritchard. "Diffraction of atoms by light: The near-resonant Kapitza-Dirac effect". In: *Physical review letters* 56.8 (1986), p. 827.

[56] Markus Greiner et al. "Quantum phase transition from a superfluid to a Mott insulator in a gas of ultracold atoms". In: *nature* 415.6867 (2002), pp. 39–44.

[57] Rudolf Grimm, Matthias Weidemüller, and Yurii B Ovchinnikov. "Optical dipole traps for neutral atoms". In: *Advances in atomic, molecular, and optical physics* 42 (2000), pp. 95–170.

[58] M Guilleumas et al. "Spin mixing in colliding spinor condensates: Formation of an effective barrier". In: *EPL (Europhysics Letters)* 84.6 (2009), p. 60005.

[59] Zoran Hadzibabic et al. "Berezinskii-Kosterlitz-Thouless crossover in a trapped atomic gas". In: *arXiv preprint cond-mat/0605291* (2006).

[60] Edward W Hagley et al. "A well-collimated quasi-continuous atom laser". In: *Science* 283.5408 (1999), pp. 1706–1709.

[61] DM Harber et al. "Measurement of the Casimir-Polder force through center-of-mass oscillations of a Bose-Einstein condensate". In: *Physical Review A* 72.3 (2005), p. 033610.

[62] X. He et al. "Coherent spin-mixing dynamics in thermal ^{87}Rb spin-1 and spin-2 gases". In: *Phys. Rev. A* 91 (3 Mar. 2015), p. 033635.

[63] D Hellweg et al. "Phase fluctuations in Bose–Einstein condensates". In: *Applied Physics B: Lasers and Optics* 73.8 (2001), pp. 781–789.

[64] Carsten Henkel, Tim-O Sauer, and NP Proukakis. "Cross-over to quasi-condensation: mean-field theories and beyond". In: *Journal of Physics B: Atomic, Molecular and Optical Physics* 50.11 (2017), p. 114002.

[65] Tin-Lun Ho. "Spinor Bose condensates in optical traps". In: *Physical Review Letters* 81.4 (1998), p. 742.

[66] Tin-Lun Ho and Sung Kit Yip. "Fragmented and single condensate ground states of spin-1 Bose gas". In: *Physical review letters* 84.18 (2000), p. 4031.

[67] Chen-Lung Hung et al. "Accelerating evaporative cooling of atoms into Bose-Einstein condensation in optical traps". In: *Physical Review A* 78.1 (2008), p. 011604.

[68] David A Huse and Eric D Siggia. "The density distribution of a weakly interacting Bose gas in an external potential". In: *Journal of Low Temperature Physics* 46.1 (1982), pp. 137–149.

[69] Adilet Imambekov, Mikhail Lukin, and Eugene Demler. "Magnetization plateaus for spin-one bosons in optical lattices: Stern-Gerlach experiments with strongly correlated atoms". In: *Physical review letters* 93.12 (2004), p. 120405.

[70] Adilet Imambekov, Mikhail Lukin, and Eugene Demler. "Spin-exchange interactions of spin-one bosons in optical lattices: Singlet, nematic, and dimerized phases". In: *Physical Review A* 68.6 (2003), p. 063602.

[71] A Imambekov et al. "Density ripples in expanding low-dimensional gases as a probe of correlations". In: *Physical Review A* 80.3 (2009), p. 033604.

[72] S Inouye et al. "Observation of Feshbach resonances in a Bose-Einstein condensate". In: *Nature* 392.6672 (1998), p. 151.

[73] T. Isoshima, T. Ohmi, and K. Machida. "Double Phase Transitions in Magnetized Spinor Bose-Einstein Condensation". In: *Journal of the Physical Society of Japan* 69.12 (2000), pp. 3864–3869.

[74] Tomoya Isoshima, Kazushige Machida, and Tetsuo Ohmi. "Spin-domain formation in spinor Bose-Einstein condensation". In: *Physical Review A* 60.6 (1999), p. 4857.

[75] David Jacob. "Condensats de Bose-Einstein de spin 1: étude expérimentale avec des atomes de sodium dans un piege optique". PhD thesis. Université Pierre et Marie Curie-Paris VI, 2012.

[76] David Jacob et al. "Phase diagram of spin-1 antiferromagnetic Bose-Einstein condensates". In: *Physical Review A* 86.6 (2012), p. 061601.

[77] D. Jacob et al. "Production of Sodium Bose–Einstein condensates in an optical dimple trap". In: *New Journal of Physics* 13.6 (2011), p. 065022.

[78] A. J. A. James and A. Lamacraft. "Phase Diagram of Two-Dimensional Polar Condensates in a Magnetic Field". In: *Phys. Rev. Lett.* 106 (14 Apr. 2011), p. 140402.

[79] S.-C. Ji et al. "Experimental determination of the finite-temperature phase diagram of a spin-orbit coupled Bose gas". In: *Nat Phys* 10.4 (Apr. 2014), pp. 314–320. ISSN: 1745-2473.

[80] Robert Jördens et al. "A Mott insulator of fermionic atoms in an optical lattice". In: *arXiv preprint arXiv:0804.4009* (2008).

[81] P Juncar et al. "Absolute determination of the wavelengths of the sodium D1 and D2 lines by using a cw tunable dye laser stabilized on iodine". In: *Metrologia* 17.3 (1981), p. 77.

[82] Kao, Y.-M. and Jiang, T. F. "Transition temperatures of the trapped ideal spinor Bose gas". In: *Eur. Phys. J. D* 40.2 (2006), pp. 263–269.

[83] Y. Kawaguchi, N. T. Phuc, and P. B. Blakie. "Finite-temperature phase diagram of a spin-1 Bose gas". In: *Phys. Rev. A* 85 (5 May 2012), p. 053611.

[84] Yuki Kawaguchi and Masahito Ueda. "spinor Bose–Einstein condensates". In: *Physics Reports* 520.5 (2012), pp. 253–381.

[85] Wolfgang Ketterle. "Nobel lecture: When atoms behave as waves: Bose-Einstein condensation and the atom laser". In: *Reviews of Modern Physics* 74.4 (2002), p. 1131.

[86] Wolfgang Ketterle, Dallin S Durfee, and DM Stamper-Kurn. "Making, probing and understanding Bose-Einstein condensates". In: 1999.

[87] Wolfgang Ketterle and NJ Van Druten. "Bose-Einstein condensation of a finite number of particles trapped in one or three dimensions". In: *Physical Review A* 54.1 (1996), p. 656.

[88] Wolfgang Ketterle and NJ Van Druten. "Evaporative cooling of trapped atoms". In: *Advances in atomic, molecular, and optical physics* 37 (1996), pp. 181–236.

[89] Toshiya Kinoshita, Trevor Wenger, and David S Weiss. "All-optical Bose-Einstein condensation using a compressible crossed dipole trap". In: *Physical Review A* 71.1 (2005), p. 011602.

[90] Toshiya Kinoshita, Trevor Wenger, and David S Weiss. "Observation of a one-dimensional Tonks-Girardeau gas". In: *Science* 305.5687 (2004), pp. 1125–1128.

[91] C. Klempt et al. "Multiresonant Spinor Dynamics in a Bose-Einstein Condensate". In: *Phys. Rev. Lett.* 103 (19 Nov. 2009), p. 195302.

[92] C Klempt et al. "Parametric amplification of vacuum fluctuations in a spinor condensate". In: *Physical review letters* 104.19 (2010), p. 195303.

[93] S Knoop et al. "Feshbach spectroscopy and analysis of the interaction potentials of ultracold sodium". In: *Physical Review A* 83.4 (2011), p. 042704.

[94] S. Knoop et al. "Feshbach spectroscopy and analysis of the interaction potentials of ultracold sodium". In: *Phys. Rev. A* 83 (4 Apr. 2011), p. 042704.

[95] W. Krauth. "Quantum Monte Carlo Calculations for a Large Number of Bosons in a Harmonic Trap". In: *Phys. Rev. Lett.* 77.18 (Oct. 1996), p. 3695.

[96] T. Kuwamoto et al. "Magnetic field dependence of the dynamics of ^{87}Rb spin-2 Bose-Einstein condensates". In: *Phys. Rev. A* 69 (6 June 2004), p. 063604.

[97] Thierry Lahaye et al. "d-wave collapse and explosion of a dipolar Bose-Einstein condensate". In: *Physical review letters* 101.8 (2008), p. 080401.

[98] Thierry Lahaye et al. "Strong dipolar effects in a quantum ferrofluid". In: *arXiv preprint arXiv:0706.1670* (2007).

[99] Lev Davidovich Landau and Evgenii Mikhailovich Lifshitz. *Quantum mechanics: non-relativistic theory*. Vol. 3. Elsevier, 2013.

[100] G. Lang and E. Witkowska. "Thermodynamics of a spin-1 Bose gas with fixed magnetization". In: *Phys. Rev. A* 90 (4 Oct. 2014), p. 043609.

[101] CK Law, Han Pu, and NP Bigelow. "Quantum spins mixing in spinor Bose-Einstein condensates". In: *Physical review letters* 81.24 (1998), p. 5257.

[102] L.-P. Levy. *Magnetism and Superconductivity*. Springer, Berlin, 2000.

[103] Xiaolin Li et al. “Reduction of interference fringes in absorption imaging of cold atom cloud using eigenface method”. In: *Chinese Optics Letters* 5.3 (2007), pp. 128–130.

[104] Yingmei Liu et al. “Quantum phase transitions and continuous observation of spinor dynamics in an antiferromagnetic condensate”. In: *Physical review letters* 102.12 (2009), p. 125301.

[105] Fritz London. “On the bose-einstein condensation”. In: *Physical Review* 54.11 (1938), p. 947.

[106] O. J. Luiten, M. W. Reynolds, and J. T. M. Walraven. “Kinetic theory of the evaporative cooling of a trapped gas”. In: *Phys. Rev. A* 53 (1 Jan. 1996), pp. 381–389.

[107] P Maddaloni et al. “Collective oscillations of two colliding bose-einstein condensates”. In: *Physical review letters* 85.12 (2000), p. 2413.

[108] KW Madison et al. “Vortex formation in a stirred Bose-Einstein condensate”. In: *Physical Review Letters* 84.5 (2000), p. 806.

[109] A Munoz Mateo and V Delgado. “Effective mean-field equations for cigar-shaped and disk-shaped Bose-Einstein condensates”. In: *Physical Review A* 77.1 (2008), p. 013617.

[110] M. R. Matthews". “Vortices in a Bose-Einstein Condensate”. In: *Physical Review Letters* 83.13 (1999), pp. 2498–2501. DOI: 10.1103/PhysRevLett.83.2498.

[111] Michał Matuszewski. “Ground states of trapped spin-1 condensates in magnetic field”. In: *Physical Review A* 82.5 (2010), p. 053630.

[112] Michal Matuszewski, Tristram J Alexander, and Yuri S Kivshar. “Spin-domain formation in antiferromagnetic condensates”. In: *Physical Review A* 78.2 (2008), p. 023632.

[113] Michał Matuszewski, Tristram J Alexander, and Yuri S Kivshar. “Excited spin states and phase separation in spinor Bose-Einstein condensates”. In: *Physical Review A* 80.2 (2009), p. 023602.

[114] DJ McCarron et al. “Dual-species Bose-Einstein condensate of Rb 87 and Cs 133”. In: *Physical Review A* 84.1 (2011), p. 011603.

[115] Chiara Menotti and Sandro Stringari. “Collective oscillations of a one-dimensional trapped Bose-Einstein gas”. In: *Physical Review A* 66.4 (2002), p. 043610.

[116] KM Mertes et al. “Nonequilibrium dynamics and superfluid ring excitations in binary Bose-Einstein condensates”. In: *Physical review letters* 99.19 (2007), p. 190402.

[117] H-J Miesner et al. “Observation of metastable states in spinor Bose-Einstein condensates”. In: *Physical Review Letters* 82.11 (1999), p. 2228.

[118] Emmanuel Mimoun. “Condensat de Bose-Einstein de sodium dans un piege mésoscopique”. PhD thesis. Université Pierre et Marie Curie-Paris VI, 2010.

[119] Emmanuel Mimoun et al. "Fast production of ultracold sodium gases using light-induced desorption and optical trapping". In: *Physical Review A* 81.2 (2010), p. 023631.

[120] Christophe Mora and Yvan Castin. "Extension of Bogoliubov theory to quasicondensates". In: *Physical Review A* 67.5 (2003), p. 053615.

[121] S. Mukerjee, C. Xu, and J. E. Moore. "Topological Defects and the Superfluid Transition of the $s = 1$ Spinor Condensate in Two Dimensions". In: *Phys. Rev. Lett.* 97 (12 Sept. 2006), p. 120406.

[122] CJ Myatt et al. "Production of two overlapping Bose-Einstein condensates by sympathetic cooling". In: *Physical Review Letters* 78.4 (1997), p. 586.

[123] M. Naraschewski and D. M. Stamper-Kurn. "Semi-analytical description of a trapped Bose gas at finite temperature". In: *Phys. Rev. A* 58 (1998), p. 2423.

[124] M Naraschewski and DM Stamper-Kurn. "Analytical description of a trapped semi-ideal Bose gas at finite temperature". In: *Physical Review A* 58.3 (1998), p. 2423.

[125] B. Naylor et al. "Competition between Bose-Einstein Condensation and Spin Dynamics". In: *Phys. Rev. Lett.* 117 (18 Oct. 2016), p. 185302.

[126] B. Naylor et al. "Cooling of a Bose-Einstein Condensate by Spin Distillation". In: *Phys. Rev. Lett.* 115 (24 Dec. 2015), p. 243002.

[127] M. R. Norman. "The Challenge of Unconventional Superconductivity". In: *Science* 332.6026 (2011), pp. 196–200. ISSN: 0036-8075.

[128] Caspar F Ockeloen. "Probing fluctuations in a lattice of mesoscopic atomic ensembles". PhD thesis. Msc. thesis, University of Amsterdam, 2010. URL http://www.science. uva. nl/research/aplp/eprints/Caspar_ Ockeloen_MSc2010. pdf, 2010.

[129] CF Ockeloen et al. "Detection of small atom numbers through image processing". In: *Physical Review A* 82.6 (2010), p. 061606.

[130] K. M. O'Hara et al. "Scaling laws for evaporative cooling in time-dependent optical traps". In: *Phys. Rev. A* 64 (5 Oct. 2001), p. 051403.

[131] Tetsuo Ohmi and Kazushige Machida. "Bose-Einstein condensation with internal degrees of freedom in alkali atom gases". In: *Journal of the Physical Society of Japan* 67.6 (1998), pp. 1822–1825.

[132] R. Olf et al. "Thermometry and cooling of a Bose gas to 0.02 times the condensation temperature". In: *Nat. Phys.* 11.9 (Sept. 2015), pp. 720–723. ISSN: 1745-2473.

[133] Maxim Olshanii. "Atomic scattering in the presence of an external confinement and a gas of impenetrable bosons". In: *Physical Review Letters* 81.5 (1998), p. 938.

[134] Yu B Ovchinnikov et al. "Diffraction of a released Bose-Einstein condensate by a pulsed standing light wave". In: *Physical review letters* 83.2 (1999), p. 284.

[135] SB Papp, JM Pino, and CE Wieman. "Tunable miscibility in a dual-species Bose-Einstein condensate". In: *Physical review letters* 101.4 (2008), p. 040402.

[136] Belén Paredes et al. "Tonks-girardeau gas of ultracold atoms in an optical lattice". In: *Nature* 429.6989 (2004), p. 277.

[137] Benjamin Pasquiou et al. "Spontaneous demagnetization of a dipolar spinor bose gas in an ultralow magnetic field". In: *Physical Review Letters* 106.25 (2011), p. 255303.

[138] B. Pasquiou et al. "Thermodynamics of a Bose-Einstein Condensate with Free Magnetization". In: *Phys. Rev. Lett.* 108 (4 Jan. 2012), p. 045307.

[139] H. K. Pechkis et al. "Spinor Dynamics in an Antiferromagnetic Spin-1 Thermal Bose Gas". In: *Phys. Rev. Lett.* 111 (2 July 2013), p. 025301.

[140] Christopher J Pethick and Henrik Smith. *Bose-Einstein condensation in dilute gases*. Cambridge university press, 2002.

[141] DS Petrov, DM Gangardt, and GV Shlyapnikov. "Low-dimensional trapped gases". In: *Journal de Physique IV (Proceedings)*. Vol. 116. EDP sciences. 2004, pp. 5–44.

[142] DS Petrov, GV Shlyapnikov, and JTM Walraven. "Phase-fluctuating 3D Bose-Einstein condensates in elongated traps". In: *Physical review letters* 87.5 (2001), p. 050404.

[143] William D Phillips. "Nobel Lecture: Laser cooling and trapping of neutral atoms". In: *Reviews of Modern Physics* 70.3 (1998), p. 721.

[144] TE Phipps and JB Taylor. "The magnetic moment of the hydrogen atom". In: *Physical Review* 29.2 (1927), p. 309.

[145] N. T. Phuc, Y. Kawaguchi, and M. Ueda. "Effects of thermal and quantum fluctuations on the phase diagram of a spin-1 ^{87}Rb Bose-Einstein condensate". In: *Phys. Rev. A* 84 (4 Oct. 2011), p. 043645.

[146] L. P Pitaevskii and S. Stringari. *Bose-Einstein condensation*. Oxford University Press, 2003.

[147] Lev Pitaevskii and Sandro Stringari. *Bose-Einstein condensation and superfluidity*. Vol. 164. Oxford University Press, 2016.

[148] H Pu and NP Bigelow. "Collective excitations, metastability, and nonlinear response of a trapped two-species Bose-Einstein condensate". In: *Physical review letters* 80.6 (1998), p. 1134.

[149] H Pu and NP Bigelow. "Properties of two-species Bose condensates". In: *Physical review letters* 80.6 (1998), p. 1130.

[150] C Raman et al. "Evidence for a critical velocity in a Bose-Einstein condensed gas". In: *Physical Review Letters* 83.13 (1999), p. 2502.

[151] G Reinaudi et al. "Strong saturation absorption imaging of dense clouds of ultracold atoms". In: *Optics letters* 32.21 (2007), pp. 3143–3145.

[152] Wolfgang Rohringer et al. "Non-equilibrium scale invariance and shortcuts to adiabaticity in a one-dimensional Bose gas". In: *Scientific reports* 5 (2015), p. 9820.

[153] Arko Roy and D Angom. "Thermal suppression of phase separation in condensate mixtures". In: *Physical Review A* 92.1 (2015), p. 011601.

[154] Richard Roy et al. "Rapid cooling to quantum degeneracy in dynamically shaped atom traps". In: *Physical Review A* 93.4 (2016), p. 043403.

[155] Richard Roy et al. "Two-element mixture of Bose and Fermi superfluids". In: *Physical Review Letters* 118.5 (2017), p. 055301.

[156] L Salasnich, A Parola, and L Reatto. "Effective wave equations for the dynamics of cigar-shaped and disk-shaped Bose condensates". In: *Physical Review A* 65.4 (2002), p. 043614.

[157] Christian Sanner et al. "Correlations and pair formation in a repulsively interacting Fermi gas". In: *Physical review letters* 108.24 (2012), p. 240404.

[158] Alberto Sartori and Alessio Recati. "Dynamics of highly unbalanced Bose-Bose mixtures: miscible vs immiscible gases". In: *arXiv preprint arXiv:1305.2094* (2013).

[159] H. Schmaljohann et al. "Dynamics of $F = 2$ Spinor Bose-Einstein Condensates". In: *Phys. Rev. Lett.* 92 (4 Jan. 2004), p. 040402.

[160] Matthias Scholl. "Probing an ytterbium Bose-Einstein condensate using an ultra-narrow optical line: towards artificial gauge fields in optical lattices". PhD thesis. Université Pierre et Marie Curie-Paris VI, 2014.

[161] Lingxuan Shao. "Theoretical and experimental study of spin-1 antiferromagnetic Bose-Einstein Condensates". PhD thesis. Ecole Normale Supérieure, 2014.

[162] Jon H Shirley. "Modulation transfer processes in optical heterodyne saturation spectroscopy". In: *Optics Letters* 7.11 (1982), pp. 537–539.

[163] Eric D. Siggia and Andrei E. Ruckenstein. "Bose Condensation in Spin-Polarized Atomic Hydrogen". In: *Phys. Rev. Lett.* 44 (21 May 1980), pp. 1423–1426.

[164] Alice Sinatra and Yvan Castin. "Binary mixtures of Bose-Einstein condensates: Phase dynamics and spatial dynamics". In: *The European Physical Journal D-Atomic, Molecular, Optical and Plasma Physics* 8.3 (2000), pp. 319–332.

[165] A Sinatra et al. "Dynamics of two interacting Bose-Einstein condensates". In: *Physical review letters* 82.2 (1999), p. 251.

[166] DW Snoke and JP Wolfe. "Population dynamics of a Bose gas near saturation". In: *Physical Review B* 39.7 (1989), p. 4030.

[167] Ian B Spielman, William D Phillips, and James V Porto. "Mott-insulator transition in a two-dimensional atomic Bose gas". In: *Physical Review Letters* 98.8 (2007), p. 080404.

[168] Dan M Stamper-Kurn and Wolfgang Ketterle. "Spinor condensates and light scattering from Bose-Einstein condensates". In: *Coherent atomic matter waves*. Springer, 2001, pp. 139–217.

[169] Dan M Stamper-Kurn and Masahito Ueda. "Spinor Bose gases: Symmetries, magnetism, and quantum dynamics". In: *Reviews of Modern Physics* 85.3 (2013), p. 1191.

[170] DM Stamper-Kurn et al. "Optical confinement of a Bose-Einstein condensate". In: *Physical Review Letters* 80.10 (1998), p. 2027.

[171] DM Stamper-Kurn et al. "Quantum tunneling across spin domains in a Bose-Einstein condensate". In: *Physical review letters* 83.4 (1999), p. 661.

[172] Daniel A Steck. "Sodium D line data". In: *Report, Los Alamos National Laboratory, Los Alamos* 124 (2000).

[173] J Stenger et al. "Spin domains in ground-state Bose–Einstein condensates". In: *Nature* 396.6709 (1998), pp. 345–348.

[174] Thilo Stöferle et al. "Transition from a strongly interacting 1D superfluid to a Mott insulator". In: *Physical review letters* 92.13 (2004), p. 130403.

[175] S Stringari. "Dynamics of Bose-Einstein condensed gases in highly deformed traps". In: *Physical Review A* 58.3 (1998), p. 2385.

[176] Sandro Stringari. "Collective excitations of a trapped Bose-condensed gas". In: *Physical review letters* 77.12 (1996), p. 2360.

[177] Julian Struck et al. "Quantum simulation of frustrated classical magnetism in triangular optical lattices". In: *Science* 333.6045 (2011), pp. 996–999.

[178] Jürgen Stuhler et al. "Observation of dipole-dipole interaction in a degenerate quantum gas". In: *Physical Review Letters* 95.15 (2005), p. 150406.

[179] LM Symes, RI McLachlan, and PB Blakie. "Efficient and accurate methods for solving the time-dependent spin-1 Gross-Pitaevskii equation". In: *Physical Review E* 93.5 (2016), p. 053309.

[180] J-B Trebbia et al. "Experimental evidence for the breakdown of a Hartree-Fock approach in a weakly interacting Bose gas". In: *Physical review letters* 97.25 (2006), p. 250403.

[181] S. Trotzky et al. "Suppression of the critical temperature for superfluidity near the Mott transition". In: *Nat. Phys.* 6.12 (Dec. 2010), pp. 998–1004. ISSN: 1745-2473.

[182] S. Uchino, M. Kobayashi, and M. Ueda. "Bogoliubov theory and Lee-Huang-Yang corrections in spin-1 and spin-2 Bose-Einstein condensates in the presence of the quadratic Zeeman effect". In: *Phys. Rev. A* 81 (6 June 2010), p. 063632.

[183] G Valtolina et al. "Exploring the ferromagnetic behaviour of a repulsive Fermi gas via spin dynamics". In: *arXiv preprint arXiv:1605.07850* (2016).

[184] NJ Van Druten and Wolfgang Ketterle. "Two-step condensation of the ideal Bose gas in highly anisotropic traps". In: *Physical review letters* 79.4 (1997), p. 549.

[185] D. Vollhardt and P. Wölfle. *The Superfluid Phases of Helium 3.* Taylor and Francis, London, 1990.

[186] Tino Weber et al. "Bose-Einstein condensation of cesium". In: *Science* 299.5604 (2003), pp. 232–235.

[187] H. Wu, E. Arimondo, and C. J. Foot. "Dynamics of evaporative cooling for Bose-Einstein condensation". In: *Phys. Rev. A* 56 (1 July 1997), pp. 560–569.

[188] K. Yamada. "Thermal Properties of the System of Magnetic Bosons : Bose-Einstein Ferromagnetism". In: *Progress of Theoretical Physics* 67.2 (1982), p. 443.

[189] Tarik Yefsah et al. "Exploring the thermodynamics of a two-dimensional Bose gas". In: *Physical review letters* 107.13 (2011), p. 130401.

[190] S Yi and H Pu. "Spontaneous spin textures in dipolar spinor condensates". In: *Physical review letters* 97.2 (2006), p. 020401.

[191] S. Yi et al. "Single-mode approximation in a spinor-1 atomic condensate". In: *Phys. Rev. A* 66 (1 July 2002), p. 011601.

[192] W. Zhang, S. Yi, and L. You. "Bose-Einstein condensation of trapped interacting spin-1 atoms". In: *Phys. Rev. A* 70 (4 Oct. 2004), p. 043611.

[193] Wenxian Zhang, Su Yi, and Li You. "Mean field ground state of a spin-1 condensate in a magnetic field". In: *New Journal of Physics* 5.1 (2003), p. 77.

[194] Wenxian Zhang et al. "Coherent spin mixing dynamics in a spin-1 atomic condensate". In: *Physical Review A* 72.1 (2005), p. 013602.

[195] Wenxian Zhang et al. "Dynamical instability and domain formation in a spin-1 Bose-Einstein condensate". In: *Physical review letters* 95.18 (2005), p. 180403.

[196] Tilman Zibold et al. "Spin-nematic order in antiferromagnetic spinor condensates". In: *Physical Review A* 93.2 (2016), p. 023614.

Dans ce manuscrit, nous présentons une étude expérimentale d'un gaz de Bose de spin-1 avec des interactions antiferromagnétiques, réalisée pour des atomes de sodium ultra-froids dans l'état hyperfin F=1. Gr au refroidissement évaporatif, nous obtenons un condensat de Bose-Einstein (CBE) spineur, soit dans un piege tres confinant ("piege 0D"), soit sous la forme d'un quasi-condensat quasi-unidimensionnel dans un piege tres allongé. Les deux systemes présentent un ordre magnétique a tres basse température, qui résulte de la compétition entre les interactions d'échange et l'énergie Zeeman quadratique q dans un champ magnétique externe. Nous étudions dans un premier temps l'ordre magnétique se forme dans le piege 0D. A tres basse température deux phases magnétiques sont possible : une phase dite "antiferromagnétique" pour $q < U_s$, ou une phase dite "a aimantation transverse" dans le cas inverse. Dans ce travail, nous nous plas pres de la température critique. Nous mesurons plusieurs scénarios de condensation séquentielles en changeant la magnétisation et le champ magnétique externe, ou une composante Zeeman condense toujours en premier et ou l'ordre magnétique n'apparau'a une seconde température de condensation. Les résultats expérimentaux pour les températures critiques sont bien décrits par une théorie d'Hartree-Fock simplifiée dans les cas ou une seule composante Zeeman est condensée. Dans un second temps, nous étudions l'ordre magnétique du systeme quasi-unidimensionnel a basse température. On observe la formation de domaines de spin ou les composantes Zeeman se sépare spontanément en domaines disjoints en l'asbence de force extérieure (par exemple, un gradient de champ magnétique). On étudie l'état d'équilibre du systeme en fonction de la magnétisation et du champ magnétique. On observe une transition de phase entre une phase miscible et une phase immiscible ou la composante Zeeman $m_F = 0$ forme un domaine séparé de $m_F = \pm 1$ dans le centre du piege. L'équation d'état d'un nuage polarisé (atomes dans l'état $m_F = +1$) est utilisée pour mesurer la température du systeme. Enfin, nous mesurons la réponse mécanique a une force magnétique appliquée pour un systeme binaire $m_F = 0, +1$. Nous mesures une exaltation de la réponse par rapport a l'attente na basée sur l'effet Zeeman habituel, d'un facteur qui peut varier de plusieurs dizaines a environ cent. La configuration spatiale des domaines est ainsi sensible a de tres faibles gradients de champ magnétique inférieurs au mG/cm.

Mots Clés

Condensats de Bose-Einstein, magnétisme, spineur, gaz ultrafroids, thermodynamique, domaines de spin, équation d'état, polarisabilité de spin.

In this manuscript we present the experimental study of a spin-1 Bose gas with antiferromagnetic interactions in the $F = 1$ manifold of Na ultra-cold atoms. Thanks to evaporative cooling in optical traps we obtain a spinor Bose-Einstein condensates (BEC) in a strongly confining trap (" 0D trap") and quasi- condensates in an elongated trap. Due to the competition between the exchange energy U_s and the quadratic Zeeman energy q, the two systems present a magnetic ordering at very low temperatures. The first part of the manuscript is devoted to the study of the magnetic ordering in the 0D trap. At very low temperature, for $q < U_s$ the system is in the antiferromagnetic phase while, for $q > U_s$, is in the transverse magnetised phase. We study the system near to the critical temperature. We investigate different condensation scenarios varying magnetisation and external magnetic field. We observe the condensation of a first component and the appearing of the magnetic ordering at a lower critical temperature, corresponding to the condensation of a second component. We find a good agreement between the experimental data and a simplified Hartree-Fock model when only one Zeeman component is condensed. In the second part of the manuscript, we study of the quasi-1D system at low temperatures. We observe the formation of spin domains: the Zeeman components spontaneously separate in the absence of an external force (i.e., magnetic field gradient). We study the ground state of the system varying magnetisation and q. We observe a first order magnetic transition from a miscible to the immiscible phase. The immiscible phase is characterised by a $m_F = 0$ domain, separated by the $m_F = \pm 1$ components, located in the trap centre. The equation of state of a polarised cloud (all atoms in $m_F = +1$) was measured and the system temperature was determined using it. Finally, we prepare the system in the immiscible phase $m_F = 0, +1$ and we measure the equilibrium response of the system to a magnetic field gradient. The mixture present a response much higher than the response of a single particle. This latter determined considering only the linear Zeeman effect. This configuration is sensible to very low magnetic field gradients $<$ mG/cm.

Keywords

Bose-Einstein condensates, quantum magnetism, spinor, ultra-cold gases, thermodynamics, spin domains, equation of state, spin-dipole polarisability.